

박사 학위논문
Ph. D. Dissertation

PU 기반 쉘 유한요소

Partition of unity based shell finite elements



전 형 민 (全 鏐 民 Jun, Hyungmin)
기계항공시스템학부 해양시스템공학전공
School of Mechanical, Aerospace and Systems Engineering
Division of Ocean Systems Engineering

KAIST

2015

PU 기반 쉘 유한요소

Partition of unity based shell finite elements



Partition of unity based shell finite elements

Advisor : Professor Lee, Phill-Seung

by

Jun Hyungmin

Department of Mechanical, Aerospace and Systems Engineering

Division of Ocean Systems Engineering

KAIST

A thesis submitted to the faculty of KAIST in partial fulfillment of the requirements for the degree of Doctor of Philosophy in the School of Mechanical, Aerospace and Systems Engineering, Division of Ocean Systems Engineering. The study was conducted in accordance with Code of Research Ethics¹



2014. 11. 4

Approved by

Professor Lee, Phill-Seung

[Major Advisor]

¹ Declaration of Ethical Conduct in Research: I, as a graduate student of KAIST, hereby declare that I have not committed any acts that may damage the credibility of my research. These include, but are not limited to: falsification, thesis written by someone else, distortion of research findings or plagiarism. I affirm that my thesis contains honest conclusions based on my own careful research under the guidance of my thesis advisor.

PU 기반 셀 유한요소

전 형 민

위 논문은 한국과학기술원 박사학위논문으로
학위논문심사위원회에서 심사 통과하였음.



2014 년 11 월 4 일

한국과학기술원

심사위원장 이 필 승 (인)

심사위원 정 현 (인)

심사위원 조 연 우 (인)

심사위원 노 혁 천 (인)

심사위원 유 승 화 (인)

DOSE
20105398

전 형 민. Jun, Hyungmin. Partition of unity based shell finite elements. PU 기반 셀 유한요소. School of Mechanical Aerospace and Systems Engineering, Division of Ocean Systems Engineering. 2015. 198 p. Advisor Prof. Lee, Phill-Seung.

ABSTRACT

The partition of unity based shell finite elements are presented. To circumvent locking phenomena, the MITC method is used for the standard and high order displacement interpolations. The partition of unity based shell finite elements not only capture higher gradients but also decrease inter-elemental stress jumps. In particular, the enrichment scheme provided by the partition of unity approximation increases solution accuracy without any traditional local mesh refinement. A partition of unity based shell element with improved membrane behaviors is also proposed. The total Lagrangian formulation is employed allowing for large displacements and large rotations. Considering several benchmark problems, the solutions using the shell element with improved membrane behaviors are compared with those obtained using other shell elements. It is demonstrated that the partition of unity based shell finite elements are reliable and very effective in both linear and non-linear analysis.

Keywords: Partition of unity; Partition of unity based finite element method; Shell element; 3-node triangular element; 4-node quadrilateral element; MITC method; Geometric nonlinear analysis; Large displacements and rotations



Table of Contents

Abstract	i
Table of Contents	ii
List of Tables	vi
List of Figures	xii

Chapter 1. Introduction

1.1 Research Background	1
1.2 Research Purpose	2
1.3 Dissertation Organization	4

Chapter 2. Reviews of Related Literatures and Studies

2.1 The Treatment of the Locking Phenomenon	6
2.1.1 Transverse Shear Locking	6
2.1.2 Membrane Locking	8
2.1.3 In-Plane Shear / Trapezoidal / Volumetric Locking	8
2.1.3.1 In-Plane Shear Locking	8
2.1.3.2 Trapezoidal Locking	10
2.1.3.3 Volumetric Locking	11
2.1.4 Various Methods of Improving Membrane Behaviors	12
2.1.4.1 SRI (Selective Reduced Integration) Method	12
2.1.4.2 Additional Bubble Node	13
2.1.4.3 Incompatible Modes	14
2.1.4.4 Assumed Strain Fields	15
2.1.4.5 Drilling DOFs (Degrees Of Freedom)	16
2.2 The Continuum Mechanics Based Shell Finite Elements	18
2.2.1 Displacement Interpolation	18
2.2.2 The MITC (Mixed Interpolation of Tensorial Components) Approaches	22
2.2.2.1 MITC4 Method for the 4-Node Quadrilateral Shell Element	23
2.2.2.2 MITC9 Method for the 9-Node Quadrilateral Shell Element	24
2.2.2.3 MITC3 Method for the 3-Node Triangular Shell Element	25

2.2.2.4 MITC6 Method for the 6-Node Triangular Shell Element	26
2.3 PU (Partition of Unity) Approximation	27
2.3.1 Mesh Free Methods	28
2.3.2 Hybrid Methods	28
2.3.2 Partition of Unity Based Finite Element Methods	29
Chapter 3. A Partition of Unity Based 3-Node Triangular Shell Element	
3.1 The Finite Element Method Enriched by Interpolation Covers	31
3.2 The Enriched MITC3 Shell Finite Element	33
3.2.1 Enriched Displacement Interpolation	33
3.2.2 Assumed Covariant Transverse Shear Strain Fields	34
3.2.3 Basic Tests	37
3.2.3.1 Isotropic Element Test	37
3.2.3.2 Zero Energy Mode Test	37
3.2.3.3 Patch Test	37
3.3 Computational Efficiency	39
3.4 Convergence Studies	42
3.4.1 Fully Clamped Square Plate Problem	43
3.4.2 Cylindrical Shell Problem	47
3.4.3 Hyperboloid Shell Problem	51
3.5 Local Use of Cover Interpolations	54
3.5.1 Shaft-Shaft Interaction Problem	55
3.5.2 Highly-Sensitive Shell Problem	57
Chapter 4. A Partition of Unity Based 4-Node Quadrilateral Shell Element	
4.1 A 4-Node Element Based on Partition of Unity	60
4.1.1 Partition of Unity Approximation	61
4.1.2 Linear Dependence	63
4.2 The Enriched MITC4 Shell Finite Element	67
4.2.1 Enriched Displacement Interpolation	67
4.2.2 Assumed Covariant Transverse Shear Strain Fields	68
4.3 Benchmark Problems	72
4.3.1 Morley's 30° Skew Plate Under Uniform Pressure	73
4.3.2 Circular Plate Under Uniform Pressure	76

4.3.3 Partly Clamped Hyperbolic Paraboloid Shell	80
4.3.4 Twisted Beam Subjected to Vertical Tip Load	82
4.3.5 Pinched Cylinder	83
4.3.6 Semi-Cylindrical Shell Subjected to an End Pinching Force	87
4.3.7 Scordelis-Lo (Barrel Vault) Roof	90
Chapter 5. MITC3+ Shell Element in Geometric Nonlinear Analysis	
5.1 The MITC3+ Shell Finite Element for Linear Analysis	94
5.1.1 Geometry and Displacement Interpolations	94
5.1.2 Assumed Covariant Transverse Shear Strain Fields	95
5.2 The MITC3+ Shell Element for Geometric Nonlinear Analysis	99
5.2.1 Large Displacement Kinematics	99
5.2.2 Green-Lagrange Strain and Its Interpolation	101
5.3 Numerical Examples	103
5.3.1 Cantilever Plate Subjected to End Shear Force	104
5.3.2 Cantilever Plate Subjected to End Moment	106
5.3.3 Slit Annular Plate under End Shear Force	109
5.3.4 Hemisphere Shell Subjected to Alternating Radial Forces	112
5.3.5 Clamped Semi-Cylindrical Shell under Point Load	115
5.3.6 Fully Clamped Plate under Uniform Pressure	120
Chapter 6. 3-Node Triangular Shell Element with Improved Membrane Behaviors	
6.1 The Enriched MITC3+ Shell Finite Element for Linear Analysis	126
6.1.1 Displacement Interpolation of the MITC3+ Shell Element	126
6.1.2 The Partition of Unity Approximation to Improve Membrane Behaviors	127
6.1.3 Assumed Covariant Transvers Shear Strain Fields	129
6.2 The Enriched MITC3+ Shell Element for Geometric Nonlinear Analysis	131
6.2.1 Large Displacement Kinematics	131
6.2.2 Green-Lagrange Strain and Its Interpolation	134
6.2.3 Total Lagrangian Formulation and Incremental Equilibrium Equation	135
6.2.4 Condensing Out in the Present Element	136
6.3 Computational Efficiency	137
6.4 Numerical Examples	139
6.4.1 Linear Benchmark Problems	141

6.4.1.1 Cantilever Beam for Mesh Distortion Test	141
6.4.1.2 Cook's Skew Beam	142
6.4.1.3 MacNeal's Cantilever Beam	144
6.4.1.4 Curved Cantilever Beam	146
6.4.1.5 Hemispherical Shell	147
6.4.1.6 Scordelis-Lo (Barrel Vault) Roof	151
6.4.1.7 Raasch's Hook Problem	154
6.4.2 Nonlinear Benchmark Problems	155
6.4.2.1 Cantilever Beam Subjected to a Tip Moment	156
6.4.2.2 Column under an Eccentric Compressive Load	158
6.4.2.3 Curved Cantilever Beam	159
6.4.2.4 Hemispherical Shell	162
6.4.2.5 Scordelis-Lo (Barrel Vault) Roof	167
6.4.2.6 Slit Annular Plate	171
Chapter 7. Conclusions and Future Works	
7.1 Conclusions	175
7.2 Future Works	176
Appendices	
Appendix A The Finite Rotations	177
Appendix B Path Following Techniques	182
References	186
Summary (in Korean)	198

List of Tables

Table 2.1. The popular solutions available for eliminating the locking phenomenon.	12
Table 3.1. Basic test results of the MITC3, MITC6 and enriched MITC3 triangular shell finite elements.....	39
Table 3.2. Detailed information on the stiffness matrices of the 3-, 6-, and enriched 3-node shell finite elements for the meshes shown in Figure 3.6.	40
Table 3.3. Solution times (in second) for solving the linear equations. The element meshes are $2N \times 2N$ and $N \times N$ for linear and quadratic shell elements, respectively. (DOFs: degrees of freedom, HB: half-bandwidth)	42
Table 3.4. Relative errors in maximum effective stress in the shaft-shaft interaction problem for the five different shell models in Figure 3.24. Relative error (%) = $(\sigma_{\max}^{ref} - \sigma_{\max}^h) / \sigma_{\max}^{ref} \times 100$	57
Table 3.5. Relative errors in strain energy in the monster shell problem for the five different shell models in Figure 3.26. Relative error (%) = $(E_{ref} - E_h) / E_{ref} \times 100$	59
Table 4.1. Results of eigenvalue analyses of the partition of unity based finite element method, see Figure 4.3 for the meshes. This work was conducted by Tian [93].	66
Table 4.2. List of seven benchmark problems considered in this chapter.	72
Table 4.3. List of shell finite element models for comparison.	73
Table 4.4. Relative errors in the vertical displacement at point A for the Morley's 30° skew plate under uniform pressure. Relative error (%) = $ w_A^{ref} - w_A / w_A^{ref} \times 100$ where w_A^{ref} and w_A denote the reference and finite element solutions, respectively.....	75
Table 4.5. Relative errors in the vertical displacement at point A for the simply supported circular plate under uniform pressure. Relative error (%) = $ w_A^{ref} - w_A / w_A^{ref} \times 100$ where w_A^{ref} and w_A denote the reference and finite element solutions, respectively.	79
Table 4.6. Relative errors in the vertical displacement at point A for the clamped circular plate under uniform pressure. Relative error (%) = $ w_A^{ref} - w_A / w_A^{ref} \times 100$ where w_A^{ref} and w_A denote the reference and finite element solutions, respectively.	79
Table 4.7. Relative errors in the vertical displacement at point A for the partly clamped hyperbolic paraboloid shell. Relative error (%) = $ w_A^{ref} - w_A / w_A^{ref} \times 100$ where w_A^{ref} and w_A denote the reference and finite element solutions, respectively.	81
Table 4.8. Relative errors in displacement at point A for the twisted beam subjected to	

vertical tip load. Relative error (%) = $|w_A^{ref} - w_A| / |w_A^{ref}| \times 100$ where w_A^{ref} and w_A denote the reference and finite element solutions, respectively. 83

Table 4.9. Relative errors in the radial displacement at point A for the pinched cylinder with the uniform meshes. Relative error (%) = $|w_A^{ref} - w_A| / |w_A^{ref}| \times 100$ where w_A^{ref} and w_A denote the reference and finite element solutions, respectively..... 86

Table 4.10. Relative errors in the radial displacement at point A for the pinched cylinder with the distorted meshes. Relative error (%) = $|w_A^{ref} - w_A| / |w_A^{ref}| \times 100$ where w_A^{ref} and w_A denote the reference and finite element solutions, respectively. 87

Table 4.11. Relative errors in the vertical displacement at point A for the semi-cylindrical shell with the uniform meshes. Relative error (%) = $|w_A^{ref} - w_A| / |w_A^{ref}| \times 100$ where w_A^{ref} and w_A denote the reference and finite element solutions, respectively..... 89

Table 4.12. Relative errors in the vertical displacement at point A for the semi-cylindrical shell with the distorted meshes. Relative error (%) = $|w_A^{ref} - w_A| / |w_A^{ref}| \times 100$ where w_A^{ref} and w_A denote the reference and finite element solutions, respectively..... 90

Table 4.13. Relative errors in the vertical displacement at point A for the Scordelis-Lo roof with the uniform meshes. Relative error (%) = $|w^{ref} - w^h| / |w^{ref}| \times 100$ where w^{ref} and w^h denote the reference and finite element solutions, respectively. 92

Table 4.14. Relative errors in the displacement at the point A for the Scordelis-Lo roof with the distorted meshes. Relative error (%) = $|w^{ref} - w^h| / |w^{ref}| \times 100$ where w^{ref} and w^h denote the reference and finite element solutions, respectively. 93

Table 5.1. Tying positions for the assumed transverse shear strain for the MITC3+ shell elements. The distance d is defined in Figure 5.2(c), and $d = 1/10,000$ is used [29]... 96

Table 5.2. Relative errors in the vertical and horizontal displacements at the free end for the cantilever plate subjected to end shear force. Relative error (%) = $|w^{ref} - w^h| / |w^{ref}| \times 100$ or $|v^{ref} - v^h| / |v^{ref}| \times 100$ where w^{ref} and v^{ref} denote the reference solution, and w^h and v^h are finite element solutions..... 105

Table 5.3. Relative errors in the vertical and horizontal displacements at the free end for the cantilever plate subjected to end moment. Relative error (%) = $|w^{ref} - w^h| / |w^{ref}| \times 100$ or $|u^{ref} - u^h| / |u^{ref}| \times 100$ where w^{ref} and u^{ref} denote the reference solution, and w^h and u^h are finite element solutions..... 108

Table 5.4. Relative errors in the vertical displacements at point A and B for slit annular plate under transverse end shear force. Relative error (%) = $|w^{ref} - w^h| / |w^{ref}| \times 100$ where

w^{ref} and w^h denote the reference and finite element solutions, respectively.....	111
Table 5.5. Relative errors in the radial displacements at point A and B for the hemisphere shell subjected to alternating radial forces. Relative error (%) = $ u^{ref} - u^h / u^{ref} \times 100$ or $ v^{ref} - v^h / v^{ref} \times 100$ where u^{ref} and v^{ref} denote the reference solution, and u^h and v^h are finite element solutions.....	114
Table 5.6. Relative errors in the vertical and horizontal displacements at point A for the clamped semi-cylindrical shell under a point load. Relative error (%) = $ w^{ref} - w^h / w^{ref} \times 100$ or $ v^{ref} - v^h / v^{ref} \times 100$ where w^{ref} and v^{ref} denote the reference solution, and w^h and v^h are finite element solutions.....	117
Table 5.7. Relative errors in the vertical displacement at point C for the fully clamped plate under uniform pressure (for the cases $h/L=1/10$ and $h/L=1/100$). Relative error (%) = $ w^{ref} - w^h / w^{ref} \times 100$ where w^{ref} and w^h is denote the reference and finite element solutions, respectively.....	122
Table 5.8. Relative errors in the vertical displacement at point C for the fully clamped plate under uniform pressure (for the cases $h/L=1/1,000$ and $h/L=1/10,000$). Relative error (%) = $ w^{ref} - w^h / w^{ref} \times 100$ where w^{ref} and w^h denote the reference and finite element solutions, respectively.....	123
Table 6.1. Tying positions for the assumed transverse shear strain of the enriched MITC3+ shell element. The distance d defined in Figure 6.3(b), and $d=1/10,000$ is used [29, 156].....	131
Table 6.2. Solution times (in second) for solving the linear problem shown in Figure 6.12. (DOFs: degrees of freedom).....	138
Table 6.3. List of ten benchmark problems solved.....	139
Table 6.4. Summary of element models for comparison.....	140
Table 6.5. Vertical deflections and relative errors at point A for the cantilever beam for distortion test shown in Figure 6.5(a). Relative error (%) = $(v_A^{ref} - v_A) / v_A^{ref} \times 100$ where v_A^{ref} and v_A denote the reference and finite element solutions, respectively.....	142
Table 6.6. Vertical displacements and relative errors at point A for the Cook's skew beam shown in Figure 6.6(a). Relative error (%) = $(v_A^{ref} - v_A) / v_A^{ref} \times 100$ where v_A^{ref} and v_A denote the reference and finite element solutions, respectively.....	143
Table 6.7. Vertical displacements and relative errors at point A for the MacNeal's thin cantilever beam subjected to unit shear force shown in Figure 6.7(a). Relative error	

(%) = $(v_A^{ref} - v_A) / v_A^{ref} \times 100$ where v_A^{ref} and v_A denote the reference and finite element solutions, respectively.....	145
Table 6.8. Vertical displacements and relative errors at point A for the MacNeal's thin cantilever beam subjected to end moment shown in Figure 6.7(a). Relative error (%) = $(v_A^{ref} - v_A) / v_A^{ref} \times 100$ where v_A^{ref} and v_A denote the reference and finite element solutions, respectively.....	145
Table 6.9. Displacements and normalized displacements at point A for the curved cantilever beam shown in Figure 6.8(a). The solutions are obtained with a 1×6 element mesh. Normalized displacement (ND) = v_A / v_A^{ref} and w_A / w_A^{ref} , where v_A^{ref} and w_A^{ref} is the reference solution and v_A and w_A denote the finite element solutions.	147
Table 6.10. Radial displacements and normalized displacements at point A for the hemispherical shell with 18° hole shown in Figure 6.9(a). Normalized displacement (ND) = u_A / u_A^{ref} where u_A^{ref} and u_A denote the reference and finite element solutions, respectively.....	149
Table 6.11. Strain energy (SE) and relative errors in strain energy for the full hemispherical shell shown in Figure 6.9(b). Relative error (RE) (%) = $(SE^{ref} - SE) / SE^{ref} \times 100$ where SE^{ref} and SE denote the reference and finite element strain energy, respectively.	150
Table 6.12. Displacements and normalized displacements at point A for the Scordelis-Lo roof using the uniform meshes. Normalized displacement (ND) = w_A / w_A^{ref} where w_A^{ref} and w_A denote the reference and finite element solutions, respectively.....	153
Table 6.13. Displacements and normalized displacements at point A for the Scordelis-Lo roof using the distorted meshes. Normalized displacement (ND) = w_A / w_A^{ref} where w_A^{ref} and w_A denote the reference and finite element solutions, respectively.....	154
Table 6.14. Displacements and normalized displacements at point A for the Raasch's Hook problem shown in Figure 6.14(a). Normalized displacement (ND) = w_A / w_A^{ref} where w_A^{ref} and w_A denote the reference and finite element solutions, respectively.....	155
Table 6.15. Normalized load-vertical deflections at point A for the cantilever beam subjected a tip moment.	157
Table 6.16. Normalized load-horizontal deflections at point A for the column under an eccentric compressive load.	159
Table 6.17. Normalized load-vertical displacements at point A for the curved beam.	160
Table 6.18. Normalized load-horizontal displacements at point A for the curved beam. ..	161

Table 6.19. Normalized load-radial displacements at the point <i>B</i> for the hemispherical shell with an 18° hole with the uniform meshes. The results are obtained using the 6×6 element mesh of the shell elements.	163
Table 6.20. Normalized load-radial displacements at the point <i>A</i> for the hemispherical shell with an 18° hole with the uniform meshes. The results are obtained using the 6×6 element mesh of the shell elements.	163
Table 6.21. Normalized load-radial displacements at the point <i>B</i> for the hemispherical shell with an 18° hole with the distorted meshes shown in Figure 6.10. The results are obtained using the 6×6 element mesh of the shell elements.	164
Table 6.22. Normalized load-radial displacements at the point <i>A</i> for the hemispherical shell with an 18° hole with the distorted meshes shown in Figure 6.10. The results are obtained using the 6×6 element mesh of the shell elements.	164
Table 6.23. Normalized load-vertical displacements at the point <i>C</i> for the full hemispherical shell with 3×4×4 element meshes.....	166
Table 6.24. Normalized load-vertical displacements at the point <i>C</i> for the full hemispherical shell with 3×6×6 element meshes.....	167
Table 6.25. Normalized load-horizontal displacements at the point <i>A</i> for the Scordelis-Lo roof with the uniform meshes. The results are obtained using the 14×14 element mesh of the shell elements.....	169
Table 6.26. Normalized load-vertical displacements at the point <i>A</i> for the Scordelis-Lo roof with the uniform meshes. The results are obtained using the 14×14 element mesh of the shell elements.	169
Table 6.27. Normalized load-horizontal displacements at the point <i>A</i> for the Scordelis-Lo roof with the distorted meshes. The results are obtained using the 14×14 element mesh of the shell elements.....	170
Table 6.28. Normalized load-vertical displacements at the point <i>A</i> for the Scordelis-Lo roof with the distorted meshes. The results are obtained using the 14×14 element mesh of the shell elements.	170
Table 6.29. Normalized load-vertical displacements at the point <i>A</i> for the slit annular plate subjected to lift line force when the 6×30 element mesh is used.....	173
Table 6.30. Normalized load-vertical displacements at the point <i>C</i> for the slit annular plate subjected to lift line force when the 6×30 element mesh is used.....	174

Table A.1. Rotation tensor with several spin tensor normalizations..... 180



List of Figures

Figure 2.1. Beam deformation assumptions. (a) Beam deformation including transverse shear effect. (b) A two node isoparametric beam element modeling a cantilever beam subjected to a tip moment.	6
Figure 2.2. A isolated 4-node element subjected to the pure bending moment: (a) Initial geometry, (b) Deformation of a single 4-node finite element, (c) Correct deformation of a beam segment in pure bending.	9
Figure 2.3. The graphical descriptions of the (a) trapezoidal and (b) volumetric locking phenomenon.....	10
Figure 2.4. The quadrilateral finite elements with (a) the additional bubble node and (b) incompatible modes.	13
Figure 2.5. Interpolation used. (a) Nodes used for displacements interpolation. (b) Sampling points used for strain interpolation.	16
Figure 2.6. (a) Side displacement associated with drilling degree of freedom w_i and w_j . (b) Nodal displacements of the 6-node triangular element. (c) 3-node triangular element with drilling degree of freedom.	17
Figure 2.7. Continuum mechanics based shell finite element. (a) Geometry of the 9-node shell element. (b) Definition of rotational degrees of freedom α_k and β_k	19
Figure 2.8. MITC4 shell finite element in natural coordinate system and its tying points..	23
Figure 2.9. Strain interpolations and its tying positions of the MITC9 shell element (the e_{ss}^{AS} and e_{st}^{AS} components are interpolated in a symmetric manner); $a = 1/\sqrt{3}$, $b = \sqrt{3}/5$, $c = 1$	24
Figure 2.10. Transverse shear strain tying positions of the 3-node MITC triangular shell element with the constant transverse shear strain along its edges; $r_1 = s_1 = 1/2$	25
Figure 2.11. Strain tying positions of the 6-node MITC triangular shell element; $r_1 = s_1 = 1/2 - 1/2\sqrt{3}$, $r_2 = s_2 = 1/2 + 1/2\sqrt{3}$ and $r_3 = s_3 = 1/3$	26
Figure 3.1. Description of sub-domain for enriched over interpolations; (a) usual interpolation function, (b) cover region or elements affected by the interpolation cover, and (c) an element.	31
Figure 3.2. A 3-node triangular continuum mechanics based shell finite element.....	33
Figure 3.3. Tying points for the covariant transverse shear strains of the enriched MITC3	

shell finite element: (a) for the standard linear displacement interpolation; $r_1 = s_1 = 1/2$, and (b) for the additional quadratic displacement interpolation; $r_1 = s_1 = 1/2 - 1/2\sqrt{3}$ and $r_2 = s_2 = 1/2 + 1/2\sqrt{3}$	35
Figure 3.4. Isotropic test of the present triangular shell element.	37
Figure 3.5. Mesh used for the membrane and bending patch tests.....	38
Figure 3.6. Meshes used and stiffness matrix structures: (a) and (d) for the 3-node shell element, (b) and (e) for the 6-node shell element, and (c) and (f) for the enriched 3-node shell elements. Non-zero entries are colored in black.....	40
Figure 3.7. The total number of degrees of freedom (DOFs) when increasing the number of element layers, N , along an edge p denotes the number of degrees of freedom per node, hence $p = 3$ for the simply supported plate problem.....	41
Figure 3.8. Fully clamped square plate under uniform pressure ($L = 1.0$, $E = 1.7472 \times 10^7$, $q = 1.0$ and $\nu = 0.3$) with three different 4×4 mesh patterns: (a) and (b) triangular mesh for the MITC3, MITC6 and enriched MITC6 shell elements, and (c) quadrilateral mesh for the MITC4 shell element.	44
Figure 3.9. Distorted meshes used for the fully clamped square plate problem, cylindrical shell problems, and hyperboloid shell problems when (a) $N = 4$ and (b) $N = 8$. The number of triangular elements for an $N \times N$ mesh is $2N^2$	45
Figure 3.10. Convergence curves for the fully clamped square plate problem with uniform meshes. For triangular shell elements, the mesh pattern in Figure 3.8(a) is used. The bold line represents the optimal convergence rate, which is 2.0 for linear elements and 4.0 for quadratic elements.	45
Figure 3.11. Convergence curves for the fully clamped square plate problem with uniform meshes. The solid and dotted lines correspond to the results obtained by the mesh patterns in Figure 3.8(a) and (b), respectively. The bold line represents the optimal convergence rate, which is 2.0 for linear elements and 4.0 for quadratic elements.	46
Figure 3.12. Convergence curves for the fully clamped square plate problem with the distorted meshes shown in Figure 3.9. The bold line represents the optimal convergence rate, which is 2.0 for linear elements and 4.0 for quadratic elements.....	47
Figure 3.13. Cylindrical shell problem (4×4 mesh, $L = R = 1.0$, $E = 2.0 \times 10^5$, $\nu = 1/3$ and $p_0 = 1.0$).....	48
Figure 3.14. Convergence curves for the clamped cylindrical shell problem with uniform	

meshes. The bold line represents the optimal convergence rate, which is 2.0 for linear elements and 4.0 for quadratic elements.....	49
Figure 3.15. Convergence curves for the clamped cylindrical shell problem with the distorted meshes shown in Figure 3.9. The bold line represents the optimal convergence rate, which is 2.0 for linear elements and 4.0 for quadratic elements.....	49
Figure 3.16. Convergence curves for the free cylindrical shell problem with uniform meshes. The bold line represents the optimal convergence rate, which is 2.0 for linear elements and 4.0 for quadratic elements.....	50
Figure 3.17. Convergence curves for the free cylindrical shell problem with the distorted meshes shown in Figure 3.9. The bold line represents the optimal convergence rate, which is 2.0 for linear elements and 4.0 for quadratic elements.....	50
Figure 3.18. Hyperboloid shell problem ($E = 2.0 \times 10^{11}$, $\nu = 1/3$ and $p_0 = 1.0$). (a) Shell geometry and boundary conditions, (b) Graded mesh for the clamped case (8×8 mesh, $t/L = 1/1,000$), (c) Mesh for the free case (8×8 mesh).	51
Figure 3.19. Convergence curves for the clamped hyperboloid shell problem with uniform meshes. The bold line represents the optimal convergence rate, which is 2.0 for linear elements and 4.0 for quadratic elements.....	52
Figure 3.20. Convergence curves for the clamped hyperboloid shell problem with the distorted meshes shown in Figure 3.9. The bold line represents the optimal convergence rate, which is 2.0 for linear elements and 4.0 for quadratic elements.....	53
Figure 3.21. Convergence curves for the free hyperboloid shell problem with uniform meshes. The bold line represents the optimal convergence rate, which is 2.0 for linear elements and 4.0 for quadratic elements.....	53
Figure 3.22. Convergence curves for the free hyperboloid shell problem with the distorted meshes shown in Figure 3.9. The bold line represents the optimal convergence rate, which is 2.0 for linear elements and 4.0 for quadratic elements.....	54
Figure 3.23. Shaft-shaft interaction problem with fillets ($E = 2.07 \times 10^{11}$, $\nu = 0.29$).	55
Figure 3.24. Distributions of effective stress for the shaft-shaft interaction problem: for (a) the 2,193 node model of the MITC4 shell elements, (b) the 2,582 node model of the MITC3 shell elements, (c) the 641 node model of the MITC3 shell elements, (d) the 641 node model fully enriched, and (e) the 641 node model locally enriched. The red dot represents enriched nodes (DOFs: total number of degrees of freedom used, Error =	

$(\sigma_v^{ref} - \sigma_v^h) / \sigma_v^{ref} \times 100$	56
Figure 3.25. A “highly-sensitive” shell problem. ($L = R = 10, E = 6.285 \times 10^7, \nu = 0.3$, and $p(r) = e^{-4r^2}$).....	58
Figure 3.26. Deformed shapes for the monster shell problem ($t / L = 1/10,000$): for (a) the $48(\text{axial}) \times 192(\text{circumferential})$ mesh of the MITC4 shell elements, (b) the 48×192 mesh of the MITC3 shell elements, (c) the 16×64 mesh of the MITC3 shell elements, (d) the 16×64 mesh model fully enriched, and (e) the 16×64 mesh model locally enriched. In the figure (e), the red dot represents enriched nodes. (DOFs: the total number of degrees of freedom used, Error = $(E_{ref} - E_h) / E_{ref} \times 100$).....	58
Figure 4.1. Description of sub-domain; finite element shape function h_i , an element e and cover region C_i and C_j constructed by all the elements connected to node i and j , respectively.....	61
Figure 4.2. Linear dependence and independence problem in the partition of unity based finite element method: (a) one-dimensional element of unit length, (b) linearly independent interpolations with prescribed boundary conditions for the 3-node triangular element and (c) linearly dependent interpolations for the 4-node quadrilateral element even though prescribed boundary conditions are applied.....	64
Figure 4.3. Element meshes of the eigenvalue analysis for 4-node quadrilateral elements and mixed meshes with the 3-node triangular and 4-node quadrilateral elements. This work was done by Tian [93].....	66
Figure 4.4. The MITC4 shell finite element: (a) Geometry of the MITC4 shell finite element. (b) Definition of rotational degrees of freedom α_k and β_k	67
Figure 4.5. Polynomial terms in two-dimensional analysis: Pascal triangle for (a) the standard 3-node triangular element, the partition of unity based 3-node triangular element, the (b) standard 4-node quadrilateral element and the partition of unity based 4-node quadrilateral element.	69
Figure 4.6. Tying positions for the covariant transverse shear strains of the PU based 4-node quadrilateral shell finite element: (a) for the standard bilinear displacement interpolations and (b) for the additional high order displacement interpolations. Note that the scheme referred to as MITC9 in Reference [26] is used.....	71
Figure 4.7. Morley’s 30° skew plate under uniform pressure. (a) Problem description and mesh patterns (4×4) used for the MITC3 and enriched MITC3 shell elements. (b)	

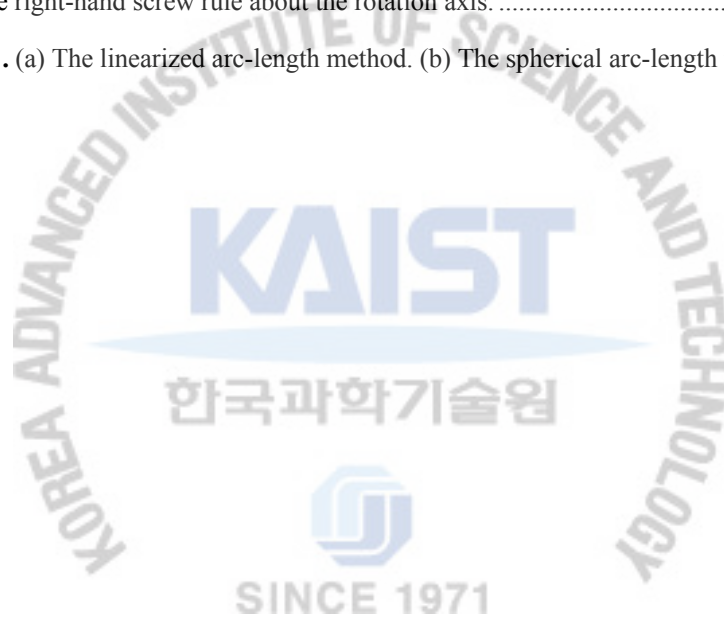
Normalized displacement at point A for the Morley's 30° skew plate.....	74
Figure 4.8. Normalized displacement at point A for the Morley's 30° skew plate when the (a) triangular and (b) quadrilateral shell elements are used.	75
Figure 4.9. Circular plate under uniform pressure.	76
Figure 4.10. Mesh used for the circulate plate under uniform pressure. Mesh pattern I and II are used for the MITC3 and enriched MITC3 shell elements.	77
Figure 4.11. Normalized displacement at the center for the circular plate with $h/r = 0.1$ and $h/r = 0.01$ when the circulate plate is (a) simply supported and (b) clamped.	78
Figure 4.12. Partly clamped hyperbolic paraboloid shell. (a) Problem description and mesh pattern (8×4) used for the MITC and enriched MITC3 shell elements. (b) Normalized displacement at point A in the analysis of the partly clamped hyperbolic paraboloid shell.	80
Figure 4.13. Normalized displacement at point A for the partly clamped hyperbolic paraboloid shell when the (a) triangular and (b) quadrilateral shell elements are used.	81
Figure 4.14. Twisted beam subjected to vertical tip load. (a) Problem description. (b) Mesh patterns used for the MITC3 and enriched MITC3 shell elements.....	82
Figure 4.15. Normalized displacement of the twisted beam subjected to vertical tip load for different thickness cases (left) $h = 0.32$ and (right) $h = 0.0032$	82
Figure 4.16. Pinched cylinder. (a) Problem description. (b) Mesh patterns (4×4) used for the MITC3 and enriched MITC3 shell elements and the distorted mesh.....	84
Figure 4.17. Distorted meshes used for the pinched cylinder, semi-cylindrical shell subjected to an end pinching force and Scordelis-Lo roof when $N = 4$. Two mesh patterns for the MITC3 and enriched MITC3 shell elements.....	85
Figure 4.18. Normalized displacement of the pinched cylinder with (a) the uniform meshes (b) the distorted meshes shown in Figure 4.16(b) and Figure 4.17	86
Figure 4.19. Semi-cylindrical shell subjected to an end pinching force. (a) Problem description. (b) Meshes used (4×4) for the MITC3 and enriched MITC3 shell elements.	88
Figure 4.20. Normalized displacement of the semi-cylindrical shell with (a) the uniform meshes (b) the distorted meshes shown in Figure 4.19(b) and Figure 4.17	89
Figure 4.21. Scordelis-Lo (Barrel Vault) roof. (a) Problem description. (b) Mesh patterns (4×4) used for the MITC3 and enriched MITC3 shell elements.	91
Figure 4.22. Normalized displacement of the Scordelis-Lo roof with (a) the uniform meshes (b) the distorted meshes shown in Figure 4.21(b).	92

Figure 5.1. The MITC3+ shell finite element with the bubble node: (a) Geometry of the MITC3+ shell finite element. (b) Definition of rotational degrees of freedom α_k and β_k .	94
Figure 5.2. Transverse shear strains $e_{1\xi}$, $e_{2\xi}$ and $e_{3\xi}$, and the tying positions (A), (B), (C), (D), (E) and (F) for the assumed transverse shear strain field.	96
Figure 5.3. Flow chart of the iterative procedures for solving the linearized equilibrium equation in the total Lagrangian formulation.	103
Figure 5.4. Cantilever plate subjected to end shear force. (a) Problem description. (b) Meshes used for the MITC4 (top), MITC3 and MITC3+ (bottom) shell elements.	104
Figure 5.5. Load-displacement curves for the cantilever plate subjected to end shear force. For the triangular element meshes, essentially the same response is measured at the two corners.	105
Figure 5.6. Deformed configurations of the cantilever plate under end shear force.	106
Figure 5.7. Cantilever plate subjected to end moment. (a) Problem description. (b) Meshes used for the MITC4 (top), MITC3 and MITC3+ (bottom) shell elements.	107
Figure 5.8. Load-displacement curves for the cantilever plate subjected to end moment. For the triangular element meshes, essentially the same response is measured at the two corners.	108
Figure 5.9. Deformed configurations of the cantilever plate under end moment.	109
Figure 5.10. Slit annular plate under end shear force. (a) Problem description. (b) Meshes used.	110
Figure 5.11. Load-displacement curves for the slit annular plate under end shear force.	111
Figure 5.12. Deformed configurations of the slit annular plate under end shear force.	112
Figure 5.13. Hemisphere shell subjected to alternating radial forces. (a) Problem solved. (b) Meshes used (8×32).	113
Figure 5.14. Load-displacement curves for the hemisphere shell subjected to alternating radial forces when (a) 8×32 and (b) 12×48 element meshes are used.	114
Figure 5.15. Deformed configurations of the hemisphere shell subjected to alternating radial forces.	115
Figure 5.16. Clamped semi-cylindrical shell under point load. (a) Problem description (b) Meshes used (20×20).	116
Figure 5.17. Load-displacement curves for the clamped semi-cylindrical shell under point	

load when (a) 20×20 and (b) 32×32 element meshes are used.....	117
Figure 5.18. Deformed configurations of the clamped semi-cylindrical shell under point load.	118
Figure 5.19. Distorted mesh patterns of the clamped semi-cylindrical shell ($N = 4$) (a) for the MITC4 shell element and (b) for the MITC3 and MITC3+ shell elements.	119
Figure 5.20. Load-displacement curves for the clamped semi-cylindrical shell with the distorted mesh patterns shown in Figure 5.19.....	120
Figure 5.21. Fully clamped plate under uniform pressure and mesh used (4×4).....	121
Figure 5.22. Load-displacement curves for the fully clamped plate under uniform pressure.	122
Figure 5.23. Distorted meshes of the fully clamped plate (a) for the MITC4 shell element and (b) for the MITC3 and MITC3+ shell elements.	124
Figure 5.24. Load-displacement curves for the fully clamped plate with the distorted meshes shown in Figure 5.23.....	125
Figure 6.1. The MITC3+ shell finite element with the bubble node: (a) Geometry of the MITC3+ shell finite element. (b) Definition of rotational degrees of freedom α_k and β_k	126
Figure 6.2. Description of sub-domain; (a) usual interpolation function, h_i and an element, e , (b) cover region, C_i constructed by all the elements connected to node i	128
Figure 6.3. Tying points (A), (B), (C), (D), (E) and (F) for the assumed transverse shear strains of the MITC3+ shell finite element.	130
Figure 6.4. (a) The total number of degrees of freedom (DOFs) and (b) solution times for solving the linear equations when increasing the number of element layers, N , along an edge p denotes the number of DOFs per node in the standard shell element, hence $p = 5$ for Scordelis-Lo roof shown in Figure 6.12.	137
Figure 6.5. Cantilever beam for distortion test. (a) Problem description and mesh pattern used for the MITC3, MITC3+ and enriched MITC3+ shell elements. (b) Vertical deflection versus distortion parameter e	141
Figure 6.6. Cook's skew beam. (a) Problem description. (b) Mesh patterns (2×2) used for the MITC3, MITC3+ and enriched MITC3+ shell elements.	143
Figure 6.7. MacNeal's cantilever beam subjected to two different loading: Unit tip shear force, P and tip bending moment, M . (a) Problem description. (b) Mesh patterns (1×6)	

used for the MITC3, MITC3+ and enriched MITC3+ shell elements.	144
Figure 6.8. Curved cantilever beam. (a) Problem description and mesh patterns (1×6) used for the MITC3, MITC3+ and enriched MITC3+ shell elements. (b) Normalized strain energy in the linear analysis of the curved cantilever beam.	146
Figure 6.9. Descriptions of the hemispherical shell problems: (a) Hemispherical shell with 18° hole and (b) full hemispherical shell. Mesh patterns used for the MITC3, MITC3+ and enriched MITC3+ shell elements. Distorted meshes shown in Figure 6.10 are used.	148
Figure 6.10. Distorted meshes used for the numerical problems solved when $N = 4$	149
Figure 6.11. Convergence curves for the hemispherical shell problems. (a) Normalized displacement of the hemispherical shell with an 18° hole using the uniform meshes (left) and the distorted meshes (right). (b) Normalized strain energy of the full hemispherical shell with the uniform meshes (left) and the distorted meshes (right).	151
Figure 6.12. Scordelis-Lo roof. (a) Problem description. (b) Mesh patterns (4×4) used for the MITC3, MITC3+ and enriched MITC3+ shell elements.	152
Figure 6.13. Normalized displacement of the Scordelis-Lo roof with (a) the uniform meshes (b) the distorted meshes shown in Figure 6.10.	153
Figure 6.14. Raasch's Hook. (a) Problem description. (b) Normalized displacement in the linear analysis of the Raasch's Hook problem.	154
Figure 6.15. Cantilever beam subjected to a tip moment. (a) Problem description. (b) Load-displacement curve for the cantilever beam subjected to a tip moment.	156
Figure 6.16. Deformed configurations of the cantilever beam subjected a tip moment.	157
Figure 6.17. Column under an eccentric compressive load. (a) Problem description. (b) Load-displacement curves for the column.	158
Figure 6.18. Deformed configurations for the column under an eccentric compressive load.	159
Figure 6.19. Load-displacement curves for the curved cantilever beam.	160
Figure 6.20. Deformed configurations for the curved cantilever beam.	161
Figure 6.21. Load-displacement curves for the hemispherical shell with an 18° hole when (a) the uniform meshes and (b) the distorted meshes are used.	162
Figure 6.22. Deformed configurations for the hemispherical shell with an 18° hole.	165
Figure 6.23. Load-displacement curves for the full hemispherical shell with a $3 \times 4 \times 4$ element mesh (left) and a $3 \times 6 \times 6$ element mesh (right).	166

Figure 6.24. Load-displacement curves for the Scordelis-Lo roof with (a) the uniform meshes and (b) the distorted meshes.....	168
Figure 6.25. Deformed configurations for the Scordelis-Lo roof.	171
Figure 6.26. Slit annular plate subjected to lifting line force. (a) Problem description. (b) Mesh patterns used for the MITC3, MITC3+ and enriched MITC3+ shell elements.	172
Figure 6.27. Load-displacement curves for the slit annular plate subjected to lifting line force.....	173
Figure 6.28. Deformed configuration for the slit annular plate subjected to lifting line force.	174
Figure A.1. (a) Representations of finite spatial rotations. (b) The rotation angle is positive obeying the right-hand screw rule about the rotation axis.	178
Figure B.1. (a) The linearized arc-length method. (b) The spherical arc-length method. .	184



Chapter 1. Introduction

1.1 Research Background

The finite element method is a popular and effective procedure for the analysis of solid, fluid, and multi-physics problems. In particular, shell elements are probably the most widely used in finite element analysis, since there are a myriad of shell structures which are widely encountered in many engineering applications [1-4].

A promising approach in the development of general shell elements has been the use of the isoparametric continuum mechanics based shell element which is generally known as a displacement based Mindlin-Reissner shell element [5-7]. The continuum mechanics based shell element was very naturally developed from the three-dimensional continuum isoparametric element formulation by imposing kinematic constraints. In general, transverse shear is accounted for by making use of the Mindlin-Reissner plate/shell theory, denoted “first order theory”, which involves a constant through-the-thickness transverse shear distribution.

Even though the introduction of shear deformations in the shell element seems to be desirable for the analysis of thick shells, these shear deformations cause the main difficulty called “locking”, which must be alleviated for reliable shell finite element analysis. It is well known that displacement based Mindlin-Reissner plate/shell elements often exhibit transverse shear locking as the shell thickness decreases. For shell elements and curved geometries, membrane locking might also occur. Shear and membrane locking are particularly severe for low order shell elements.

To alleviate the transverse shear locking, many methods have been proposed. Commonly adopted remedies to circumvent transverse shear locking are the URI (Uniform Reduced Integration) and SRI (Selective Reduced Integration) first suggested by Zienkiewicz [8-13]. An alternative method for reducing the transverse shear locking is the hybrid and mixed formulation in which separate interpolations are used for the stresses and displacements [14, 15]. Another approach to alleviate locking phenomenon is the ANS (Assumed Natural Strain) method, suggested by MacNeal [16, 17], which is generally reported to be an efficient method using complete numerical integration rules. In this method, the transverse shear strains are interpolated from the displacement dependent strains defined at the mid-side of element edges to reduce locking phenomenon. Based on this concept, some efficient methods have been proposed, including the MITC (Mixed Interpolation of Tensorial Component) method developed by Bathe’s group [18-29] and the DSG (Discrete Strain Gap) approach suggested by Bischoff’s group [30, 31]. Another interesting approach arising from mixed variational formulations is the EAS (Enhanced Assumed Strain) method first presented by Simo and Rifai [32]. The key idea of this approach is based on the use of a strain field composed of a compatible strain field and an en-

hanced strain field based on the Hu-Washizu variational principle to reduce transverse shear locking. Some of these methods are also used to remedy membrane locking, especially the selective reduced integration and the mixed interpolation approach.

Furthermore, it is very difficult to develop effective shell finite elements that give reliable and robust solutions for general shell problems, when considering the various shell geometries, boundary and loading conditions, and mesh patterns used. Specifically, solution accuracy highly depends on how the geometries are meshed. To obtain reliable solutions with desired accuracy special mesh refinements are frequently required, in particular, in areas where non-smooth and near-singular solutions are sought [1-4].

To obtain more accurate solutions, a promising approach, which is referred to as the partition of unity based finite element method, is used to incorporate special enrichment functions within traditional finite element formulations. Within the framework of the partition of unity based finite element method, the partition of unity approximation can be easily achieved by directly adopting high order polynomial local approximations. The concept of the partition of unity approximation was established in the PUM (Partition of Unity Method) by Babuška and Melenk [33] and PUFEM (Partition of Unity Finite Element Method) by Melenk and Babuška [34]. An idea similar to the partition of unity approximation was also introduced and extensively investigated in the *hp* clouds method by Duarte and Oden [35, 36], the GFEM (Generalized Finite Element Method) by Strouboulis et al. [37, 38] and Duarte et al. [39, 40], and the partition of unity based hierarchical finite element method by Taylor et al. [41].

The scheme increases solution accuracy of the traditional low order finite element discretization of solids without any changes in the mesh. The major advantage of the method is that the higher order enrichment is available without introducing additional nodes. That is, traditional nodal point movements or mesh refinements are not used to improve solution accuracy. The partition of unity approximation not only captures higher gradients but also decreases inter-element stress jumps.

In this thesis, the MITC methods are adopted to reduce the transverse shear locking. There are two major reasons for choosing MITC methods in this work. The MITC methods are very attractive because its formulation is simple and general, and in particular, the behavior of the triangular element with the MITC method is isotropic, that is, the stiffness matrix of the element does not depend on the sequence of node numbering. Another important reason is that the MITC method can be directly integrated into the partition of unity approximation to improve performances of the shell finite element.

1.2 Research Purpose

The first objective of this thesis is to present 3-node triangular and 4-node quadrilateral shell finite elements enriched by the high order local approximations within the MITC (Mixed Interpolation of Tensorial

Component) framework, which are called the enriched MITC3 and enriched MITC4, respectively [28]. The key idea of enriched MITC shell elements is to use and treat the assumed covariant transverse shear strain fields separately for the standard linear and the additional high order displacement interpolations. The enriched MITC shell finite elements pass the patch tests and show good convergence behaviors considering a full clamped square plate problem, cylindrical shell problems, and hyperboloid shell problems even when distorted meshes are used. Highly varying stresses in shells can be captured only by locally using high order local approximations.

The second objective in this thesis is to propose the formulation of the 3-node triangular element with enrichment by a cubic bubble function for the rotations in geometric nonlinear analysis [42]. This element is referred to as the MITC3+ shell element. The standard total Lagrangian formulation is employed allowing for large displacement and large rotations. Solving various shell problems, the performance of the MITC3+ shell element is evaluated by comparing the solution accuracies obtained with the other shell elements. The study reveals that the performance of the MITC3+ shell element in nonlinear analysis is as good as the performance of the MITC4 shell element, which is the 4-node quadrilateral shell element, even when highly distorted meshes are used.

Finally, based on the MITC3+ shell element, a 3-node triangular shell element with improved membrane behaviors is presented in this thesis. The partition of unity approximation is only applied to the membrane strains in order to improve the membrane action of the MITC3+ shell element. This element is referred to as the enriched MITC3+ shell element. For geometric nonlinear analysis, the standard total Lagrangian formulation is adopted allowing for large displacement and large rotations. A number of benchmark problems were studied to evaluate its performances in linear and geometric nonlinear ranges. The results confirm that the present method can provide accurate solutions for the membrane dominant problems. It is concluded that the partition of unity approximation is an effective scheme for improving membrane behaviors in the triangular shell element.

Hence the research for this thesis has been divided into three major parts:

- I. Development of the partition of unity based 3-node triangular and 4-node quadrilateral shell finite elements.
- II. Extension of formulation of the 3-node triangular shell element with an enrichment by a cubic bubble function for the rotations to geometric nonlinear analysis.
- III. Performance evaluation of the 3-node triangular shell finite element for improving membrane behaviors in linear and geometric nonlinear analysis.

The present shell finite elements are applicable to simple plate geometries as well as complex shell geometries for both thick and thin shell structures. They provide excellent solution accuracy in both displacement and stresses with relatively low computational cost. Also, the proposed shell elements are sufficiently robust, i.e., present low sensitivity to element distortion, and are generally applicable to both linear and geo-

metric nonlinear shell analyses with high reliability.

1.3 Dissertation Organization

This thesis is organized as follows:

In Chapter 2, the general description of the locking phenomenon in elastic shell theory and some methods to alleviate the locking phenomena are reviewed. In the following sections, the continuum mechanics based shell finite element and the key aspects of the MITC method are presented in detail. Also, various methods using concept of the partition of unity approximation are briefly reviewed in the last section.

In Chapter 3, the finite element procedure to enrich by local approximations is briefly reviewed and the formulation of the partition of unity based 3-node triangular shell element is presented. In the following sections, the key theoretical and numerical aspects of the scheme regarding the computational expense and the convergence of the method are discussed. The results of convergence studies considering a fully clamped square plate problem, cylindrical shell problems, and hyperboloid shell problems are given. Two illustrative example solutions, a shaft-shaft interaction problem and a 'highly-sensitive' shell problem, show the effectiveness of using the partition of unity based 3-node triangular shell finite element, also only locally, that is, only in areas of high stress gradients.

In Chapter 4, the formulation of the partition of unity based 4-node quadrilateral element is briefly reviewed. The issue of the so-called linear dependence problem for the element and a simple scheme to avoid the linear dependence are discussed. The partition of unity based 4-node quadrilateral shell element is proposed in the following section. The results of various benchmark problems including Morley's 30° skew plate, circular plate with uniform load, partly clamped hyperbolic parabolic shell, twisted beam subjected to vertical tip load, pinched cylinder, semi-cylindrical shell subjected to an end pinching force, and Scordelis-lo roof are given.

In Chapter 5, the linear formulation of the MITC3+ shell element is reviewed. In the following section, the geometric nonlinear formulation of the MITC3+ shell element is presented. Also, the performance of the MITC3+ shell element in geometric nonlinear analysis through the solutions of various shell problems including the cantilever plate subjected to end shear force, cantilever plate subjected to end moment, slit annular plate under end shear force, hemisphere shell subjected to alternating radial forces, clamped semi-cylindrical shell under point load, and fully clamped plate under uniform pressure is examined.

Chapter 6 presents the partition of unity based 3-node triangular shell element with improved membrane behaviors. The key theoretical and numerical aspects of this element are studied and the geometric nonlinear formulation of the shell element is also presented. The performance of the proposed shell element in

linear and geometric nonlinear analysis is tested through the solution of various two-dimensional planestress and shell problems, the cantilever beam for mesh distortion test, Cook's skew beam, MacNeal's cantilever beam, curved cantilever beam, hemispherical shell, Scordelis-Lo roof, Raasch's hook problem, cantilever beam subjected to a tip moment, column under an eccentric compressive load, and slit annular plate.

Chapter 7 draws the conclusions and discusses further studies.



Chapter 2. Reviews of Related Literatures and Studies

2.1 The Treatment of the Locking Phenomenon

In finite element analyses, solution accuracy and convergence rate to the analytical solution significantly decrease when non-physical stresses appear, that is the locking phenomenon. These may be transverse shear, membrane, in-plane shear, trapezoidal locking and Poisson locking phenomenon. The locking phenomenon results from numerical backgrounds which are usually related to the low order interpolation functions. This section is aimed to review the general descriptions of locking phenomenon and introduce some remedies to alleviate the locking in an analysis of the finite element method. The mathematical description of the locking phenomenon is beyond the scope of this thesis.

2.1.1 Transverse Shear Locking

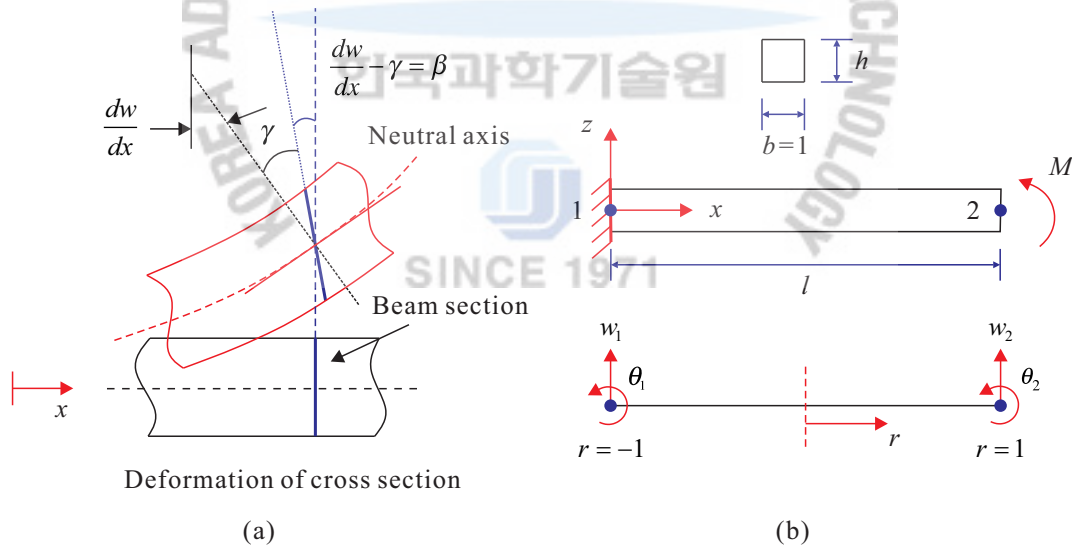


Figure 2.1. Beam deformation assumptions. (a) Beam deformation including transverse shear effect. (b) A two node isoparametric beam element modeling a cantilever beam subjected to a tip moment.

In the shear deformable shell based on the Mindlin-Reissner theory [6, 7], the shell element is subjected to transverse shear locking; that is, the shell finite element becomes too stiff as the shell thickness decreases in bending situations. This transverse shear locking phenomenon also occurs in three-dimensional solid

elements and can be observed in the analysis of thin-walled structures. To explain the transverse shear locking phenomenon, a two-node Timoshenko beam element which includes shear deformations, see **Figure 2.1** is considered. The transverse displacement and in-plane rotation interpolations are represented by

$$w = h_1 w_1 + h_2 w_2 \quad \text{and} \quad \beta = h_1 \theta_1 + h_2 \theta_2 \quad \text{with} \quad h_1 = \frac{1-r}{2} \quad \text{and} \quad h_2 = \frac{1+r}{2} \quad (2.1)$$

and

$$w = \frac{1+r}{2} w_2 \quad \text{and} \quad \beta = \frac{1+r}{2} \theta_2, \quad (2.2)$$

where h_i is the one-dimensional interpolation functions that satisfy the C^0 continuity requirement, w_i and θ_i are the nodal displacements and rotation variables, respectively. For a very thin shell subjected to moment only, the Bernoulli condition (the shear strain is to be zero) should be fulfilled by the displacements and rotations. Imposing this condition gives

$$\gamma = \frac{dw}{dx} - \beta = \frac{w_2}{l} - \frac{1+r}{2} \theta_2 \equiv 0. \quad (2.3)$$

However, for Equation (2.3) to be zero all along the beam, we should have $w_2 = \theta_2 = 0$. Hence, a zero shear strain in the beam can be reached only when there are no deformations. The transverse shear locking occurs since the functions used to interpolate w and β cannot satisfy the condition of zero shear strain all over the element. It is noted that the source of the transverse shear locking is the fact that interpolation functions cannot properly represent the pure bending condition with zero shear stresses, regardless of the use of finite or exact algebra [1].

With the development of shell, plate and beam elements, many methods have been proposed to circumvent the transverse shear locking phenomenon. Remedies to alleviate transverse shear locking commonly used are the RI (Reduced Integration) and SRI (Selective Reduced Integration) approach first suggested by Zienkiewicz [8-13]. However, the reduced integration technique requires the stabilization matrices to avoid spurious modes (hour glass modes). [43, 44]. An alternative method for reducing the transverse shear locking is the hybrid and mixed formulation in which separate interpolations are used for the stresses and displacements [14, 15]. Another approach to alleviate transverse shear locking is the ANS (Assumed Natural Strain) method, suggested by MacNeal [16, 17], which is generally reported to be an efficient method utilizing complete numerical integration rules. In this approach, the transverse shear strains are interpolated from the displacement dependent strains defined at the mid-side of element edges to reduce transverse shear locking. Based on this concept, some efficient methods were proposed, including the MITC (Mixed Interpolation of Tensorial Component) method proposed by Bathe's group [18-29] and the DSG (Discrete Strain Gap) approach suggested by Bischoff's group [30, 31]. To alleviate the transverse shear locking behavior, while preserving the properties of consistency and ellipticity, the MITC method has been successfully used to establish quadrilateral and triangular shell element. DSG method has some unique features. It is directly applicable to both 3-node triangular and 4-node quadrilateral element, without any considerations, like a particular choice of sampling points or the introduction of additional nodes or degrees of freedom and it applies directly to elements of arbitrary polynomial order. Another interesting approach arising from mixed variational formulations

is the EAS (Enhanced Assumed Strain) method first presented by Simo and Rifai [32]. The key idea of this method is based on the use of a strain field composed of a compatible strain field and an enhanced strain field based on the Hu-Washizu variational principle to reduce transverse shear locking.

2.1.2 Membrane Locking

The membrane locking (also known as inextensional locking) addresses the inability of curved shell finite elements to exactly represent pure bending (inextensional bending) deformations, severely overestimating bending stiffness and exhibiting parasitic membrane stresses. Membrane locking phenomenon is different from locking problems within the membrane part of shell elements - namely in-plane shear locking, volumetric locking and trapezoidal locking, see Section 2.1.3. Membrane locking comes from the effect of coupling membrane and bending and becomes more pronounced as shell thickness becomes zero. A typical symptom of the membrane locking is parasitic membrane stresses in the pure bending situations. It is noted that the 3-node triangular shell elements are always flat and therefore free from membrane locking. Even though 4-node quadrilateral shell elements are flat in many situations, if the shell elements are warped, i.e., all four nodes are not in the same plane, the membrane locking occurs in some problems. The modifications of the membrane part of shell finite elements to alleviate membrane locking can automatically improve the in-plane behaviors of the elements. Also, methods for alleviating the in-plane shear locking, trapezoidal locking and volumetric locking influence the behavior with respect to membrane locking. However, this is not guaranteed and there seem to be some conflicts [31].

The ANS (Assumed Natural Strain) methods [17, 45, 46] to eliminate the membrane locking phenomenon have been successfully proposed, especially considering 9-node quadrilateral elements. For the 4-node quadrilateral element the EAS (Enhanced Assumed Strain) method is often adopted to improve the membrane part of shell finite elements [32, 47]. In commercial codes the method of incompatible modes still has some significance, although it is similar to the EAS approach from a theoretical point of view. Like in all locking problems RI (Reduced Integration) with hourglass control to avoid spurious modes also has a great significance especially in commercial codes. Koschnick [31] focused on the application of the DSG (Discrete Strain Gap) method to the problem of membrane locking of both beam elements and shell elements.

2.1.3 In-Plane Shear / Trapezoidal / Volumetric Locking

2.1.3.1 In-Plane Shear Locking

Both the 3-node triangular and the 4-node quadrilateral membrane elements show excellent perfor-

mances in the tractive or compressive dominant problems. However, in situations where bending effects are significant, the solution accuracy of both membrane elements dramatically deteriorates.

Conversely, the accuracy of both membrane elements deteriorates in situations where bending actions are dominantly involved, and very fine meshes or high order elements are needed to obtain accurate solutions in these cases. This is due to the fact that the both 3-node triangular element and 4-node quadrilateral element cannot be used to model bending dominated fields. **Figure 2.2** considers a single 4-node element subjected to the pure bending moment [4].

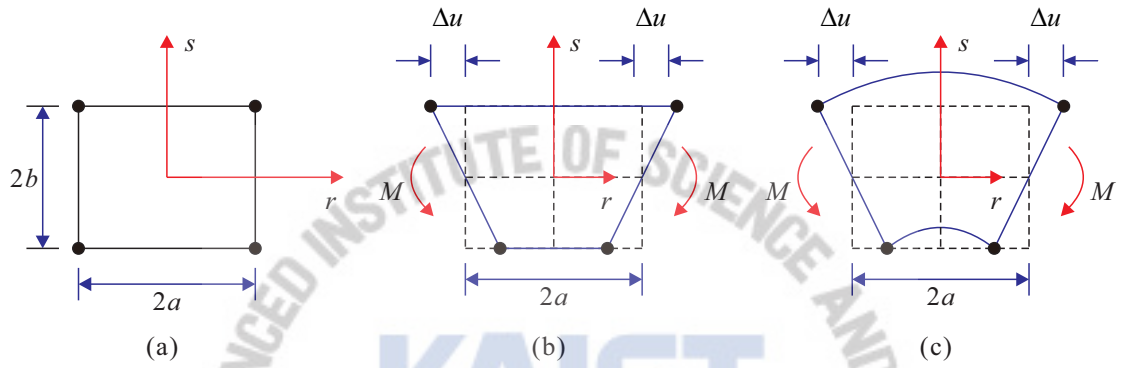


Figure 2.2. A isolated 4-node element subjected to the pure bending moment: (a) Initial geometry, (b) Deformation of a single 4-node finite element, (c) Correct deformation of a beam segment in pure bending.

The analytic solution from beam theory is written as [48]

$$u(r, s) = \frac{M}{EI} rs \quad \text{and} \quad v(r, s) = \frac{Ma^2}{2EI} \left(1 - \frac{r^2}{a^2} \right) + \frac{Mb^2}{2EI} \left(1 - \frac{s^2}{b^2} \right), \quad (2.4)$$

where E is the elastic modulus, I is the second moment of area of the beam's cross-section. Since the 4-node finite element sides are always straight as shown in **Figure 2.2(b)**, the finite element cannot represent the proper bending mode. From **Figure 2.2(b)** the finite element solution becomes

$$u(r, s) = \Delta u r s \quad \text{and} \quad v = 0. \quad (2.5)$$

It is obvious from the Equation (2.5) that the finite element cannot properly reproduce the quadratic distribution of vertical displacements for the pure bending case shown in **Figure 2.2(c)**. This lead to excessive stiffness, which is a natural consequence of the inability of the element sides to be curved. In the pure bending analysis, the exact shear strain should be zero and only normal strains and stresses exist. The exact shear strain from Equation (2.4) is calculated by

$$\gamma_{xy} = \frac{\partial u}{\partial y} + \frac{\partial v}{\partial x} = 0. \quad (2.6)$$

Also, the shear strain of the 4-node finite element from Equation (2.5) is given by

$$\gamma_{xy} = \frac{\partial u}{\partial y} + \frac{\partial v}{\partial x} = \Delta ur . \quad (2.7)$$

In the above equation, the 4-node element has an excess of shear strain which leads to a parasitic stiffness. This contributes to the poor ability of the element to reproduce the bending situation. Similar results are obtained for moments acting on the horizontal sides by changing the coordinate r for s in Equation (2.7). The deficiencies of the 4-node element also appear for severely distorted quadrilateral shapes. These disadvantages can be usually overcome in practice by using very fine meshes or high order interpolation functions. Other alternative methods to improve in-plane behaviors are presented in the Section 2.1.4.

2.1.3.2 Trapezoidal Locking

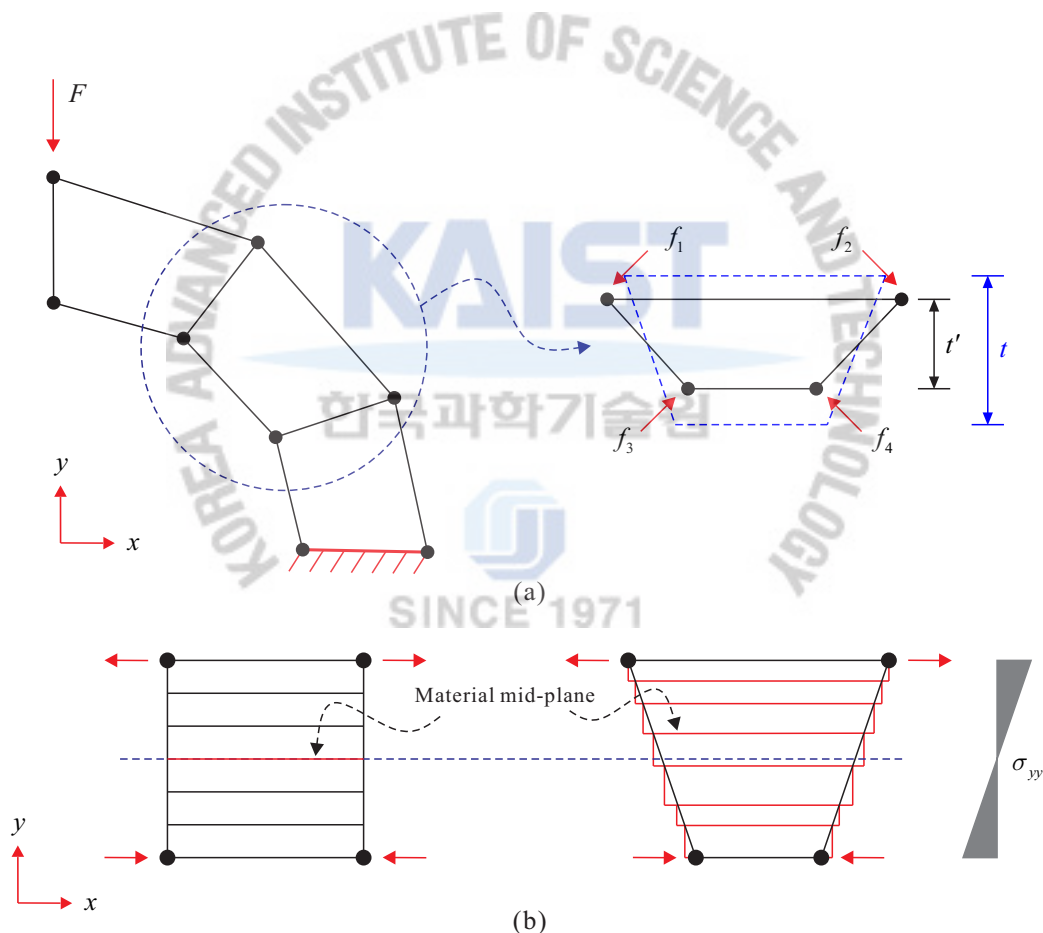


Figure 2.3. The graphical descriptions of the (a) trapezoidal and (b) volumetric locking phenomenon.

When the finite elements are distorted, the phenomenon of the trapezoidal locking (also called curvature thickness locking) phenomenon appears. The trapezoidal locking occurs when the solid elements are used to model the curved structures, for example a curved beam subjected to bending. Due to the geometry of the

model, the trapezoidal shaped elements appear for a regular mesh. **Figure 2.3(a)** illustrates the trapezoidal locking phenomenon in the curved cantilever beam subjected to the end shear force. Due to the curved geometry and the loading condition, the 4-node element shown in **Figure 2.3(a)** deforms in such a way that the element thickness should be decreased. The change of the element thickness causes the parasitic normal stresses along the thickness direction of the element. Physically, the thickness of the curved beam should not change. Hence these stresses are non-physical and cause the trapezoidal locking. The critical parameter for trapezoidal locking is the slenderness of the element.

2.1.3.3 Volumetric Locking

Unlike other locking phenomenon, the volumetric locking (also called dilation or Poisson locking) is caused by neither kinematic nor geometric reasons. The critical parameter in volumetric locking is the Poisson's ratio ν and ultimately the bulk modulus of elasticity κ . The bulk modulus of elasticity is defined as $\kappa = E / (3 - 6\nu)$. Thus, as the Poisson ratio ν closes to 0.5, the bulk modulus of elasticity, κ becomes infinity which means the material behaves as if it is incompressible. **Figure 2.3(b)** demonstrates the volumetric locking phenomenon in a physical point of view. In the undeformed element, the upper portion of the element tries to expand and this demands the shift of the mid-plane of the element. However, the element mid-plane cannot move and force to be in the original position because all the points inside the element are linearly interpolated. Thus there evolves a normal strain without any normal force acting on the element. The upper part of the element experiences tensile and the lower part of experiences compressive stress. This parasitic stress uses up a portion of strain energy that lead to volumetric locking.

To alleviate the volumetric locking phenomenon, Nagtegaal et al. [49] proposed special crossed patch arrangements of 3-node triangular elements. Hughes [50] used the B-bar approach for 4-node quadrilateral elements. Simo and Rifai [32] employed the EAS (Enhanced Assumed Strain) method to reduce the volumetric locking. Doll et al. [51] describe volumetric locking of low order solid and solid-shell elements. Wells et al. [52] developed a p -adaptive scheme to prevent volumetric locking in low order elements. In another approach to reduce the volumetric locking, the SRI (Selective Reduced Integration) technique [53, 54], the penalty function approach based on a reduced constraint concept [55, 56] and mixed formulation methods [57-60] are proposed. Schleich et al. [61] described the utilization of the EAS approach to prevent Poisson locking and demonstrated application in numerical examples.

To sum up, the popular solutions available for alleviating the various locking phenomenon, see **Table 2.1**, are as follows:

- ANS (Assumed Natural Strain) method
- MITC (Mixed Interpolation of Tensorial Components) method
- DSG (Discrete Strain Gap) method
- RI (Reduce Integration) method with stabilization

- SRI (Selective Reduced Integration) with stabilization
- Method of Incompatible modes
- EAS (Enhanced Assumed Strain) method
- Hybrid Stress method
- High order element (p -element)

Table 2.1. The popular solutions available for eliminating the locking phenomenon.

Type of the locking	Methods to alleviating the locking phenomenon
Transverse shear locking	RI, SRI, ANS, MITC, DSG, EAS, p -element
Membrane locking	ANS, EAS, RI, DSG
In-plane shear locking	EAS, RI, SRI, Hybrid stress, p -element, Incompatible modes
Trapezoidal locking	DSG, RI, SRI, p -element
Volumetric locking	EAS, RI, SRI, Hybrid stress, p -element, B-bar method

2.1.4 Various Methods of Improving Membrane Behaviors

In this section, various methods to improve the performance of the membrane elements are reviewed. Depending on element type, these some procedures reduce or even eliminate parasitic shear strain.

2.1.4.1 SRI (Selective Reduced Integration) Method

Equation (2.6) obviously shows that the shear strain in pure bending case should be zero at the element center only. Therefore, the excess of shear strain can be eliminated by sampling the shear strain at the element center ($r = s = 0$). This is simply achieved by using a reduced one point Gauss quadrature for the shear terms in the stiffness matrix, that is SRI (Selective Reduced Integration) method. For this purpose the element stiffness matrix can be divided into two parts:

$$\mathbf{K}^{(e)} = \mathbf{K}_a^{(e)} + \mathbf{K}_s^{(e)}. \quad (2.8)$$

In Equation (2.8) $\mathbf{K}_a^{(e)}$ and $\mathbf{K}_s^{(e)}$ are the element stiffness matrices including the axial and shear contributions, respectively. These stiffness matrices can be rewritten by

$$\mathbf{K}_{aij}^{(e)} = \iint_{A^{(e)}} \mathbf{B}_{ai}^T \mathbf{C} \mathbf{B}_{aj} t dA \quad \text{and} \quad \mathbf{K}_{sij}^{(e)} = \iint_{A^{(e)}} \mathbf{B}_{si}^T \mathbf{C} \mathbf{B}_{sj} t dA \quad (2.9)$$

with

$$\mathbf{B}_{ai} = \begin{bmatrix} \frac{\partial h_i}{\partial x} & 0 \\ 0 & \frac{\partial h_i}{\partial y} \end{bmatrix}, \quad \mathbf{B}_{si} = \begin{bmatrix} \frac{\partial h_i}{\partial y} & 0 \\ 0 & \frac{\partial h_i}{\partial x} \end{bmatrix}, \quad C_a = \begin{bmatrix} c_{11} & c_{12} \\ c_{12} & c_{22} \end{bmatrix} \quad \text{and} \quad C_s = [c_{33}]. \quad (2.10)$$

where $\mathbf{K}_a^{(e)}$ is integrated exactly, either analytically or via a 2×2 Gauss quadrature, whereas a single integration point is used for $\mathbf{K}_s^{(e)}$. This SRI technique can also improve the behavior of 4-node quadrilateral element of arbitrary shapes. The reduced integration of $\mathbf{K}_s^{(e)}$ can also be interpreted as a simple procedure to reduce the excessive influence of the shear terms in the element stiffness matrix. A disadvantage of reduced integration is that 4-node quadrilateral elements applied this technique are not geometric-invariant (also called frame-invariant, geometric or spatial isotropic), although it passes the patch test [62] and, therefore, it converges to the exact solution as the element mesh is refined [1, 4].

2.1.4.2 Additional Bubble Node

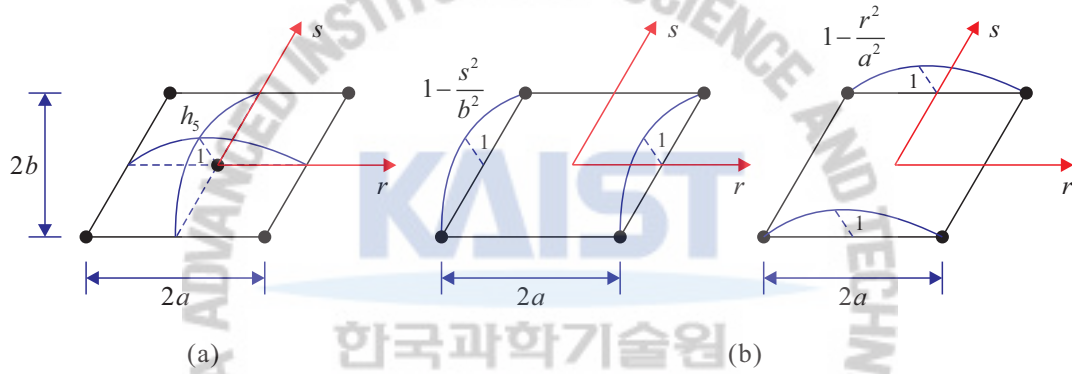


Figure 2.4. The quadrilateral finite elements with (a) the additional bubble node and (b) incompatible modes.

The flexibility of the 4-node quadrilateral element can be improved by adding internal displacement modes to original two-dimensional interpolation function. One of the simplest mode is a bubble function associated with an additional central node, see **Figure 2.4(a)**. The displacement interpolation with the additional bubble node can be expressed by

$$u = \sum_{i=1}^5 h_i u_i \quad \text{and} \quad v = \sum_{i=1}^5 h_i v_i \quad \text{with} \quad h_5 = \left(1 - \frac{r^2}{a^2}\right) \left(1 - \frac{s^2}{b^2}\right), \quad (2.11)$$

where h_i ($i=1,2,3,4$) are the two-dimensional interpolation function corresponding to node i and the internal degrees of freedom u_5 and v_5 (also called hierarchical degrees of freedom) can be eliminated after the element stiffness matrix is constructed (also known as static condensation). It is noted that unknown variables, u_5 and v_5 , are non-physical displacements which represent the differences between the total displacements of the central node and the bilinear field defined by the four corner displacements. For example, the horizontal displacement of the central node is obtained as follows:

$$u(0,0) = \left(\sum_{i=1}^4 h_i u_i \right) + u_5. \quad (2.12)$$

Also, the behavior of the 4-node quadrilateral element with the additional bubble node can be improved by using a reduced single Gauss quadrature for the shear terms as described in the previous section.

2.1.4.3 Incompatible Modes

The 4-node quadrilateral element can be also enhanced by using incompatible modes, $1 - r^2 / a^2$ and $1 - s^2 / b^2$ shown in **Figure 2.4(b)**. In 1971 Wilson [63] first suggested the incompatible modes for 4-node isoparametric finite elements. Taylor [64] presented a method to correct the incompatible mode using a constant Jacobian during the integration of the incompatible modes, which passed the patch test. In 1986 Simo and Rafai [32] introduced the B bar approach to correct the strains produced by incompatible displacements, achieving excellent results for non-rectangular elements. The new displacement interpolations with incompatible modes are written as

$$u = \sum_{i=1}^4 h_i u_i + \left(1 - \frac{r^2}{a^2} \right) \alpha_1 + \left(1 - \frac{s^2}{b^2} \right) \alpha_2, \quad (2.13)$$

$$v = \sum_{i=1}^4 h_i v_i + \left(1 - \frac{r^2}{a^2} \right) \alpha_3 + \left(1 - \frac{s^2}{b^2} \right) \alpha_4, \quad (2.14)$$

where α_1 , α_2 , α_3 and α_4 are the additional degrees of freedom (also called nodeless degrees of freedom) which are internal to each element and can be eliminated by static condensation after the element stiffness matrix is obtained. However, the displacements along the interelemental boundaries are discontinuous and the element is incompatible.

The 4-node quadrilateral element with incompatible modes fails to pass the patch test under constant stress states unless the shape of the element is rectangular. Fortunately, the element satisfies the patch test for arbitrary quadrilateral shapes if the shear terms of the stiffness matrix are evaluated using a reduced point Gauss quadrature, whereas the rest terms of the stiffness matrix can be exactly integrated via a 2×2 Gauss quadrature. The resulting element is geometric-invariant and does not have any spurious mechanisms [4, 64, 65].

The incompatible modes approach can also be successfully applied to 4-node quadrilateral element of arbitrary shape [4, 66]. The strain-displacement matrix with incompatible modes can be written as

$$\mathbf{d} = [\mathbf{B}_C \quad \mathbf{B}_I] \begin{bmatrix} \mathbf{u} \\ \boldsymbol{\alpha} \end{bmatrix}, \quad (2.15)$$

where $\mathbf{u} = [u_1 \ u_2 \ u_3 \ \dots \ v_3 \ v_4]^T$ and $\boldsymbol{\alpha} = [\alpha_1 \ \alpha_2 \ \alpha_3 \ \alpha_4]^T$ are the nodal displacement vector and additional degrees of freedom vector, respectively. Using the $\mathbf{d} = [\varepsilon_{xx} \ \varepsilon_{yy} \ \gamma_{xy}]^T$ and $\mathbf{f} = [\sigma_{xx} \ \sigma_{yy} \ \tau_{xy}]^T$, the strain

energy with the incompatible modes is represented by

$$W = \frac{1}{2} \int \mathbf{f}^T \mathbf{d} dV = \frac{1}{2} \int \mathbf{f}^T \mathbf{B}_C \mathbf{u} dV + \frac{1}{2} \int \mathbf{f}^T \mathbf{B}_I \boldsymbol{\alpha} dV, \quad (2.16)$$

where V is the volume of the element. To pass the patch test, the strain energy term related to the incompatible modes should be zero for a state of constant element stress. Therefore, the following conditions should be satisfied:

$$\frac{1}{2} \mathbf{f}^T \int \mathbf{B}_I \boldsymbol{\alpha} dV = 0 \quad \text{or} \quad \int \mathbf{B}_I dV = 0. \quad (2.17)$$

Equation (2.17) can be fulfilled by adding a constant correction matrix \mathbf{B}_{IC} to the matrix \mathbf{B}_I . To obtain a new strain-displacement, $\bar{\mathbf{B}}_I = \mathbf{B}_I + \mathbf{B}_{IC}$, so that the following equation is satisfied:

$$\int (\mathbf{B}_I + \mathbf{B}_{IC}) dV = 0 \quad \text{or} \quad \int \mathbf{B}_I dV + V \mathbf{B}_{IC} = 0. \quad (2.18)$$

Therefore, the correction matrix can be calculated from

$$\mathbf{B}_{IC} = -\frac{1}{V} \int \mathbf{B}_I. \quad (2.19)$$

This approach is general and can be used to add any number of incompatible displacement modes, or strain patterns, to all types of isoparametric elements. The same numerical integration rules are used to evaluate the element stiffness matrices.

Recently, Sussman and Bathe [67] reported that the element with incompatible modes can display non-physical behavior in analyses modeling very large strain and meshes of incompatible modes elements can also contain spurious modes in rather simple nonlinear analyses. Nevertheless, The method of incompatible modes still has some significance in commercial codes.

2.1.4.4 Assumed Strain Fields

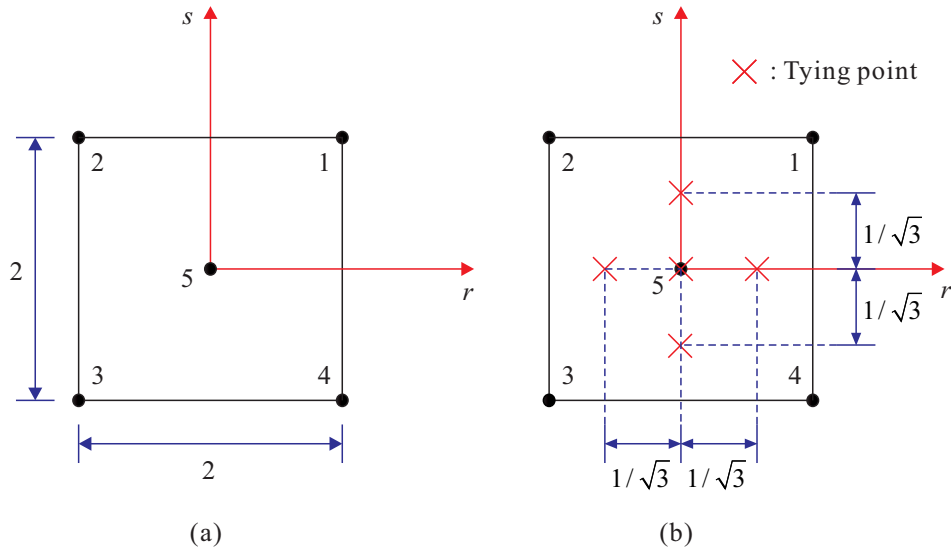


Figure 2.5. Interpolation used. (a) Nodes used for displacements interpolation. (b) Sampling points used for strain interpolation.

Another method to improve the performance of the 4-node quadrilateral element is to impose over the element the assumed strain fields compatible with the condition $\gamma_{xy} = 0$ for the pure bending case. Dvorkin and Vassolo [20] proposed the assumed strain fields for improving the performance of the 4-node quadrilateral element. To interpolate the displacement field inside the element, the interpolation functions of a 5-node isoparametric element are used as shown in **Figure 2.5(a)**. At the element level, the two displacements corresponding to node 5 are condensed resulting only eight degrees of freedom. The strain fields are interpolated by

$$\varepsilon_{xx} = \alpha_1 + \alpha_2 x + \alpha_3 y, \quad \varepsilon_{yy} = \alpha_4 + \alpha_5 x + \alpha_6 y \quad \text{and} \quad \gamma_{xy} = \alpha_7, \quad (2.20)$$

where the α_i ($i=1,2,\dots,7$) are expressed in terms of the nodal displacements by sampling the assumed strains at a number of element points and equaling their values to those given by the strains deduced from the original displacement field. This leads to a substitute strain matrix from which the element stiffness matrix can be directly obtained on [20]. The proposed element with assumed strain fields does not contain spurious zero energy modes and the element passes the path test.

2.1.4.5 Drilling DOFs (Degrees of Freedom)

The drilling DOFs (degrees of freedom) are rotational degrees of freedom which lie at right angles to the plane. First striking feature of drilling degrees of freedom is that the shell elements can be directly formed as the combination of a plane element and a plate bending element [68]. The second advantage of drilling degrees of freedom is to improve better membrane performances with only corner nodes. For example, 3-node triangular element with drilling degrees of freedom performs much better than the original 3-node triangular

element, although not as well as the 6-node triangular element.

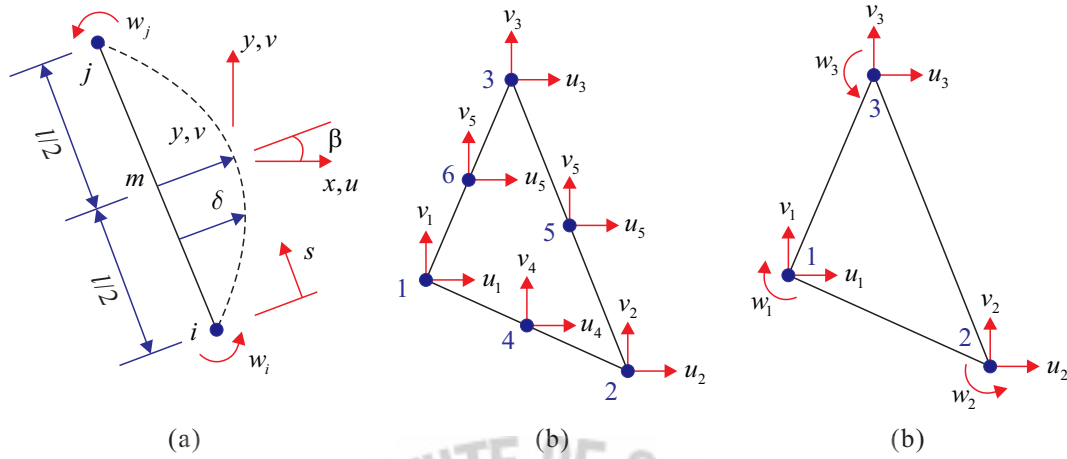


Figure 2.6. (a) Side displacement associated with drilling degree of freedom w_i and w_j . (b) Nodal displacements of the 6-node triangular element. (c) 3-node triangular element with drilling degree of freedom.

The drilling degrees of freedom are simply implemented by adding one rotational degrees of freedom at each corner while removing two degrees of freedom at the middle of each side, see **Figure 2.6**. Hence, the 6-node triangular element can be converted to elements that have corner nodes only with three degrees of freedom per node. In the large finite element mesh of 6-node triangular elements, the conversion reduces the total number of degrees of freedom by a factor of 5/8.

Figure 2.6(a) shows a typical side of a plane element. The δ is the component of side-normal displacement due to drilling degrees of freedom w_i and w_j at node i and j . The δ and its midside value δ_m are represented by

$$\delta = \frac{s(l-s)}{2l}(w_j - w_i) \quad \text{and} \quad \delta_m = \frac{l}{8}(w_j - w_i). \quad (2.21)$$

When w_i is equal to w_j , the side becomes straight. When $w_i = -w_j$, the midside displacement δ_m can be regarded as the mid-span deflection of a simply supported beam of length l , loaded by end moments such that end rotations are of equal magnitude but opposite sign. Equation (2.21) can be converted by substituting the x and y components of δ_m and l , specifically $\delta_m \cos \beta = u_m$, $\delta_m \sin \beta = v_m$, $l \cos \beta = y_j - y_i$, and $l \sin \beta = x_j - x_i$. Side-tangent displacement at midside is taken as the average of side-tangent displacements at the corner nodes at the two ends of the side. Therefore, after adding the contribution to displacement from nodes i and j , the midside displacement components can be obtained by

$$\begin{bmatrix} u_m \\ v_m \end{bmatrix} = \frac{1}{2} \begin{bmatrix} u_i \\ v_j \end{bmatrix} + \frac{1}{2} \begin{bmatrix} u_j \\ v_i \end{bmatrix} + \frac{w_j - w_i}{8} \begin{bmatrix} y_j - y_i \\ x_i - x_j \end{bmatrix}. \quad (2.22)$$

Using the transformation matrix, the complete relation between degree of freedom in 6-node triangular element and triangular element with drilling degrees of freedom, see **Figure 2.6**, can be represented by

$$\begin{bmatrix} u_1 & v_1 & u_2 & v_2 & \cdots & u_6 & v_6 \end{bmatrix}^T = [\mathbf{T}] \begin{bmatrix} u_1 & v_1 & w_1 & u_2 & v_2 & w_2 & u_3 & v_3 & w_3 \end{bmatrix}^T, \quad (2.23)$$

in which $[\mathbf{T}]$ is the transformation matrix which contains information from Equation (2.22) to relate the six translational degrees of freedom at midside nodes to translational and drilling degrees of freedom at nodes.

In the development of drilling degree of freedom, A zero energy mode exists in elements with drilling degree of freedom. For example, u_m and v_m are zero when translational degree of freedom are zero at corner nodes and $w_i = w_j$. The results are that a mesh of elements formulated in this way displays no strain energy if all drilling degrees of freedom in mesh are equal. Therefore, the global stiffness matrix becomes singular. To eliminating the singularity in this formulation, one drilling degrees of freedom in the mesh should be zero. For 4-node elements, an alternative approach to avoid the singularity is to invoke a penalty constraint by associating strain energy with the function $w_1 - w_2 + w_3 - w_4$.

2.2 The Continuum Mechanics Based Shell Finite Elements

In 1970 Ahmad et al. [5] proposed the isoparametric continuum shell element with independent C^0 interpolations for displacements and rotations. The most promising feature of this shell element is that the interpolation functions require only C^0 continuity. However the price for this low order continuity requirement is the introduction of shear deformations in the formulation. Hence, these elements are generically known as Reissner / Mindlin shell elements [6, 7]. The continuum mechanics based shell element was very naturally developed from the three-dimensional continuum isoparametric element formulation by imposing kinematic constraints. Even though the introduction of shear deformations in the formulation seems to be desirable for the analysis of thick shells, and also makes very natural the transition from 3D to shell elements [1], these shear deformations cause the main numerical difficulty of the continuum mechanics based shell element: the transverse shear locking phenomenon [1-4]. The extension of the continuum mechanics based shell element for nonlinear analysis (small strains) was independently proposed by Ramm [69] and by Krakeland [70].

2.2.1 Displacement Interpolation

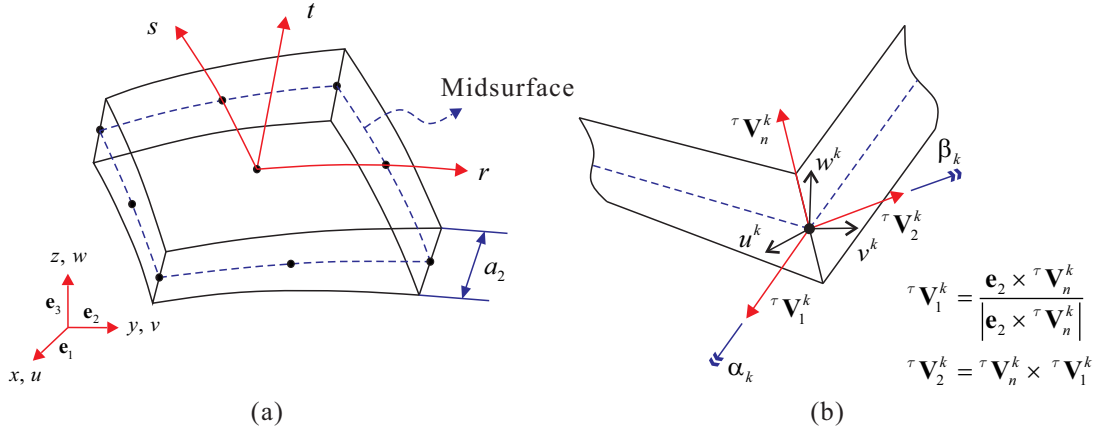


Figure 2.7. Continuum mechanics based shell finite element. (a) Geometry of the 9-node shell element. (b) Definition of rotational degrees of freedom α_k and β_k .

A continuum mechanics based shell element is shown in **Figure 2.7**. In order to define its configuration at a given time τ , we use the coordinates of the mid-surface nodes referred to a global Cartesian system with base vector \mathbf{e}_i and director vectors defined at the mid-surface nodes. These nodal director vectors are defined so as to approximate as closely as possible the shell normal at those nodes. An arbitrary point inside the shell element is defined by its natural coordinates system (r, s, t) and its geometry interpolation is obtained by

$${}^\tau \mathbf{x}(r, s, t) = \sum_{i=1}^q h_i(r, s) {}^\tau \mathbf{x}_i + \frac{t}{2} \sum_{i=1}^q a_i h_i(r, s) {}^\tau \mathbf{V}_n^i, \quad (2.24)$$

where q is the number of nodes per element, h_i is the two-dimensional interpolation functions of the standard isoparametric procedure corresponding to node i , ${}^\tau \mathbf{x}_i$ is the position vector of the node i at time τ , a_i is shell thickness at node i (assumed as invariant during the deformation), and ${}^\tau \mathbf{V}_n^k$ is the director vector corresponding to the i -th mid-surface node at time τ , which is defined taking into account that $|\tau \mathbf{V}_n^k| = 1$. While the natural coordinates (r, s) are defined on the element mid-surface ($t = 0$) the natural coordinate t is measured at any point along the corresponding director vector direction. The second term on the RHS in Equation (2.24) shows that at any point on the element mid-surface the unit director vector times the thickness is interpolated from the nodal values.

The geometry interpolation in Equation (2.24) satisfies C^0 continuity. For describing the kinematics of the continuum mechanics based shell element, the two main assumptions are following. The element thickness remains constant due to the assumed infinitesimal strains deformation and the director vectors remain straight during the deformation.

From Equation (2.24) the covariant base vectors of the natural coordinate system (r, s, t) are given by

$${}^{\tau}\mathbf{g}_i = \frac{\partial {}^{\tau}\mathbf{x}}{\partial r_i} \quad \text{with } r_1 = r, r_2 = s, r_3 = t \quad (2.25)$$

and the contravariant base vectors need to satisfy the following relation:

$${}^{\tau}\mathbf{g}^i \cdot {}^{\tau}\mathbf{g}_j = \delta_j^i. \quad (2.26)$$

The symbol δ_j^i in the above equation denotes the Kronecker delta and is defined as follows:

$$\delta_j^i = \begin{cases} 1 & i = j \\ 0 & i \neq j \end{cases}. \quad (2.27)$$

For linear kinematics the τ -configuration is considered to be coincident with the 0-configuration (reference configuration). The displacements for the configuration at time τ can be expressed as

$${}^{\tau}\mathbf{u} = {}^{\tau}\mathbf{x} - {}^0\mathbf{x} \quad (2.28)$$

and hence

$${}^{\tau}\mathbf{u}(r, s, t) = \sum_{i=1}^q h_i(r, s) {}^{\tau}\mathbf{u}_i + \frac{t}{2} \sum_{i=1}^q a_i h_i(r, s) ({}^{\tau}\mathbf{V}_n^i - {}^0\mathbf{V}_n^i), \quad (2.29)$$

in which ${}^{\tau}\mathbf{u}_i$ is the vector of incremental nodal displacements at node i and ${}^0\mathbf{V}_n^i$ denotes the director vector at node i in the configuration at time 0. In the reference configuration, two vectors, ${}^0\mathbf{V}_1$ and ${}^0\mathbf{V}_2$, are defined as shown **Figure 2.7(b)** and nodal director vector forms the orthonormal basis (${}^0\mathbf{V}_1, {}^0\mathbf{V}_2, {}^0\mathbf{V}_n$). For the infinitesimal rotations, director vector corresponding to node i at time τ can be written by [42, 71, 72]

$${}^{\tau}\mathbf{V}_n^k = {}^0\mathbf{V}_n^k + {}^{\tau}\boldsymbol{\theta}_i \times {}^0\mathbf{V}_n^k, \quad (2.30)$$

$${}^{\tau}\boldsymbol{\theta}_i = \alpha_i {}^0\mathbf{V}_1^i + \beta_i {}^0\mathbf{V}_2^i, \quad (2.31)$$

$${}^{\tau}\mathbf{V}_n^i = {}^0\mathbf{V}_n^i + \beta_i {}^0\mathbf{V}_1^i - \alpha_i {}^0\mathbf{V}_2^i. \quad (2.32)$$

Therefore, substituting Equation (2.32) into Equation (2.29), displacement interpolation for the linear analysis is obtained by

$${}^{\tau}\mathbf{u}(r, s, t) = \sum_{i=1}^q h_i(r, s) {}^{\tau}\mathbf{u}_i + \frac{t}{2} \sum_{i=1}^q a_i h_i(r, s) (-\alpha_i {}^0\mathbf{V}_2^i + \beta_i {}^0\mathbf{V}_1^i). \quad (2.33)$$

Dropping the superscript τ in Equation (2.33), the displacement interpolation is rewritten by

$$\mathbf{u}(r, s, t) = \sum_{i=1}^q h_i(r, s) \mathbf{u}_i + \frac{t}{2} \sum_{i=1}^q a_i h_i(r, s) (-\alpha_i \mathbf{V}_2^i + \beta_i \mathbf{V}_1^i), \quad (2.34)$$

where \mathbf{u}_i is the vector of nodal displacements at node i , \mathbf{V}_1^i and \mathbf{V}_2^i are the unit vectors orthogonal to \mathbf{V}_n^i and to each other, and α_i and β_i are the rotations of the director vector \mathbf{V}_n^i about \mathbf{V}_1^i and \mathbf{V}_2^i , respectively, at node i . It is apparent from Equation (2.34) that this continuum mechanics based shell element has 5 degrees of freedom per node.

The infinitesimal strain tensor at any point inside the shell can be written by

$$\mathbf{e} = e_{ij} \mathbf{g}^i \otimes \mathbf{g}^j, \quad (2.35)$$

where e_{ij} is the covariant strain components, \mathbf{g}^i and \mathbf{g}^j are the contravariant base vectors. We use the notation (${}^0\mathbf{g}^i \otimes {}^0\mathbf{g}^j$), to indicate the dyadic tensorial product between the two contravariant base vectors. In Equation (2.35), $e_{tt} = 0$ because the shell thickness is constant. From the kinematic relations between strain components and displacements, the covariant strain components are

$$e_{ij} = \frac{1}{2} \left(\mathbf{g}_i \cdot \frac{\partial \mathbf{u}}{\partial r_j} + \mathbf{g}_j \cdot \frac{\partial \mathbf{u}}{\partial r_i} \right) = \mathbf{B}_{ij} \mathbf{U} \quad (2.36)$$

with

$$\mathbf{U} = [u_1 \quad u_2 \quad \cdots \quad v_1 \quad \cdots \quad w_n \quad \alpha_1 \quad \cdots \quad \alpha_n \quad \beta_1 \quad \cdots \quad \beta_n]_{5n \times 1}^T. \quad (2.37)$$

The complete strain tensor is then written as

$$\mathbf{e} = e_{ij} \mathbf{g}^i \otimes \mathbf{g}^j = (\mathbf{B}_{ij} \mathbf{g}^i \otimes \mathbf{g}^j) \mathbf{U}, \quad (2.38)$$

where the strain matrix \mathbf{e} contains all six strain components (ε_{xx} , ε_{yy} , ε_{zz} , ε_{xy} , ε_{yz} , ε_{zx}) in the global Cartesian coordinate system and the \mathbf{g}^i are already mentioned in Equation (2.26). The strain-displacement matrix $\hat{\mathbf{B}}$ of the shell element is constructed as

$$\tilde{\mathbf{e}} = \hat{\mathbf{B}} \mathbf{U}, \quad (2.39)$$

where $\tilde{\mathbf{e}}$ is $[\varepsilon_{xx} \quad \varepsilon_{yy} \quad \varepsilon_{zz} \quad 2\varepsilon_{xy} \quad 2\varepsilon_{yz} \quad 2\varepsilon_{zx}]^T$.

In order to apply the plane stress assumption, that is, the stress normal to the surface should be zero, let us introduce the local Cartesian shell-aligned coordinate system,

$$\mathbf{e}_{\bar{r}} = \frac{\mathbf{g}^1 \times \mathbf{g}^3}{\|\mathbf{g}^1 \times \mathbf{g}^3\|}, \quad \mathbf{e}_{\bar{s}} = \frac{\mathbf{g}^3 \times \mathbf{e}_{\bar{r}}}{\|\mathbf{g}^3 \times \mathbf{e}_{\bar{r}}\|}, \quad \mathbf{e}_t = \frac{\mathbf{g}^3}{\|\mathbf{g}^3\|}. \quad (2.40)$$

The strain in the local coordinate system ($\mathbf{e}_{\bar{r}}$, $\mathbf{e}_{\bar{s}}$, \mathbf{e}_t) is then given

$$\tilde{\mathbf{e}}^* = \mathbf{Q} \hat{\mathbf{B}} \mathbf{U} = \mathbf{B}^* \mathbf{U}, \quad (2.41)$$

in which \mathbf{Q} represents a matrix that transforms the strain in the global Cartesian system to the local Cartesian system. The elements of the matrix \mathbf{Q} are obtained from the direction cosines of the local base vectors ($\mathbf{e}_{\bar{r}}$, $\mathbf{e}_{\bar{s}}$, \mathbf{e}_t),

$$\mathbf{Q} = \begin{bmatrix} l_1^2 & m_1^2 & n_1^2 & l_1 m_1 & m_1 n_1 & n_1 l_1 \\ l_2^2 & m_2^2 & n_2^2 & l_2 m_2 & m_2 n_2 & n_2 l_2 \\ l_3^2 & m_3^2 & n_3^2 & l_3 m_3 & m_3 n_3 & n_3 l_3 \\ 2l_1 l_2 & 2m_1 m_2 & 2n_1 n_2 & l_1 m_2 + l_2 m_1 & m_1 n_2 + m_2 n_1 & n_1 l_2 + n_2 l_1 \\ 2l_2 l_3 & 2m_2 m_3 & 2n_2 n_3 & l_2 m_3 + l_3 m_2 & m_2 n_3 + m_3 n_2 & n_2 l_3 + n_3 l_2 \\ 2l_3 l_1 & 2m_3 m_1 & 2n_3 n_1 & l_3 m_1 + l_1 m_3 & m_3 n_1 + m_1 n_3 & n_3 l_1 + n_1 l_3 \end{bmatrix} \quad (2.42)$$

with

$$l_1 = (\mathbf{e}_{\bar{r}})_1, \quad m_1 = (\mathbf{e}_{\bar{r}})_2, \quad n_1 = (\mathbf{e}_{\bar{r}})_3, \quad (2.43)$$

$$l_2 = (\mathbf{e}_{\bar{s}})_1, \quad m_2 = (\mathbf{e}_{\bar{s}})_2, \quad n_2 = (\mathbf{e}_{\bar{s}})_3, \quad (2.44)$$

$$l_3 = (\mathbf{e}_t)_1, \quad m_3 = (\mathbf{e}_t)_2, \quad n_3 = (\mathbf{e}_t)_3. \quad (2.45)$$

The stress-strain law containing the plane-stress assumption, that is the stress normal to the shell surface is zero, is given by

$$\mathbf{C} = \frac{E}{1-\nu^2} \begin{bmatrix} 1 & \nu & 0 & 0 & 0 & 0 \\ \nu & 1 & 0 & 0 & 0 & 0 \\ 0 & 0 & 0 & 0 & 0 & 0 \\ 0 & 0 & 0 & \frac{1-\nu}{2} & 0 & 0 \\ 0 & 0 & 0 & 0 & k\frac{1-\nu}{2} & 0 \\ 0 & 0 & 0 & 0 & 0 & k\frac{1-\nu}{2} \end{bmatrix} \quad (2.46)$$

where k is a shear correction factor which is to attain results consistent with classical bending theory. In Equation (2.46), this amounts to multiplying the transverse shearing moduli by $k = 1$.

2.2.2 The MITC (Mixed Interpolation of Tensorial Components) Approaches

The MITC (Mixed Interpolation of Tensorial Components) approach was originally proposed a 4-node shell element, MITC4, by Dvorkin and Bathe [18, 19] as a solution for the transverse shear locking problem that does not incorporate numerical drawbacks. Later, this method extended for the high order quadrilateral and the triangular shell elements such as MITC3, MITC6, MITC8, MITC9 and MITC16 [21, 23]. In this section, the MITC formulations of the continuum mechanics based shell finite elements are briefly reviewed. Again, the covariant strain component is as follows:

$$e_{ij} = \frac{1}{2}(\mathbf{g}_i \cdot \mathbf{u}_{,j} + \mathbf{g}_j \cdot \mathbf{u}_{,i}), \quad (2.47)$$

where

$$\mathbf{g}_i = \frac{\partial \mathbf{x}}{\partial r_i}, \quad \mathbf{u}_{,i} = \frac{\partial \mathbf{u}}{\partial r_i} \quad \text{with } r_1 = r, \quad r_2 = s, \quad r_3 = t. \quad (2.48)$$

Now let us define a set of the co-called tying points $k = 1, \dots, n_{ij}$ on the shell midsurface with coordinate (r_k, s_k) , and define the assumed covariant strain components e_{ij}^{AS} as

$$e_{ij}^{AS}(r, s, t) = \sum_{k=1}^{n_{ij}} h_{ij}^k(r, s) e_{ij} \Big|_{(r_j^k, s_j^k, t)}, \quad (2.49)$$

where n_{ij} is the number of tying points for the assumed covariant strain component e_{ij}^{AS} , and h_{ij}^k are the assumed interpolation functions satisfying

$$h_{ij}^k(r_{ij}^l, s_{ij}^l) = \delta_{kl}, \quad l = 1, \dots, n_{ij} \quad (2.50)$$

for the covariant strain component e_{ij} . It is noted that this tying procedure is carried out on the elemental level for each individual element. The covariant strain in terms of the nodal displacement is obtained by

$$e_{ij} = \mathbf{B}_{ij} \mathbf{U}, \quad (2.51)$$

where \mathbf{B} is the strain-displacement matrix and \mathbf{U} is the nodal displacement vector. Hence the assumed covariant strain components are rewritten as

$$e_{ij}^{AS} = \left[\sum_{k=1}^{n_{ij}} h_{ij}^k(r, s) \mathbf{B}_{ij} \Big|_{(r_{ij}^k, s_{ij}^k, t)} \right] \mathbf{U} = \mathbf{B}_{ij}^{AS} \mathbf{U}. \quad (2.52)$$

After applying the proper stress-strain law including the shell assumption, the element stiffness matrix is constructed in the same manner as the displacement based shell element.

2.2.2.1 MITC4 Method for the 4-Node Quadrilateral Shell Element

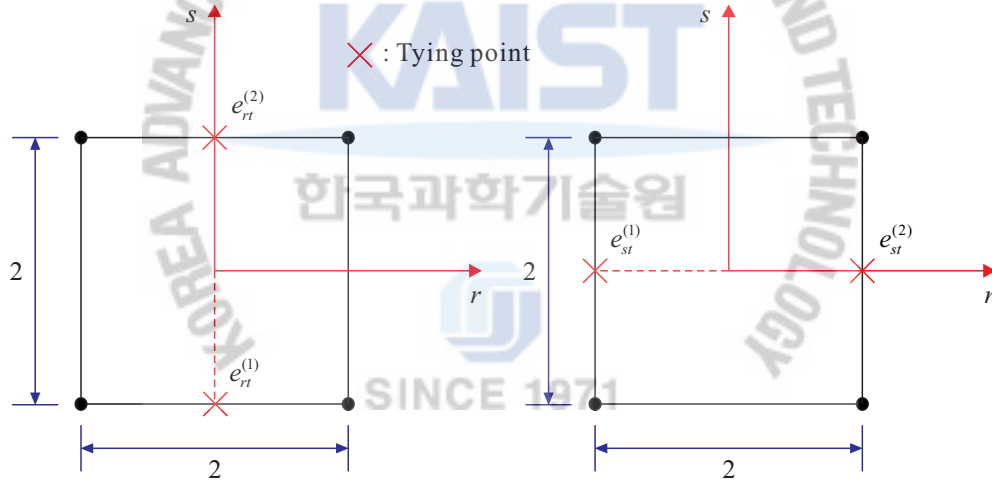


Figure 2.8. MITC4 shell finite element in natural coordinate system and its tying points.

Using the interpolation and tying position shown in Figure 2.8, the transverse shear components of the covariant strain are written by

$$e_{rt}^{AS} = \frac{1}{2}(1-s)e_{rt}^{(1)} + \frac{1}{2}(1+s)e_{rt}^{(2)}, \quad (2.53)$$

$$e_{st}^{AS} = \frac{1}{2}(1-r)e_{st}^{(1)} + \frac{1}{2}(1+r)e_{st}^{(2)}. \quad (2.54)$$

This assumed transverse shear strain fields in Equation (2.53) are derived as follows:

$$e_{rt}^{AS} = a + br + cs + drs . \quad (2.55)$$

To construct constant strains along the bottom and top edges of the element by the given tying points, the following conditions should be satisfied, see **Figure 2.8**,

$$e_{rt}^{AS}(-1, -1) = e_{rt}^{(1)}, \quad e_{rt}^{AS}(1, -1) = e_{rt}^{(1)}, \quad (2.56)$$

$$e_{rt}^{AS}(-1, 1) = e_{rt}^{(2)}, \quad e_{rt}^{AS}(1, 1) = e_{rt}^{(2)}. \quad (2.57)$$

From above conditions, the four linear equations are obtained by

$$a - b - c - d = e_{rt}^{(1)}, \quad a + b - c - d = e_{rt}^{(1)}, \quad (2.58)$$

$$a - b + c - d = e_{rt}^{(2)}, \quad a + b + c + d = e_{rt}^{(2)}. \quad (2.59)$$

and the coefficients are

$$a = \frac{1}{2}(e_{rt}^{(1)} + e_{rt}^{(2)}), \quad c = \frac{1}{2}(e_{rt}^{(2)} - e_{rt}^{(1)}) \quad \text{and} \quad c = d = 0. \quad (2.60)$$

The coefficients for the r terms disappear since the transverse shear strain is constant for the r direction. Hence, substituting Equation (2.60) into Equation (2.55), the assumed transverse shear strain, that is the same to Equation (2.53), can be obtained.

2.2.2.2 MITC9 Method for the 9-Node Quadrilateral Shell Element

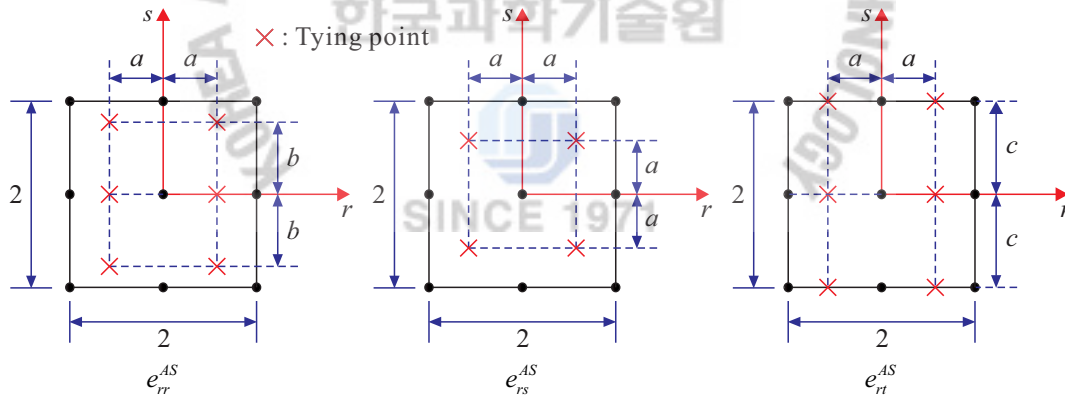


Figure 2.9. Strain interpolations and its tying positions of the MITC9 shell element (the e_{ss}^{AS} and e_{st}^{AS} components are interpolated in a symmetric manner); $a = 1/\sqrt{3}$, $b = \sqrt{3/5}$, $c = 1$.

The MITC9 element has been studied in many publications [1, 21, 22, 26]. **Figure 2.9** gives the strain interpolations and tying points used for the MITC9 method in which the covariant strain component fields for the in-plane actions are interpolated and tied to the also interpolated displacement field. The assumed transverse shear strain fields for the MITC9 can be derived as the same procedures of the MITC4 method. For the

MITC9, the strain components e_{rr} , e_{ss} , e_{rt} and e_{st} have six tying points and in-plane shear strain component e_{rs} is interpolated based on four tying points. This approach takes care of both membrane and transverse shearing locking problems. The stiffness matrix of the element is then formed based on these interpolated strain components and full integration is used. The element does not present any spurious energy modes. In view of the more complicated strain interpolation and full integration scheme, the MITC9 is a more computationally expensive element, but it is accurate and fairly insensitive to element deformations. The MITC9 shell element is known to satisfy the ellipticity and consistency conditions and to show good convergence behaviors [1, 21, 22, 26].

2.2.2.3 MITC3 Method for the 3-Node Triangular Shell Element

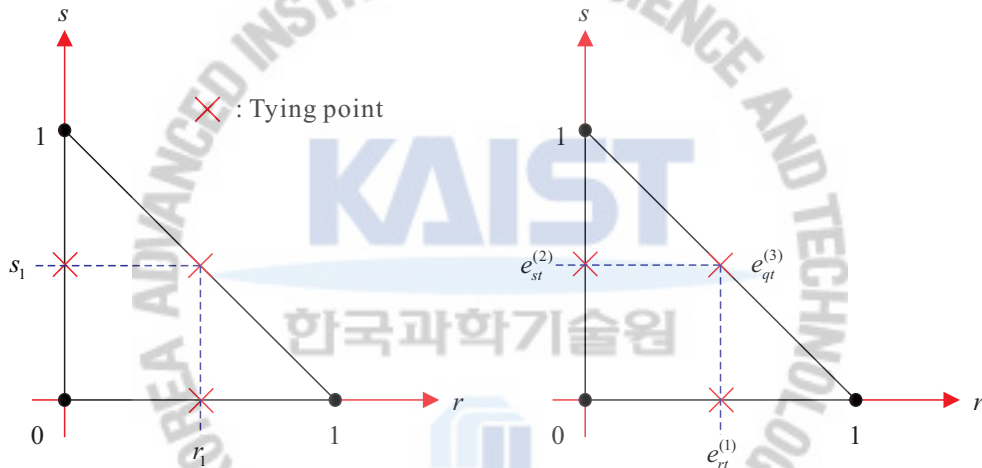


Figure 2.10. Transverse shear strain tying positions of the 3-node MITC triangular shell element with the constant transverse shear strain along its edges; $r_1 = s_1 = 1/2$.

Lee and Bathe [23] proposed the MITC3 shell element which satisfies spatially isotropic condition. Since the geometry of the 3-node triangular shell element is always flat, only the mixed (assumed) interpolation for the transverse shear strains are used. The tying and interpolation schemes are shown in **Figure 2.10** and its assumed transverse shear components are obtained by

$$e_{rt}^{AS} = e_{rt}^{(1)} + cs, \quad (2.61)$$

$$e_{st}^{AS} = e_{st}^{(2)} - cr, \quad (2.62)$$

where $c = e_{st}^{(2)} - e_{rt}^{(1)} - e_{st}^{(3)} + e_{rt}^{(3)}$ and, at tying points, $e_{rt}^{(n)}$ and $e_{st}^{(n)}$ are calculated from Equation (2.47), see **Figure 2.10**.

2.2.2.4 MITC6 Method for the 6-Node Triangular Shell Element

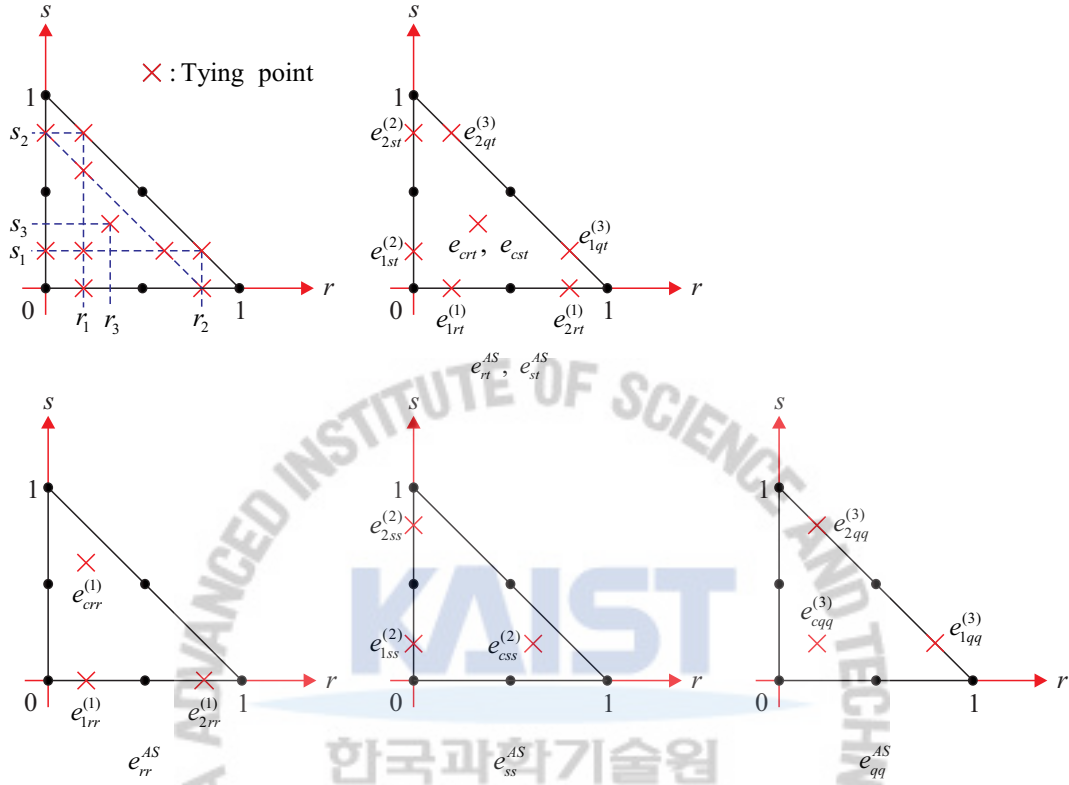


Figure 2.11. Strain tying positions of the 6-node MITC triangular shell element; $r_1 = s_1 = 1/2 - 1/2\sqrt{3}$, $r_2 = s_2 = 1/2 + 1/2\sqrt{3}$ and $r_3 = s_3 = 1/3$.

For the 6-node shell element, in-plane strains are also assumed to avoid the membrane locking. The assumed in-plane shear strain component e_{rs}^{AS} is obtained as follows [23]:

$$e_{rs}^{AS} = \frac{1}{2}(e_{rr}^{AS} + e_{ss}^{AS}) - e_{qq}^{AS}. \quad (2.63)$$

Figure 2.11 shows the tying points corresponding to each normal strain. We assumed the starting polynomials

$$e_{rr}^{AS} = a_1 + b_1 r + c_1 s, \quad (2.64)$$

$$e_{ss}^{AS} = a_2 + b_2 r + c_2 s, \quad (2.65)$$

$$e_{qq}^{AS} = a_3 + b_3 r + c_3 (1 - r - s), \quad (2.66)$$

and have

$$a_1 = \tilde{m}_{rr}^{(1)} - \tilde{l}_{rr}^{(1)}, \quad b_1 = 2\tilde{l}_{rr}^{(1)}, \quad c_1 = \sqrt{3}(e_{cr}^{(1)} - a_1 - b_1 r_1), \quad (2.67)$$

$$a_1 = \tilde{m}_{ss}^{(2)} - \tilde{l}_{ss}^{(2)}, \quad b_2 = \sqrt{3}(e_{css}^{(2)} - a_2 - c_2 s_1), \quad c_2 = 2\tilde{l}_{ss}^{(2)}, \quad (2.68)$$

$$a_3 = \tilde{m}_{qq}^{(3)} - \tilde{l}_{qq}^{(3)}, \quad b_3 = -2\tilde{l}_{qq}^{(3)}, \quad c_3 = \sqrt{3}(e_{cqq}^{(3)} - a_3 - b_3 r_1), \quad (2.69)$$

where

$$\tilde{m}_{jj}^{(i)} = \frac{1}{2}(e_{1jj}^{(i)} + e_{2jj}^{(i)}), \quad \tilde{l}_{jj}^{(i)} = \frac{\sqrt{3}}{2}(e_{2jj}^{(i)} + e_{1jj}^{(i)}) \quad \text{with } j = r, s, q \text{ for } i = 1, 2, 3. \quad (2.70)$$

Consequently, the isotropic in-plane strain field is obtained and the interpolation function for the in-plane shear strain e_{rs}^{AS} is immediately given by Equation (2.63). For this MITC6 triangular shell element, linear transverse shear strains along edges are assumed as

$$e_{rt}^{AS} = a_1 + b_1 r + c_1 s + d_1 r s + e_1 r^2 + f_1 s^2, \quad (2.71)$$

$$e_{st}^{AS} = a_2 + b_2 r + c_2 s + d_2 r s + e_2 r^2 + f_2 s^2 \quad (2.72)$$

and have

$$a_1 = \tilde{m}_{rt}^{(1)} - \tilde{l}_{rt}^{(1)}, \quad b_1 = 2\tilde{l}_{rt}^{(1)}, \quad e_1 = 0, \quad (2.73)$$

$$a_2 = \tilde{m}_{st}^{(2)} - \tilde{l}_{st}^{(2)}, \quad c_2 = 2\tilde{l}_{st}^{(2)}, \quad f_2 = 0, \quad (2.74)$$

$$c_1 = 6e_{crt} - 3e_{cst} + 2\tilde{m}_{st}^{(3)} - 2\tilde{m}_{rt}^{(3)} - 4a_1 - b_1 + a_2, \quad (2.75)$$

$$b_2 = -3e_{crt} + 6e_{cst} - 2\tilde{m}_{st}^{(3)} + 2\tilde{m}_{rt}^{(3)} + a_1 - 4a_2 - c_2, \quad (2.76)$$

$$e_2 = 3e_{crt} - 6e_{cst} + 3\tilde{m}_{st}^{(3)} - \tilde{l}_{st}^{(3)} - 3\tilde{m}_{rt}^{(3)} + \tilde{l}_{rt}^{(3)} + b_1 + 3a_2 + c_2, \quad (2.77)$$

$$f_1 = -6e_{crt} + 3e_{cst} - 3\tilde{m}_{st}^{(3)} - \tilde{l}_{st}^{(3)} + 3\tilde{m}_{rt}^{(3)} + \tilde{l}_{rt}^{(3)} + 3a_1 + b_1 + c_2, \quad (2.78)$$

$$d_1 = -e_2, \quad d_2 = -f_1, \quad (2.79)$$

where

$$\tilde{m}_{ji}^{(i)} = \frac{1}{2}(e_{1ji}^{(i)} + e_{2ji}^{(i)}), \quad \tilde{l}_{ji}^{(i)} = \frac{\sqrt{3}}{2}(e_{2ji}^{(i)} + e_{1ji}^{(i)}) \quad \text{with } j = r, s \text{ for } i = 1, 2, 3 \quad (2.80)$$

The formulation of the MITC6 shell element given here represents the peculiar unstable behaviors reported in Reference [24]. Kim and Bathe [25] improved the MITC6 shell element which does not show the instable sometimes observed with the MITC6 shell element given here.

2.3 PU (Partition of Unity) Approximation

Partition of unity approximations have unique features for p -adaptivity and local refinement without any traditional local mesh refinement of the problem domain. Some of the recent developments of the methods associated with the partition of unity approximation are reviewed in this section.

2.3.1 Mesh Free Methods

The key feature of the meshfree methods is that they do not need a mesh to discretize the domain considered. In simulations where the material can move around or where large deformations can occur, the connectivity of the mesh can be difficult to maintain without introducing error into the simulation. Meshfree methods are an excellent approach to solve these problems. Hence, there has been much interest in these methods in recent years. Furthermore, meshfree approximations are usually smoother than the finite element interpolations and the results from the meshfree approximations are more accurate. The origin of meshfree approach can be trace back to the SPH (Smooth Particle Hydrodynamics) proposed by Lucy [73]. Presently, a huge amount of literature on meshfree methods have been published. Some of the important works in the meshfree method include the DEM (Diffuse Element Method) by Nayroles and Touzot [74], EFG (Element Free Galerkin) method by Belytschko et al. [75], RKPM (Reproducing Kernel Particle Method) by Liu et al. [76], PIM (Point Interpolation Method) by Liu and Gu [77], MLPG (Meshless Local Petrov-Galerkin) method by Atluri and Zhu [78], LBIE (Local Boundary Integral Equation) method by Zhu et al. [79], and LPIM (Local Point Interpolation Method) by Liu and Gu [80], LoKriging (Local Kriging) method by Lam and Wang [81], MLNNI (Meshfree Local Natural Neighbour Interpolation) method by Yongchang and Hehua [82] and NEM (Natural Element Method) by Braun and Sambridge [83], and so forth.

Although the meshfree methods are free from the drawbacks of finite element method, they have also fatal disadvantages. For instance, the meshfree method possess the lack of Kronecker-delta property of shape functions which make it rather cumbersome to implement the essential boundary conditions. Furthermore, the computational cost of the meshfree methods are in general more expensive than that of the finite element methods due to the use of MLS (Moving Least Square) approximation. Choice of an appropriate order of numerical integration influences the convergence of numerical solutions of meshfree methods. Unfortunately, the nodal shape functions of meshfree methods, such as MLS, are highly complex in nature and this leads to difficulty evaluating an accurate numerical integration [84].

2.3.2 Hybrid Methods

As a result, there have been tremendous efforts in recent years to develop hybrid methods combining the finite element methods with meshfree methods. The aim of these methods is to incorporating the strengths of both the finite element method and meshfree methods while avoiding their weaknesses. Examples of such efforts include combining the FEM (Finite Element Method) with EFG (Element Free Galerkin) [85, 86] and coupling the FEM and BEM (Boundary Element Method) with MLPG method [87]. In these methods, the domain of the problem is usually divided into two sub-domains which are modelled by the FEM/BEM and meshfree methods, respectively. Other approaches, such as hierarchical mixed approximation method proposed by Huerta and Fernandez [88] and coupling of FE (Finite Element) method and EFG method using collocation approach developed by Xiao and Dhanasekar [89] have also been presented. The coupled finite element method with meshfree method offers significant advantages in reducing the computational time of the

meshfree methods and imposing the essential boundary conditions easily. Hao et al. [90] presented a new method called the MPFEM (Moving Particle Finite Element Method) which provides continuity of both the approximated solution and its gradient. The MPFEM do not require any treatment for imposing essential boundary conditions. Based on the similar concept of the MPFEM, Liu et al. [91] developed the RKEM (Reproducing Kernel Element Method) by combining the virtues of finite element approximations and reproducing kernel particle approximations. Two distinguished features of RKEM are: the arbitrarily high order smoothness and the interpolation property of the shape functions. These properties are desirable especially in solving Galerkin weak forms of higher order partial differential equations and in treating Dirichlet boundary conditions.

2.3.3 Partition of Unity Based Finite Element Methods

Another type of hybrid methods called PU (Partition of Unity) based finite element methods has been proposed in recent years. The partition of unity based finite elements have been attracted much interest from researchers in computational solid mechanics since they offer several advantages over the conventional finite element method. The feature of the partition of unity based finite element method is the use of the partition of unity approximation. The partition of unity approximation is constructed by the partition of unity function and local approximation function that can be defined by user. A free choice of local approximation function allows flexibility for modelling complicated problems and the construction of high order approximations without the addition of extra nodes. The displacement interpolation of the partition of unity based finite element is represented by

$$u_h(x) = \sum_{i \in I} h_i u_i + \sum_{i \in I} h_i \sum_k \varphi_k^p a_{i(k)}^p, \quad (2.81)$$

in which $\sum_{i=1}^N h_i(x) \equiv 1$ form the partition of unity, φ_k^p is the user-defined local function on cover P_i which is composed of elements surrounding node i , and $a_{i(k)}^p$ are the additional degrees of freedom at node i . The concept of partition of unity approximation was established in the PUM (Partition of Unity Method) [33] and PUFEM (Partition of Unity Finite Element Method) [34] proposed by Babuška and Melenk. The similar idea to the partition of unity method was also introduced and extensively investigated in the hp clouds method by Duarte and Oden [35, 36], the GFEM (Generalized Finite Element Method) by Strouboulis et al. [37, 38] and Duarte et al. [39, 40], and the partition of unity-based hierarchical finite element method by Taylor et al. [41]. The similar partition of unity approximation can also be found, earlier, in the MM (Manifold Method) proposed by Shi [92]. In the MM, the partition of unity is the finite element shape function and the local function is called cover function. Recently, Jeon et al. [28] proposed a 3-node shell finite element enriched by interpolation covers based on the MITC method. The proposed shell element shows the good convergence behaviors in the analysis of various shell problems, even when distorted meshes are used.

The major disadvantage of the partition of unity based finite element methods is the linear dependence problem which occurs when both the partition of unity functions and the local functions are taken as explicit

polynomials [33, 34, 93]. In order to avoid the linear dependence problem, Oden et al. [36] suggested excluding the space spanned by the terms of finite element shape functions from that of the local approximation functions. The mapped quadrilateral shape functions were used in the work of Strouboulis et al. [37, 38], but they could not eliminate the linear dependencies completely. Tian et al. [94] studied some effective approaches to eliminate the linear dependency problems. These approaches include suppressing the additional unknown degrees of freedom, using constant local functions at the boundary nodes, using triangular mesh around quadrilateral mesh, and deleting the polynomial terms included in the span of the partition of unity function, which was first suggested by Oden et al. [36]. A recent progress on this aspect is the SGFEM (Stable Generalized Finite Element Method) by Babuška and Banerjee [95], which is aiming to improve the conditioning property of the GFEM (Generalized Finite Element Method). The basic idea of the SGFEM is to use a modified local function. Rajendran et al. [84, 96] proposed PU-based FE-meshfree element wherein the FE shape functions are used for partition of unity, and the least-square PIM (Point Interpolation Method) shape function are used for local approximation. With this choice, the proposed PU-based FE-meshfree element is free of the linear dependence problem. Cai et al. [97] suggested that the local approximation at a boundary node is constructed by a modified least-squares approach and that at an inner node using a polynomial basis. These dually constructed local approximation avoid the linear dependency problems.



Chapter 3. A Partition of Unity Based 3-Node Triangular Shell Element

In this chapter, A new scheme to the partition of unity based 3-node triangular shell finite element within the MITC method (also called hereafter enriched MITC3) is presented. The MITC method is used for the standard and enriched displacement interpolations. The partition of unity based 3-node shell finite element not only captures higher gradients but also decreases inter-elemental stress jumps. In particular, the partition of unity approach increases solution accuracy without any traditional local mesh refinement. Convergence studies considering a fully clamped square plate problem, cylindrical shell problems, and hyperboloid shell problems demonstrate the good predictive capability of the enriched MITC3 shell finite element, even when distorted meshes are used. We evaluate the effectiveness of the method, and also illustrate the use of the enrichment scheme applied only locally through the solution of two additional shell problems: a shaft-shaft interaction problem and a monster shell problem.

3.1 The Finite Element Method Enriched by Interpolation Covers

Enriching the finite element procedure is in principle, and theoretically, straightforward but difficulties are encountered in obtaining effective schemes. To introduce the basic procedure for the enrichment scheme considered here, let us briefly consider in this section a two-dimensional analysis problem.

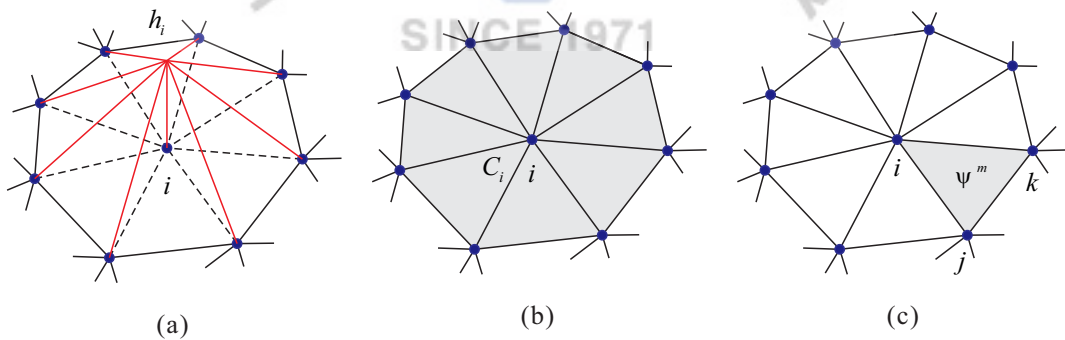


Figure 3.1. Description of sub-domain for enriched over interpolations; (a) usual interpolation function, (b) cover region or elements affected by the interpolation cover, and (c) an element.

Let $\mathbf{Q}^n = \{\mathbf{x}_i\}_{i=1}^n$ be a set of n nodal point position vectors $\mathbf{x}_i = [x_i \ y_i]^\top \in \Omega$, and let $\{\lambda_n\} = \{\psi^m\}_{m=1}^q$ be a family of q triangles generated by \mathbf{Q}^n . The triangles correspond to the domain Ω in

which we seek the solution variable u

$$\bigcup_{m=1}^q \psi^m = \Omega. \quad (3.1)$$

The triangles do not overlap, that is, $\psi^j \cap \psi^k = \emptyset$ for $j \neq k$. **Figure 3.1** shows the piecewise interpolation function $h_i(x, y)$ used in the solution. Let C_i be the support domain of h_i , i.e. $C_i = \text{supp}(h_i)$, $\forall i = 1, \dots, N$, which we call the cover region. Hence the cover region C_i corresponds to the union of elements attached to the node i , see **Figure 3.1**(b). For each ψ^m , let $i_c(m)$ be the set of cover indices defined by

$$i_c(m) = \{i : C_i \cap \psi^m \neq \emptyset\}. \quad (3.2)$$

In **Figure 3.1**, the 3-node triangular element m coincides with the overlapped region of the three cover regions C_i , C_j and C_k and hence $i_c(m) = \{i, j, k\}$. To enrich the standard finite element interpolation for the solution variable u , we use interpolation cover functions

$$\Phi_i^p[u] = \bar{u}_i + [\xi_i \ \eta_i \ \xi_i^2 \ \xi_i \eta_i \ \eta_i^2 \ \dots \ \eta_i^p] \hat{\mathbf{u}}_i \quad \text{with} \quad \xi_i = \frac{(x - x_i)}{\chi_i}, \quad \eta_i = \frac{(y - y_i)}{\chi_i}, \quad (3.3)$$

where \bar{u}_i is the standard nodal point variable, $\hat{\mathbf{u}}_i = [\hat{u}_i^\xi \ \hat{u}_i^\eta \ \hat{u}_i^{\xi^2} \ \hat{u}_i^{\xi\eta} \ \hat{u}_i^{\eta^2} \ \dots \ \hat{u}_i^{\eta^p}]^T$ lists the additional degrees of freedom for the cover region, p is the order of the complete polynomial used, and χ_i is the diameter of the largest finite element sharing the node i . The use of χ_i can improve the conditioning of the coefficient matrix.

The enriched approximation for the solution variable is then given by

$$u = \sum_{m=1}^q \sum_{i \in i_c(m)} h_i \Phi_i^p[u] = \sum_{m=1}^q \left(\sum_{i \in i_c(m)} h_i \bar{u}_i + \sum_{i \in i_c(m)} \mathbf{H}_i \hat{\mathbf{u}}_i \right)$$

with

$$\mathbf{H}_i = h_i [\xi_i \ \eta_i \ \xi_i^2 \ \xi_i \eta_i \ \eta_i^2 \ \dots \ \eta_i^p]. \quad (3.4)$$

Considering Equation (3.4), the enriched cover approximation consists of the standard finite element interpolation plus additional higher order terms. To obtain a well-conditioned stiffness matrix, the local coordinate systems (ξ_i, η_i) instead of the global coordinates (x, y) are used. Also, not only $\bar{u}_i = 0$ but also $\hat{\mathbf{u}}_i = \mathbf{0}$ are always restricted (although not mentioned in the example solutions) when imposing the essential boundary conditions at the node i .

The basic properties of the finite element method enriched by interpolation covers were studied for general 2D and 3D finite element analyses in Reference. [98]. These basic properties pertain also to the finite element analysis of shells.

3.2 The Enriched MITC3 Shell Finite Element

In this section, the displacement interpolation of the MITC3 shell finite element enriched by the linear interpolation cover is presented. Therefore, the resulting enriched displacement interpolation can give quadratic convergence. Also, the assumed covariant strain fields used for the enriched MITC3 shell finite element are proposed in this section.

3.2.1 Enriched Displacement Interpolation

The geometry of the 3-node continuum mechanics based triangular shell finite element is interpolated using [23, 99]

$$\mathbf{x}(r, s, t) = \sum_{i=1}^3 h_i(r, s) \mathbf{x}_i + \frac{t}{2} \sum_{i=1}^3 a_i h_i(r, s) \mathbf{V}_n^i$$

with $h_1 = r$, $h_2 = s$, $h_3 = 1 - r - s$,

(3.5)

where r , s , and t are natural coordinates, h_i is the two-dimensional interpolation function corresponding to node i , \mathbf{x}_i is the position vector of node i in the global Cartesian coordinate system, and a_i , \mathbf{V}_n^i denote the shell thickness and the director vector at node i , respectively, see **Figure 3.2**.

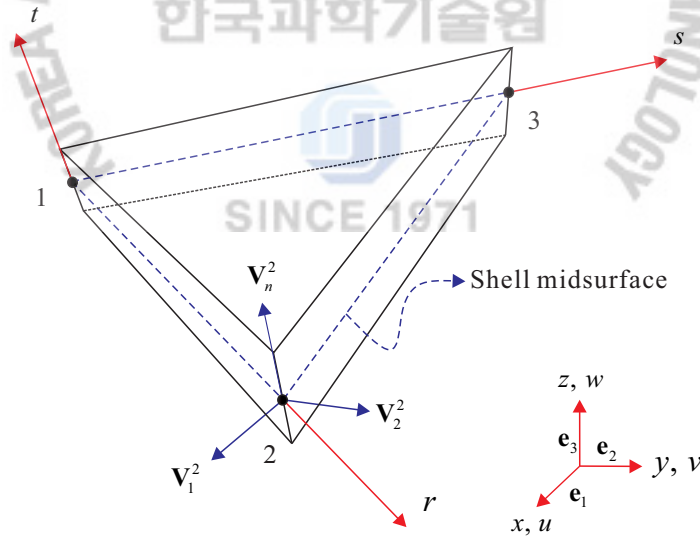


Figure 3.2. A 3-node triangular continuum mechanics based shell finite element.

The standard displacement interpolation of the shell element is given by

$$\bar{\mathbf{u}} = \sum_{i=1}^3 h_i \bar{\mathbf{u}}_i + \sum_{i=1}^3 \frac{t}{2} a_i h_i (-\mathbf{V}_2^i \bar{\alpha}_i + \mathbf{V}_1^i \bar{\beta}_i),$$
(3.6)

in which $\bar{\mathbf{u}}_i = [\bar{u}_i \ \bar{v}_i \ \bar{w}_i]^T$ is the nodal displacement vector in the global Cartesian coordinate system, $\mathbf{V}_1^i = [V_{1x}^i \ V_{1y}^i \ V_{1z}^i]^T$ and $\mathbf{V}_2^i = [V_{2x}^i \ V_{2y}^i \ V_{2z}^i]^T$ are unit vectors orthogonal to \mathbf{V}_n^i and to each other, and $\bar{\alpha}_i$ and $\bar{\beta}_i$ are the rotations of the director vector \mathbf{V}_n^i about \mathbf{V}_1^i and \mathbf{V}_2^i at node i .

The linear interpolation cover, that is, the first order degree of polynomial bases is used to enrich the displacement interpolation in Equation (3.6). The enriched displacement interpolation for the 3-node triangular shell finite element is given by

$$\mathbf{u} = \bar{\mathbf{u}} + \hat{\mathbf{u}} \quad (3.7)$$

$$\text{with } \hat{\mathbf{u}} = \sum_{i=1}^3 \mathbf{H}_i \hat{\mathbf{u}}_i + \sum_{i=1}^3 \frac{t}{2} a_i \mathbf{H}_i (-\mathbf{D}_2^i \hat{\boldsymbol{\alpha}}_i + \mathbf{D}_1^i \hat{\boldsymbol{\beta}}_i), \quad (3.8)$$

in which $\hat{\mathbf{u}}_i = [\hat{u}_i^\xi \ \hat{u}_i^\eta \ | \ \hat{v}_i^\xi \ \hat{v}_i^\eta \ | \ \hat{w}_i^\xi \ \hat{w}_i^\eta]^T$, $\hat{\boldsymbol{\alpha}}_i = [\hat{\alpha}_i^\xi \ \hat{\alpha}_i^\eta]^T$ and $\hat{\boldsymbol{\beta}}_i = [\hat{\beta}_i^\xi \ \hat{\beta}_i^\eta]^T$ are unknown coefficient vectors for the displacements and rotations, and the \mathbf{H}_i are the linear cover interpolation matrices for the displacements and rotations

$$\mathbf{H}_i = h_i \begin{bmatrix} \xi_i & \eta_i & 0 & 0 & 0 & 0 \\ 0 & 0 & \xi_i & \eta_i & 0 & 0 \\ 0 & 0 & 0 & 0 & \xi_i & \eta_i \end{bmatrix}, \quad \mathbf{D}_1^i = \begin{bmatrix} V_{1x}^i & 0 \\ 0 & V_{1x}^i \\ V_{1y}^i & 0 \\ 0 & V_{1y}^i \\ V_{1z}^i & 0 \\ 0 & V_{1z}^i \end{bmatrix}, \quad \text{and } \mathbf{D}_2^i = \begin{bmatrix} V_{2x}^i & 0 \\ 0 & V_{2x}^i \\ V_{2y}^i & 0 \\ 0 & V_{2y}^i \\ V_{2z}^i & 0 \\ 0 & V_{2z}^i \end{bmatrix}. \quad (3.9)$$

Note that the enriched displacement interpolation for \mathbf{u} in Equations (3.7) consists of two parts: the standard linear term $\bar{\mathbf{u}}$ and the additional quadratic term $\hat{\mathbf{u}}$.

3.2.2 Assumed Covariant Transverse Shear Strain Fields

The covariant strain components are directly obtained by

$$e_{ij} = \frac{1}{2} (\mathbf{g}_i \cdot \mathbf{u}_{,j} + \mathbf{g}_j \cdot \mathbf{u}_{,i}), \quad (3.10)$$

$$\text{where } \mathbf{g}_i = \frac{\partial \mathbf{x}}{\partial r_i}, \quad \mathbf{u}_{,i} = \frac{\partial \mathbf{u}}{\partial r_i} = \frac{\partial (\bar{\mathbf{u}} + \hat{\mathbf{u}})}{\partial r_i} \quad \text{with } r_1 = r, \ r_2 = s, \ r_3 = t.$$

Therefore, the enriched covariant strain components are also divided into two parts

$$e_{ij} = \bar{e}_{ij} + \hat{e}_{ij}$$

$$\text{with } \bar{e}_{ij} = \frac{1}{2} (\mathbf{g}_i \cdot \bar{\mathbf{u}}_{,j} + \mathbf{g}_j \cdot \bar{\mathbf{u}}_{,i}) \quad \text{and} \quad \hat{e}_{ij} = \frac{1}{2} (\mathbf{g}_i \cdot \hat{\mathbf{u}}_{,j} + \mathbf{g}_j \cdot \hat{\mathbf{u}}_{,i}), \quad (3.11)$$

in which \bar{e}_{ij} and \hat{e}_{ij} correspond to the standard linear and additional quadratic displacement interpolations, respectively.

To alleviate the locking phenomenon, the MITC method for the covariant transverse shear strains is adopted. However, different assumed covariant transverse shear strain fields are employed for the standard and additional quadratic displacement interpolations. The assumed covariant transverse shear strain fields of the MITC3 and MITC6 shell elements are used for the strains \bar{e}_{ij} and \hat{e}_{ij} , respectively [23]. Note that, in the MITC6 shell element, the covariant membrane strains are also assumed to reduce membrane locking, but this treatment is not necessary and not used for the enriched MITC3 shell element due to its flat geometry.

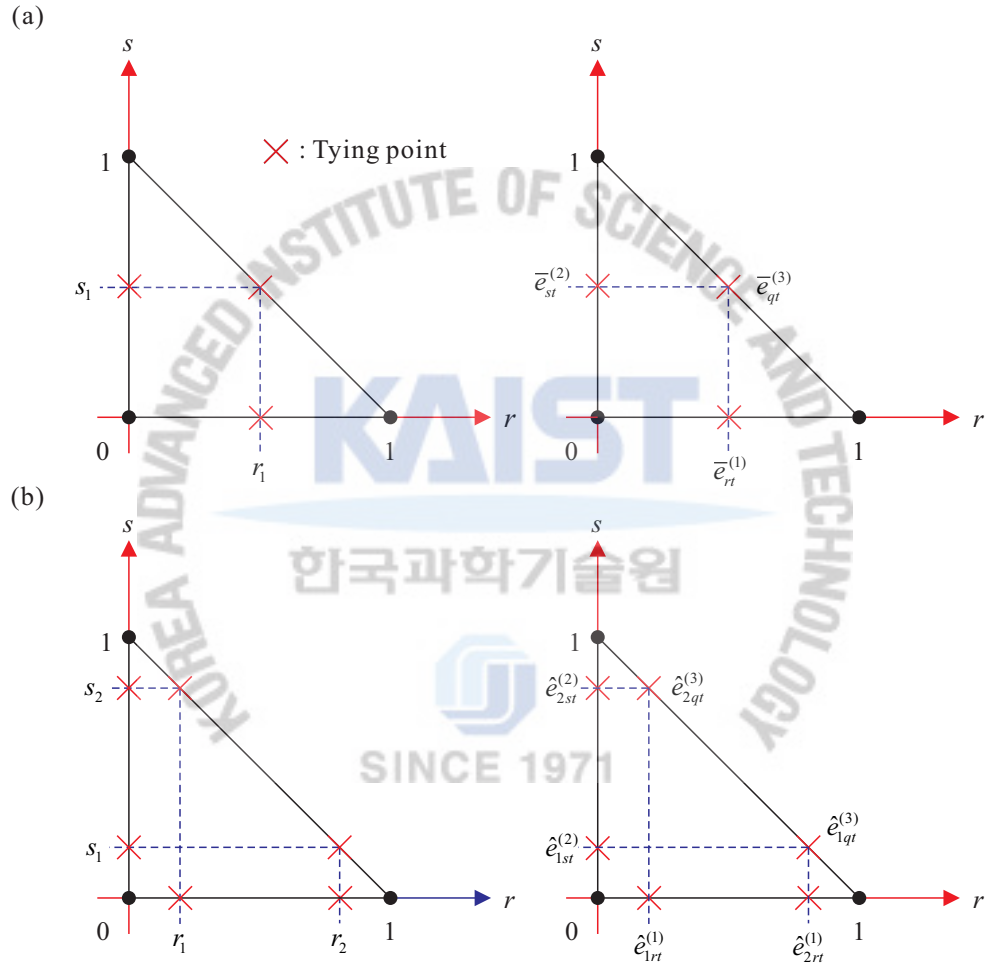


Figure 3.3. Tying points for the covariant transverse shear strains of the enriched MITC3 shell finite element: (a) for the standard linear displacement interpolation; $r_1 = s_1 = 1/2$, and (b) for the additional quadratic displacement interpolation; $r_1 = s_1 = 1/2 - 1/2\sqrt{3}$ and $r_2 = s_2 = 1/2 + 1/2\sqrt{3}$.

The assumed covariant transverse shear strain field used for the standard displacement interpolation is [23]

$$\bar{e}_{rt}^{AS} = \bar{e}_{rt}^{(1)} + cs, \quad \bar{e}_{st}^{AS} = \bar{e}_{st}^{(2)} - cr, \quad (3.12)$$

where $c = \bar{e}_{st}^{(2)} - \bar{e}_{rt}^{(1)} - \bar{e}_{st}^{(3)} + \bar{e}_{rt}^{(3)}$ and, at the tying points, $\bar{e}_{rt}^{(n)}$ and $\bar{e}_{st}^{(n)}$ are calculated from Equation (3.11), see **Figure 3.3(a)**.

For the additional quadratic displacement interpolation, the assumed covariant transverse shear strain field are used.

$$\begin{aligned}\hat{e}_{rt}^{AS} &= a_1 + b_1 r + c_1 s, \\ \hat{e}_{st}^{AS} &= a_2 + b_2 r + c_2 s\end{aligned}\quad (3.13)$$

and the coefficients are

$$\begin{aligned}a_1 &= m_{rt}^{(1)} - l_{rt}^{(1)}, \quad b_1 = 2l_{rt}^{(1)}, \quad a_2 = m_{st}^{(2)} - l_{st}^{(2)}, \quad c_2 = 2l_{st}^{(2)}, \\ c_1 &= (a_2 + c_2 - a_1) - (m_{st}^{(3)} + l_{st}^{(3)} - m_{rt}^{(3)} - l_{rt}^{(3)}), \\ b_2 &= (a_1 + b_1 - a_2) + (m_{st}^{(3)} - l_{st}^{(3)} - m_{rt}^{(3)} + l_{rt}^{(3)})\end{aligned}\quad (3.14)$$

$$\text{with } m_{jt}^{(i)} = \frac{1}{2}(\hat{e}_{1jt}^{(i)} + \hat{e}_{2jt}^{(i)}), \quad l_{jt}^{(i)} = \frac{\sqrt{3}}{2}(\hat{e}_{2jt}^{(i)} - \hat{e}_{1jt}^{(i)}) \quad \text{with } j = r, s \quad \text{for } i = 1, 2, 3, \quad (3.15)$$

where $\hat{e}_{1jt}^{(i)}$ and $\hat{e}_{2jt}^{(i)}$ are calculated at the tying points in **Figure 3.3(b)**.

Finally, the assumed covariant transverse shear strain fields for the enriched MITC3 shell element are obtained as

$$e_{jt}^{AS} = \bar{e}_{jt}^{AS} + \hat{e}_{jt}^{AS} = \mathbf{B}_{jt}^{AS} \mathbf{U} \quad \text{with } j = r, s, \quad (3.16)$$

in which \mathbf{B}_{jt}^{AS} is the covariant transverse shear strain-displacement matrix and \mathbf{U} is the vector that contains the degrees of freedom $\bar{\mathbf{u}}_i$, $\bar{\alpha}_i$, $\bar{\beta}_i$ and the additional degrees of freedom $\hat{\mathbf{u}}_i$, $\hat{\alpha}_i$, $\hat{\beta}_i$. Note that other covariant components use only displacement based formulations and hence the scheme will not give spurious modes in membrane strains [24, 25].

Then, using the appropriate stress-strain matrix for shells, the element stiffness is constructed in the same manner as for the displacement-based shell element [1]. The 7-point Gauss integration is adopted to evaluate the stiffness matrix because the order of the enriched displacement interpolation is quadratic.

Since the cover interpolation is based on the existing nodes, the enriched displacement interpolation can be locally used assigning or not assigning interpolation covers in different regions. Without enrichment, the element is identical to the original MITC3 shell element.

The enriched MITC3 shell element passes the membrane, bending, and transverse shearing patch tests for arbitrary local enrichments, see Refs. [1, 18, 23] for the patch tests performed. Of course, in the tests, the nodal forces corresponding to not only the standard degrees of freedom ($\bar{\mathbf{u}}_i$, $\bar{\alpha}_i$, and $\bar{\beta}_i$) but also the additional degrees of freedom ($\hat{\mathbf{u}}_i$, $\hat{\alpha}_i$, and $\hat{\beta}_i$) must be applied [98].

3.2.3 Basic Tests

The following basic tests are performed as a basic requirement to be satisfied for the new triangular shell elements.

3.2.3.1 Isotropic Element Test

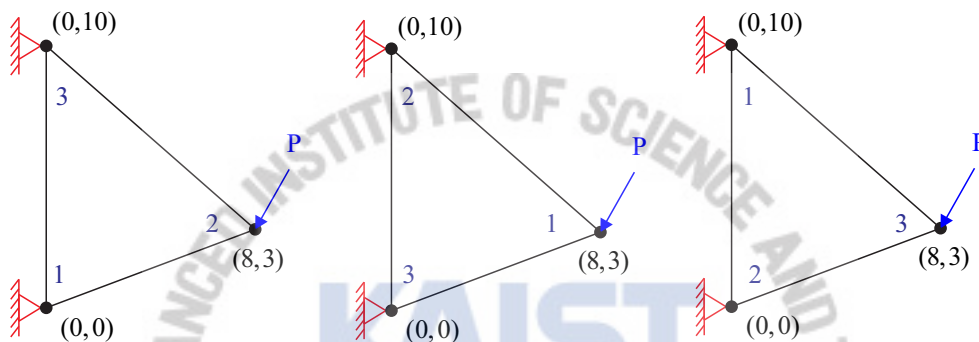


Figure 3.4. Isotropic test of the present triangular shell element.

The isotropic element is to test whether the element considered is indeed isotropic. This test is performed by analyzing the three same equilateral triangular elements with different numbering sequences as shown in **Figure 3.4**. To pass this test, exactly the same tip displacement should be obtained by the models for all possible tip force P .

3.2.3.2 Zero Energy Mode Test

This test is performed by counting the number of zero eigenvalues of the stiffness matrix of one unsupported shell finite element, which should be exactly six. We recommend that, when doing this test, various possible geometries should be taken into account. The considered element passes this test for certain geometry but may not pass the test for other geometries.

3.2.3.3 Patch Test

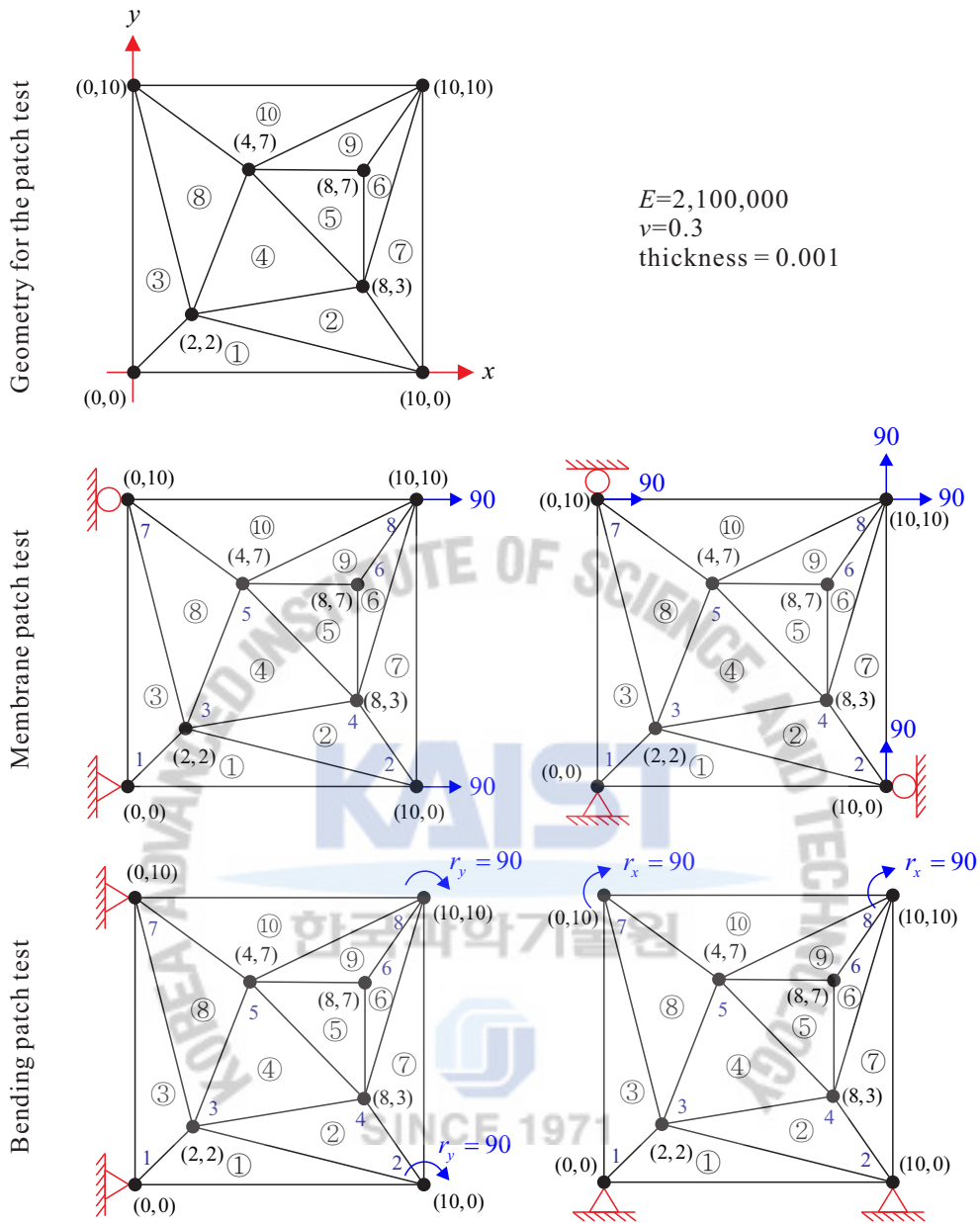


Figure 3.5. Mesh used for the membrane and bending patch tests

The patch test has been widely used as a test for element convergence, despite its limitations for mixed formulations. In this thesis, numerical form of the patch test is used to merely assess the sensitivity of our element to geometric distortions. The mesh used for the patch test is shown in **Figure 3.5**. The minimum number of degrees of freedom is fixed to prevent rigid body motion and the nodal point forces which result in constant stress condition is considered. The constant stress field should be given by the patch models subjected membrane forces and bending forces, respectively. It is noted that nodal forces should properly applied to not only standard degrees of freedom but also additional degrees of freedom to calculate the constant stresses, see following Equation.

$$\mathbf{R} = \mathbf{R}_B + \mathbf{R}_S \quad (3.17)$$

with

$$\mathbf{R}_B = \sum_{m=1}^e \mathbf{R}_B^{(m)} = \sum_{m=1}^e \int_{\Omega^{(m)}} [\bar{\mathbf{H}}^{(m)} \quad \mathbf{H}^{(m)}]^T \mathbf{f}^B d\Omega, \quad (3.18)$$

$$\mathbf{R}_S = \sum_{m=1}^e \int_{S_f^{(m)}} [\bar{\mathbf{H}}^{s_f^{(m)}} \quad \mathbf{H}^{s_f^{(m)}}]^T \mathbf{f}^{S_f} dS, \quad (3.19)$$

where \mathbf{R} is the load vector, \mathbf{f}^B is the body force, \mathbf{f}^{S_f} is the surface traction applied on S_f and $\bar{\mathbf{H}}^{(m)}$ is the classical finite element interpolation matrix.

The results of the basic test are reported in **Table 3.1**. The MITC3, MITC6 and enriched MITC3 shell element pass all the basic patch tests.

Table 3.1. Basic test results of the MITC3, MITC6 and enriched MITC3 triangular shell finite elements.

Element	Isotropic element test	Zero energy mode test	Patch test	
			Membrane	Bending
MITC3	Pass	Pass	Pass	Pass
MITC6a	Pass	Pass	Pass	Pass
MITC6b	Pass	Pass	Pass	Pass
Enriched MITC3	Pass	Pass	Pass	Pass

3.3 Computational Efficiency

In this section, some important aspects of the computational efficiency when using the enriched element are studied. The standard 3- and 6-node shell elements (the MITC3 and MITC6 shell elements) and the enriched 3-node shell element (the enriched MITC3 shell element) are considered.

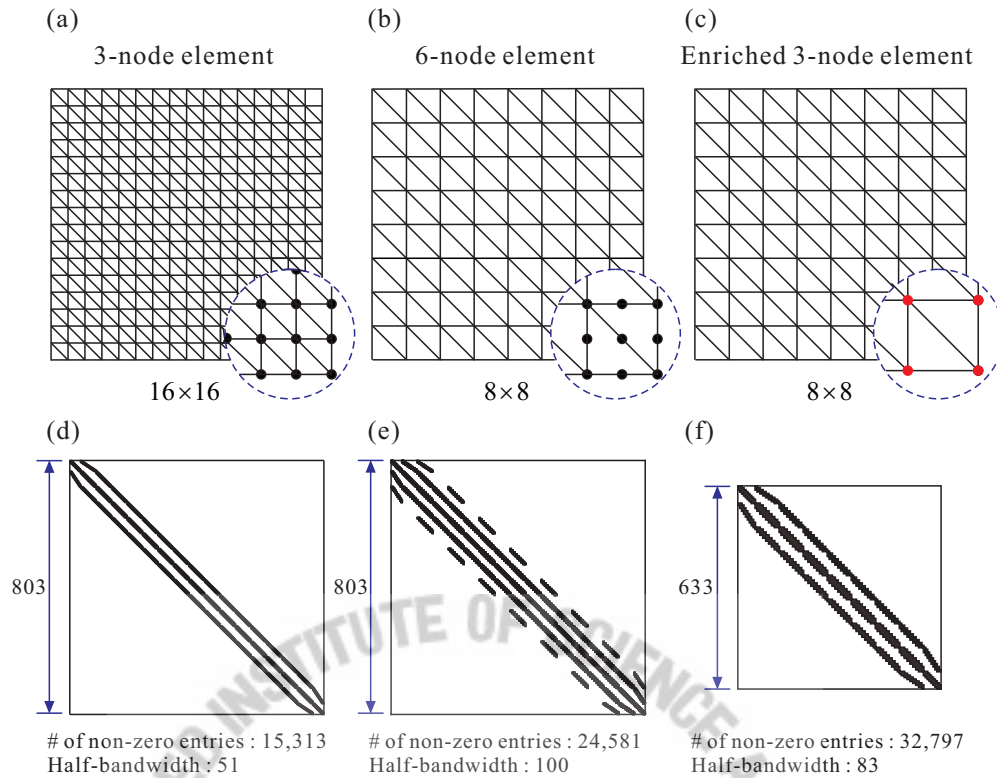


Figure 3.6. Meshes used and stiffness matrix structures: (a) and (d) for the 3-node shell element, (b) and (e) for the 6-node shell element, and (c) and (f) for the enriched 3-node shell elements. Non-zero entries are colored in black.

Figure 3.6 shows the size and sparseness of the stiffness matrices when using the enriched 3-node shell finite element and the standard 3- and 6-node shell elements for the meshes. A simply supported square plate problem is considered. The meshes used are given in **Figure 3.6**(a), (b) and (c) when $N = 8$. Since the standard 3-node shell element is based on the linear displacement interpolation, and the 6-node and enriched 3-node shell elements are based on quadratic displacement interpolations, we use a twice finer mesh for the standard 3-node shell element.

Table 3.2. Detailed information on the stiffness matrices of the 3-, 6-, and enriched 3-node shell finite elements for the meshes shown in Figure 3.6.

	Linear shell element	Quadratic shell elements	
	Standard 3-node	Standard 6-node	Enriched 3-node
Elements	512 ($2N = 16$)	128 ($N = 8$)	128 ($N = 8$)
Nodes	289	289	81
DOFs	803	803	633
Non-zero entries	15,313	24,581	32,797
Half-bandwidth	51	100	83

The stiffness matrix entries for the simply supported square plate problem with for some equivalent mesh patterns are plotted in **Figure 3.6(d)**, (e)-(f), where the non-zero entries are colored in black. The size of the stiffness matrices for the meshes used is 803×803 for the 3- and 6-node shell elements and 633×633 for the enriched 3-node shell element. The standard 3- and 6-node shell elements and the enriched 3-node shell element give 15,313, 24,581 and 32,797 non-zero entries in the matrices, respectively. Also, the matrix half-bandwidths are 51, 100 and 83 for the 3- and 6-node shell elements and the enriched 3-node shell element, respectively. **Table 3.2** lists the information regarding these cases.

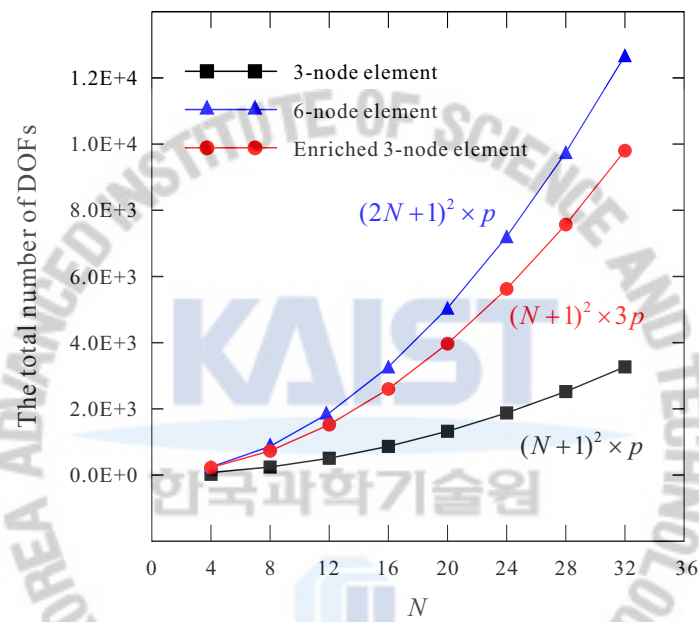


Figure 3.7. The total number of degrees of freedom (DOFs) when increasing the number of element layers, N , along an edge p denotes the number of degrees of freedom per node, hence $p = 3$ for the simply supported plate problem.

The number of non-zero entries in the stiffness matrix for the enriched 3-node shell element is substantially larger than in the corresponding matrix for the 6-node shell element. This is due to the fact that the support of the higher order interpolation functions in the enriched 3-node shell element is larger than for the 3- and 6-node shell elements. However, using the enriched 3-node shell element, all degrees of freedom are associated with vertex nodes which are shared by several elements and the assembled system of equations is in general smaller than when using the 6-node shell element where edge nodes are only shared by 2 elements. Therefore, the enriched 3-node shell element gives less equations and here also a smaller bandwidth than the 6-node shell element. This fact shows the effectiveness of the enriched 3-node shell element from a computational point of view. **Figure 3.7** shows how the number of nodal degrees of freedom increases as a function of the number of elements used in the meshing of **Figure 3.6**.

Table 3.3. Solution times (in second) for solving the linear equations. The element meshes are $2N \times 2N$ and $N \times N$ for linear and quadratic shell elements, respectively. (DOFs: degrees of freedom, HB: half-bandwidth)

N	Linear shell element			Quadratic shell elements					
	Standard 3-node			Standard 6-node			Enriched 3-node		
	DOFs	HB	Time	DOFs	HB	Time	DOFs	HB	Time
4	211	27	0.001	211	52	0.001	177	47	0.001
8	803	51	0.016	803	100	0.016	633	83	0.016
16	3,139	99	0.062	3,139	196	0.125	2,409	155	0.062
32	12,419	195	0.733	12,419	388	1.591	9,417	199	1.045
64	49,411	387	10.70	49,411	772	23.88	37,257	587	15.49

It is valuable to compare solution times required for the three shell finite elements considered. In all the cases, of course, symmetric stiffness matrices are generated. To obtain more insight into the computational efforts needed in the respective solutions, results are focused on the solution of the linear equations using direct Gauss elimination, in which the factorization of the stiffness matrices represents the major expense. To check computational times, a quad-core machine (Intel(R) Core i7-3770 CPU @ 3.40 GHz, 8 GB RAM, Windows 7 64bit) for all solution cases is used. **Table 3.3** shows the solution times for the simply supported square plate problem. As expected, the factorization time for the enriched 3-node shell element is much smaller than for the standard 6-node shell element.

3.4 Convergence Studies

This section presents convergence studies on well-established problems for the enriched MITC3 shell element. The solutions can show at most quadratic convergence in the s-norm and the results are compared with those of the MITC3, MITC4, and MITC6 shell elements. Various problems are considered: a fully clamped square plate problem, cylindrical shell problems, and hyperboloid shell problems using uniform and distorted meshes [23, 26, 99, 100].

The s-norm proposed by Hiller and Bathe [101] is used to measure the convergence of the finite element solutions. The s-norm is suitable to check whether the finite element solutions satisfy consistency and the inf-sup condition [27, 101-104], and is defined as follows

$$\|\mathbf{u} - \mathbf{u}_h\|_s^2 = \int_{\Omega} \Delta \boldsymbol{\varepsilon}^T \Delta \boldsymbol{\tau} d\Omega, \quad (3.20)$$

where \mathbf{u} is the exact solution, \mathbf{u}_h is the solution obtained using the finite element discretization, $\boldsymbol{\varepsilon}$ and $\boldsymbol{\tau}$ are the strain and stress vectors, and

$$\Delta \boldsymbol{\varepsilon} = \boldsymbol{\varepsilon} - \boldsymbol{\varepsilon}_h, \quad \Delta \boldsymbol{\tau} = \boldsymbol{\tau} - \boldsymbol{\tau}_h. \quad (3.21)$$

The theoretical convergence behavior can be estimated to be

$$\|\mathbf{u} - \mathbf{u}_h\|_s^2 \cong ch^k, \quad (3.22)$$

in which c is a constant and h denotes the element size. If a shell element is uniformly optimal, the constant is independent of the shell thickness and k represents the optimal order of convergence, with $k = 2$ for the 3-node shell finite element, and $k = 4$ for the 6-node and the enriched 3-node shell elements.

Instead of the unknown exact solution, a reference finite element solution \mathbf{u}_{ref} calculated using a very fine mesh and a known reliable element can be used, hence Equation (3.20) becomes

$$\|\mathbf{u}_{ref} - \mathbf{u}_h\|_s^2 = \int_{\Omega_{ref}} \Delta \boldsymbol{\varepsilon}^T \Delta \boldsymbol{\tau} d\Omega_{ref} \quad \text{with} \quad \Delta \boldsymbol{\varepsilon} = \boldsymbol{\varepsilon}_{ref} - \boldsymbol{\varepsilon}_h, \quad \Delta \boldsymbol{\tau} = \boldsymbol{\tau}_{ref} - \boldsymbol{\tau}_h. \quad (3.23)$$

To measure the convergence of the finite elements in the shell problems, the relative error E_h are used and expressed as

$$E_h = \frac{\|\mathbf{u}_{ref} - \mathbf{u}_h\|_s^2}{\|\mathbf{u}_{ref}\|_s^2}. \quad (3.24)$$

The numerical procedure to calculate the s-norm for shell finite element solutions with general types of elements and general meshes is explained in detail in Reference [23]. In the use of Equation (3.24), it is very important to use accurate reference solutions calculated by a reliable shell finite element. In this study, we use well-converged reference solutions calculated using fine meshes of the MITC9 shell finite element. Of course, the MITC9 shell finite element is known to satisfy the ellipticity and consistency conditions and to show adequate convergence behavior, see Refs. [22, 26, 101].

The following sections presents the convergence curves of the MITC3, MITC4, MITC6 shell elements and the fully enriched MITC3 shell element to identify the performance of the enriched MITC3 shell element compared to other shell elements. Note that some convergence curves of the MITC3, MITC4, and MITC6 shell elements have been published before in Refs. [23, 99, 100].

3.4.1 Fully Clamped Square Plate Problem

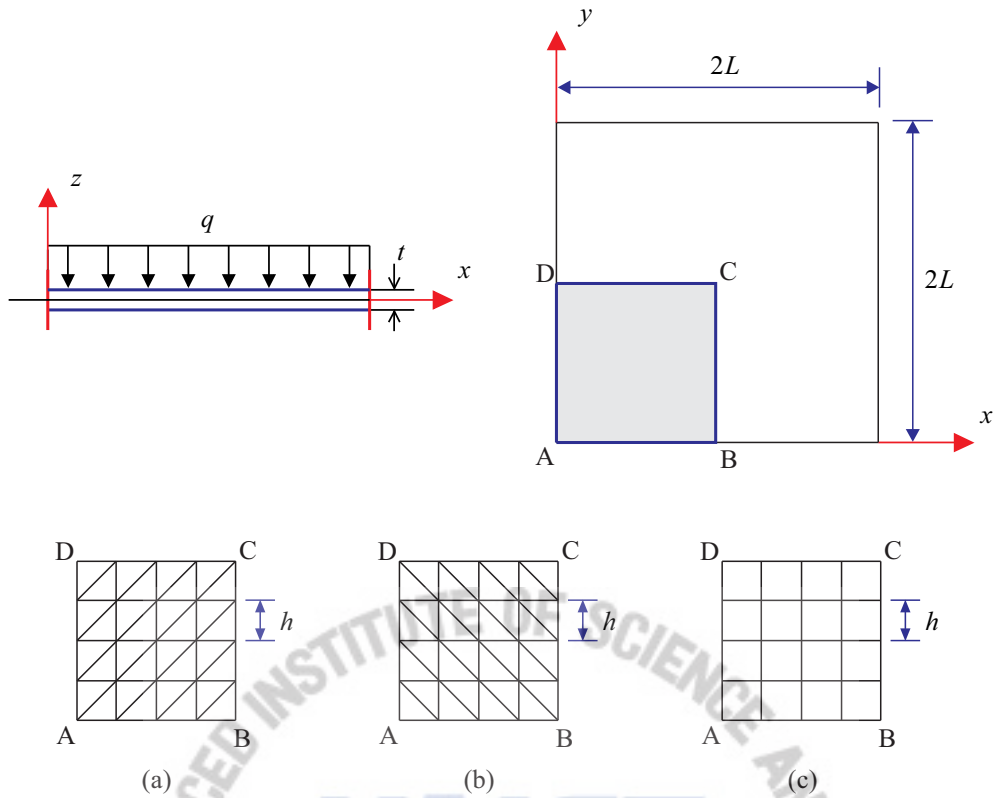


Figure 3.8. Fully clamped square plate under uniform pressure ($L=1.0$, $E=1.7472 \times 10^7$, $q=1.0$ and $\nu=0.3$) with three different 4×4 mesh patterns: (a) and (b) triangular mesh for the MITC3, MITC6 and enriched MITC6 shell elements, and (c) quadrilateral mesh for the MITC4 shell element.

The plate problem shown in **Figure 3.8** is solved. A square plate of size $2L \times 2L$ and constant thickness t is subjected to a uniform pressure load. Due to symmetry, only one quarter of the plate is modeled, with $u_x = \theta_y = 0$ along BC, $u_y = \theta_x = 0$ along DC, and $u_x = u_y = u_z = \theta_x = \theta_y = 0$ along AB and AD [23, 99].

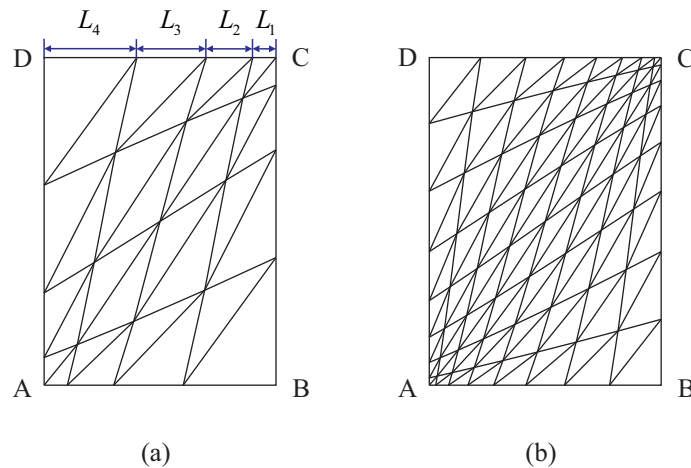


Figure 3.9. Distorted meshes used for the fully clamped square plate problem, cylindrical shell problems, and hyperboloid shell problems when (a) $N = 4$ and (b) $N = 8$. The number of triangular elements for an $N \times N$ mesh is $2N^2$.

The convergence behavior is studied not only using uniform meshes but also distorted meshes, as shown in **Figure 3.9**. When the $N \times N$ distorted mesh is used, each edge is divided by the ratio $L_1 : L_2 : L_3 : \dots : L_N = 1 : 2 : 3 : \dots : N$, leading to quite distorted meshes. The reference solution is obtained with a uniform mesh of 96×96 MITC9 shell finite elements. For the MITC3 and MITC4 shell elements, $N = 8, 16, 32$ and 64 are used and for MITC6 shell element and the enriched MITC3 shell element, $N = 4, 8, 16$ and 32 are adopted. Note that in these $N \times N$ meshes N^2 MITC4 elements and $2N^2$ triangular elements are used throughout the dissertation. Also, in the figures of results we consider the cases $t/L = 1/100, 1/1,000$ and $1/10,000$ and use as the “element size” $h = L/N$. To fairly compare convergence behaviors among different shell elements, the equivalent element sizes $2h, h$ and $1.2h$ are used for the MITC3 and MITC4 shell elements, the MITC6 shell element, and the enriched MITC3 shell element. When using these equivalent element sizes, the numbers of degrees of freedom are similar.

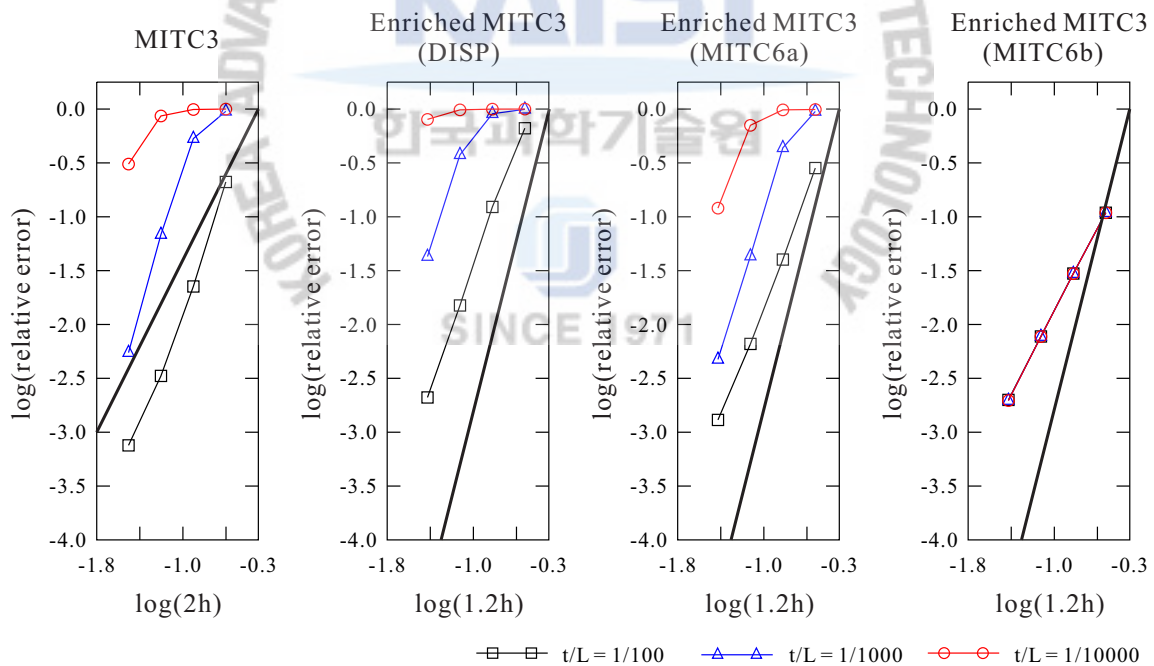


Figure 3.10. Convergence curves for the fully clamped square plate problem with uniform meshes. For triangular shell elements, the mesh pattern in Figure 3.8(a) is used. The bold line represents the optimal convergence rate, which is 2.0 for linear elements and 4.0 for quadratic elements.

To identify the dependency of the convergence behavior on the MITC scheme chosen for the enriched

MITC3 shell element, the following three schemes are considered for the covariant transverse shear strain field of the additional quadratic displacement interpolation:

- No MITC scheme is used (denoted by DISP in **Figure 3.10**).
- The MITC6a scheme is used, for this scheme see Ref. [23].
- The MITC6 scheme in Equation (3.13) is used (referred to as MITC6b in **Figure 3.10**)

In all these cases, of course, the MITC3 scheme in Equation (3.12) is used for the assumed covariant transverse shear strain field of the standard linear displacement interpolation.

Figure 3.10 shows the convergence curves of the original MITC3 shell element and the enriched MITC3 shell elements based on the different assumptions for the transverse shear strain fields. The enriched MITC3 shell element shows different solution accuracy highly depending on the assumed covariant transverse shear strain field used. When the assumed covariant transverse shear strain field of the MITC6 shell element is employed, an almost ideal convergence behavior is observed in this fully clamped square plate problem. Note that the other enriched MITC3 shell elements show an even worse convergence behavior than the original MITC3 shell element. Therefore, in the following sections, we only use the enriched MITC3 shell element based on the MITC6 scheme in Equation (3.13).

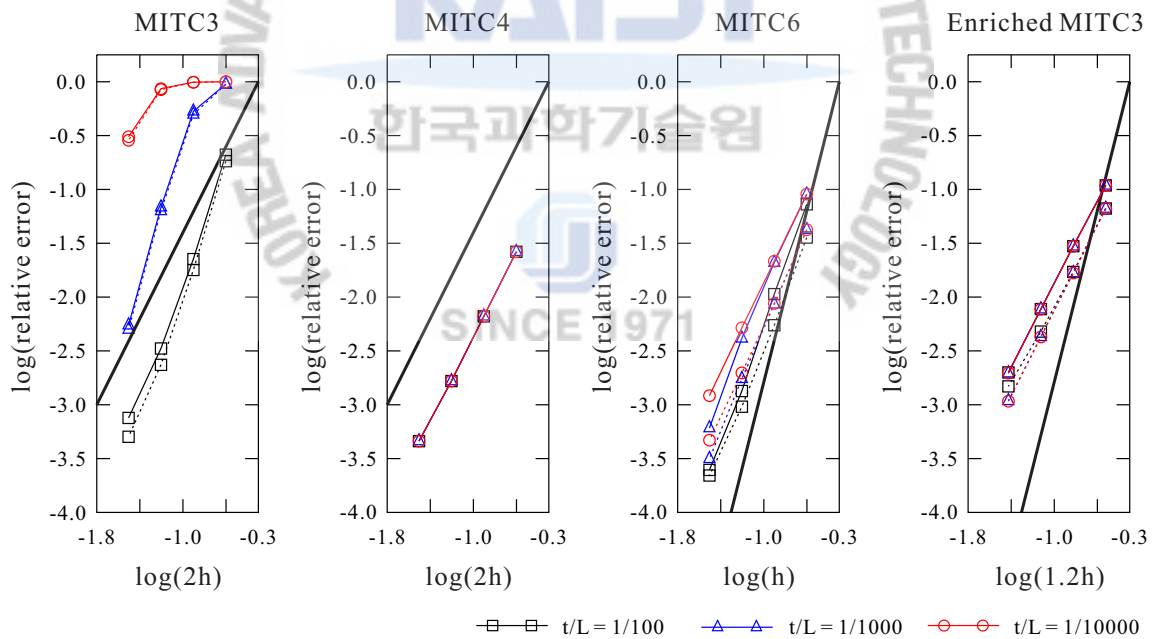


Figure 3.11. Convergence curves for the fully clamped square plate problem with uniform meshes. The solid and dotted lines correspond to the results obtained by the mesh patterns in Figure 3.8(a) and (b), respectively. The bold line represents the optimal convergence rate, which is 2.0 for linear elements and 4.0 for quadratic elements.

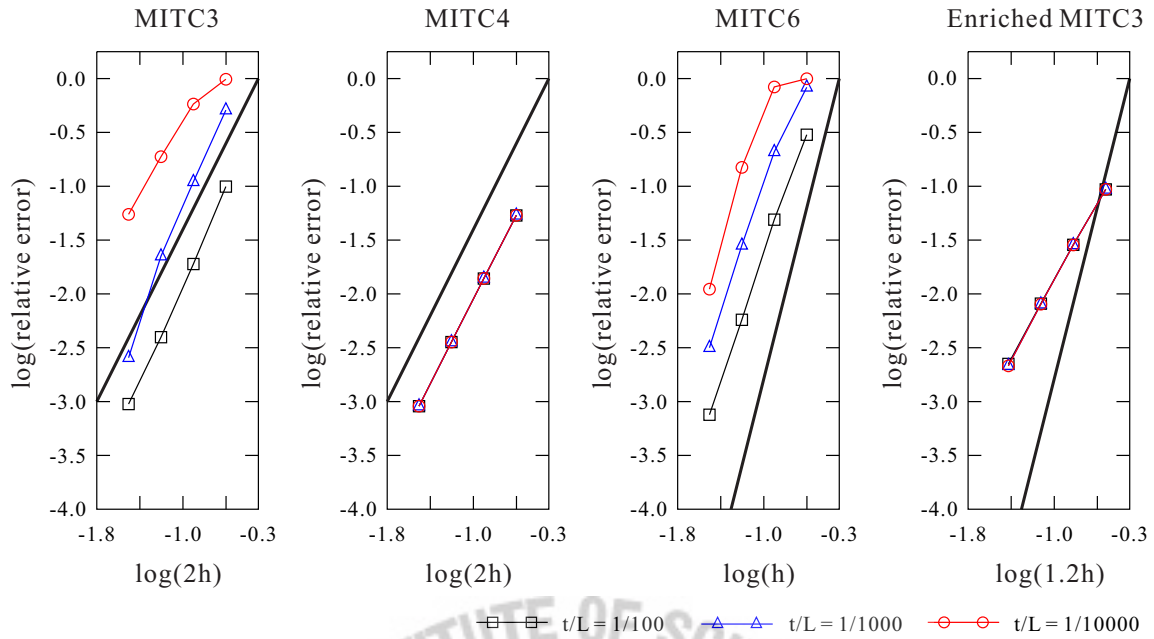


Figure 3.12. Convergence curves for the fully clamped square plate problem with the distorted meshes shown in Figure 3.9. The bold line represents the optimal convergence rate, which is 2.0 for linear elements and 4.0 for quadratic elements.

Figure 3.11 and **Figure 3.12** present the convergence curves for the fully clamped square plate problems using uniform and distorted meshes, respectively. The performance of the enriched MITC3 shell element is much better than the performance of the MITC3 and MITC6 shell elements. One reason is probably that the enrichments span over the cover regions and distortions within the regions are not as severe (are smoothed out) in comparison to not using covers. The MITC4 and enriched MITC3 shell finite elements show almost optimal convergence behaviors, even though the distorted meshes are used.

3.4.2 Cylindrical Shell Problem

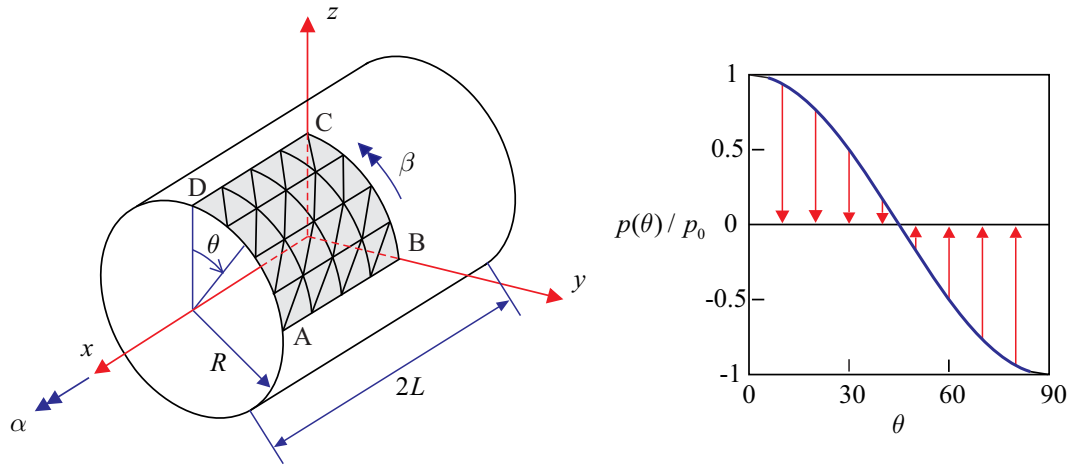


Figure 3.13. Cylindrical shell problem (4×4 mesh, $L = R = 1.0$, $E = 2.0 \times 10^5$, $\nu = 1/3$ and $p_0 = 1.0$).

A cylindrical shell with uniform thickness t , length $2L$, and radius R is considered, as shown in **Figure 3.13**. The loading is a smoothly varying periodic pressure $p(\theta)$ normal to the shell surface

$$p(\theta) = p_0 \cos(2\theta). \quad (3.25)$$

The shell problem gives two different asymptotic behaviors depending on the boundary conditions at both ends: the bending-dominated behavior under free boundary conditions and the membrane-dominated behavior under clamped boundary conditions.

Using the symmetry of the problem, the region ABCD in **Figure 3.13** is modeled. In the membrane-dominated case, the clamped boundary condition is imposed: $u_x = \beta = 0$ along BC, $u_y = \alpha = 0$ along DC, $u_z = \alpha = 0$ along AB, and $u_x = u_y = u_z = \alpha = \beta = 0$ along AD. In the bending-dominated case, the free boundary condition is imposed: $u_x = \beta = 0$ along BC, $u_y = \alpha = 0$ along DC, and $u_z = \alpha = 0$ along AB [23].

The reference solution is calculated using a mesh of 96×96 MITC9 shell finite elements for both cases. The solutions using the MITC3, MITC4, MITC6 and enriched MITC3 shell elements are obtained with $N \times N$ meshes ($N = 8, 16, 32$ and 64 for the MITC3 and MITC4 shell elements and $N = 4, 8, 16,$ and 32 for the MITC6 and enriched MITC3 shell elements). The element size used in the figures is $h = L/N$. The distorted meshes used are generated as shown in **Figure 3.9**.

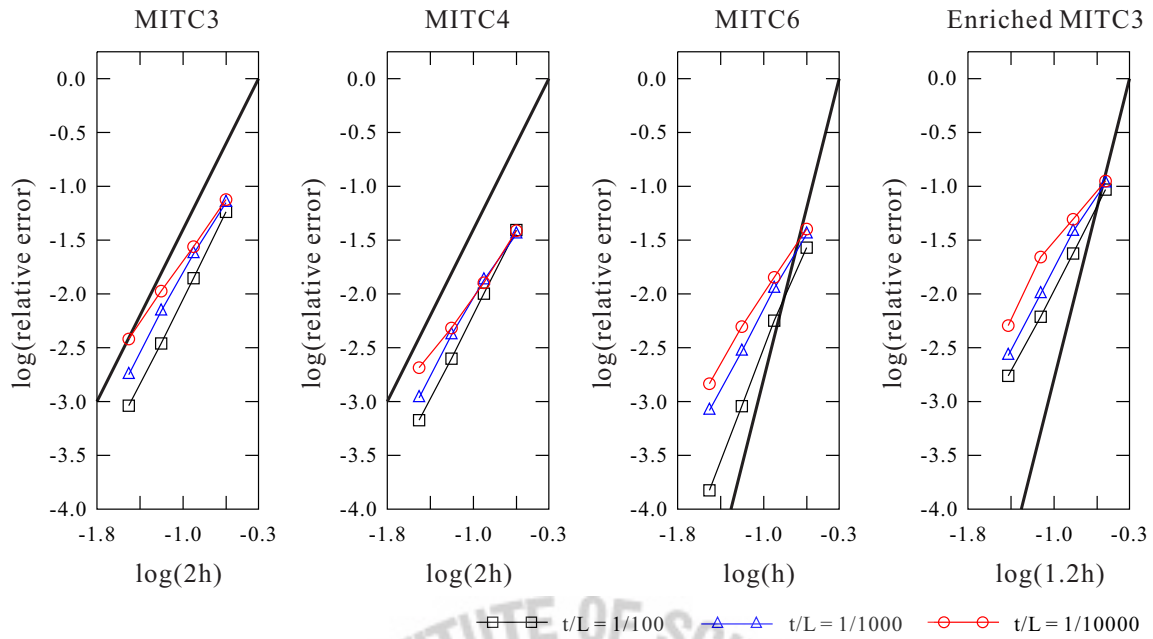


Figure 3.14. Convergence curves for the clamped cylindrical shell problem with uniform meshes. The bold line represents the optimal convergence rate, which is 2.0 for linear elements and 4.0 for quadratic elements.

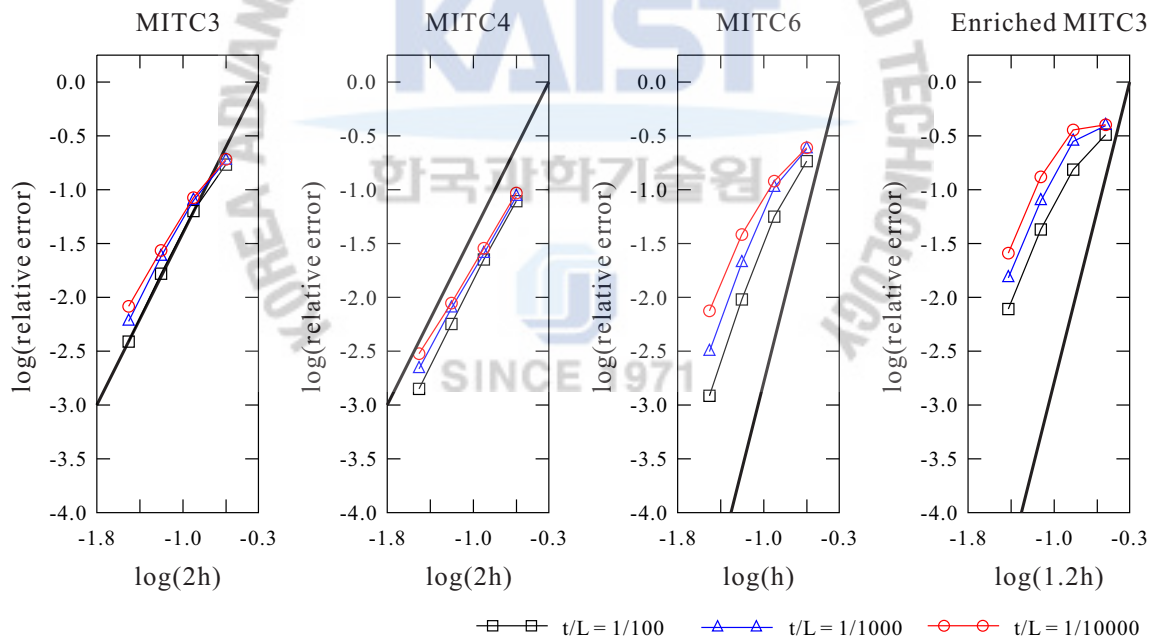


Figure 3.15. Convergence curves for the clamped cylindrical shell problem with the distorted meshes shown in Figure 3.9. The bold line represents the optimal convergence rate, which is 2.0 for linear elements and 4.0 for quadratic elements.

Figure 3.14 and **Figure 3.15** present the convergence behaviors for the clamped cylindrical shell problems with uniform and distorted meshes, respectively. All the shell finite elements considered show excellent

convergence behavior with uniform and distorted meshes.

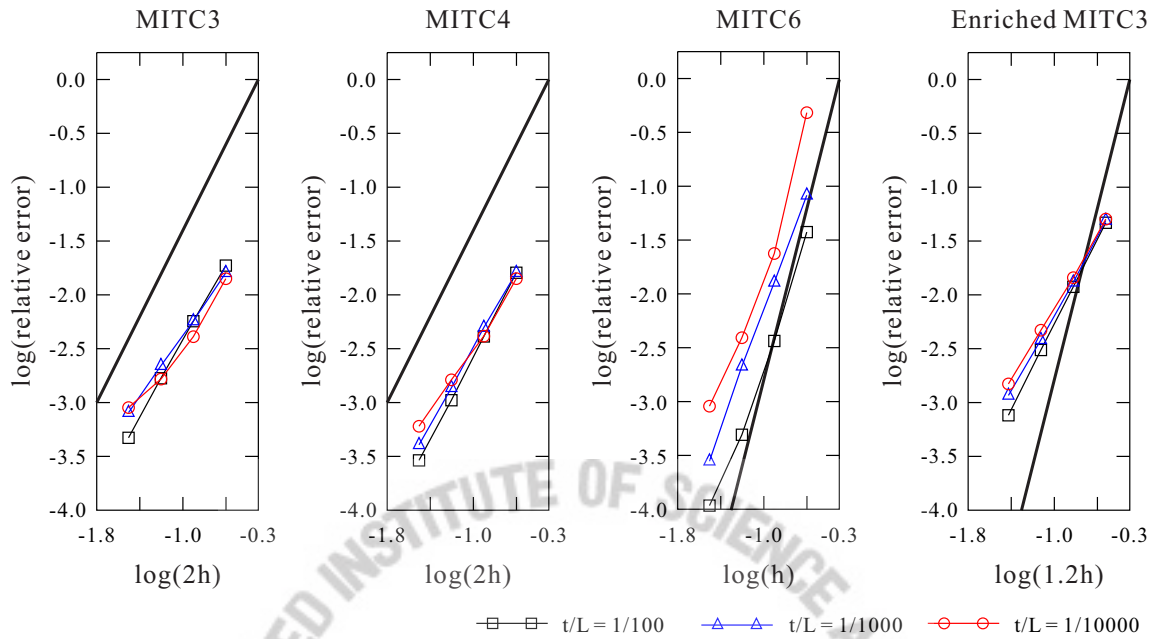


Figure 3.16. Convergence curves for the free cylindrical shell problem with uniform meshes. The bold line represents the optimal convergence rate, which is 2.0 for linear elements and 4.0 for quadratic elements.

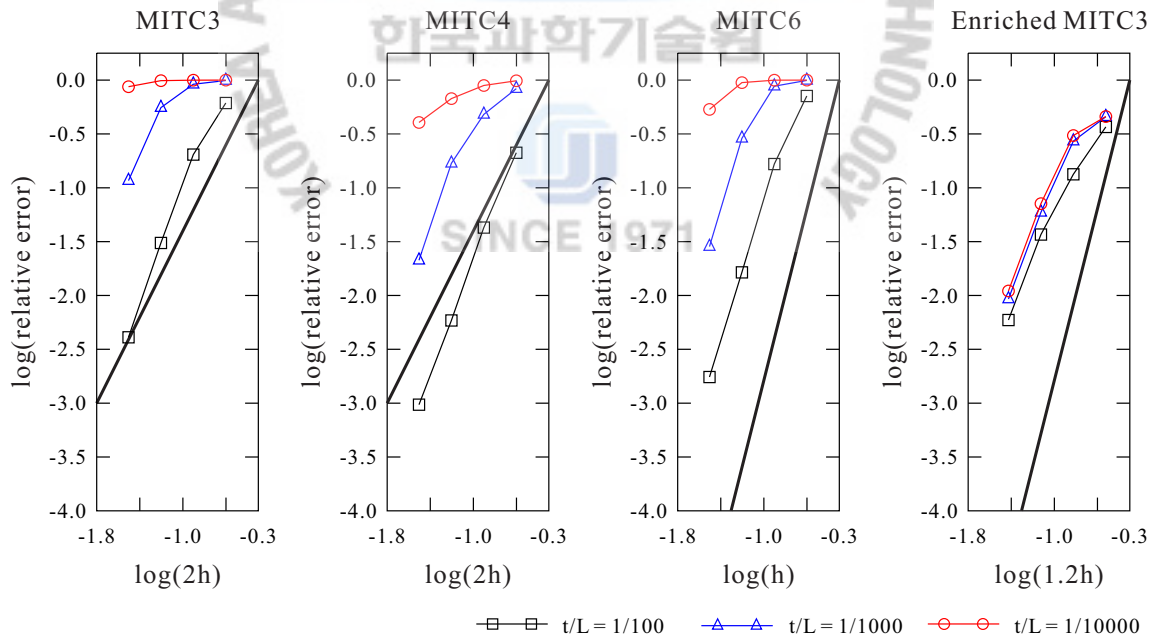


Figure 3.17. Convergence curves for the free cylindrical shell problem with the distorted meshes shown in Figure 3.9. The bold line represents the optimal convergence rate, which is 2.0 for linear elements and 4.0 for quadratic elements.

Figure 3.16 and **Figure 3.17** present the convergence curves for the free cylindrical shell problems obtained with uniform and distorted meshes, respectively. When distorted meshes are used, the solutions of the MITC3, MITC4, and MITC6 shell elements deteriorate as the shell thickness decreases, due to some locking. However, the enriched MITC3 shell element presents good convergence behavior even when using the distorted meshes.

3.4.3 Hyperboloid Shell Problem

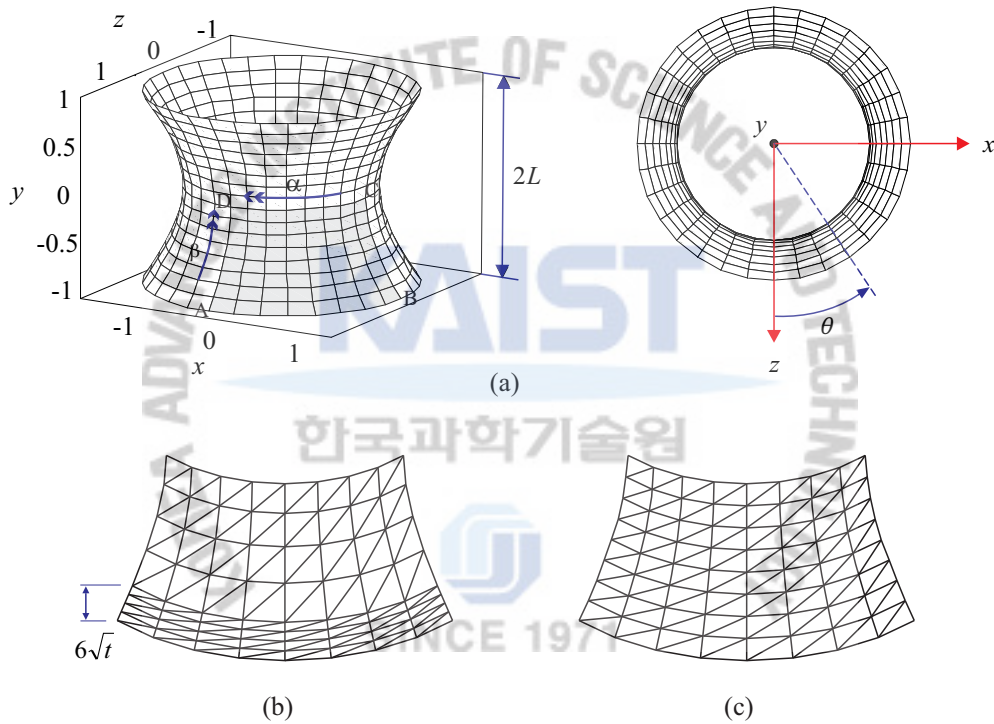


Figure 3.18. Hyperboloid shell problem ($E = 2.0 \times 10^{11}$, $\nu = 1/3$ and $p_0 = 1.0$). (a) Shell geometry and boundary conditions, (b) Graded mesh for the clamped case (8×8 mesh, $t/L = 1/1,000$), (c) Mesh for the free case (8×8 mesh).

The hyperboloid shell shown in **Figure 3.18** is considered, where the mid-surface of the shell structure is given by

$$x^2 + y^2 = 1 + z^2, \quad y \in [-1, 1]. \quad (3.26)$$

A smoothly varying periodic pressure is applied normal to the surface, as in **Figure 3.13**,

$$p(\theta) = p_0 \cos(2\theta), \quad (3.27)$$

When both ends are clamped, a membrane-dominated problem is obtained, and when the ends are free, a bending-dominated problem is obtained. The bending-dominated hyperboloid shell problem is known to be difficult to solve [23, 99, 105].

Due to symmetry, the analyses are carried out using one-eighth of the structure, corresponding to the shaded region ABCD in **Figure 3.18(a)**. For the membrane-dominated case, the clamped boundary condition is imposed using: $u_z = \beta = 0$ along BC, $u_x = \beta = 0$ along AD, and $u_y = \alpha = 0$ along DC, and $u_x = u_y = u_z = \alpha = \beta = 0$ along AB. For the bending-dominated case, the free boundary condition is imposed using: $u_z = \beta = 0, u_{,z} = \beta = 0$ along BC, $u_x = \beta = 0$ along AD, and $u_y = \alpha = 0$ along DC [23, 99].

In common with previous problems, the reference solutions calculated with a mesh of 96×96 MITC9 shell elements are used. The solutions using the MITC3, MITC4, MITC6 and enriched MITC3 shell elements are obtained with $N \times N$ meshes ($N = 8, 16, 32$ and 64 for the MITC3 and MITC4 shell elements and $N = 4, 8, 16,$ and 32 for the MITC6 and enriched MITC3 shell elements). The element size used in the convergence curves is $h = L/N$. In the clamped hyperboloid shell problem, a boundary layer of width $6\sqrt{t}$ is used for half of the mesh, see **Figure 3.18(b)**. In the free hyperboloid shell problem, the thin boundary layer is not specially meshed.

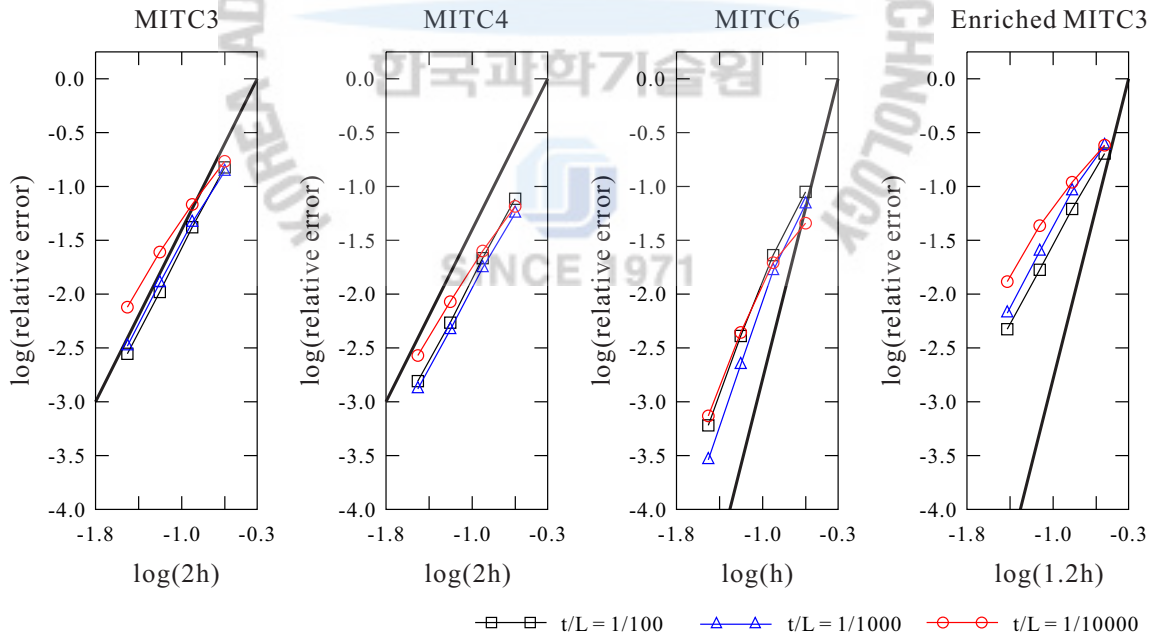


Figure 3.19. Convergence curves for the clamped hyperboloid shell problem with uniform meshes. The bold line represents the optimal convergence rate, which is 2.0 for linear elements and 4.0 for quadratic elements.

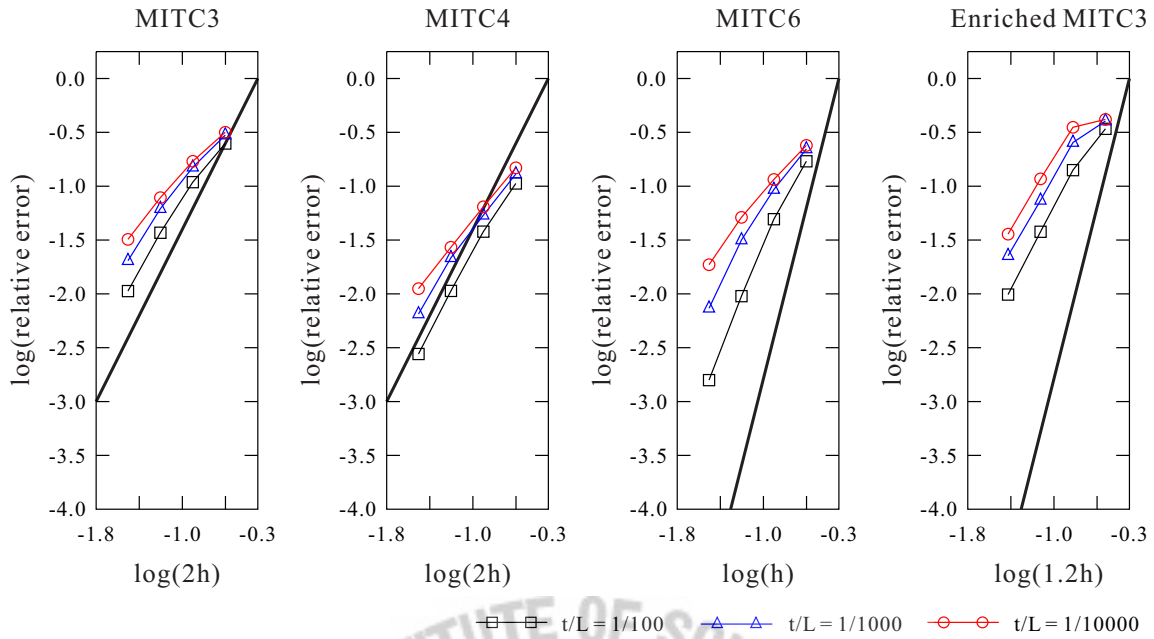


Figure 3.20. Convergence curves for the clamped hyperboloid shell problem with the distorted meshes shown in Figure 3.9. The bold line represents the optimal convergence rate, which is 2.0 for linear elements and 4.0 for quadratic elements.

Figure 3.19 and **Figure 3.20** show the convergence curves for both uniform and distorted meshes in the membrane dominated case (that is, the clamped hyperboloid shell problem). The performance of all shell elements is good.

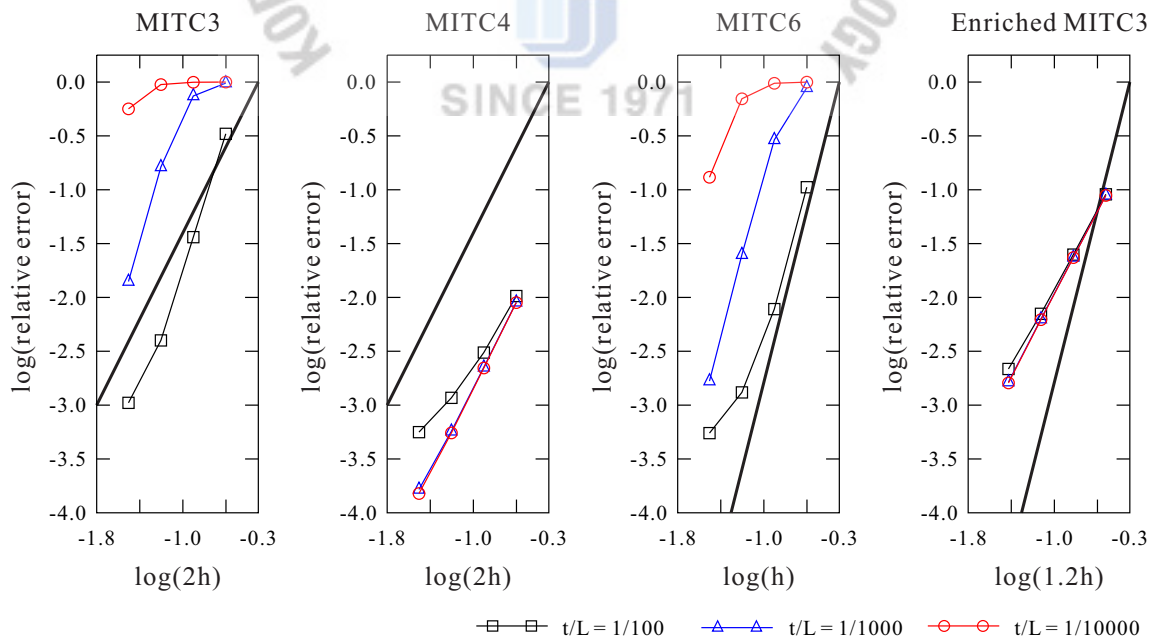


Figure 3.21. Convergence curves for the free hyperboloid shell problem with uniform meshes. The bold line

represents the optimal convergence rate, which is 2.0 for linear elements and 4.0 for quadratic elements.

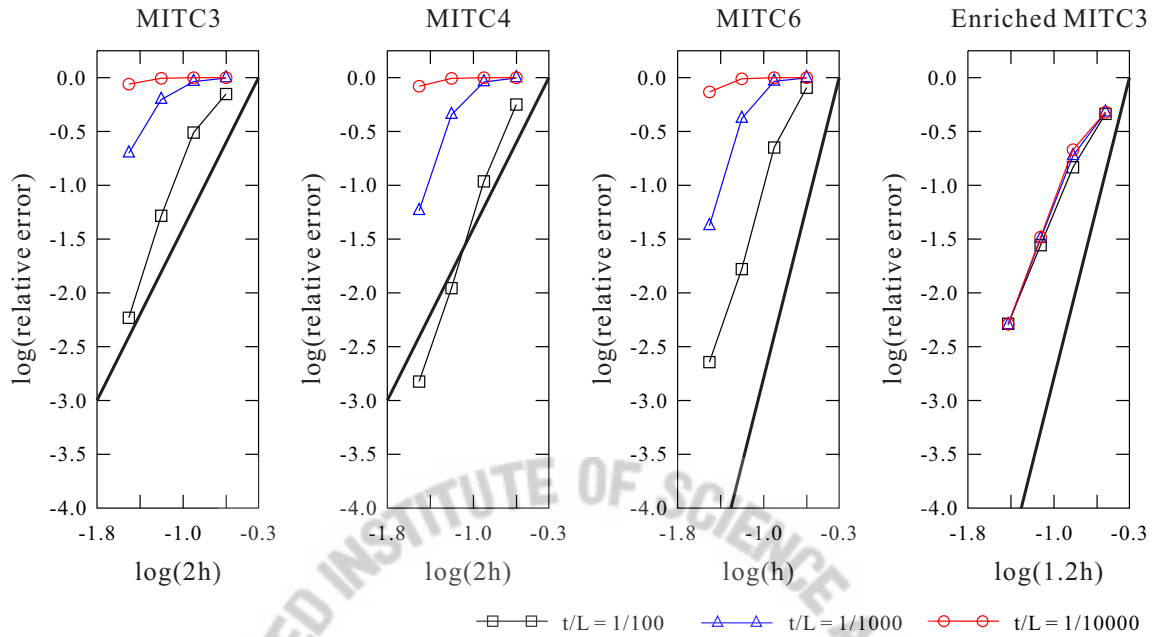


Figure 3.22. Convergence curves for the free hyperboloid shell problem with the distorted meshes shown in Figure 3.9. The bold line represents the optimal convergence rate, which is 2.0 for linear elements and 4.0 for quadratic elements.

For the bending-dominated case (that is, the free hyperboloid shell problem), the convergence curves are shown in **Figure 3.21** and **Figure 3.22**. The enriched MITC3 shell element shows the best convergence behavior among the shell elements considered. Even in the use of distorted meshes, the performance of the enriched MITC3 shell element is excellent since the other shell elements show some degree of locking.

3.5 Local Use of Cover Interpolations

In the convergence studies given in Section 3.4, the enriched MITC3 shell finite element showed a good performance when its element is used throughout the mesh. In this section, the local use of cover interpolation functions over the solution domains is illustrated. This scheme of increasing solution accuracy is quite different from using conventional standard shell finite elements with mesh refinements. Two numerical examples are considered: a shaft-shaft interaction problem and a ‘monster’ shell problem. The maximum effective stress, the strain energy and the deformed shape will be evaluated with and without using local enrichments.

3.5.1 Shaft-Shaft Interaction Problem

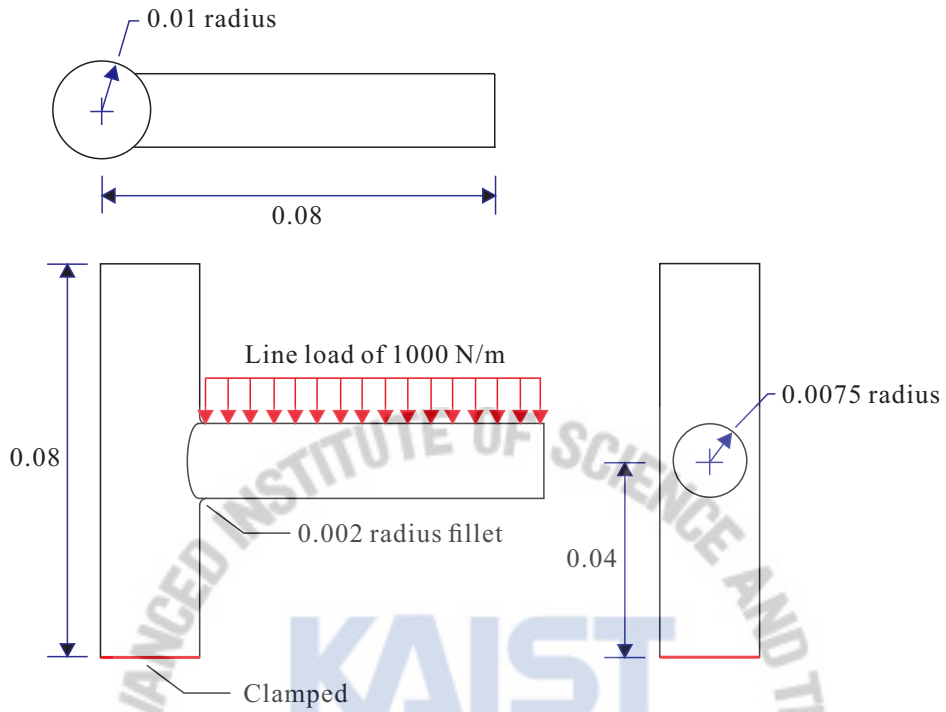


Figure 3.23. Shaft-shaft interaction problem with fillets ($E = 2.07 \times 10^{11}$, $\nu = 0.29$).

한국과학기술원



SINCE 1971

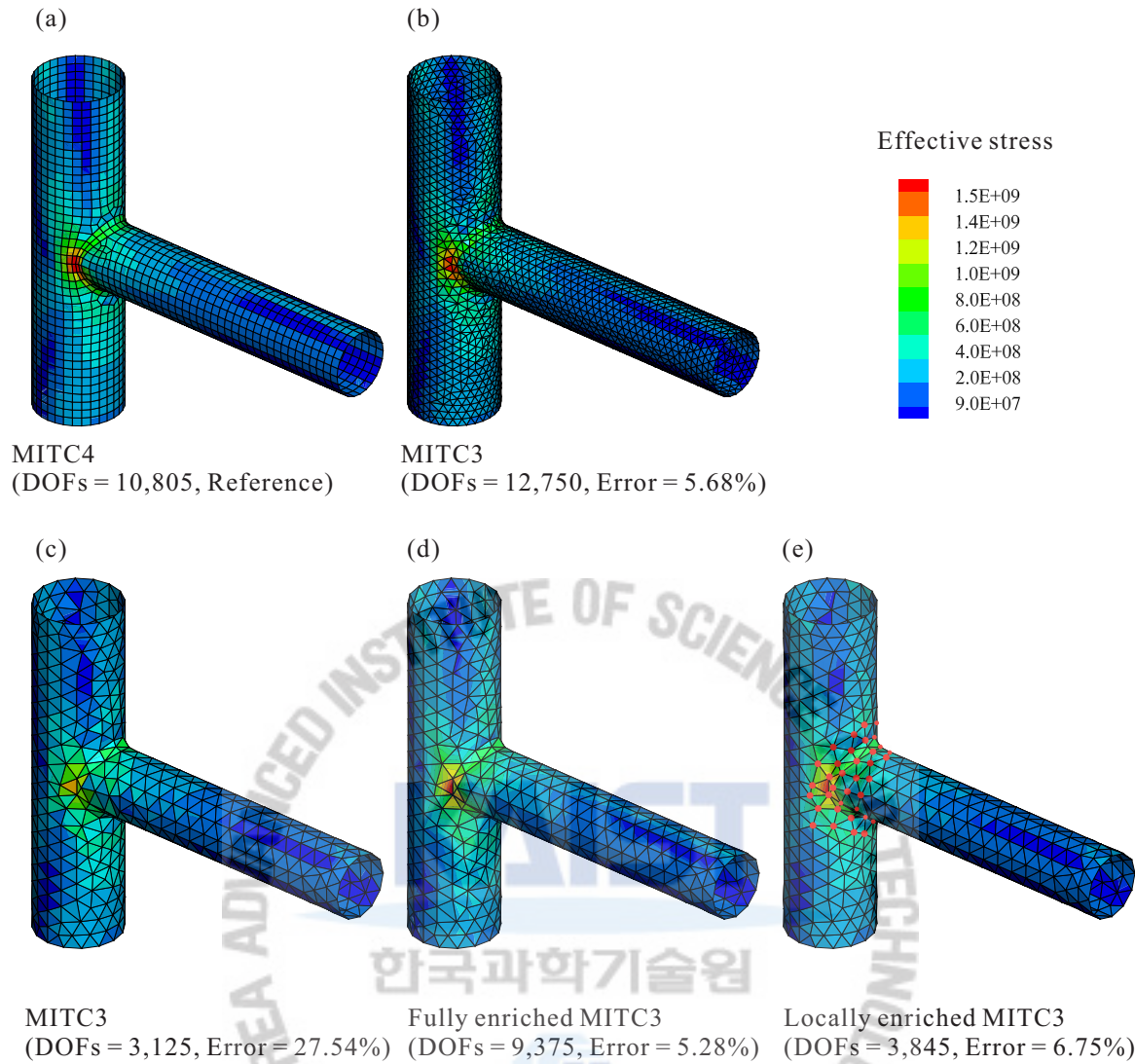


Figure 3.24. Distributions of effective stress for the shaft-shaft interaction problem: for (a) the 2,193 node model of the MITC4 shell elements, (b) the 2,582 node model of the MITC3 shell elements, (c) the 641 node model of the MITC3 shell elements, (d) the 641 node model fully enriched, and (e) the 641 node model locally enriched. The red dot represents enriched nodes (DOFs: total number of degrees of freedom used, Error = $(\sigma_v^{ref} - \sigma_v^h) / \sigma_v^{ref} \times 100$).

Consider the two cylindrical shafts connected with fillets of radius 0.002m, in which the horizontal shaft is subjected to a line load of $1000 \text{ N} / \text{m}$, as shown in **Figure 3.23**, and the vertical shaft is fully clamped at its lower end. **Figure 3.24** presents the distribution of the effective stress (von Mises stress) obtained using the MITC4 and MITC3 shell elements, and using the enriched MITC3 shell element throughout the mesh or only locally. The reference solution is given by a fine mesh of the MITC4 shell element, in which 2,150 elements and 10,805 DOFs are used, see **Figure 3.24(a)**. **Figure 3.24(b)** presents a finer mesh of the MITC3 shell element and **Figure 3.24(c)-(e)** show the same coarse mesh used for the MITC3 shell element and the fully and locally enriched shell models. The red dots in **Figure 3.24(e)** represent the selected nodes carrying

interpolation covers around the fillet area where stress concentration is expected.

Table 3.4. Relative errors in maximum effective stress in the shaft-shaft interaction problem for the five different shell models in Figure 3.24. Relative error (%) = $(\sigma_{\max}^{ref} - \sigma_{\max}^h) / \sigma_{\max}^{ref} \times 100$.

	Fine mesh		Coarse mesh		
	MITC4 (reference)	MITC3	MITC3	Fully enriched MITC3	Locally enriched MITC3
Elements	2,150	5,078	1,240	1,240	1,240
Nodes	2,193	2,582	641	641	641
Enriched nodes	-	-	-	641	72
Free DOFs	10,805	12,750	3,125	9,375	3,845
Max. effective stress (σ_{\max})	1.78E+09	1.68E+09	1.29E+09	1.69E+09	1.66E+09
Relative error (%)	-	5.68	27.54	5.28	6.75

Table 3.4 gives the numbers of elements, nodes, degrees of freedom used, and the relative errors in the maximum effective stress obtained when using the shell models in **Figure 3.24**. In the shaft-shaft interaction problem, the maximum effective stress is obtained around the fillet area. Using the local enrichments, the maximum effective stress is well predicted with a much smaller number of degrees of freedom.

3.5.2 Highly-Sensitive Shell Problem

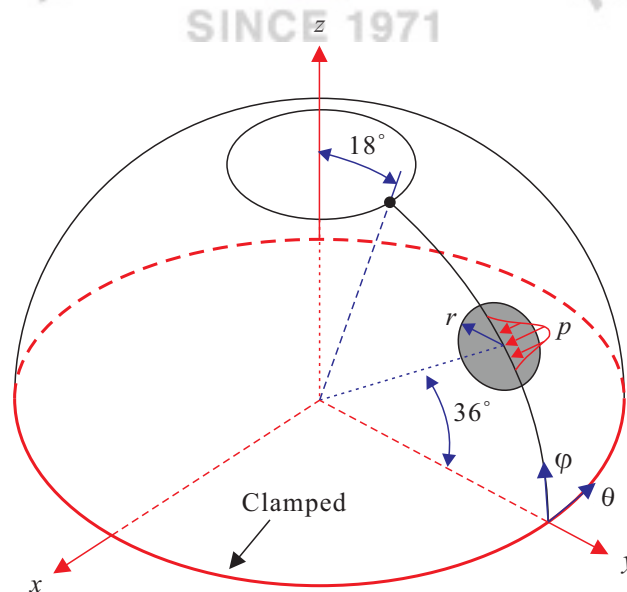


Figure 3.25. A “highly-sensitive” shell problem. ($L = R = 10$, $E = 6.285 \times 10^7$, $\nu = 0.3$, and $p(r) = e^{-4r^2}$).

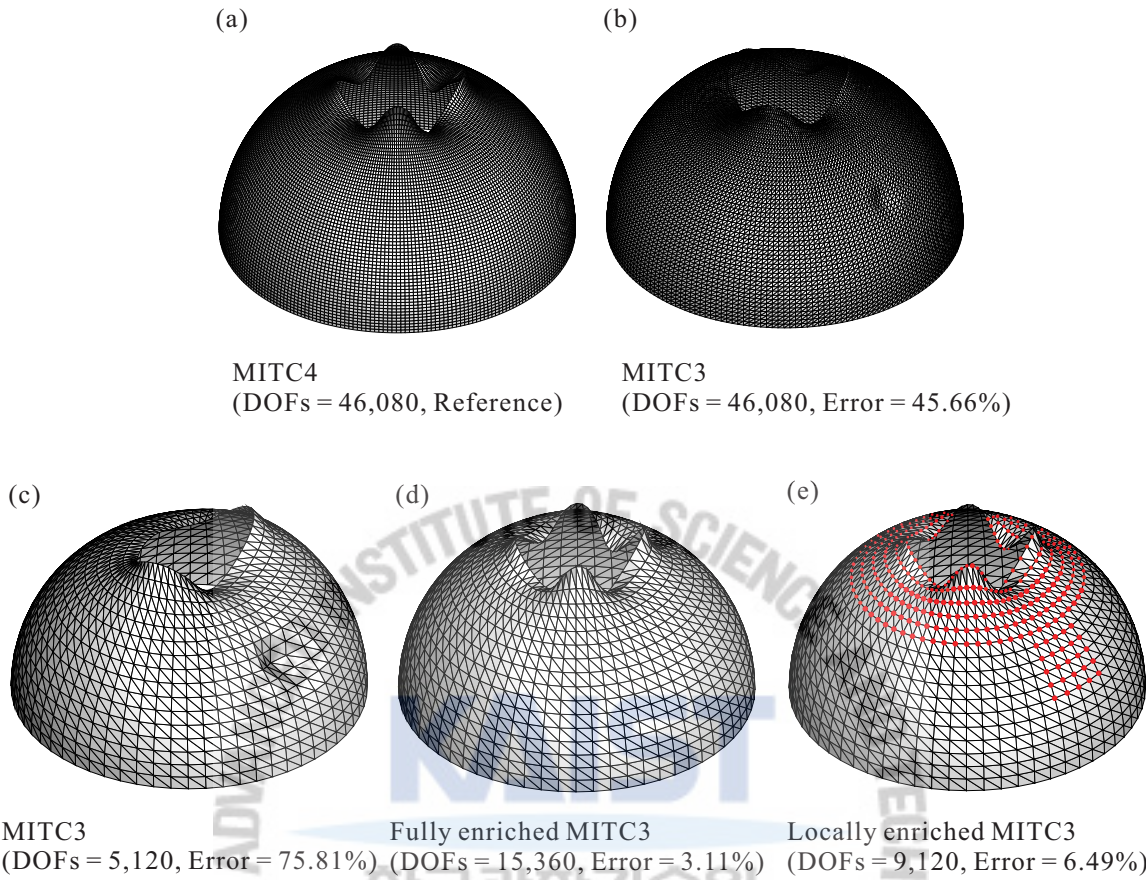


Figure 3.26. Deformed shapes for the monster shell problem ($t/L = 1/10,000$): for (a) the $48(\text{axial}) \times 192(\text{circumferential})$ mesh of the MITC4 shell elements, (b) the 48×192 mesh of the MITC3 shell elements, (c) the 16×64 mesh of the MITC3 shell elements, (d) the 16×64 mesh model fully enriched, and (e) the 16×64 mesh model locally enriched. In the figure (e), the red dot represents enriched nodes. (DOFs: the total number of degrees of freedom used, $\text{Error} = (E_{ref} - E_h) / E_{ref} \times 100$).

Figure 3.25 shows the problem considered (referred to also as “the monster shell problem”) [106]. The shell geometry corresponds to a half-sphere with the top sliced off. The shell is clamped around its entire lower boundary. A smoothly distributed pressure is applied over a small part of the interior of the shell. Since there is no exact solution to the problem, the reference solution is calculated by a fine mesh of $48(\text{axial}) \times 192(\text{circumferential})$ MITC4 shell elements; see **Figure 3.26(a)**. This is a sufficiently fine mesh to identify and reasonably resolve the boundary layer on the free top. **Figure 3.26(b)** presents a finer mesh of MITC3 shell elements, and **Figure 3.26(c)-(e)** show a coarser mesh for the MITC3 shell element and the fully and locally enriched cases.

Table 3.5. Relative errors in strain energy in the monster shell problem for the five different shell models in Figure 3.26. Relative error (%) = $(E_{ref} - E_h) / E_{ref} \times 100$.

	Fine mesh 48(axial) × 192(circumferential)		Coarse mesh 16(axial) × 64(circumferential)		
	MITC4 (reference)	MITC3	MITC3	Fully enriched MITC3	Locally enriched MITC3
Elements	9,216	18,432	2,048	2,048	2,048
Nodes	9,408	9408	1,088	1,088	1,088
Enriched nodes	-	-	-	1,088	409
Free DOFs	46,080	46,080	5,120	15,360	9,120
Oscillations	4	3	2	4	4
Strain energy (E)	5.21E-04	2.83E-04	1.26E-04	5.37E-04	4.87E-04
Relative error (%)	-	45.66	75.81	3.11	6.49

Figure 3.26 shows the deformed shapes of the shell problem when the shell thickness is 0.001 ($t/L = 1/10,000$). For visualization, the displacements are normalized so that the maximum outward total displacement value is equal to 2.0. Note that the displacements are dominant in the immediate vicinity of the free boundary, namely within the boundary layer. **Figure 3.26(b)** and (c) show that the MITC3 shell element meshes are not effective in predicting the displacement oscillations² in the circumferential direction within the boundary layer. However, when the coarse MITC3 shell element mesh is fully enriched, the displacements in the boundary layer are calculated accurately as shown in **Figure 3.26(d)**. Also, the local use of the cover interpolations within the boundary layer results in excellent overall accuracy with a significantly reduced number of degrees of freedom, see **Figure 3.26(e)**. **Table 3.5** shows the number of elements, nodes and degrees of freedom used, the number of displacement oscillations, and the relative errors in the strain energies.

² In the monster shell problem, the number of displacement oscillations in the boundary layer increases as the shell thickness decreases. The number is given by $\log(L/t)$.

Chapter 4. A Partition of Unity Based 4-Node Quadrilateral Shell Element

4.1 A 4-Node Element Based on Partition of Unity

The partition of unity (PU) approximation offers enormous advantages over the standard finite element approximation by its local enrichments and excellent solution accuracy. This feature is particularly advantageous for modeling crack propagation and areas where non-smooth and near singular solution are sought. This is due to the fact that solution accuracy can effectively increase without any local mesh refinements. However, the partition of unity approximation faces some difficulties such as the linear dependence problem. When both the partition of unity function and the local approximation function are taken as polynomials, the global stiffness matrix becomes singular, that is rank deficient [33, 34, 93].

Many researchers have studied the elimination of the singularity of the stiffness matrix in the methods using the partition of unity approximation concept. Oden et al. [36] proposed excluding the space spanned by the terms of finite element shape functions from that of the local approximation functions in order to avoid the linear dependence. Strouboulis et al. [37, 38] suggested the mapped quadrilateral shape functions, but the linear dependencies are not completely eliminated in their method. Tian et al. [94] studied some effective approaches to avoid the linear dependency problems. These approaches include suppressing the additional unknown degrees of freedom, using constant local functions at the boundary nodes, using the triangular mesh around quadrilateral mesh, and deleting the polynomial terms included in the span of the partition of unity function, which was first suggested by Oden et al. [36]. Babuška and Banerjee [95] developed the SGFEM (Stable Generalized Finite Element Method) which is aim to improve the conditioning property of the GFEM (Generalized Finite Element Method). The basic idea of the SGFEM is to use a modified local function. Rajendran et al. [84, 96] suggested the partition of unity based FE-meshfree element. They adopted the finite element shape functions as the partition of unity and the least-square PIM (Point Interpolation Method) shape function as the local approximation. With this choice, the proposed scheme eliminates the linear dependence problem. Cai et al. [97] suggested that the local approximation at a boundary node is constructed by a modified least-squares approach and that at an inner node using a polynomial basis. These dually constructed local approximation avoid the linear dependence problem. Schweitzer used the flat hat functions as a partition of unity to construct a parallel multilevel partition of unity method [107]. The linear dependence issue is also discussed in the context of XFEM (eXtended Finite Element Method) [108, 109].

In this chapter, a partition of unity based 4-node quadrilateral shell finite element (also herein called enriched MITC4) is presented. The MITC (Mixed Interpolation of Tensorial Components) method is applied to avoid the transverse shear locking phenomenon. To eliminate the linear dependence problem, the additional unknown coefficients around the domain boundary are constrained and the standard MITC4 shell elements are only used in that region.

4.1.1 Partition of Unity Approximation

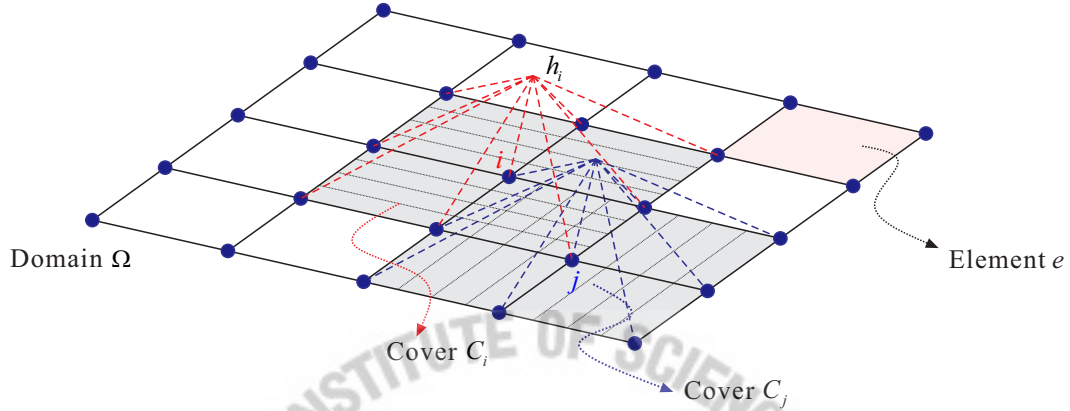


Figure 4.1. Description of sub-domain; finite element shape function h_i , an element e and cover region C_i and C_j constructed by all the elements connected to node i and j , respectively.

A partition of unity is a set of functions that sum to unity at an arbitrary point in the domain considered. In order to construct the partition of unity, the domain Ω under consideration is discretized by a set of covers C_i and C_j which satisfy a certain overlap condition, see Figure 4.1. The functions φ_i which satisfy the partition of unity are defined by

$$\sum_i \varphi_i = 1, \quad (4.1)$$

where the functions φ_i form a partition of unity subordinate to the cover C_i . Let a set of functions $V_i = \{v^j \mid v^j \in H^1(C_i \cap \Omega)\}$ associated with each cover C_i be given. Then, a partition of unity approximation is represented by

$$u_{PUM} = \sum_i \varphi_i V_i = \sum_i \varphi_i \left(\sum_j v_j^i d_j^i \right), \quad v_j^i \in V_i. \quad (4.2)$$

Equation (4.2) is the basic definition of the PUM (partition of unity method) and a more detailed description of the partition of unity method can be found in References [33, 34, 93]. The key feature of the partition of unity method is that any functions that reflect the local characteristics of the solution can be adopted in the partition of unity functions to construct the high order approximation. However, when both the partition of unity functions $\{\varphi_i\}$ and the local functions $\{v_j^i\}$ in Equation (4.2) are polynomials, the partition of unity approximation is linearly dependent.

With this concept of the partition of unity method, the partition of unity based finite element method based on the concept of the PU approximation has been developed. The finite element shape functions naturally satisfy a partition of unity. Then, the partition of unity based finite element method is constructed by replacing the partition of unity functions φ_i with the finite element shape function h_i . The displacement interpolation for the partition of unity based 4-node quadrilateral element is given by

$$\bar{u}(\mathbf{x}) = \sum_{i=1}^4 h_i u_i^l(\mathbf{x}) = \mathbf{h} \mathbf{u}^e, \quad (4.3)$$

in which \mathbf{x} is the position vector collecting nodal coordinates at a point and $\mathbf{h} = [h_1 \ h_2 \ h_3 \ h_4]$ is a matrix of shape functions as for a conventional 4-node ($i = 1, 2, 3, 4$) quadrilateral finite element. In Equation (4.3), the vector \mathbf{u}^e is not a nodal displacement vector as in the standard finite element method but a vector of nodal displacement functions (also called local approximation) and is defined by

$$\mathbf{u}^e = [u_1^l(\mathbf{x}) \ u_2^l(\mathbf{x}) \ u_3^l(\mathbf{x}) \ u_4^l(\mathbf{x})]^T, \quad (4.4)$$

where the superscript l indicates the local nature of the functions. The local approximation over the cover C_i is constructed by [28, 36-39, 84, 93, 96-98, 110-112]

$$u_i^l(\mathbf{x}) = \mathbf{p}^T(\mathbf{x}) \mathbf{a}(\mathbf{x}) = \sum_{k=0}^{m-1} p_{k+1}(\mathbf{x}) a_{ki}, \quad (4.5)$$

where $\mathbf{p}^T(\mathbf{x}) = [1 \ x \ y \ xy \ \dots]$ is a polynomial basis vector, m is the number of monomials in the basis, and a_{ki} are the corresponding unknown coefficients to each monomial in the basis. Using only bilinear polynomial in Equation (4.5), the local approximation can be rewritten as

$$u_i^l(\mathbf{x}) = a_{0i} + a_{1i}x + a_{2i}y + a_{3i}xy, \quad (4.6)$$

where i is the node index and a_{0i} to a_{3i} are the corresponding unknown coefficients to be determined.

By enforcing $u_i^l(\mathbf{x})$ to be equal to the nodal value at node i , Equation (4.6) can be rewritten as

$$u_i^l(x_i, y_i) = a_{0i} + a_{1i}x_i + a_{2i}y_i + a_{3i}x_i y_i = \bar{u}_i \quad (4.7)$$

and

$$a_{0i} = \bar{u}_i - a_{1i}x_i - a_{2i}y_i - a_{3i}x_i y_i, \quad (4.8)$$

where \bar{u}_i is the unknown nodal displacement at the node i in the x direction. Substituting Equation (4.8) into Equation (4.6), the local approximation is obtained by

$$u_i^l(\mathbf{x}) = \bar{u}_i + \xi_i \hat{u}_i^\xi + \eta_i \hat{u}_i^\eta + \xi \eta_i \hat{u}_i^{\xi\eta} \quad (4.9)$$

with

$$x - x_i = \xi_i, \quad y - y_i = \eta_i, \quad xy - x_i y_i = \xi \eta_i, \quad \hat{u}_i^\xi = a_{1i}, \quad \hat{u}_i^\eta = a_{2i}, \quad \hat{u}_i^{\xi\eta} = a_{3i}, \quad (4.10)$$

where the \hat{u}_i^ξ , \hat{u}_i^η and $\hat{u}_i^{\xi\eta}$ are the additional unknown coefficients over the cover C_i .

Finally, substituting Equation (4.9) and Equation (4.10) into Equation (4.3), displacement approximation for the partition of unity based 4-node element is represented by

$$u = \bar{u} + \hat{u} \quad (4.11)$$

with

$$\bar{u} = \sum_{i=1}^4 h_i \bar{u}_i, \quad \hat{u} = \sum_{i=1}^4 h_i (\xi_i \hat{u}_i^\xi + \eta_i \hat{u}_i^\eta + \zeta_i \eta_i \hat{u}_i^{\xi\eta}). \quad (4.12)$$

The partition of unity based displacement approximation in (4.11) consists of two parts: the standard displacement interpolation of the 4-node element, \bar{u} and the additional high order term, \hat{u} .

4.1.2 Linear Dependence

The linear dependence problem occurs when the partition of unity function and the local approximation are polynomials in the partition of unity method. Tian et al. [93] introduced the linear dependence problem of the partition of unity method when solving the Helmholtz problem. One dimensional Helmholtz equation is given by

$$-u'' + k^2 u = f \in C^2 \quad [0,1] \quad \text{on} \quad (0,1], \quad (4.13)$$

$$u(0) = 0, \quad u'(1) = g \in R. \quad (4.14)$$

The PUM approximation of the above equation is constructed by

$$u_{PUM} = \varphi_0 v_0 + \sum_{i=1}^n \varphi_i v_i, \quad (4.15)$$

in which the total $n+1$ nodes are arranged at $x_i = ih$, $i = 0, 1, \dots, n$ evenly in the domain $[0,1]$, $h = 1/n$. The partition of unity functions φ_i ($i = 0, 1, \dots, n$) are the usual piecewise linear hat functions defined at the nodes. These functions form the partition of unity. Using the polynomial, the local approximations are represented by

$$v_0 = x a_0^1 + \dots + x^p a_p^0, \quad (4.16)$$

$$v_i = a_0^i + (x - x_i) a_1^i + \dots + (x - x_i)^p a_p^i, \quad p \geq 0, \quad (4.17)$$

at the Dirichlet boundary $x = 0$ and inside the domain $(0,1]$, respectively. The local approximation v_0 at the Dirichlet boundary is defined such that the Equation (4.14) is satisfied naturally. The approximation $\{\sum_i \varphi_i v_i\}$ for the partition of unity method has a total of $n(p+1)+p$ unknowns, i.e., a total of $n(p+1)+p$ shape functions $\varphi_i v_i$, but the partition of unity method basis has a width of only $n(p+1)$. Therefore, for $p \geq 1$, $n(p+1)+p > n(p+1)$, the approximation for the partition of unity method is linearly dependent and the resulting stiffness matrix of the method becomes singular.

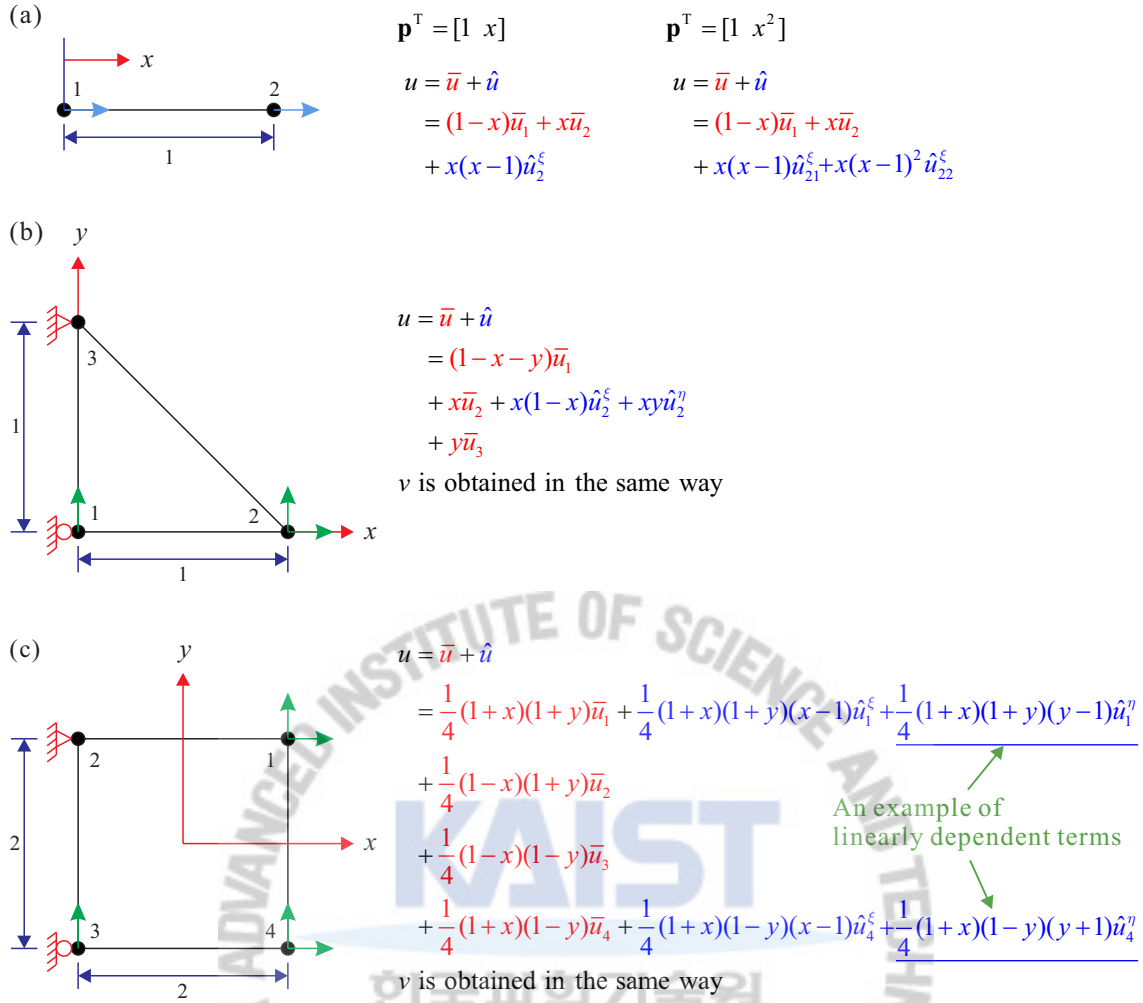


Figure 4.2. Linear dependence and independence problem in the partition of unity based finite element method: (a) one-dimensional element of unit length, (b) linearly independent interpolations with prescribed boundary conditions for the 3-node triangular element and (c) linearly dependent interpolations for the 4-node quadrilateral element even though prescribed boundary conditions are applied.

To verify the linear dependence in the partition of unity based finite element method, one-dimensional single element shown in Figure 4.2(a) is considered. The displacement approximation for a one-dimensional element with the partition of unity approximation ($\mathbf{p}^T(\mathbf{x}) = [1 \ x]$) is expressed as follows:

$$u = h_1\bar{u}_1 + h_2\bar{u}_2 + h_1(x-x_1)\hat{u}_1^\xi + h_2(x-x_2)\hat{u}_2^\xi \quad (4.18)$$

with

$$h_1 = 1-x, \quad h_2 = x, \quad x_1 = 0 \quad \text{and} \quad x_2 = 1. \quad (4.19)$$

Hence Equation (4.18) becomes

$$u = (1-x)\bar{u}_1 + x\bar{u}_2 + \underline{(1-x)x}\hat{u}_1^\xi + \underline{x(x-1)}\hat{u}_2^\xi. \quad (4.20)$$

Using quadratic polynomials into the local approximation ($\mathbf{p}^T(\mathbf{x}) = [1 \ x \ x^2]$), displacement approximation is obtained by

$$u = h_1\bar{u}_1 + h_2\bar{u}_2 + h_1(x-x_1)\hat{u}_{11}^\xi + h_1(x^2-x_1^2)\hat{u}_{12}^\xi + h_2(x-x_2)\hat{u}_{21}^\xi + h_2(x^2-x_2^2)\hat{u}_{22}^\xi \quad (4.21)$$

and using the Equation (4.19), the displacement approximation is rewritten as

$$u = (1-x)\bar{u}_1 + x\bar{u}_2 + \underline{(1-x)x\hat{u}_{11}^\xi} + \underline{(1-x)x^2\hat{u}_{12}^\xi} + \underline{x(x-1)\hat{u}_{21}^\xi} + x(x^2-1)\hat{u}_{22}^\xi. \quad (4.22)$$

In the above Equations (4.20) and (4.22), the displacement approximations are linearly dependent due to the unknown degrees of freedom \hat{u}_1^ξ , \hat{u}_2^ξ , \hat{u}_{11}^ξ and \hat{u}_{21}^ξ . The linearly dependent terms in the displacement approximations are underlined.

However, assume that we impose at node 1 the displacement \bar{u}_1 (as usual, to take out the rigid body mode) and also eliminate the additional unknown degrees of freedom \hat{u}_1^ξ at that node. Then the remaining interpolation functions are linearly independent, for the local approximation using linear polynomials

$$u = (1-x)\bar{u}_1 + x\bar{u}_2 + x(x-1)\hat{u}_2^\xi \quad (4.23)$$

where \bar{u}_1 would now be prescribed, and for the local approximation using quadratic polynomials

$$u = (1-x)\bar{u}_1 + x\bar{u}_2 + x(x-1)\hat{u}_{21}^\xi + x(x^2-1)\hat{u}_{22}^\xi \quad (4.24)$$

where \bar{u}_1 would be also prescribed.

The partition of unity approximation of a 3-node triangular element is obtained by

$$u = \bar{u} + \hat{u}, \quad (4.25)$$

where

$$\bar{u} = h_1\bar{u}_1 + h_2\bar{u}_2 + h_3\bar{u}_3, \quad (4.26)$$

$$\hat{u} = h_1(x-x_1)\hat{u}_1^\xi + h_2(x-x_2)\hat{u}_2^\xi + h_3(x-x_3)\hat{u}_3^\xi + h_1(y-y_1)\hat{u}_1^\eta + h_2(y-y_2)\hat{u}_2^\eta + h_3(y-y_3)\hat{u}_3^\eta \quad (4.27)$$

with

$$h_1 = 1-x-y, \quad h_2 = x, \quad h_3 = y, \quad x_1 = 0, \quad x_2 = 1, \quad x_3 = 0, \quad y_1 = 0, \quad y_2 = 0 \quad \text{and} \quad y_3 = 1. \quad (4.28)$$

Therefore,

$$\hat{u} = \underline{(1-x-y)x\hat{u}_1^\xi} + \underline{x(x-1)\hat{u}_2^\xi} + yx\hat{u}_3^\xi + (1-x-y)y\hat{u}_1^\eta + \underline{xy\hat{u}_2^\eta} + y(y-1)\hat{u}_3^\eta. \quad (4.29)$$

The displacement interpolation v is obtained in the same way. The displacement approximation in Equation (4.29) is linearly independent. If the displacements are prescribed at nodes 1 and 3, as in Figure 4.2(b), the additional unknown degrees of freedom \hat{u}_1^ξ and \hat{u}_3^ξ are all fixed, and the linearly independent interpolations are obtained as follows:

$$u = (1-x-y)\bar{u}_1 + x\bar{u}_2 + y\bar{u}_3 + x(x-1)\hat{u}_2^\xi + xy\hat{u}_2^\eta, \quad (4.30)$$

$$v = (1-x-y)\bar{v}_1 + x\bar{v}_2 + y\bar{v}_3 + x(x-1)\hat{v}_2^\xi + xy\hat{v}_2^\eta. \quad (4.31)$$

This implies that the stiffness matrix is positive definite for the single elements considered provided the rigid body modes have been removed, as usual by constraining appropriate degrees of freedom, with all \hat{u}_i^ξ and \hat{u}_i^η degrees of freedom also removed at the nodes with any prescribed displacements. Consider now that additional elements are attached to these single elements, with no further \bar{u}_i degrees of freedom pre-

scribed and all \hat{u}_i^ξ and \hat{u}_i^η degrees of freedom free at the additional nodes used in the mesh. Then, by the above argument, for any nonzero values of the \bar{u}_i , \hat{u}_i^ξ and \hat{u}_i^η degrees of freedom in the mesh, positive strain energy is stored in the mesh. Therefore, all eigenvalues of the stiffness matrix are positive, which means that the matrix is positive definite.

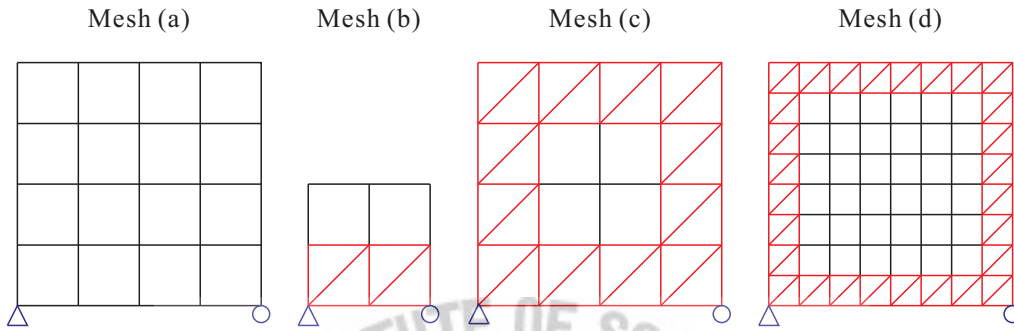


Figure 4.3. Element meshes of the eigenvalue analysis for 4-node quadrilateral elements and mixed meshes with the 3-node triangular and 4-node quadrilateral elements. This work was done by Tian [93].

However, for a 4-node quadrilateral element shown in Figure 4.2(c), displacement interpolation is linearly dependent even though the additional unknown degrees of freedom are constrained in the same manner as the partition of unity based 3-node triangular element. For the partition of unity based 4-node quadrilateral element, Tian et al. [93] conducted the eigenvalue analyses as shown in Figure 4.3. The mesh (a) consists of only 4-node quadrilateral elements. It is well known that the partition of unity based 4-node quadrilateral element definitely suffers from the linearly dependence. Meshes (b), (c) and (d) are generated by mixing 3-node triangular elements and the problematic squares in specified manners. Table 4.1 shows the number of spurious zero eigenvalues after the support treatments. Using the 3-node triangular elements around mesh boundaries as in meshes (c) and (d), the spurious zero eigenvalues can be completely removed. In this thesis, to apply the partition of unity approximation into the 4-node quadrilateral shell element, the additional unknown degrees of freedom around mesh boundaries are constrained instead of using the 3-node triangular elements.

Table 4.1. Results of eigenvalue analyses of the partition of unity based finite element method, see Figure 4.3 for the meshes. This work was conducted by Tian [93].

Mixed meshes		Number of zero eigenvalue (zero-order local functions are specified at the two of the nodes; essential boundary conditions are applied to the two nodes)						Linearly dependent?
Method	Mesh	$p=0/\text{FEM}$	$p=1$	$p=2$	$p=3$	$p=4$	$p=5$	
Quad	(a)	0	14	28	28	28	28	Yes
Mixed	(b)	0	2	4	4	4	4	Yes
Mixed	(c)	0	0	0	0	0	0	No
Mixed	(d)	0	0	0	0	0	0	No

4.2 The Enriched MITC4 Shell Finite Element

In this section, the formulation of the partition of unity based 4-node quadrilateral shell finite element (also called enriched MITC4) is presented.

4.2.1 Enriched Displacement Interpolation

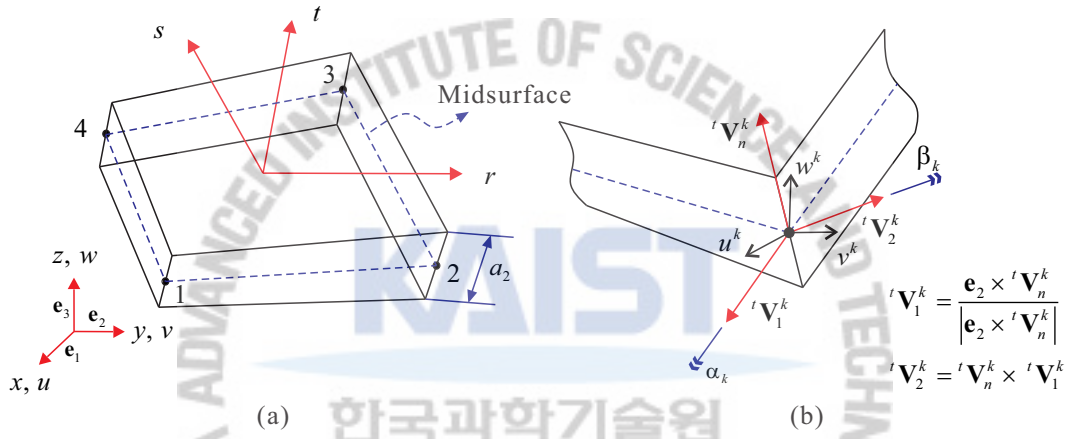


Figure 4.4. The MITC4 shell finite element: (a) Geometry of the MITC4 shell finite element. (b) Definition of rotational degrees of freedom α_k and β_k .

The geometry of the continuum mechanics based 4-node quadrilateral shell element is interpolated by

$$\mathbf{x}(r, s, t) = \sum_{i=1}^4 h_i(r, s) \mathbf{x}_i + \frac{t}{2} \sum_{i=1}^4 a_i h_i(r, s) \mathbf{V}_n^i, \quad (4.32)$$

with

$$h_1 = \frac{1}{4}(1-r)(1-s), \quad h_2 = \frac{1}{4}(1+r)(1-s), \quad (4.33)$$

$$h_3 = \frac{1}{4}(1+r)(1+s), \quad h_4 = \frac{1}{4}(1-r)(1+s), \quad (4.34)$$

where r , s and t are natural coordinates, h_i is the two-dimensional interpolation function corresponding to node i , \mathbf{x}_i is the position vector of node i in the global Cartesian coordinate system, and a_i , \mathbf{V}_n^i denote the shell thickness and the director vector at node i , respectively, see **Figure 4.4**. The standard displacement interpolation of the 4-node quadrilateral shell finite element is represented by

$$\bar{\mathbf{u}} = \sum_{i=1}^4 h_i \bar{\mathbf{u}}_i + \sum_{i=1}^4 \frac{t}{2} a_i h_i (-\mathbf{V}_2^i \bar{\alpha}_i + \mathbf{V}_1^i \bar{\beta}_i), \quad (4.35)$$

in which $\bar{\mathbf{u}}_i = [\bar{u}_i \ \bar{v}_i \ \bar{w}_i]^T$ is the nodal displacement vector in the global Cartesian coordinate system, $\mathbf{V}_1^i = [V_{1x}^i \ V_{1y}^i \ V_{1z}^i]^T$ and $\mathbf{V}_2^i = [V_{2x}^i \ V_{2y}^i \ V_{2z}^i]^T$ are unit vectors orthogonal to \mathbf{V}_n^i and to each other, and $\bar{\alpha}_i$ and $\bar{\beta}_i$ are the rotations of the director vector \mathbf{V}_n^i about \mathbf{V}_1^i and \mathbf{V}_2^i at node i .

To apply the partition of unity approximation into the 4-node shell finite element, the only bilinear polynomials are adopted in the local approximation. The partition of unity approximation of the 4-node quadrilateral shell finite element is given by

$$\mathbf{u} = \bar{\mathbf{u}} + \hat{\mathbf{u}}, \quad (4.36)$$

where

$$\hat{\mathbf{u}} = \sum_{i=1}^4 \mathbf{H}_i \hat{\mathbf{u}}_i + \sum_{i=1}^4 \frac{t}{2} a_i \mathbf{H}_i (-\mathbf{D}_2^i \hat{\alpha}_i + \mathbf{D}_1^i \hat{\beta}_i) \quad (4.37)$$

with

$$\hat{\mathbf{u}}_i = [\hat{u}_i^\xi \ \hat{u}_i^\eta \ \hat{u}_i^{\xi\eta} \ | \ \hat{v}_i^\xi \ \hat{v}_i^\eta \ \hat{v}_i^{\xi\eta} \ | \ \hat{w}_i^\xi \ \hat{w}_i^\eta \ \hat{w}_i^{\xi\eta}]^T, \quad (4.38)$$

$$\hat{\alpha}_i = [\hat{\alpha}_i^\xi \ \hat{\alpha}_i^\eta \ \hat{\alpha}_i^{\xi\eta}]^T, \ \hat{\beta}_i = [\hat{\beta}_i^\xi \ \hat{\beta}_i^\eta \ \hat{\beta}_i^{\xi\eta}]^T, \quad (4.39)$$

in which $\hat{\mathbf{u}}_i$, $\hat{\alpha}_i$ and $\hat{\beta}_i$ are unknown coefficient vectors for the displacements and rotations, and the \mathbf{H}_i are the interpolation matrices associated with the high order displacements and rotations

$$\mathbf{H}_i = h_i \begin{bmatrix} \xi_i & \eta_i & \xi\eta_i & 0 & 0 & 0 & 0 & 0 & 0 \\ 0 & 0 & 0 & \xi_i & \eta_i & \xi\eta_i & 0 & 0 & 0 \\ 0 & 0 & 0 & 0 & 0 & 0 & \xi_i & \eta_i & \xi\eta_i \end{bmatrix}, \quad (4.40)$$

$$\mathbf{D}_1^i = \begin{bmatrix} V_{1x}^i & 0 & 0 & V_{1y}^i & 0 & 0 & V_{1z}^i & 0 & 0 \\ 0 & V_{1x}^i & 0 & 0 & V_{1y}^i & 0 & 0 & V_{1z}^i & 0 \\ 0 & 0 & V_{1x}^i & 0 & 0 & V_{1y}^i & 0 & 0 & V_{1z}^i \end{bmatrix}^T, \quad (4.41)$$

$$\mathbf{D}_2^i = \begin{bmatrix} V_{2x}^i & 0 & 0 & V_{2y}^i & 0 & 0 & V_{2z}^i & 0 & 0 \\ 0 & V_{2x}^i & 0 & 0 & V_{2y}^i & 0 & 0 & V_{2z}^i & 0 \\ 0 & 0 & V_{2x}^i & 0 & 0 & V_{2y}^i & 0 & 0 & V_{2z}^i \end{bmatrix}^T. \quad (4.42)$$

Note that the partition of unity displacement approximation for \mathbf{u} in Equation (4.36) consists of two parts: the standard bilinear term $\bar{\mathbf{u}}$ and the additional high order term $\hat{\mathbf{u}}$.

4.2.2 Assumed Covariant Transverse Shear Strain Fields

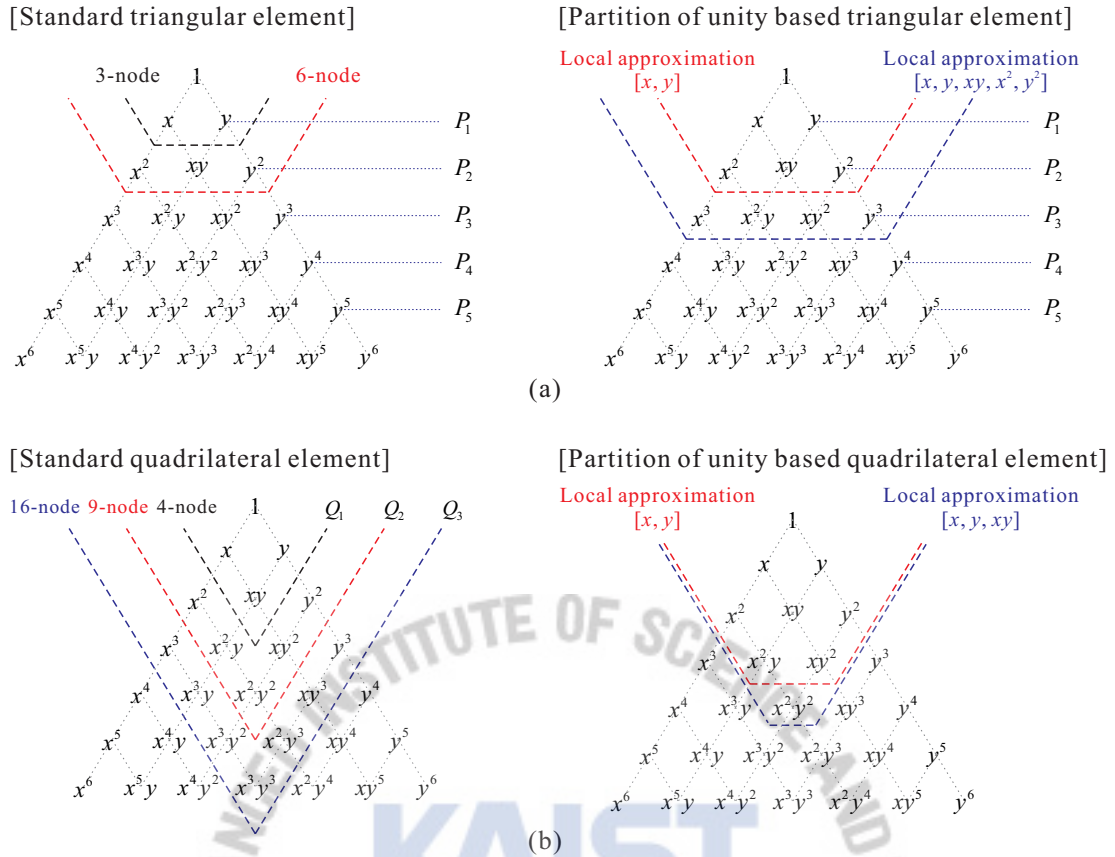


Figure 4.5. Polynomial terms in two-dimensional analysis: Pascal triangle for (a) the standard 3-node triangular element, the partition of unity based 3-node triangular element, the (b) standard 4-node quadrilateral element and the partition of unity based 4-node quadrilateral element.

Figure 4.5 shows the polynomial terms in standard elements and partition of unity based elements and they include complete polynomials in x and y for two-dimensional analysis. **Figure 4.5(a)** also shows important notation for polynomial spaces. The spaces P_k correspond to the complete polynomials up to degree k . They can also be thought of as the basis functions of standard and partition of unity based triangular element. The function in P_2 corresponds to the functions of the parabolic displacement (standard 6-node element) and the partition of unity based displacement with the local approximation $\mathbf{p}^T(\mathbf{x}) = [1 \ x \ y]$. In addition, **Figure 4.5(b)** shows the polynomial spaces Q_k , $k = 1, 2, 3$, which correspond to the 4-node, 9-node, and 16-node elements. The polynomial spaces of the standard 9-node element are exactly the same to that of the partition of unity based quadrilateral element with the local approximation $\mathbf{p}^T(\mathbf{x}) = [1 \ x \ y \ xy]$. From the results, the methods for the assumed strain field of the 9-node shell element can be used in construction of assumed strain fields for unknown high order strain components of the PU based 4-node shell element

The covariant strain components of the PU based 4-node shell element are directly obtained by

$$e_{ij} = \frac{1}{2}(\mathbf{g}_i \cdot \mathbf{u}_{,j} + \mathbf{g}_j \cdot \mathbf{u}_{,i}) \quad (4.43)$$

where

$$\mathbf{g}_i = \frac{\partial \mathbf{x}}{\partial r_i}, \quad \mathbf{u}_{,j} = \frac{\partial \mathbf{u}}{\partial r_j} = \frac{\partial(\bar{\mathbf{u}} + \hat{\mathbf{u}})}{\partial r_j} \quad \text{with } r_1 = r, r_2 = s, r_3 = t. \quad (4.44)$$

Therefore, the covariant strain components of the PU based 4-node shell element are also splitted into two parts

$$e_{ij} = \bar{e}_{ij} + \hat{e}_{ij} \quad (4.45)$$

with

$$\bar{e}_{ij} = \frac{1}{2}(\mathbf{g}_i \cdot \bar{\mathbf{u}}_{,j} + \mathbf{g}_j \cdot \bar{\mathbf{u}}_{,i}) \quad \text{and} \quad \hat{e}_{ij} = \frac{1}{2}(\mathbf{g}_i \cdot \hat{\mathbf{u}}_{,j} + \mathbf{g}_j \cdot \hat{\mathbf{u}}_{,i}), \quad (4.46)$$

in which \bar{e}_{ij} and \hat{e}_{ij} correspond to the standard bilinear and additional high order displacement interpolations, respectively.

To alleviate the transverse shear locking, the MITC (Mixed Interpolation of Tensorial Components) method for the covariant transverse shear strains is adopted. However, different assumed covariant transverse shear strain fields are employed for the standard and additional high order displacement interpolations. The assumed covariant transverse shear strain fields of the MITC4 and MITC9 shell elements are used for the strains \bar{e}_{ij} and \hat{e}_{ij} , respectively [18, 19, 21, 26]. Note that, in the MITC9 shell element, the covariant membrane strains are also assumed to reduce membrane locking, but this treatment is not necessary and not used for the PU based 4-node quadrilateral shell element.

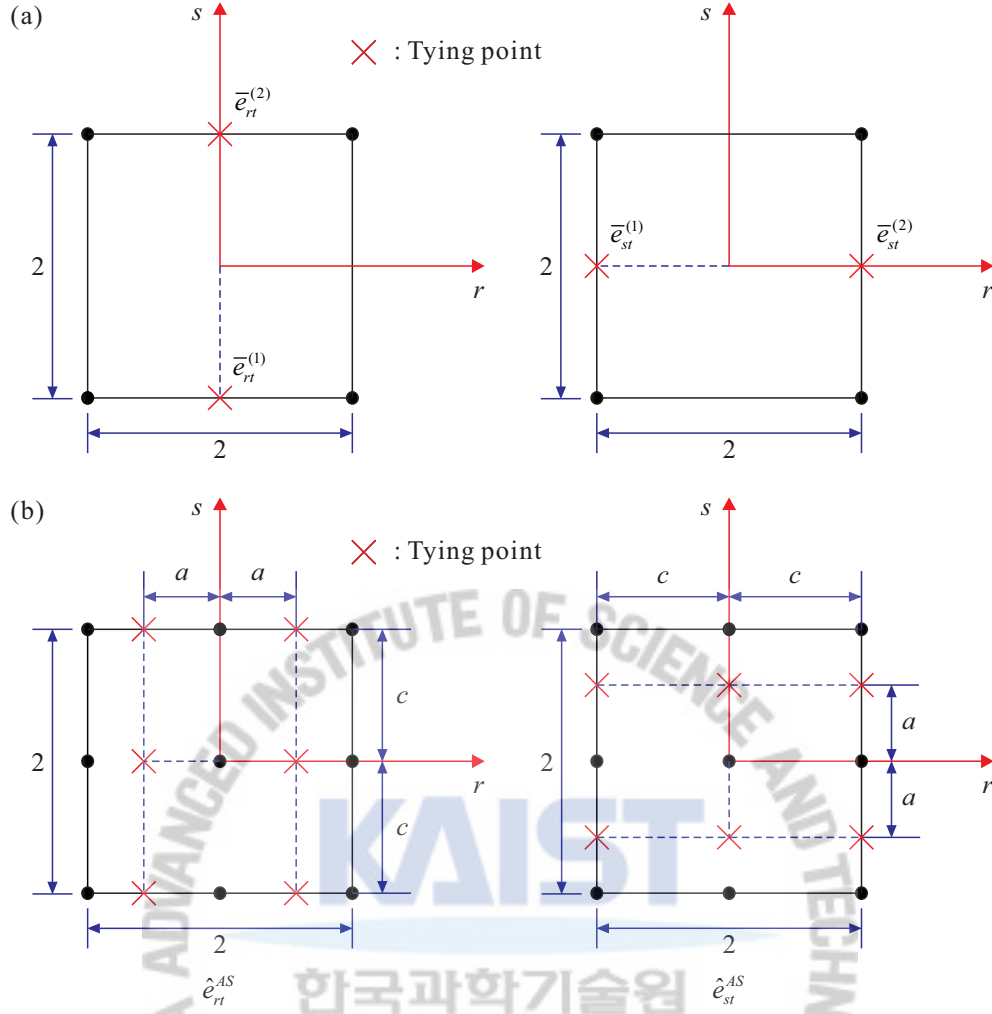


Figure 4.6. Tying positions for the covariant transverse shear strains of the PU based 4-node quadrilateral shell finite element: (a) for the standard bilinear displacement interpolations and (b) for the additional high order displacement interpolations. Note that the scheme referred to as MITC9 in Reference [26] is used.

The assumed covariant transverse shear strain field used for the standard bilinear displacement interpolation is

$$\bar{e}_{rt}^{AS} = \frac{1}{2}(1-s)\bar{e}_{rt}^{(1)} + \frac{1}{2}(1+s)\bar{e}_{rt}^{(2)}, \quad (4.47)$$

$$\bar{e}_{st}^{AS} = \frac{1}{2}(1-r)\bar{e}_{st}^{(1)} + \frac{1}{2}(1+r)\bar{e}_{st}^{(2)} \quad (4.48)$$

where the tying points $\bar{e}_{rt}^{(n)}$ and $\bar{e}_{st}^{(n)}$ are calculated from Equation (4.46), see **Figure 4.6(a)**. For the additional high order displacement interpolation, the assumed strain fields shown in **Figure 4.6(b)** are used. Finally, the assumed covariant transverse shear strain fields for the PU based 4-node shell element are obtained as

$$e_{jt}^{AS} = \bar{e}_{jt}^{AS} + \hat{e}_{jt}^{AS} = \mathbf{B}_{jt}^{AS} \mathbf{U} \quad \text{with } j = r, s, \quad (4.49)$$

in which \mathbf{B}_{jt}^{AS} is the covariant transverse shear strain-displacement matrix and \mathbf{U} is the vector that contains

the degrees of freedom $\bar{\mathbf{u}}_i, \bar{\alpha}_i, \bar{\beta}_i$ and the additional degrees of freedom $\hat{\mathbf{u}}_i, \hat{\alpha}_i, \hat{\beta}_i$. Note that the assumed covariant strain fields are only used for transverse shear strain components. This shell element is hereafter referred to as the enriched MITC4.

Then, using the appropriate stress-strain matrix for shells, the element stiffness is constructed in the same manner as for the displacement-based shell element [1]. The 3×3 Gauss integration is adopted to evaluate the stiffness matrix because the order of the additional high order displacements are quadratic. Since the partition of unity approximation is based on the existing nodes, the displacement interpolation of the enriched MITC4 shell element can be locally used assigning or not assigning polynomial expansions in different regions. With the only $\mathbf{p}^T(\mathbf{x}) = 1$, the element is identical to the original MITC4 shell element.

4.3 Benchmark Problems

In order to assess the performance of the proposed enriched MITC4 shell element, several problems selected from the literature are solved. The obtained results are compared to those previously published using well-known shell element formulations. **Table 4.2** presents a list of several benchmark problems solved in the section. Also, a list of the analyzed shell elements and the abbreviations used to identify them henceforth are contained in **Table 4.3**.

Table 4.2. List of seven benchmark problems considered in this chapter.

Benchmark problems	Descriptions	Results
Morley's 30° skew plate under uniform pressure	Figure 4.7	Figure 4.7-Figure 4.8, Table 4.4
Circular plate under uniform pressure	Figure 4.9	Figure 4.11, Table 4.5-Table 4.6
Partly clamped hyperbolic paraboloid shell	Figure 4.12	Figure 4.12, Table 4.7
Twisted beam subjected to vertical tip load	Figure 4.14	Figure 4.15, Table 4.8
Pinched cylinder	Figure 4.16	Figure 4.18, Table 4.9-Table 4.10
Semi-cylindrical shell subjected to an end pinching force	Figure 4.19	Figure 4.20, Table 4.11-Table 4.12
Scordelis-Lo (Barrel Vault) roof	Figure 4.21	Figure 4.22, Table 4.13-Table 4.14

Table 4.3. List of shell finite element models for comparison.

Symbols	Brief description	Ref.
MITC3	3-node triangular shell element with the MITC method	[23]
MITC4	4-node quadrilateral shell element with the MITC method	[19]
MITC4*	MITC4 shell element with incompatible modes	[63, 64].
Enriched MITC3	MITC3 shell element with the partition of unity approximation	[28]
Enriched MITC4	Present shell element with the local approximation $\mathbf{p}^T(\mathbf{x}) = [1 \ x \ y]$	
Enriched MITC4*	Present shell element with the local approximation $\mathbf{p}^T(\mathbf{x}) = [1 \ x \ y \ xy]$	
MITC9	9-node quadrilateral shell element with the MITC method	[21, 22]
EAS7_ANS	In-plane bilinear enhanced shell element	[113]
SIMO_1990	Enhanced shear formulation	[32]
AHMA4	Bilinear degenerated shell element	[5]
Macro-ANS	3-node macro ANS triangular shell element	[114, 115]
ANS	3-node triangular shell element based on the ANS formulation	[114]
S3R	General purpose 3-node shell element in ABAQUS	[116]
T3DISP	Displacement based 3-node shell element with reduced integration.	
Allman	Discrete Kirchhoff-Mindlin triangle with Allman's rotational DOFs	[117, 118]
Cook, Flat-stiffened	Stabilized 18 DOFs triangular flat shell element proposed by Cook	[119]
Cook, Curved-softened	Stabilized 18 DOFs triangular curved shell proposed by Cook	[119]
Providas and Kattis	Triangular shell element with an arbitrary small true drilling stiffness	[120]
ANDES (OPT)	Triangular element with the optimal assumed natural deviatoric strain	[121]
MISQ24	Mixed interpolation smoothing quadrilateral element with 24 DOFs	[122]
MIN4T	4-node flat shell with drilling DOFs via explicit Kirchhoff constraints	[123]
XSHELL41/42	4-node quasi-conforming flat shell element with drilling DOFs	[124]
SRI-4	Bilinear degenerated shell element with selective reduced integration	[12]
RSDS-4	Bilinear resultant-stress degenerated shell element with reduced integration	[125]
SHELL63 (ANSYS)	4-node thin shell element with drilling DOFs in ANSYS	[126]
QC5D-SA	4-node flat shell with drilling DOFs and 5-point quadrature	[127]
QPH	4-node quadrilateral shell element with physical hourglass control	[128]
IBRA-4	4-node shell element with drilling DOFs	[129]
DKQ-4	4-node discrete Kirchhoff quadrilateral element	[130]
QUAD4	4-node shell element with modifications which relax excessive constraints	[16]
URI-4	9-node uniformly reduced integrated element	[131]
T029 (SAMCEF)	4-node Mindlin shell element in Samtech	[132]
NMS-4F	Defect-free 4-node flat shell element with drilling DOFs	[133]

4.3.1 Morley's 30° Skew Plate Under Uniform Pressure

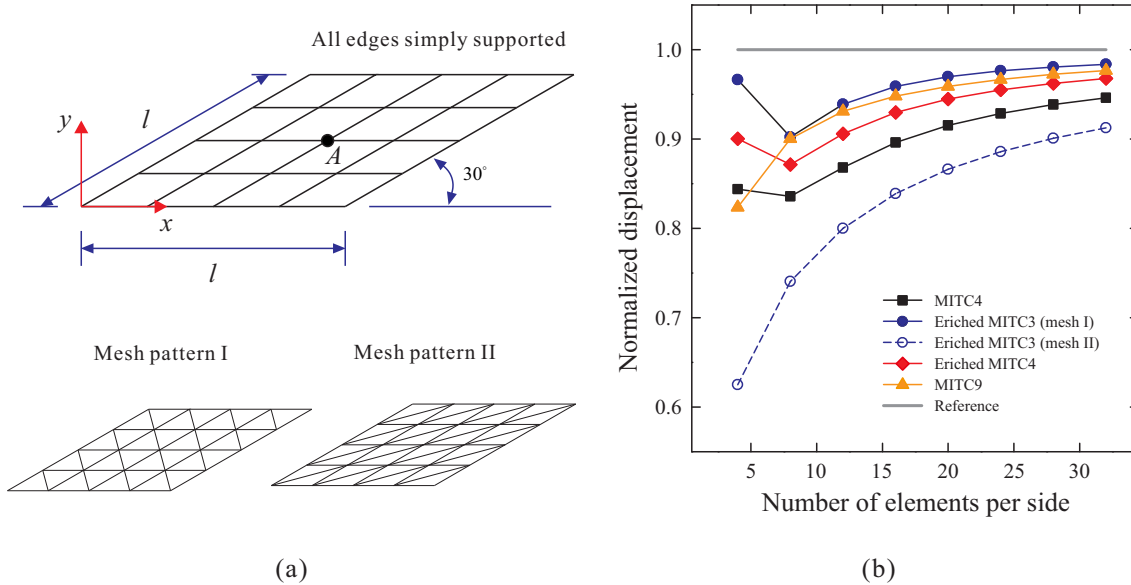


Figure 4.7. Morley's 30° skew plate under uniform pressure. (a) Problem description and mesh patterns (4×4) used for the MITC3 and enriched MITC3 shell elements. (b) Normalized displacement at point A for the Morley's 30° skew plate.

Figure 4.7(a) shows the skew plate under uniform pressure. Morley [134] originally proposed the skew plate to test the sensitivity of the proposed shell elements to mesh distortions. A plate of dimensions $l \times l$ and uniform thickness h are considered and all edges are simply supported. The material properties and length of the skew plate are $E = 10^5$, $\nu = 0.3$ and $l = 100$ which are based on the work of Andelfinger and Ramm [113]. Still following this work, the Kirchhoff reference solution of 4.455 suggested by Morley is replaced by the value 4.640, as even for the length to thickness ratio of 100 shear deformation effects cannot be neglected.

The present results are compared with the ones obtained by MITC3, MITC4, enriched MITC3 and MITC9 shell elements. The values for the central point deflection of the plate are listed in **Table 4.4** and graphically in **Figure 4.7(b)** and **Figure 4.8**. The enriched MITC4 shell element shows remarkably good results even for coarse meshes, leading to the same numerical values.

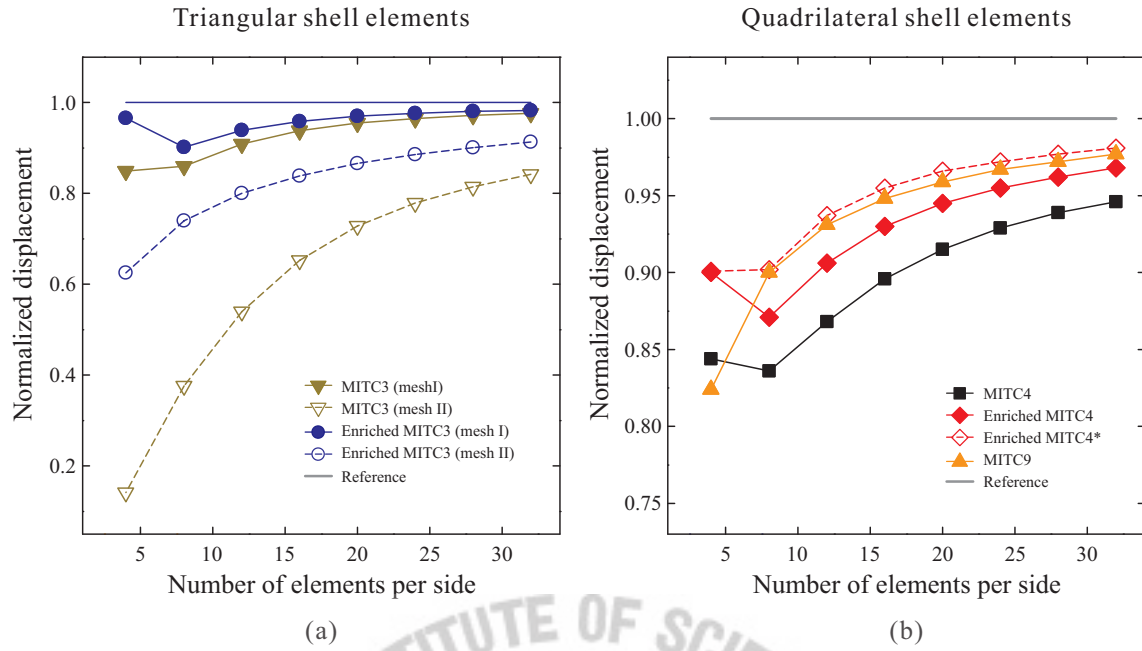


Figure 4.8. Normalized displacement at point A for the Morley's 30° skew plate when the (a) triangular and (b) quadrilateral shell elements are used.

Table 4.4. Relative errors in the vertical displacement at point A for the Morley's 30° skew plate under uniform pressure. Relative error (%) = $|w_A^{ref} - w_A| / |w_A^{ref}| \times 100$ where w_A^{ref} and w_A denote the reference and finite element solutions, respectively.

Element type	Relative errors in the vertical displacement at point A							
	Mesh							
	4×4	6×6	8×8	10×10	12×12	14×14	16×16	32×32
MITC3 ^I	0.151	0.159	0.140	0.113	0.091	0.074	0.062	0.024
MITC3 ^{II}	0.858	0.730	0.624	0.535	0.460	0.397	0.347	0.158
MITC4	0.156	0.164	0.164	0.150	0.132	0.116	0.104	0.054
Enriched MITC3 ^I	0.034	0.109	0.098	0.077	0.061	0.050	0.041	0.017
Enriched MITC3 ^{II}	0.375	0.299	0.260	0.227	0.200	0.179	0.161	0.087
Enriched MITC4	0.100	0.134	0.129	0.111	0.094	0.081	0.070	0.032
Enriched MITC4*	0.099	0.116	0.098	0.078	0.063	0.052	0.045	0.019
MITC9	0.176	0.129	0.100	0.082	0.069	0.059	0.052	0.023
EAS7_ANS [113]	0.092	-	0.090	-	-	-	0.057	0.034
Simo_1990 [32]	0.153	-	0.141	-	-	-	0.079	0.037
AHMA4 [5]	0.975	-	0.917	-	-	-	0.787	0.588

Reference solution $w_A^{ref} = -4.640$ [134]

I and II : mesh patterns shown in Figure 4.7(a)

4.3.2 Circular Plate Under Uniform Pressure

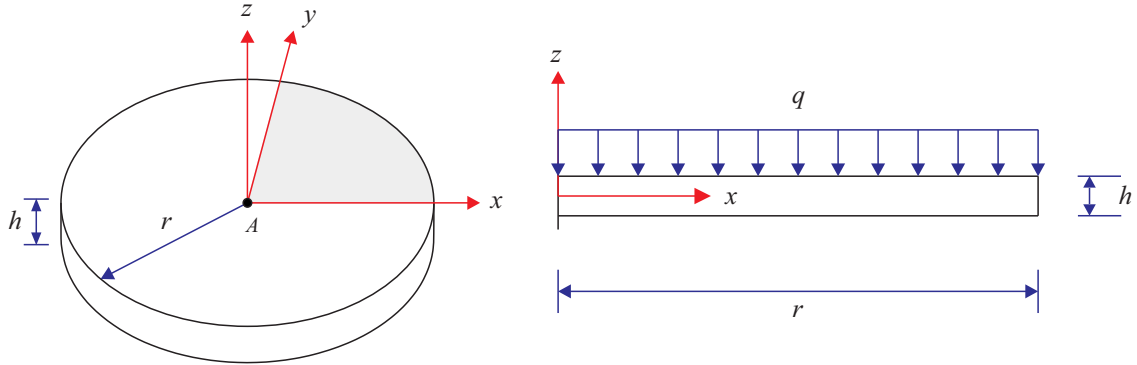


Figure 4.9. Circular plate under uniform pressure.

Figure 4.9 presents a circular plate of thickness h and radius r , loaded with a uniform downward pressure. A simply supported and clamped circular plate subjected to uniform loading are analyzed to demonstrate more features of the present element. The plate used in this test has a radius r of 1 and two kinds of thickness h (0.1 and 0.01). The material has a Young's modulus of $E = 1.7472 \times 10^7$ and Poisson's ratio of $\nu = 0.3$. The pressure load has a magnitude of $q = 1$. The classical mesh patterns are shown in **Figure 4.10** and only a quarter of the plate is modeled due to symmetry.

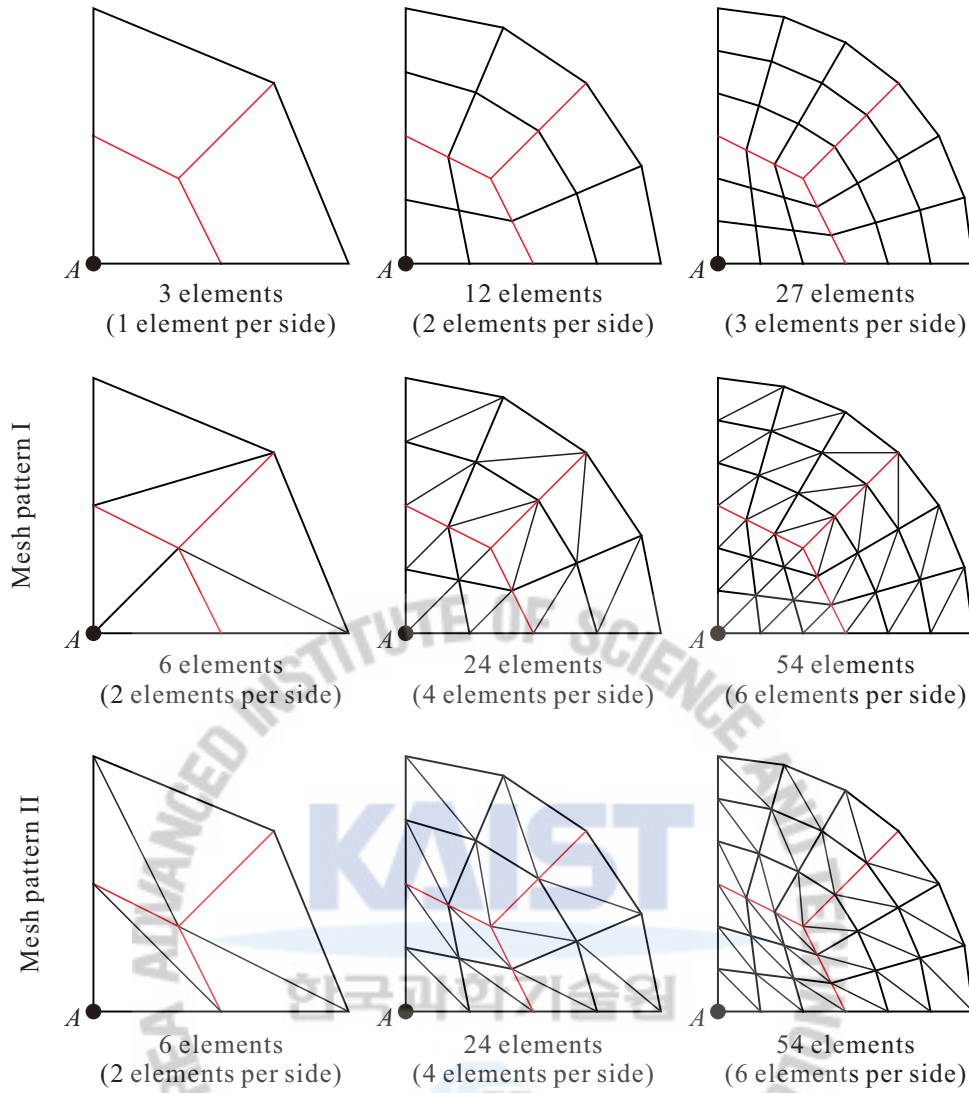


Figure 4.10. Mesh used for the circulate plate under uniform pressure. Mesh pattern I and II are used for the MITC3 and enriched MITC3 shell elements.

This problem is often used to verify results of new elements since analytical solutions are readily available in this case. Using small displacements assumption, an analytic solution for displacements can be found following the procedures in [135]. Using Resissner-Mindlin shell theory, vertical displacements at the center of the circular plate can be calculated by

$$\text{Simply supported circular plate : } w = \frac{q_0 r^4}{64D} (1 - \rho^2) \left[\frac{5 + \nu}{1 + \nu} - \rho^2 + 16 \frac{\lambda^2}{\beta} \right], \quad (4.50)$$

$$\text{Clamped circular plate : } w = \frac{q_0 r^4}{64D} (1 - \rho^2) \left[1 - \rho^2 + 16 \frac{\lambda^2}{\beta} \right], \quad (4.51)$$

where D represents its flexural rigidity. The flexural rigidity is obtained by

$$D = \frac{Eh^3}{12(1 - \nu^2)}, \quad (4.52)$$

where h is the thickness, E is the Young's modulus, ν is the Poisson's ratio, $\rho = R/r$ is an adimen-

sional radial coordinate, $\lambda = h/r$ is an index of how the plate is thin with respect to its radius and β is a characteristic parameter, which is, as far as homogeneous plates are concerned, equal to $5(1-\nu)$. Hence, the reference solution of the circular plate from Equations (4.50) and (4.51) are used.

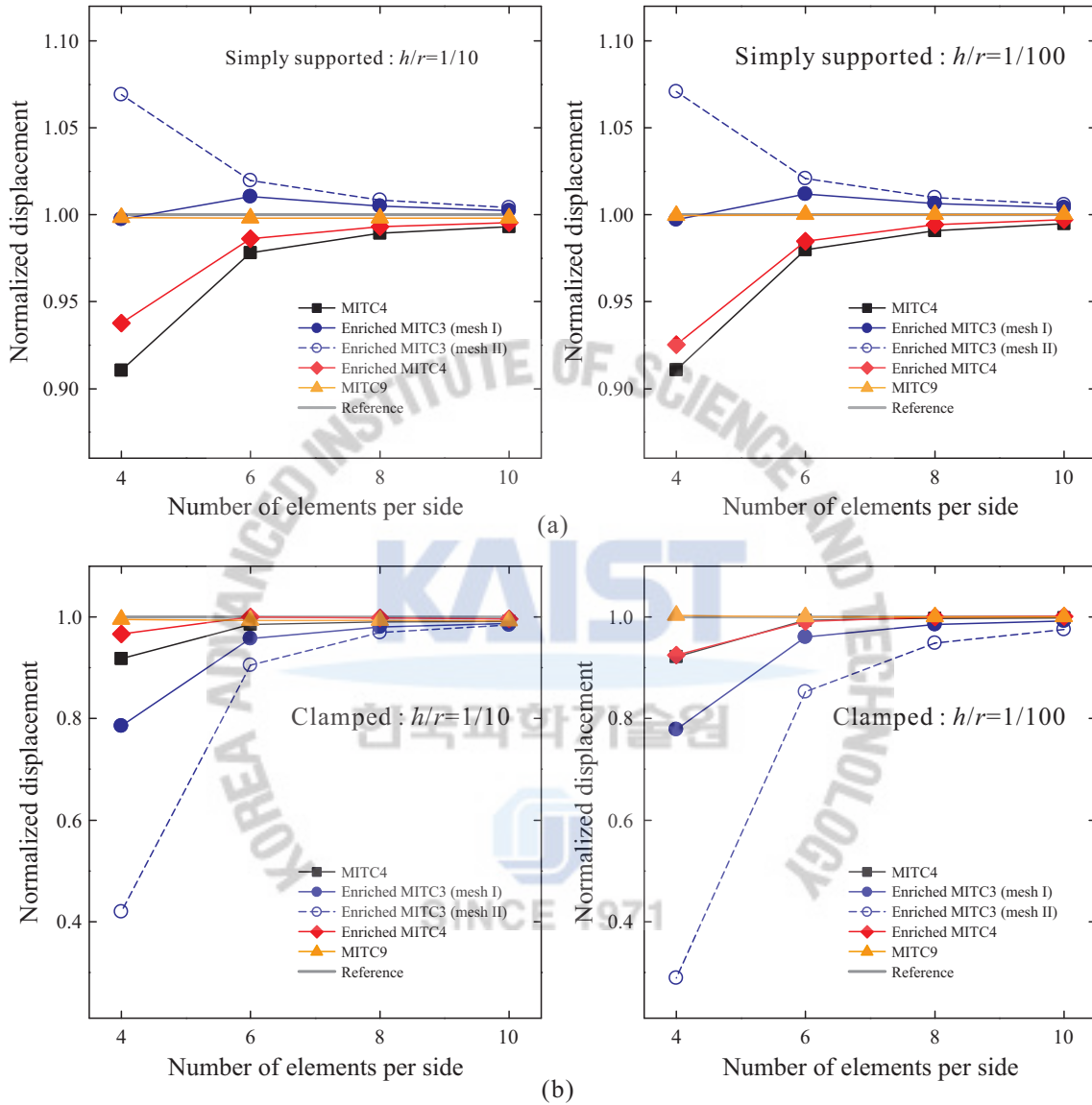


Figure 4.11. Normalized displacement at the center for the circular plate with $h/r = 0.1$ and $h/r = 0.01$ when the circular plate is (a) simply supported and (b) clamped.

Figure 4.11(a) and Figure 4.11(b) present the normalized displacements for the simply supported and clamped circular plate, respectively. Additionally, the relative errors for the central point deflection of the plate are listed in **Table 4.5** and **Table 4.6**. The enriched MITC3 shell finite element reveals some sensitivity to coarse meshes, converging to the performance of the elements as the mesh is refined. The present enriched MITC4 element produces much better solution results than other shell elements.

Table 4.5. Relative errors in the vertical displacement at point A for the simply supported circular plate under uniform pressure. Relative error (%) = $|w_A^{ref} - w_A|/|w_A^{ref}| \times 100$ where w_A^{ref} and w_A denote the reference and finite element solutions, respectively.

Element type	Relative errors in the vertical displacement at point A for the simply supported plate							
	$h/r = 0.1$				$h/r = 0.01$			
	1×1	2×2	3×3	4×4	1×1	2×2	3×3	4×4
MITC3 ^I	21.655	5.8477	2.5715	1.4896	31.370	12.984	8.0714	4.8375
MITC3 ^{II}	18.133	4.9722	2.2392	1.3105	30.003	11.126	6.0761	3.6132
MITC4	8.9344	2.1880	1.0725	0.6828	8.9120	2.0046	0.8953	0.5018
Enriched MITC3 ^I	0.2576	1.0378	0.5007	0.2355	0.2850	1.1864	0.6628	0.4058
Enriched MITC3 ^{II}	6.9076	1.9940	0.8492	0.4103	7.0804	2.0948	0.9945	0.5754
Enriched MITC4	6.2292	1.3753	0.6716	0.4478	7.4785	1.5154	0.5588	0.2933
Enriched MITC4*	8.2046	2.0646	0.9637	0.5939	8.8357	2.0209	0.8413	0.4289
MITC9	0.1525	0.1813	0.1841	0.1845	0.0452	0.0023	0.0015	0.0018

Reference solution $w_A^{ref} = -4.026E-05$ for $h/r = 0.1$ and $w_A^{ref} = -3.982E-02$ for $h/r = 0.01$

I and II : mesh patterns shown in Figure 4.10

Table 4.6. Relative errors in the vertical displacement at point A for the clamped circular plate under uniform pressure. Relative error (%) = $|w_A^{ref} - w_A|/|w_A^{ref}| \times 100$ where w_A^{ref} and w_A denote the reference and finite element solutions, respectively.

Element type	Relative errors in the vertical displacement at point A for the clamped circular plate							
	$h/r = 0.1$				$h/r = 0.01$			
	1×1	2×2	3×3	4×4	1×1	2×2	3×3	4×4
MITC3 ^I	64.785	16.887	6.9421	4.0065	99.097	87.844	55.804	27.994
MITC3 ^{II}	59.005	14.239	6.0037	3.5079	98.944	78.667	43.502	21.287
MITC4	8.2247	1.4532	1.0086	0.8754	7.8238	0.6659	0.2831	0.1450
Enriched MITC3 ^I	21.430	4.2715	1.9614	1.2955	22.135	3.9415	1.4733	0.7313
Enriched MITC3 ^{II}	58.002	9.5016	3.0473	1.5981	71.050	14.737	5.1137	2.4941
Enriched MITC4	3.3057	0.0333	0.2096	0.3809	7.5536	0.8979	0.0341	0.1252
Enriched MITC4*	4.7700	0.9587	0.5797	0.5249	7.4946	0.7353	0.0616	0.1508
MITC9	0.4769	0.7090	0.7246	0.7276	0.2951	0.0155	0.0028	0.0060

Reference solution $w_A^{ref} = -1.021E-05$ for $h/r = 0.1$ and $w_A^{ref} = -9.770E-03$ for $h/r = 0.01$

I and II : mesh patterns shown in Figure 4.10

4.3.3 Partly Clamped Hyperbolic Paraboloid Shell

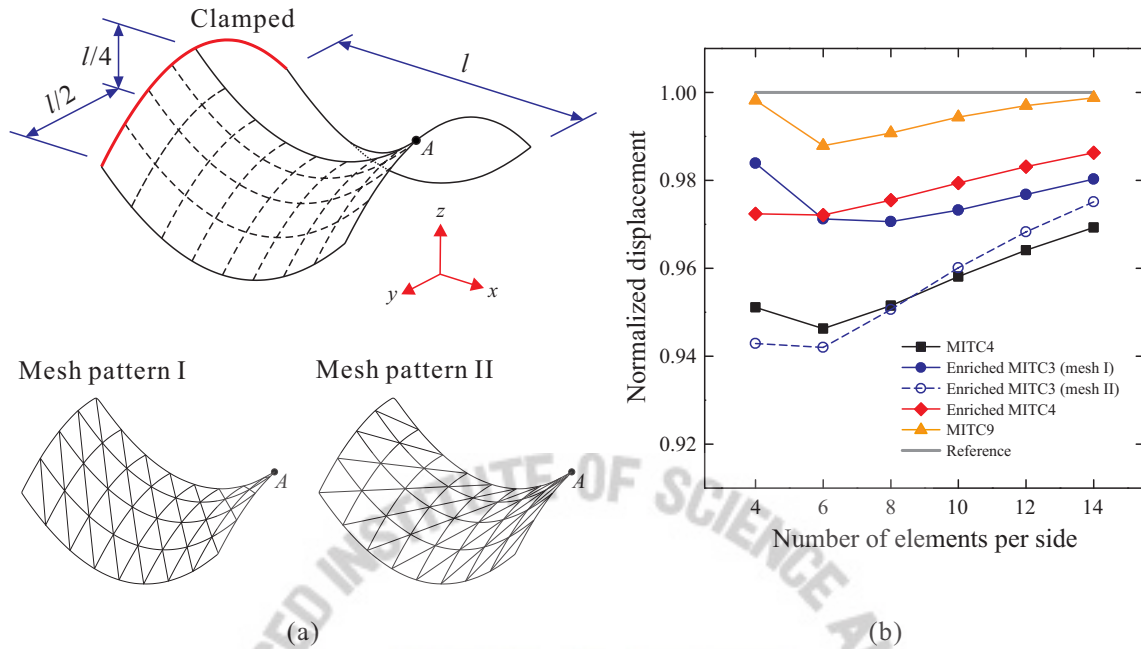


Figure 4.12. Partly clamped hyperbolic paraboloid shell. (a) Problem description and mesh pattern (8×4) used for the MITC and enriched MITC3 shell elements. (b) Normalized displacement at point A in the analysis of the partly clamped hyperbolic paraboloid shell.

The partly clamped hyperbolic paraboloid shell problem shown in **Figure 4.12(a)** is classified as a bending dominated problem. This problem was suggested as a suitable test for locking behavior [136, 137]. The surface is defined as

$$Z = X^2 - Y^2; (X, Y) \in [(-l/2; l/2)]^2, \quad (4.53)$$

clamped along the side $X = -l/2$.

The shell is clamped at one end and subjected to self-weight which is 8 per unit area. The problem geometry and material properties are $l = 1$, $E = 2 \times 10^{11}$, $\nu = 0.3$ and the thickness of the shell is $h = 0.001$. As a result of symmetry, only one half of the surface is considered in this problem. For the finite element analysis, sequences of $N \times N/2$ meshes, where N is the number of subdivisions along the x -direction.

Currently, an analytic solution is not available for this shell problem; instead, a 32×16 element mesh of the MITC9 shell element is used to obtain the reference solution. The reference solution of the vertical displacement at point A is -0.0064 . **Figure 4.12(b)** and **Figure 4.13** report the normalized displacement at point A for this shell problem and **Table 4.7** presents the relative errors in vertical deflection compared with other shell elements. The results of the enriched MITC3 shell element are sensitive to mesh patterns shown in **Fig-**

Figure 4.12(a). The enriched MITC4 shell element exhibits better results even for the coarse meshes.

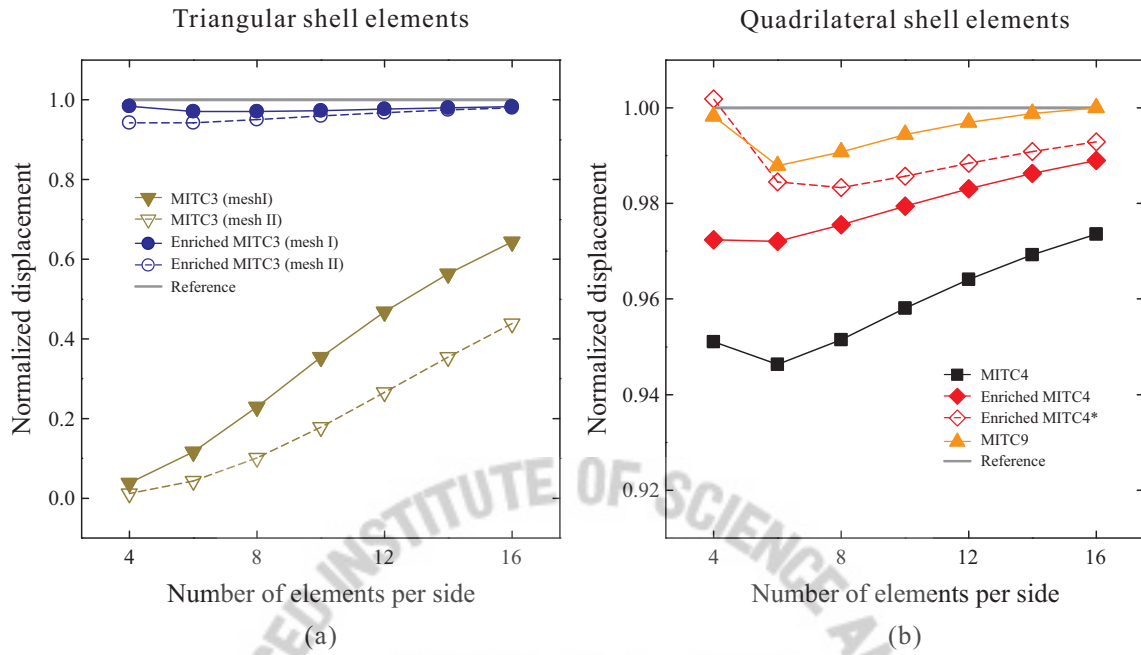


Figure 4.13. Normalized displacement at point A for the partly clamped hyperbolic paraboloid shell when the (a) triangular and (b) quadrilateral shell elements are used.

Table 4.7. Relative errors in the vertical displacement at point A for the partly clamped hyperbolic paraboloid shell. Relative error (%) = $|w_A^{ref} - w_A| / |w_A^{ref}| \times 100$ where w_A^{ref} and w_A denote the reference and finite element solutions, respectively.

Element type	Mesh							
	4×2	8×4	12×6	16×8	20×10	24×12	28×14	32×16
MITC3 ^I	99.59	96.23	88.39	77.03	64.63	53.25	43.60	35.65
MITC3 ^{II}	99.86	98.83	95.68	89.85	82.12	73.45	64.59	56.12
MITC4	2.373	4.887	5.367	4.850	4.194	3.590	3.072	2.638
Enriched MITC3 ^I	6.532	1.613	2.880	2.943	2.677	2.323	1.972	1.657
Enriched MITC3 ^{II}	1.485	5.712	5.800	4.936	3.992	3.167	2.493	1.953
Enriched MITC4	0.036	2.757	2.788	2.450	2.061	1.690	1.368	1.100
Enriched MITC4*	1.802	0.190	1.551	1.667	1.431	1.156	0.912	0.710
MITC9	15.92	0.185	1.208	0.917	0.557	0.296	0.120	0.000

Reference solution $w_A^{ref} = -0.00637115$

I and II : mesh patterns shown in Figure 4.12(a)

4.3.4 Twisted Beam Subjected to Vertical Tip Load

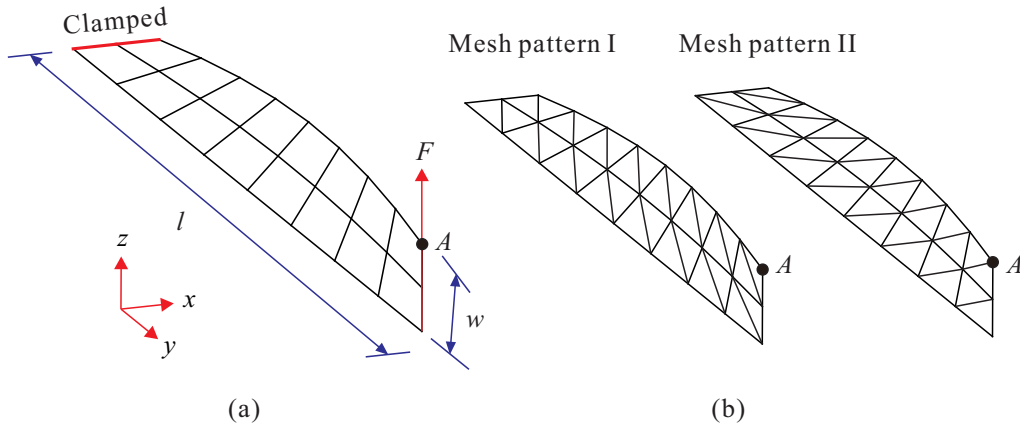


Figure 4.14. Twisted beam subjected to vertical tip load. (a) Problem description. (b) Mesh patterns used for the MITC3 and enriched MITC3 shell elements.

Figure 4.14(a) shows the twisted beam proposed by Belytschko et al. [131]. This benchmark problem is to test the effect of element warping. The performance of elements of two kind of thickness (0.32 and 0.0032) was studied under out-of-plane shear force. The geometrical property and load are $l = 12$, $w = 1.1$ and $F = 1$, respectively. The Young's modulus is $E = 29 \times 10^6$, while the Poisson's ratio is $\nu = 0.22$.

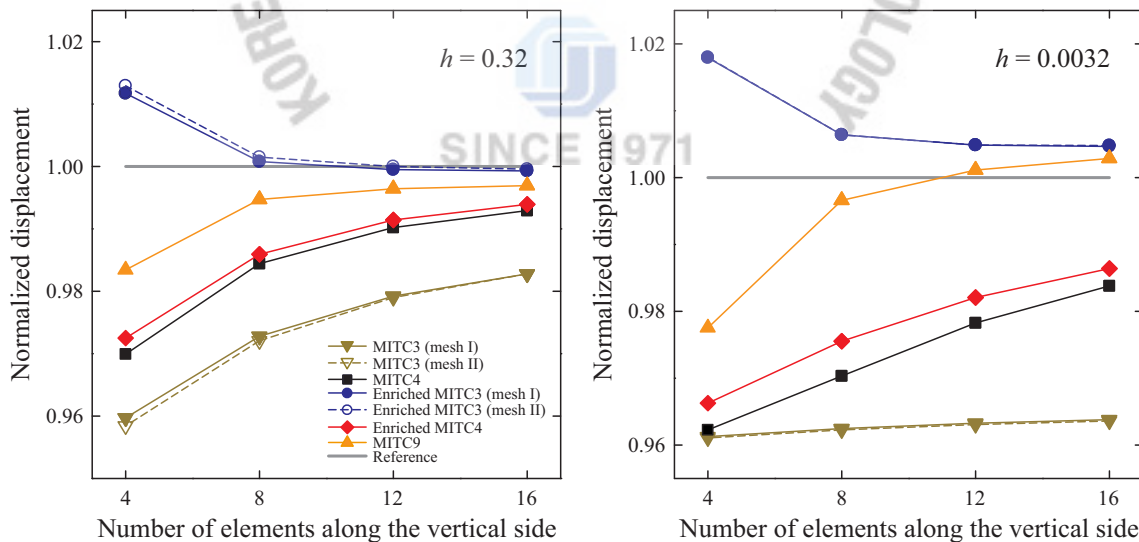


Figure 4.15. Normalized displacement of the twisted beam subjected to vertical tip load for different thickness cases (left) $h = 0.32$ and (right) $h = 0.0032$.

Figure 4.15 represents the normalized displacement at point A for the twisted beam and **Table 4.8**

shows the relative errors in vertical deflection at point A comparing with the results from other shell elements in some literatures. The solutions using the MITC3 shell element deteriorate as the shell thickness decreases. However, all enriched shell elements show excellent results when compared with the reference solutions.

Table 4.8. Relative errors in displacement at point A for the twisted beam subjected to vertical tip load. Relative error (%) = $|w_A^{ref} - w_A| / |w_A^{ref}| \times 100$ where w_A^{ref} and w_A denote the reference and finite element solutions, respectively.

Element type	$h = 0.32$				$h = 0.0032$			
	4×2	8×4	12×6	16×8	4×2	8×4	12×6	16×8
MITC3 ^I	4.029	2.717	2.075	1.722	3.867	3.748	3.672	3.617
MITC3 ^{II}	4.156	2.790	2.097	1.719	3.890	3.769	3.694	3.639
MITC4	3.015	1.563	0.983	0.707	3.774	2.967	2.169	1.621
Enriched MITC3 ^I	1.169	0.078	0.050	0.074	1.797	0.639	0.493	0.479
Enriched MITC3 ^{II}	1.294	0.152	0.001	0.039	1.787	0.639	0.493	0.470
Enriched MITC4	2.750	1.409	0.862	0.609	3.374	2.455	1.789	1.361
MITC9	1.657	0.527	0.362	0.308	2.250	0.338	0.114	0.294
Macro-ANS ^{II}	3.500	2.000	1.400	1.000	2.800	0.000	0.300	0.500
ANS ^{II}	3.500	2.100	1.500	1.100	3.100	2.700	2.100	1.600
S3R ^{II}	18.70	3.500	1.900	1.400	64.60	6.000	2.700	1.600
T3DISP ^{II}	94.60	80.30	63.10	47.40	99.99	99.99	99.88	99.76
Allman ^I	-	-	-	-	97.40	98.45	-	92.59
Cook, flat-stiffened ^I	-	-	-	-	97.69	93.71	-	55.47
Cook, curved-softened ^I	-	-	-	-	3.800	0.800	-	0.100
Providas and Kattis ^I	-	-	-	-	99.54	0.020	-	0.340
ANDES (OPT) ^I	-	-	-	-	99.54	98.04	-	91.43

Reference solution $w_A^{ref} = 5.424E-03$ for $h = 0.32$ and $w_A^{ref} = 5.256E+03$ for $h = 0.0032$
I and II : mesh patterns shown in Figure 4.14(b)

4.3.5 Pinched Cylinder

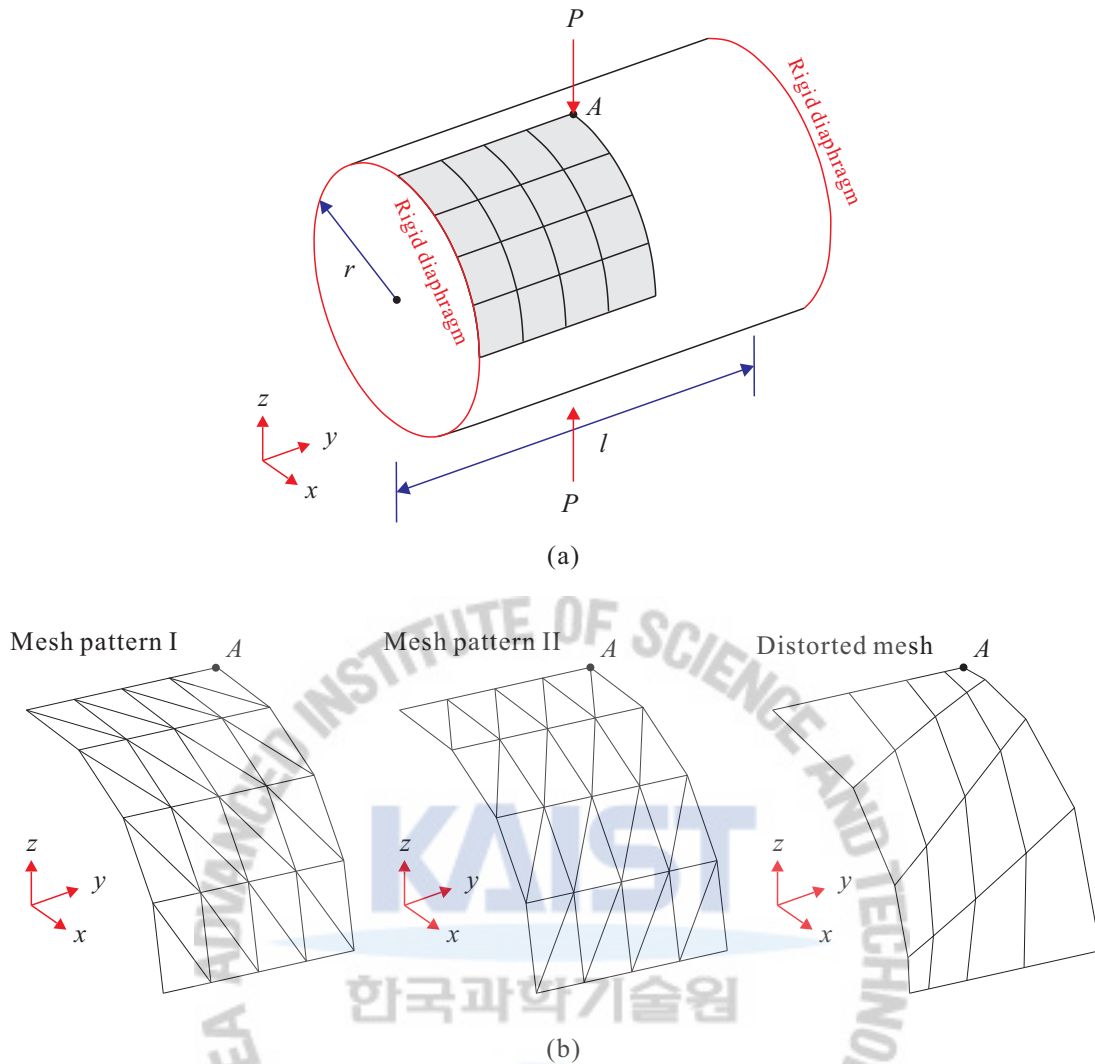


Figure 4.16. Pinched cylinder. (a) Problem description. (b) Mesh patterns (4×4) used for the MITC3 and enriched MITC3 shell elements and the distorted mesh.

Figure 4.16(a) illustrates a short cylinder subjected to two pinching forces. The shell is bounded by rigid diaphragms at each end. This pinched cylinder is one of the most severe benchmark problem which is to test an element's ability to model both inextensional bending and complex membrane states. Belytschko et al. [138] pointed out the difficulty in passing this test. Due to symmetry, only one octant of the cylinder is analyzed.

The length and radius of the full cylinder are $l = 600$ and $r = 300$, respectively. The thickness of the cylinder is $h = 3$ and the material constants are $E = 3 \times 10^7$ and $\nu = 0.3$. The load applied to the cylinder is $P = 1$. The vertical displacement at the location of the point load is $1.8248e-05$ which is given in Belytschko et al. [138].

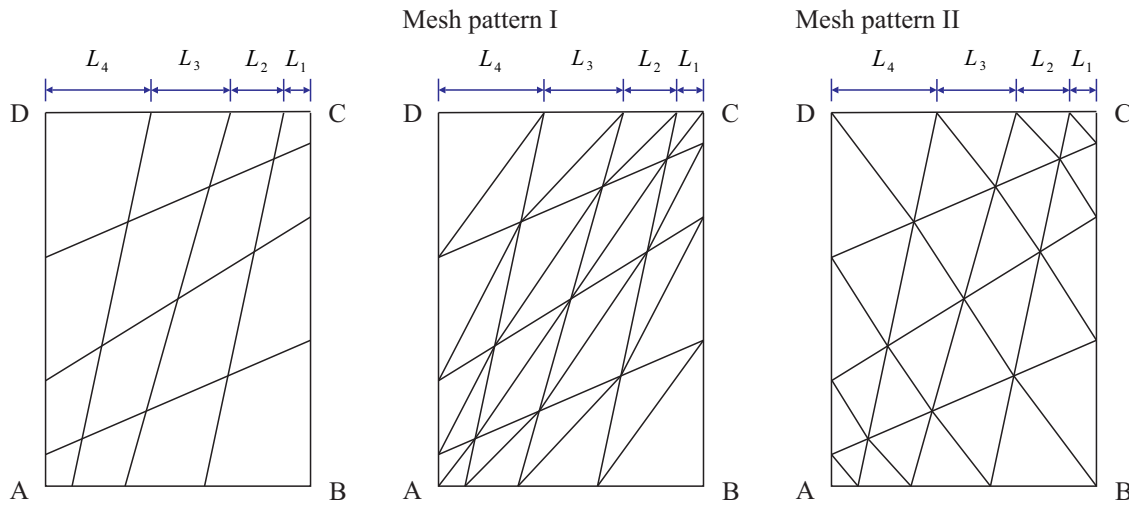


Figure 4.17. Distorted meshes used for the pinched cylinder, semi-cylindrical shell subjected to an end pinching force and Scordelis-Lo roof when $N = 4$. Two mesh patterns for the MITC3 and enriched MITC3 shell elements.

The convergence behavior not only using uniform meshes but also distorted meshes is studied in the pinched cylinder, semi-cylindrical shell subjected to an end pinching force, and Scordelis-Lo roof, see **Figure 4.17**. When the $N \times N$ distorted mesh is used, each edge is discretized by the ratio $L_1 : L_2 : L_3 : \dots, L_N = 1 : 2 : 3 : \dots, N$, leading to quite distorted meshes.

For the pinched cylinder problem, the best performance is obtained with the MITC9 shell element, and next with the enriched MITC4 shell element, as illustrated in **Figure 4.18**. **Table 4.9** and **Table 4.10** tabulate the results of MITC shell elements and other shell elements published using the uniform and distorted meshes. The enriched MITC3 shell element performs well when the uniform meshes are used. However, for the distorted meshes, the enriched MITC3 shell element shows slightly poor results when the mesh pattern II is used. When the uniform meshes are used, the enriched scheme for the 4-node shell element increases solution accuracy even though the performance of the MITC4 and enriched MITC4 are similar for this problem with the distorted meshes.

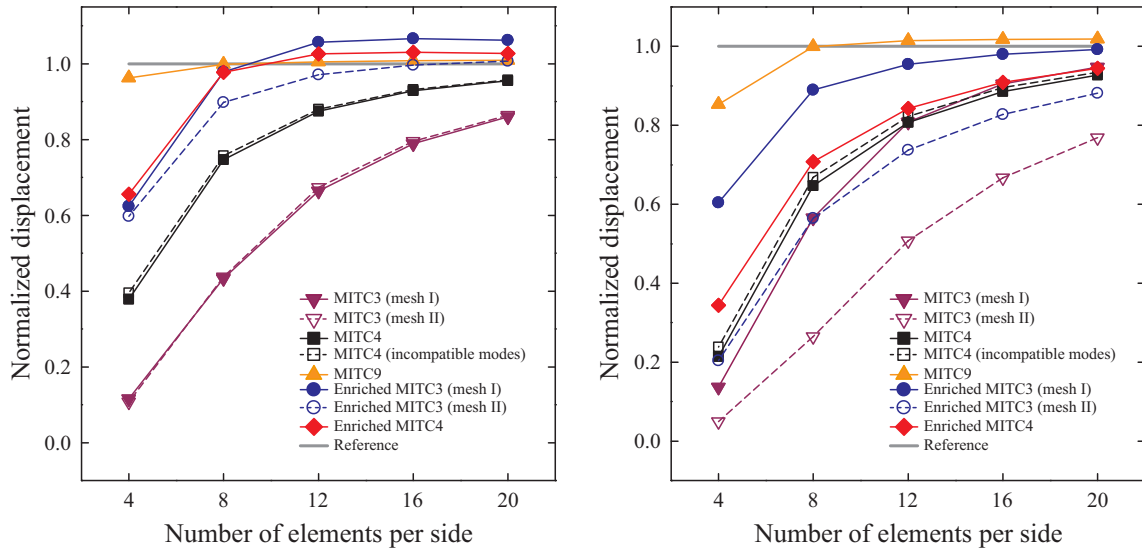


Figure 4.18. Normalized displacement of the pinched cylinder with (a) the uniform meshes (b) the distorted meshes shown in Figure 4.16(b) and **Figure 4.17**.

Table 4.9. Relative errors in the radial displacement at point A for the pinched cylinder with the uniform meshes. Relative error (%) = $|w_A^{ref} - w_A| / |w_A^{ref}| \times 100$ where w_A^{ref} and w_A denote the reference and finite element solutions, respectively.

Element type	Mesh				
	4×4	8×8	12×12	16×16	20×20
MITC3 ^I	0.8845	0.5665	0.3359	0.2111	0.1400
MITC3 ^{II}	0.8923	0.5627	0.3259	0.2043	0.1360
MITC4	0.6212	0.2531	0.1251	0.0714	0.0445
MITC4*	0.6043	0.2425	0.1194	0.0680	0.0422
Enriched MITC3 ^I	0.3763	0.0213	0.0571	0.0665	0.0622
Enriched MITC3 ^{II}	0.4021	0.1015	0.0290	0.0036	0.0072
Enriched MITC4	0.5296	0.1579	0.0593	0.0246	0.0095
MITC9	0.0369	0.0016	0.0052	0.0079	0.0092
MISQ24	0.3584	0.0589	0.0079	0.0018	-
MIN4T	0.4960	0.1626	-	0.0381	-
XSHELL41	0.3750	0.0740	-	0.0050	-
XSHELL42	0.3750	0.0820	-	0.0080	-
SRI-4	0.6270	0.2530	-	0.0650	-
RSDS-4	0.5310	0.2090	-	0.0540	-
SHELL63 (ANSYS)	0.3698	0.0629	-	0.0029	-
QC5D-SA	0.6241	0.2536	-	0.0700	-
QPH	0.6300	0.2600	-	0.0700	-
IBRA-4	0.6296	0.2633	-	0.0657	-
DKQ-4	0.3643	0.0541	-	0.0160	-
Simo et al.	0.6011	0.2372	-	0.0651	-

Allman	0.4098	0.0759	-	0.0043	-
Cook_Flat-stiffened	0.4629	0.1027	-	0.0033	-
Cook_Curved-softened	0.0260	0.0010	-	-	-
Providas and Kattis	0.5465	0.1436	0.0176	-	-
ANDES (OPT)	0.3696	0.0626	0.0064	-	-

Reference solution $w_A^{ref} = 1.8248E-05$ [138]

I and II : mesh patterns shown in Figure 4.16(b) and Figure 4.17

Table 4.10. Relative errors in the radial displacement at point A for the pinched cylinder with the distorted meshes. Relative error (%) = $\left| \frac{w_A^{ref} - w_A}{w_A^{ref}} \right| \times 100$ where w_A^{ref} and w_A denote the reference and finite element solutions, respectively.

Element type	Mesh				
	4×4	8×8	12×12	16×16	20×20
MITC3 ^I	0.8628	0.4341	0.1917	0.0953	0.0520
MITC3 ^{II}	0.9505	0.7354	0.4926	0.3327	0.2312
MITC4	0.7858	0.3530	0.1927	0.1149	0.0726
MITC4*	0.7615	0.3319	0.1779	0.1047	0.0654
Enriched MITC3 ^I	0.3959	0.1104	0.0456	0.0203	0.0076
Enriched MITC3 ^{II}	0.7960	0.4358	0.2626	0.1720	0.1181
Enriched MITC4	0.6559	0.2927	0.1575	0.0910	0.0550
MITC9	0.1470	0.0002	0.0145	0.0176	0.0189

Reference solution $w_A^{ref} = 1.8248E-05$ [138]

I and II : mesh patterns shown in Figure 4.16(b) and Figure 4.17

4.3.6 Semi-Cylindrical Shell Subjected to an End Pinching Force

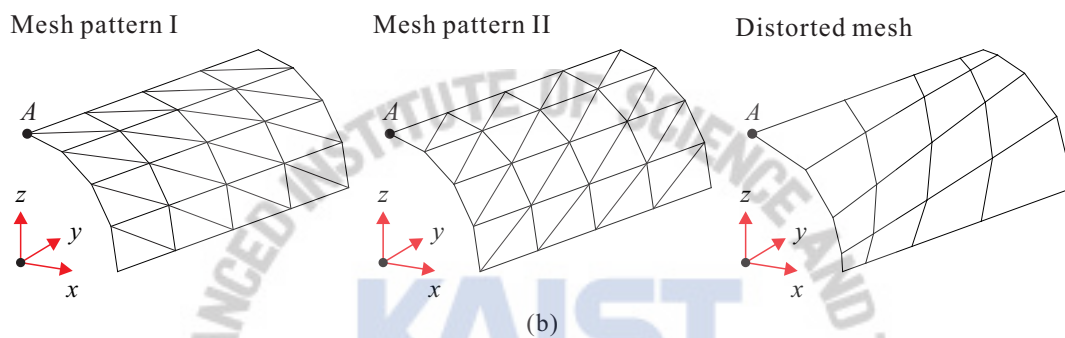
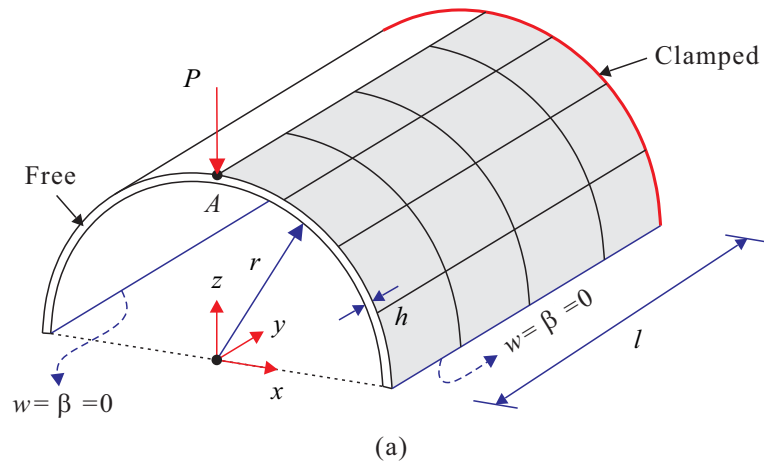


Figure 4.19. Semi-cylindrical shell subjected to an end pinching force. (a) Problem description. (b) Meshes used (4×4) for the MITC3 and enriched MITC3 shell elements.

A well-known benchmark problem is the semi-cylindrical shell under a point load shown in **Figure 4.19(a)** [139-142]. The length and radius of the half cylinder are $l = 0.3048$ and $r = 1.016$, respectively, and the thickness of the semi-cylindrical shell is $h = 0.03$. The material constants are $E = 2.0685 \times 10^7$ and $\nu = 0.3$. The unit load applied to the shell at point A . The structure is modeled using 4×4 , 8×8 , 12×12 , 16×16 and 20×20 element meshes of the MITC3, MITC4, enriched MITC3 and enriched MITC4. The reference solutions are obtained using a 30×30 element mesh of the MITC9 shell element.

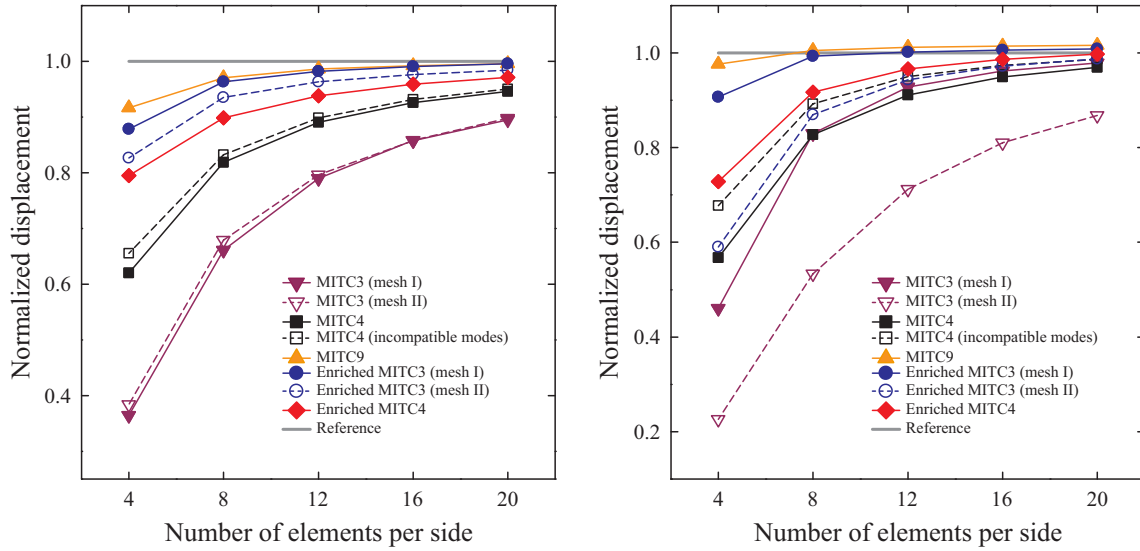


Figure 4.20. Normalized displacement of the semi-cylindrical shell with (a) the uniform meshes (b) the distorted meshes shown in Figure 4.19(b) and Figure 4.17.

Figure 4.20 shows the normalized displacement at point A for the semi-cylindrical shell with the uniform and distorted meshes. Also, the relative errors in vertical deflection at point A are listed in Table 4.11 and Table 4.12. The enriched MITC4 shell element shows good performance in the solution of this shell problem when using both the uniform and distorted meshes.

Table 4.11. Relative errors in the vertical displacement at point A for the semi-cylindrical shell with the uniform meshes. Relative error (%) = $|w_A^{ref} - w_A| / |w_A^{ref}| \times 100$ where w_A^{ref} and w_A denote the reference and finite element solutions, respectively.

Element type	Mesh				
	4×4	8×8	12×12	16×16	20×20
MITC3 ^I	0.636	0.339	0.210	0.142	0.102
MITC3 ^{II}	0.616	0.321	0.204	0.142	0.105
MITC4	0.380	0.181	0.110	0.074	0.054
MITC4*	0.345	0.167	0.101	0.069	0.050
Enriched MITC3 ^I	0.122	0.037	0.018	0.009	0.004
Enriched MITC3 ^{II}	0.173	0.065	0.037	0.024	0.016
Enriched MITC4	0.205	0.102	0.062	0.041	0.029
MITC9	0.083	0.029	0.014	0.008	0.005

Reference solution $w_A^{ref} = 4.172e-04$

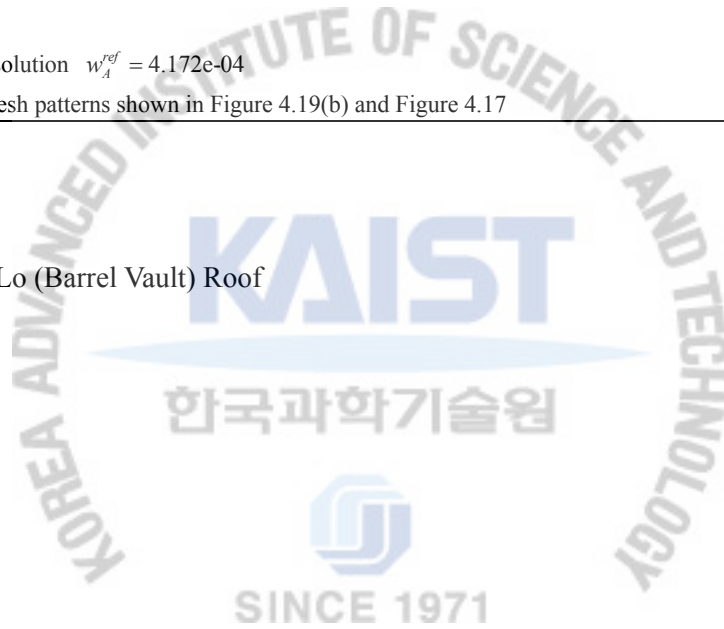
I and II : mesh patterns shown in Figure 4.19(b) and Figure 4.17

Table 4.12. Relative errors in the vertical displacement at point A for the semi-cylindrical shell with the distorted meshes. Relative error (%) = $|w_A^{ref} - w_A| / |w_A^{ref}| \times 100$ where w_A^{ref} and w_A denote the reference and finite element solutions, respectively.

Element type	Mesh				
	4×4	8×8	12×12	16×16	20×20
MITC3 ^I	0.539	0.170	0.072	0.038	0.021
MITC3 ^{II}	0.774	0.466	0.288	0.190	0.132
MITC4	0.433	0.173	0.088	0.051	0.031
MITC4*	0.322	0.108	0.050	0.026	0.013
Enriched MITC3 ^I	0.093	0.007	0.002	0.006	0.009
Enriched MITC3 ^{II}	0.409	0.130	0.056	0.028	0.013
Enriched MITC4	0.272	0.083	0.033	0.013	0.003
MITC9	0.024	0.005	0.012	0.014	0.016

Reference solution $w_A^{ref} = 4.172e-04$
 I and II : mesh patterns shown in Figure 4.19(b) and Figure 4.17

4.3.7 Scordelis-Lo (Barrel Vault) Roof



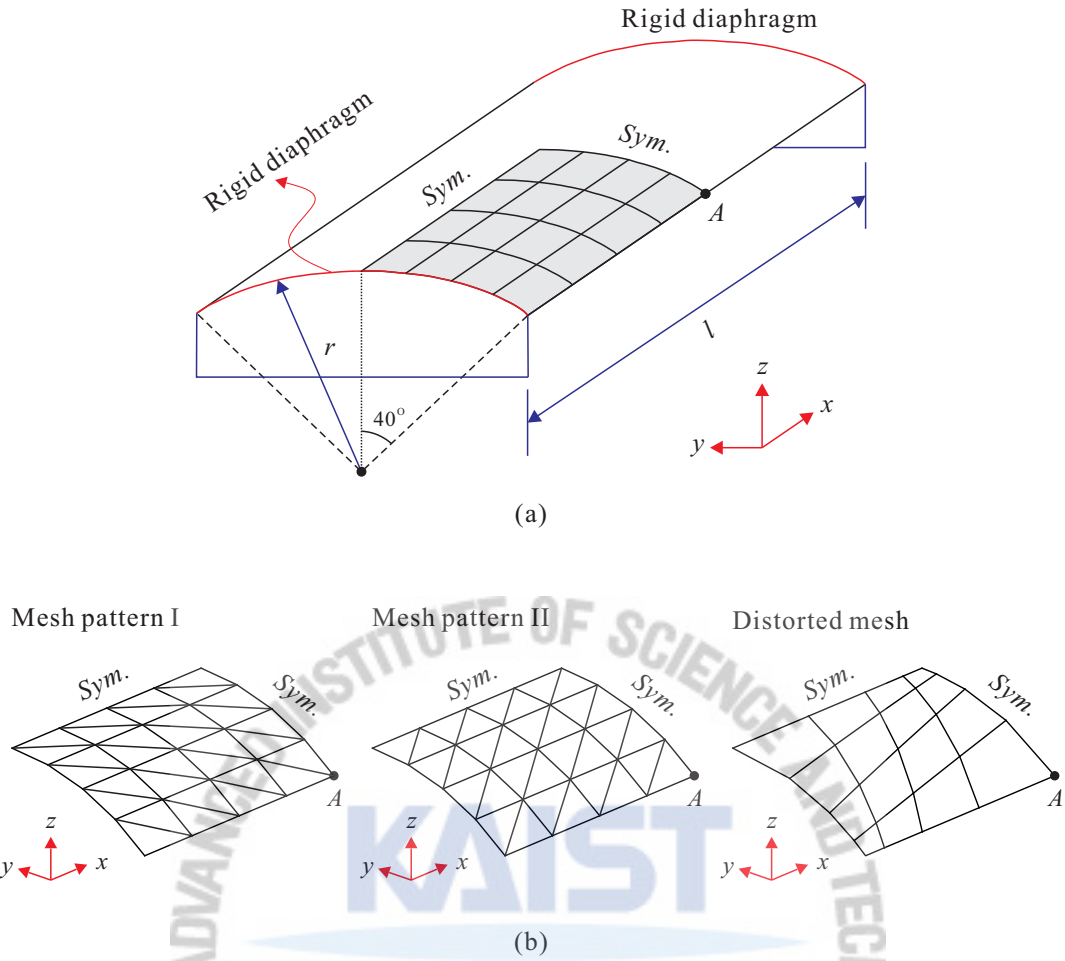


Figure 4.21. Scordelis-Lo (Barrel Vault) roof. (a) Problem description. (b) Mesh patterns (4×4) used for the MITC3 and enriched MITC3 shell elements.

The Scordelis-Lo (Barrel Vault) roof provides one of the standard tests to assess the performance of shell elements in a combined bending-membrane problem with the membrane action being dominant. The roof is modeled as a short cylinder shell, loaded by self-weight and supported by rigid diaphragms at the curved edges while the straight edges are free. The geometry of the problem is shown in **Figure 4.21(a)**. The length of the roof is $l = 50$; the radius of curvature is $r = 25$ and its thickness $h = 0.25$. The material has a Young's modulus of $E = 4.32 \times 10^8$ and a Poisson's ratio of $\nu = 0$. The load it experiences is due to its weight, amounting to the force per unit surface $f_z = 90$ per unit area. According to MacNeal and Harder [143], the theoretical value for the vertical deflection at the center of the free edge is 0.3086, but slightly lower value 0.3024 seems to have become the reference solution for many publications. In this study the latter value is used to normalize numerical results.

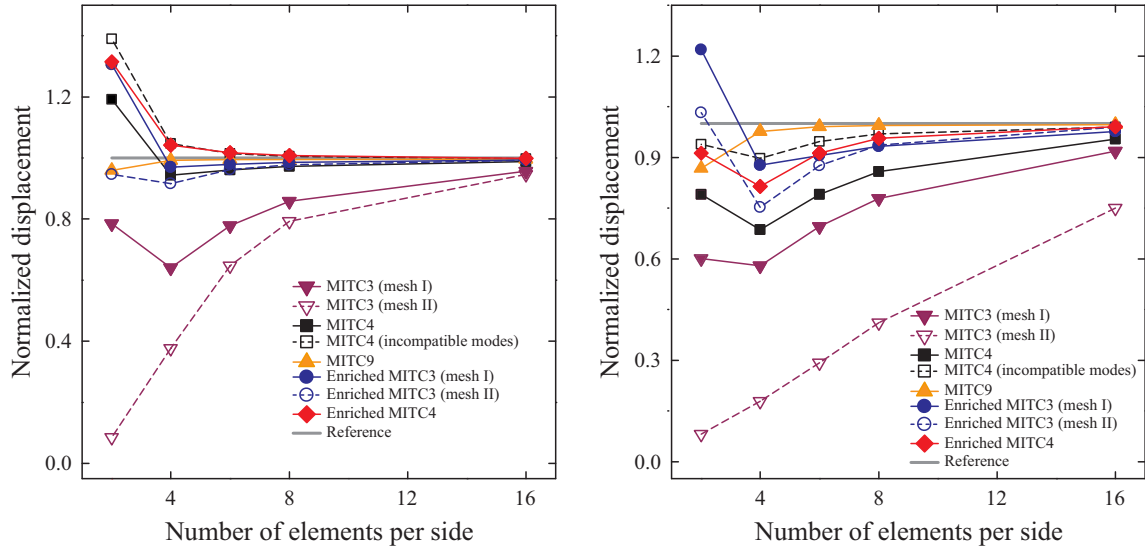


Figure 4.22. Normalized displacement of the Scordelis-Lo roof with (a) the uniform meshes (b) the distorted meshes shown in Figure 4.21(b).

The results for the normalized vertical displacement at the free edge are shown in **Figure 4.22** and the displacements and its normalized values using the uniform and distorted meshes are shown in **Table 6.12** and **Table 6.13**. The enriched MITC4 shell element shows an excellent performance even when the distorted meshes are used.

Table 4.13. Relative errors in the vertical displacement at point *A* for the Scordelis-Lo roof with the uniform meshes. Relative error (%) = $|w^{ref} - w^h| / |w^{ref}| \times 100$ where w^{ref} and w^h denote the reference and finite element solutions, respectively.

Element type	Mesh				
	2×2	4×4	6×6	8×8	16×16
MITC3 ^I	0.2159	0.3598	0.2216	0.1412	0.0437
MITC3 ^{II}	0.9147	0.6240	0.3528	0.2070	0.0532
MITC4	0.1921	0.0569	0.0397	0.0271	0.0112
MITC4*	0.3892	0.0473	0.0149	0.0053	0.0023
Enriched MITC3 ^I	0.3059	0.0301	0.0215	0.0146	0.0066
Enriched MITC3 ^{II}	0.0532	0.0840	0.0387	0.0225	0.0083
Enriched MITC4	0.3155	0.0420	0.0169	0.0079	0.0007
Enriched MITC4*	0.3131	0.0398	0.0150	0.0067	0.0009
MITC9	0.0407	0.0076	0.0056	0.0050	0.0040
QPH	-	0.0600	-	0.0200	0.0100
Simo et al.	-	0.0830	-	0.0150	0.0000
QUAD4	-	0.0500	0.0180	0.0080	-
URI-4	-	0.2190	-	0.0540	0.0170

SRI-4	-	0.0360	-	0.0160	0.0010
DKQ-4	-	0.0480	-	0.0050	0.0030
MISQ24	-	0.1912	-	0.0420	0.0063
RSDS-4	-	0.2010	-	0.0460	0.0100
T029 (SAMCEF)	-	0.0240	-	0.0140	0.0070
NMS-4F	-	0.0470	-	0.0050	0.0030
IBRA-4	-	0.0470	-	0.0050	0.0030
Allman	0.4072	0.0046	0.0129	0.0126	-
Cook_Flat-stiffened	0.3512	0.0925	0.0710	0.0494	-
Cook_Curved-softened	0.4060	0.1200	-	0.0610	-
Providas and Kattis	0.0984	0.2655	0.1853	0.1264	-
ANDES (OPT)	0.5273	0.0830	0.0304	0.0139	-
AHMA4	-	0.9319	0.8985	0.8656	-
EAS7_ANS	-	0.0407	-	0.0063	-

Reference solution $w_A^{ref}=0.3024$

I and II : mesh patterns shown in Figure 4.21(b) and Figure 4.17

Table 4.14. Relative errors in the displacement at the point A for the Scordelis-Lo roof with the distorted meshes. Relative error (%) = $|w^{ref} - w^h| / |w^{ref}| \times 100$ where w^{ref} and w^h denote the reference and finite element solutions, respectively.

Element type	Mesh				
	2×2	4×4	6×6	8×8	16×16
MITC3 ^I	0.3988	0.4203	0.3039	0.2212	0.0817
MITC3 ^{II}	0.9180	0.8214	0.7080	0.5893	0.2493
MITC4	0.2093	0.3138	0.2097	0.1415	0.0460
MITC4*	0.0618	0.1028	0.0526	0.0311	0.0099
Enriched MITC3 ^I	0.2179	0.1227	0.0942	0.0668	0.0235
Enriched MITC3 ^{II}	0.0324	0.2477	0.1243	0.0635	0.0109
Enriched MITC4	0.0874	0.1853	0.0869	0.0441	0.0087
MITC9	0.1319	0.0231	0.0089	0.0056	0.0033

Reference solution $w_A^{ref}=0.3024$

I and II : mesh patterns shown in Figure 4.21(b) and Figure 4.17

Chapter 5. MITC3+ Shell Element in Geometric Nonlinear Analysis

5.1 The MITC3+ Shell Finite Element for Linear Analysis

In this section, the linear formulation of the MITC3+ shell finite element is extended to geometric nonlinear analysis and its performance is demonstrated. The MITC3+ shell element, recently proposed for linear analysis [29], represents a further development of the MITC3 shell element. The total Lagrangian formulation is employed allowing for large displacements and large rotations. Considering several analysis problems, the nonlinear solutions using the MITC3+ shell element are compared with those obtained using the MITC3 and MITC4 shell elements. It can be concluded that the MITC3+ shell element shows, in the problems considered, the same excellent performance in geometric nonlinear analysis as already observed in linear analysis.

5.1.1 Geometry and Displacement Interpolations

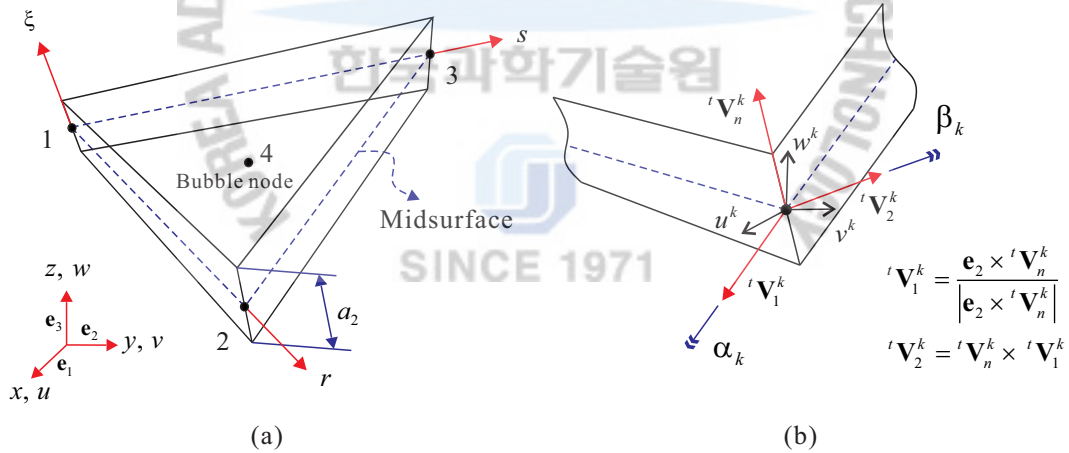


Figure 5.1. The MITC3+ shell finite element with the bubble node: (a) Geometry of the MITC3+ shell finite element. (b) Definition of rotational degrees of freedom α_k and β_k .

The geometry interpolation of the MITC3+ shell element, shown in **Figure 5.1**, is given by

$$\mathbf{x}(r, s, \xi) = \sum_{i=1}^3 h_i(r, s) \mathbf{x}_i + \frac{\xi}{2} \sum_{i=1}^4 a_i f_i(r, s) \mathbf{V}_n^i$$

with

$$h_1 = 1 - r - s, \quad h_2 = r, \quad h_3 = s, \quad a_4 \mathbf{V}_n^4 = \frac{1}{3}(a_1 \mathbf{V}_n^1 + a_2 \mathbf{V}_n^2 + a_3 \mathbf{V}_n^3), \quad (5.1)$$

in which $h_i(r, s)$ is the two-dimensional interpolation function of the standard isoparametric procedure corresponding to node i , \mathbf{x}_i is the position vector of node i in the global Cartesian coordinate system, a_i and \mathbf{V}_n^i denote the shell thickness and the director vector at node i , respectively, and $f_i(r, s)$ are the two-dimensional interpolation functions that include the cubic bubble function f_4 corresponding to the internal node 4

$$f_1 = h_1 - \frac{1}{3}f_4, \quad f_2 = h_2 - \frac{1}{3}f_4, \quad f_3 = h_3 - \frac{1}{3}f_4, \quad f_4 = 27rs(1 - r - s). \quad (5.2)$$

Unlike the standard 3-node shell elements, the MITC3+ shell element has an internal node and the corresponding cubic bubble function in the geometry interpolation.

From Equation (5.1), the displacement interpolation of the MITC3+ shell element for linear analysis is obtained by [29]

$$\mathbf{u}(r, s, \xi) = \sum_{i=1}^3 h_i(r, s) \mathbf{u}_i + \frac{\xi}{2} \sum_{i=1}^4 a_i f_i(r, s) (-\mathbf{V}_2^i \alpha_i + \mathbf{V}_1^i \beta_i), \quad (5.3)$$

in which \mathbf{u}_i is the nodal displacement vector in the global Cartesian coordinate system, \mathbf{V}_1^i and \mathbf{V}_2^i are the unit vectors orthogonal to \mathbf{V}_n^i and to each other, and α_i and β_i are the rotations of the director vector \mathbf{V}_n^i about \mathbf{V}_1^i and \mathbf{V}_2^i , respectively, at node i .

The interior node, with rotation degrees of freedom only, is positioned on the flat surface defined by the three corner nodes of the element. Only the bending and transverse shear strain fields are enriched by the bubble function, and the geometry of the element remains flat, as for the MITC3 element, in a large deformation analysis. Of course, static condensation can be carried out on the element level for the rotations α_4 and β_4 , and hence in practice the element is really a 3-node element.

5.1.2 Assumed Covariant Transverse Shear Strain Fields

For linear analysis, the linear part of the Green-Lagrange strain tensor is used and its covariant strain components are

$$e_{ij} = \frac{1}{2}(\mathbf{g}_i \cdot \mathbf{u}_{,j} + \mathbf{g}_j \cdot \mathbf{u}_{,i}), \quad (5.4)$$

in which

$$\mathbf{g}_i = \frac{\partial \mathbf{x}}{\partial r_i}, \quad \mathbf{u}_{,i} = \frac{\partial \mathbf{u}}{\partial r_i} \quad \text{with } r_1 = r, \quad r_2 = s, \quad r_3 = \xi. \quad (5.5)$$

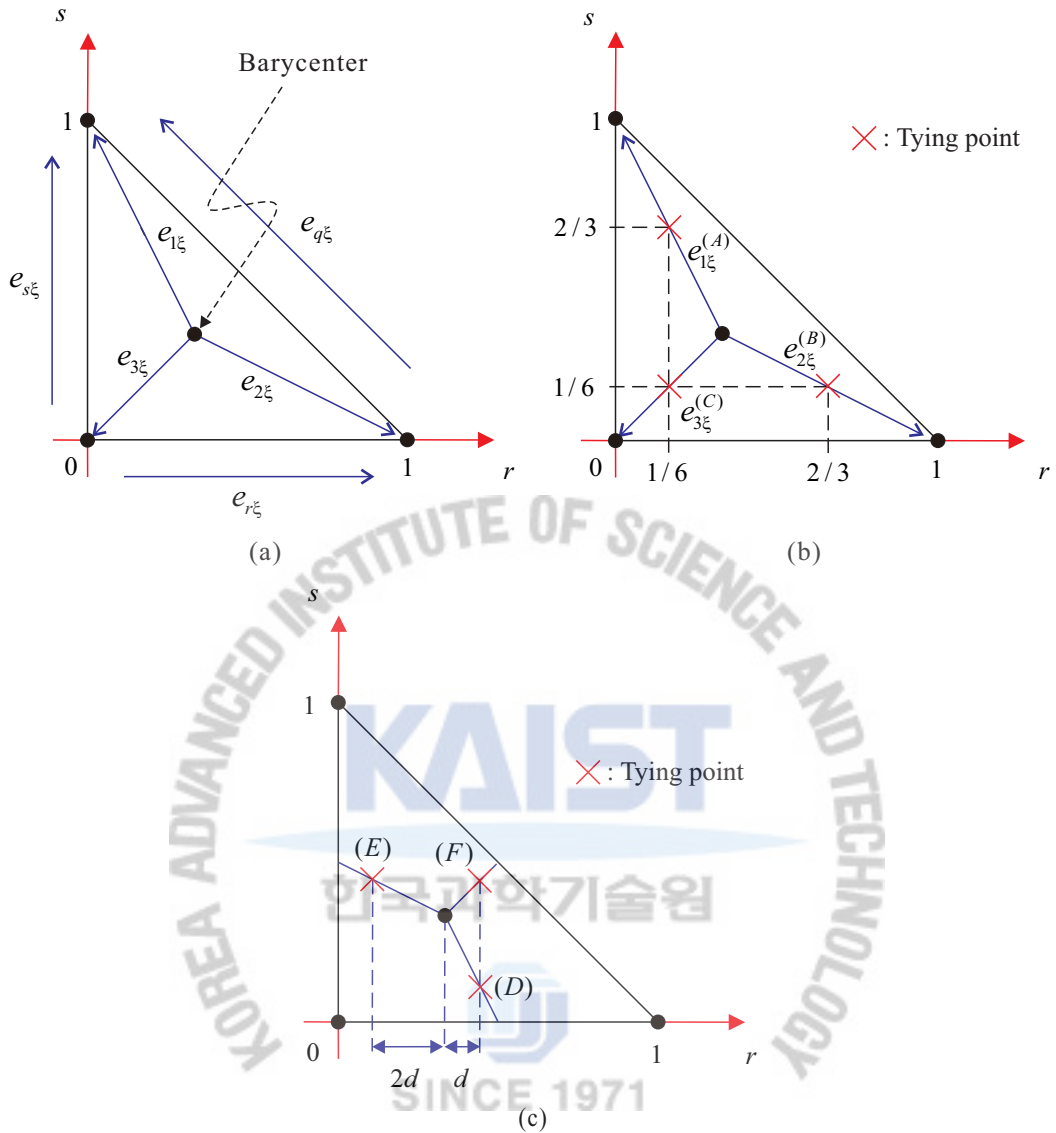


Figure 5.2. Transverse shear strains $e_{1\xi}$, $e_{2\xi}$ and $e_{3\xi}$, and the tying positions (A), (B), (C), (D), (E) and (F) for the assumed transverse shear strain filed.

Table 5.1. Tying positions for the assumed transverse shear strain for the MITC3+ shell elements. The distance d is defined in Figure 5.2(c), and $d = 1/10,000$ is used [29].

	Tying position	r	s
Figure 5.2(b)	(A)	1/6	2/3
	(B)	2/3	1/6
	(C)	1/6	1/6
Figure 5.2(c)	(D)	$1/3 + d$	$1/3 - 2d$

(E)	$1/3 - 2d$	$1/3 + d$
(F)	$1/3 + d$	$1/3 + d$

Since the MITC3+ shell element is flat, the covariant in-plane strain components are directly calculated using Equations (5.1)-(5.5). However, the covariant transverse shear strain fields are established using the MITC scheme to alleviate shear locking.

To construct the assumed transverse shear strain field for MITC3+ shell element, two important factors are considered. First, the tying positions for the assumed covariant transverse shear strain components should be inside the element since the bubble function should be zero along the element edges. Second, the stiffness associated to the in-plane twisting mode should be eliminated. For an original triangular shell element called MITC3 shell element, the transverse shear strains occur in two transverse shearing modes and in an in-plane twisting of the element about the axis normal to the mid-surface at the barycenter. Hence, the transverse shear strain field of the MITC3 shell element can be divided into the constant part corresponding to the transverse shearing modes and the linear part corresponding to the in-plane twisting mode.

$$e_{r\xi}^{AS, MITC3} = e_{r\xi}^{AS, const} + e_{r\xi}^{AS, linear}, \quad e_{s\xi}^{AS, MITC3} = e_{s\xi}^{AS, const} + e_{s\xi}^{AS, linear}. \quad (5.6)$$

At the barycenter, constant term evaluating the transverse shear strains can be obtained by

$$e_{r\xi}^{AS, const} = e_{r\xi}^{AS, MITC3} \Big|_{s=1/3} = \frac{2}{3} \left(e_{r\xi}^{(1)} + \frac{1}{2} e_{s\xi}^{(2)} \right) - \frac{1}{3} (e_{s\xi}^{(3)} - e_{r\xi}^{(3)}), \quad (5.7)$$

$$e_{s\xi}^{AS, const} = e_{s\xi}^{AS, MITC3} \Big|_{r=1/3} = \frac{2}{3} \left(e_{s\xi}^{(2)} + \frac{1}{2} e_{r\xi}^{(1)} \right) + \frac{1}{3} (e_{s\xi}^{(3)} - e_{r\xi}^{(3)}), \quad (5.8)$$

where

$$e_{r\xi}^{AS, MITC3} = e_{r\xi}^{(1)} + c s, \quad e_{s\xi}^{AS, MITC3} = e_{s\xi}^{(2)} - c r, \quad c = (e_{r\xi}^{(3)} - e_{r\xi}^{(1)}) - (e_{s\xi}^{(3)} - e_{s\xi}^{(2)}) \quad (5.9)$$

with

$$e_{r\xi}^{(1)} = e_{r\xi} \Big|_{r=1/2, s=0}, \quad e_{s\xi}^{(2)} = e_{s\xi} \Big|_{r=0, s=1/2}, \quad e_{r\xi}^{(3)} = e_{r\xi} \Big|_{r=1/2, s=1/2}, \quad e_{s\xi}^{(3)} = e_{s\xi} \Big|_{r=1/2, s=1/2}. \quad (5.10)$$

Subtracting, for the MITC3 shell element, the constant part from transverse shear strain field, the linearly varying part is calculated as follows

$$e_{r\xi}^{AS, linear} = e_{r\xi}^{AS, MITC3} - e_{r\xi}^{AS, const} = \frac{1}{3} c (3s - 1), \quad (5.11)$$

$$e_{s\xi}^{AS, linear} = e_{s\xi}^{AS, MITC3} - e_{s\xi}^{AS, const} = \frac{1}{3} c (1 - 3r). \quad (5.12)$$

If this approach were used for the MITC3+ shell element, the constant part in Equations (5.7)-(5.8) would not include the effect of the bubble function since the bubble function is zero along the element edges. To include the effect of the bubble function in the constant part, a new tying scheme using element internal

points is designed. First, the three covariant transverse shear strains e_{1r} , e_{2t} and e_{3t} are defined in the directions of the internal lines from the barycenter to the corners as shown in **Figure 5.2(a)**. The following relations are obtained for the covariant transverse shear strain components, for $0 \leq r, s \leq 1$,

$$e_{1\xi} = \frac{1}{\sqrt{5}}(2e_{s\xi} - e_{r\xi}), \quad e_{2\xi} = \frac{1}{\sqrt{5}}(2e_{r\xi} - e_{s\xi}), \quad e_{3\xi} = -\frac{1}{\sqrt{2}}(e_{r\xi} + e_{s\xi}), \quad (5.13)$$

and

$$e_{r\xi} = \frac{\sqrt{5}}{3}e_{2\xi} - \frac{\sqrt{2}}{3}e_{3\xi}, \quad e_{s\xi} = \frac{\sqrt{5}}{3}e_{1\xi} - \frac{\sqrt{2}}{3}e_{3\xi}, \quad e_{q\xi} = \frac{1}{\sqrt{2}}(e_{s\xi} - e_{r\xi}) = \frac{\sqrt{10}}{6}(e_{1\xi} - e_{2\xi}). \quad (5.14)$$

Using Equation (5.13), the transverse shear strain components are sampled at three internal tying points (*A*), (*B*) and (*C*) on the three internal lines, see **Figure 5.2(b)** and **Table 5.1**.

$$e_{1\xi}^{(A)} = \frac{1}{\sqrt{5}}(2e_{s\xi}^{(A)} - e_{r\xi}^{(A)}), \quad e_{2\xi}^{(B)} = \frac{1}{\sqrt{5}}(2e_{r\xi}^{(B)} - e_{s\xi}^{(B)}), \quad e_{3\xi}^{(C)} = -\frac{1}{\sqrt{2}}(e_{s\xi}^{(C)} + e_{r\xi}^{(C)}). \quad (5.15)$$

It is important to note that the tying points have been selected to obtain a spatially isotropic element. Using next the relations in Equation (5.14), the constant covariant transverse shear strains along the element edge directions are assumed to be

$$\hat{e}_{r\xi} = \frac{\sqrt{5}}{3}e_{2\xi}^{(B)} - \frac{\sqrt{2}}{3}e_{3\xi}^{(C)}, \quad \hat{e}_{s\xi} = \frac{\sqrt{5}}{3}e_{1\xi}^{(A)} - \frac{\sqrt{2}}{3}e_{3\xi}^{(C)}, \quad \hat{e}_{q\xi} = \frac{\sqrt{10}}{6}(e_{1\xi}^{(A)} - e_{2\xi}^{(B)}), \quad (5.16)$$

and, using Equation (5.15), a new constant transverse shear strain field is obtained

$$\hat{e}_{r\xi}^{const} = \hat{e}_{r\xi} = \frac{2}{3}(e_{r\xi}^{(B)} - \frac{1}{2}e_{s\xi}^{(B)}) + \frac{1}{3}(e_{r\xi}^{(C)} + e_{s\xi}^{(C)}), \quad (5.17)$$

$$\hat{e}_{s\xi}^{const} = \hat{e}_{s\xi} = \frac{2}{3}(e_{s\xi}^{(A)} - \frac{1}{2}e_{r\xi}^{(A)}) + \frac{1}{3}(e_{r\xi}^{(C)} + e_{s\xi}^{(C)}). \quad (5.18)$$

In order to render the in-plane twisting stiffness more flexible, the linear part is modified by using three tying point (*D*), (*E*) and (*F*).

$$\hat{e}_{r\xi}^{linear} = \frac{1}{3}\hat{c}(3s-1), \quad \hat{e}_{s\xi}^{linear} = \frac{1}{3}\hat{c}(1-3r) \quad \text{with} \quad \hat{c} = (e_{r\xi}^{(F)} - e_{r\xi}^{(D)}) - (e_{s\xi}^{(F)} - e_{s\xi}^{(E)}). \quad (5.19)$$

The tying positions (*D*), (*E*) and (*F*) are positioned on the three internal lines from the barycenter to the centers of the edges with d defined in **Figure 5.2(c)** and **Table 5.1**. As d varies from 1/6 to 0, the three tying positions move from the centers of the edges to the barycenter, resulting in a smaller in-plane twisting stiffness. An effective value for d is determined below. The assumed transverse shear strain fields of the MITC3+ shell element are given by

$$e_{r\xi}^{AS} = \frac{2}{3}(e_{r\xi}^{(B)} - \frac{1}{2}e_{s\xi}^{(B)}) + \frac{1}{3}(e_{r\xi}^{(C)} + e_{s\xi}^{(C)}) + \frac{1}{3}\hat{c}(3s-1),$$

$$e_{s\xi}^{AS} = \frac{2}{3}(e_{s\xi}^{(A)} - \frac{1}{2}e_{r\xi}^{(A)}) + \frac{1}{3}(e_{r\xi}^{(C)} + e_{s\xi}^{(C)}) + \frac{1}{3}\hat{c}(1-3r), \quad (5.20)$$

where $\hat{c} = e_{r\xi}^{(F)} - e_{r\xi}^{(D)} - e_{s\xi}^{(F)} + e_{s\xi}^{(E)}$ and the tying positions (*A*), (*B*), (*C*), (*D*), (*E*), and (*F*) are presented in **Figure 5.2** and **Table 5.1**.

The MITC3+ shell element is based on the ‘basic mathematical shell model’ [100, 103, 105] and the MITC scheme. The element passes the basic numerical tests, namely, the isotropy, zero energy mode, and patch tests. Furthermore, the MITC3+ shell element shows an excellent convergence behavior in both membrane and bending dominated shell problems, even when distorted meshes are used [29].

5.2 The MITC3+ Shell Element for Geometric Nonlinear Analysis

This section presents the geometric nonlinear formulation of the MITC3+ shell element. The total Lagrangian formulation is employed allowing for large displacements and large rotations. In the formulation, a superscript (and subscript) t is used to denote “time” for general analysis, with in static solutions “time” simply denoting the load step and configuration [1].

The large displacement kinematics and the interpolation of the Green-Lagrange strain components are discussed. With the given expressions, the now classical incremental equations used in the total Lagrangian formulation can directly be established [1].

5.2.1 Large Displacement Kinematics

The geometry of the MITC3+ shell finite element in the configuration at time t shown in **Figure 5.1** is interpolated with

$${}^t\mathbf{x}(r, s, \xi) = \sum_{i=1}^3 h_i(r, s) {}^t\mathbf{x}_i + \frac{\xi}{2} \sum_{i=1}^4 a_i f_i(r, s) {}^t\mathbf{V}_n^i, \quad (5.21)$$

in which ${}^t\mathbf{x}_i$ is the position vector of node i in the configuration at time t , and ${}^t\mathbf{V}_n^i$ denotes the director vector at node i in the configuration at time t .

The incremental displacements from the configuration at time t to the configuration at time $t + \Delta t$ are

$$\mathbf{u}(r, s, \xi) = {}^{t+\Delta t}\mathbf{x}(r, s, \xi) - {}^t\mathbf{x}(r, s, \xi), \quad (5.22)$$

and hence

$$\mathbf{u}(r, s, \xi) = \sum_{i=1}^3 h_i(r, s) \mathbf{u}_i + \frac{\xi}{2} \sum_{i=1}^4 a_i f_i(r, s) ({}^{t+\Delta t}\mathbf{V}_n^i - {}^t\mathbf{V}_n^i), \quad (5.23)$$

where \mathbf{u}_i is the vector of incremental nodal displacements at node i from time t to time $t + \Delta t$. Note that $\mathbf{u}(r, s, \xi)$ is the displacement vector in the linear formulation, see Equation (5.3), but here it is the vector of incremental displacements.

The director vector at time $t + \Delta t$ at node i is obtained from the director vector at time t

$${}^{t+\Delta t}\mathbf{V}_n^i = {}^{t+\Delta t}\mathbf{Q}^i {}^t\mathbf{V}_n^i, \quad (5.24)$$

in which ${}^{t+\Delta t}\mathbf{Q}^i$ is the rotation matrix which rotates the director vector at node i from the configuration at time t to the configuration at time $t + \Delta t$. Additionally, the two unit vectors ${}^t\mathbf{V}_1^i$ and ${}^t\mathbf{V}_2^i$ are obtained by (see **Figure 5.1(b)**),

$${}^t\mathbf{V}_1^i = \frac{\mathbf{e}_2 \times {}^t\mathbf{V}_n^i}{|\mathbf{e}_2 \times {}^t\mathbf{V}_n^i|}, \quad {}^t\mathbf{V}_2^i = {}^t\mathbf{V}_n^i \times {}^t\mathbf{V}_1^i. \quad (5.25)$$

For the vector-like parameterization of finite rotations [1, 144], the well-known formula is employed by

$${}^{t+\Delta t}\mathbf{Q}^i = \mathbf{I}_3 + \frac{\sin({}^{t+\Delta t}\theta^i)}{{}^{t+\Delta t}\theta^i} {}^{t+\Delta t}\mathbf{\Theta}^i + \frac{1}{2} \left[\frac{\sin({}^{t+\Delta t}\theta^i / 2)}{{}^{t+\Delta t}\theta^i / 2} \right]^2 ({}^{t+\Delta t}\mathbf{\Theta}^i)^2 \quad (5.26)$$

with

$${}^{t+\Delta t}\mathbf{\Theta}^i = \begin{bmatrix} 0 & -{}^{t+\Delta t}\theta_3^i & {}^{t+\Delta t}\theta_2^i \\ {}^{t+\Delta t}\theta_3^i & 0 & -{}^{t+\Delta t}\theta_1^i \\ -{}^{t+\Delta t}\theta_2^i & {}^{t+\Delta t}\theta_1^i & 0 \end{bmatrix}, \quad (5.27)$$

$${}^{t+\Delta t}\mathbf{\Theta}^i = \alpha_i {}^t\mathbf{V}_1^i + \beta_i {}^t\mathbf{V}_2^i, \quad (5.28)$$

in which \mathbf{I}_3 is the 3×3 identity matrix, ${}^{t+\Delta t}\mathbf{\Theta}^i$ is the skew-symmetric matrix operator, ${}^{t+\Delta t}\mathbf{\theta}^i = [{}^{t+\Delta t}\theta_1^i \quad {}^{t+\Delta t}\theta_2^i \quad {}^{t+\Delta t}\theta_3^i]^T$, and ${}^{t+\Delta t}\theta^i = \sqrt{({}^{t+\Delta t}\theta_1^i)^2 + ({}^{t+\Delta t}\theta_2^i)^2 + ({}^{t+\Delta t}\theta_3^i)^2}$.

Using a Taylor series expansion, the finite rotation tensor ${}^{t+\Delta t}\mathbf{Q}^i$ can be represented by

$${}^{t+\Delta t}\mathbf{Q}^i = \mathbf{I}_3 + {}^{t+\Delta t}\mathbf{\Theta}^i + \frac{1}{2!} ({}^{t+\Delta t}\mathbf{\Theta}^i)^2 + \frac{1}{3!} ({}^{t+\Delta t}\mathbf{\Theta}^i)^3 + \dots \quad (5.29)$$

Using only the terms up to quadratic order in Equation (5.29), the following equation is obtained

$${}^{t+\Delta t}\mathbf{V}_n^i - {}^t\mathbf{V}_n^i = {}^{t+\Delta t}\mathbf{\Theta}^i {}^t\mathbf{V}_n^i + \frac{1}{2} {}^{t+\Delta t}\mathbf{\Theta}^i {}^{t+\Delta t}\mathbf{\Theta}^i {}^t\mathbf{V}_n^i, \quad (5.30)$$

$${}^{t+\Delta t}\mathbf{V}_n^i - {}^t\mathbf{V}_n^i = {}^{t+\Delta t}\mathbf{\theta}^i \times {}^t\mathbf{V}_n^i + \frac{1}{2} {}^{t+\Delta t}\mathbf{\theta}^i \times ({}^{t+\Delta t}\mathbf{\theta}^i \times {}^t\mathbf{V}_n^i), \quad (5.31)$$

and using Equation (5.28) in Equation (5.31), we obtain for a ‘consistent linearization’ of the element displacements [1]

$${}^{t+\Delta t}\mathbf{V}_n^i - {}^t\mathbf{V}_n^i = -\alpha_i {}^t\mathbf{V}_2^i + \beta_i {}^t\mathbf{V}_1^i - \frac{1}{2} (\alpha_i^2 + \beta_i^2) {}^t\mathbf{V}_n^i. \quad (5.32)$$

Substituting Equation (5.32) into Equation (5.23), the vector of incremental displacements including second-order rotation effects is

$$\mathbf{u}(r, s, \xi) = \sum_{i=1}^3 h_i(r, s) \mathbf{u}_i + \frac{\xi}{2} \sum_{i=1}^4 a_i f_i(r, s) \left[-\alpha_i {}^t\mathbf{V}_2^i + \beta_i {}^t\mathbf{V}_1^i - \frac{1}{2} (\alpha_i^2 + \beta_i^2) {}^t\mathbf{V}_n^i \right], \quad (5.33)$$

in which α_i and β_i are the incremental rotations of the director vector ${}^t\mathbf{V}_n^i$ about ${}^t\mathbf{V}_1^i$ and ${}^t\mathbf{V}_2^i$, respectively, at node i .

Note that the incremental displacement in Equation (5.33) consists of two parts, the linear part \mathbf{u}_l and the quadratic part \mathbf{u}_q , hence

$$\mathbf{u}(r, s, \xi) = \mathbf{u}_l(r, s, \xi) + \mathbf{u}_q(r, s, \xi), \quad (5.34)$$

$$\text{with } \mathbf{u}_l(r, s, \xi) = \sum_{i=1}^3 h_i(r, s) \mathbf{u}_i + \frac{\xi}{2} \sum_{i=1}^4 a_i f_i(r, s) (-\alpha_i {}^t\mathbf{V}_2^i + \beta_i {}^t\mathbf{V}_1^i), \quad (5.35)$$

$$\text{and } \mathbf{u}_q(r, s, \xi) = -\frac{\xi}{4} \sum_{i=1}^4 a_i f_i(r, s) [(\alpha_i^2 + \beta_i^2) {}^t\mathbf{V}_n^i]. \quad (5.36)$$

5.2.2 Green-Lagrange Strain and Its interpolation

The Green-Lagrange strain tensor in the configuration at time t , referred to the configuration at time 0 and measured in the convected system is conventionally defined by

$${}^t\boldsymbol{\varepsilon} = \frac{1}{2} (\mathbf{F}^T \mathbf{F} - \mathbf{I}) \quad \text{with } \mathbf{F} = {}^t\mathbf{g}_i \otimes {}^0\mathbf{g}^i, \quad (5.37)$$

in which \mathbf{F} is the deformation gradient tensor in terms of the covariant and contravariant base vectors. The covariant base vectors are obtained as the partial derivatives of the position vectors with respect to the curvilinear coordinates. Thus, the covariant base vectors for any point within the shell body in the configuration at time 0 and time t is defined by

$${}^0\mathbf{g}_i = \frac{\partial {}^0\mathbf{x}}{\partial r_i}, \quad {}^t\mathbf{g}_i = \frac{\partial {}^t\mathbf{x}}{\partial r_i} = {}^0\mathbf{g}_i + {}^t\mathbf{u}_{,i} \quad \text{with } r_1 = r, \quad r_2 = s, \quad r_3 = \xi. \quad (5.38)$$

Similarly, in the incremental step from time t to $t + \Delta t$,

$${}^{t+\Delta t}\mathbf{g}_i = \frac{\partial {}^{t+\Delta t}\mathbf{x}}{\partial r_i} = {}^t\mathbf{g}_i + \frac{\partial {}^{t+\Delta t}\mathbf{u}}{\partial r_i}. \quad (5.39)$$

Using the Equation (5.38), the covariant components of the metric tensor can be determined as

$${}^0g_{ij} = {}^0\mathbf{g}_i \cdot {}^0\mathbf{g}_j, \quad {}^tg_{ij} = {}^t\mathbf{g}_i \cdot {}^t\mathbf{g}_j \quad (5.40)$$

The contravariant basis vectors needed for the calculation of the Green-Lagrange strain tensor can be derived as

$${}^0\mathbf{g}^i = {}^0\mathbf{g}^{-1} {}^0\mathbf{g}_i, \quad (5.41)$$

in which ${}^0\mathbf{g}^{-1}$ is the inverse of the metric tensor with components ${}^0g_{ij}$. Substituting Equations (5.38)-(5.41) into Equation (5.37), the covariant components of the Green-Lagrange strain tensor in the configuration at time t , referred to the configuration at time 0, are defined by

$${}^t\boldsymbol{\varepsilon} = {}^t\varepsilon_{ij} {}^0\mathbf{g}_i \otimes {}^0\mathbf{g}_j, \quad (5.42)$$

where

$${}^t\epsilon_{ij} = \frac{1}{2}({}^t\mathbf{g}_i \cdot {}^t\mathbf{g}_j - {}^0\mathbf{g}_i \cdot {}^0\mathbf{g}_j) \quad \text{with } {}^0\mathbf{g}_i = \frac{\partial {}^0\mathbf{x}}{\partial r_i}, \quad {}^t\mathbf{g}_i = \frac{\partial {}^t\mathbf{x}}{\partial r_i} = {}^0\mathbf{g}_i + {}^t\mathbf{u}_{,i}, \quad (5.43)$$

$$\text{in which } {}^t\mathbf{u}_{,i} = \frac{\partial {}^t\mathbf{u}}{\partial r_i}, \quad {}^t\mathbf{u} = {}^t\mathbf{x} - {}^0\mathbf{x}, \quad r_1 = r, \quad r_2 = s, \quad r_3 = \xi. \quad (5.44)$$

Hence the incremental covariant strains are

$${}^0\epsilon_{ij} = {}^{t+\Delta t}{}^0\epsilon_{ij} - {}^t\epsilon_{ij} = \frac{1}{2}(\mathbf{u}_{,i} \cdot {}^t\mathbf{g}_j + {}^t\mathbf{g}_i \cdot \mathbf{u}_{,j} + \mathbf{u}_{,i} \cdot \mathbf{u}_{,j}) \quad \text{with } \mathbf{u}_{,i} = \frac{\partial \mathbf{u}}{\partial r_i} \quad (5.45)$$

Using Equation (5.34) in Equation (5.45), these strains are approximated as

$${}^0\epsilon_{ij} = {}^0e_{ij} + {}^0\eta_{ij}, \quad (5.46)$$

where ${}^0e_{ij}$ and ${}^0\eta_{ij}$ are the linear and nonlinear parts, respectively,

$${}^0e_{ij} = \frac{1}{2} \left(\frac{\partial \mathbf{u}_i}{\partial r_i} \cdot {}^t\mathbf{g}_j + {}^t\mathbf{g}_i \cdot \frac{\partial \mathbf{u}_j}{\partial r_j} \right) = \mathbf{B}_{ij} \mathbf{U}, \quad (5.47)$$

$${}^0\eta_{ij} = \frac{1}{2} \left(\frac{\partial \mathbf{u}_i}{\partial r_i} \cdot \frac{\partial \mathbf{u}_j}{\partial r_j} \right) + \frac{1}{2} \left(\frac{\partial \mathbf{u}_q}{\partial r_i} \cdot {}^t\mathbf{g}_j + {}^t\mathbf{g}_i \cdot \frac{\partial \mathbf{u}_q}{\partial r_j} \right) = \frac{1}{2} \mathbf{U}^T \mathbf{N}_{ij} \mathbf{U}, \quad (5.48)$$

in which \mathbf{B}_{ij} and \mathbf{N}_{ij} are the strain-displacement matrices and \mathbf{U} is the vector of incremental nodal displacements and rotations \mathbf{u}_i , α_i and β_i for all element nodes. In addition, the strain variations are

$$\delta {}^0e_{ij} = \mathbf{B}_{ij} \delta \mathbf{U}, \quad \delta {}^0\eta_{ij} = \delta \mathbf{U}^T \mathbf{N}_{ij} \mathbf{U}. \quad (5.49)$$

Note that Equations (5.46)-(5.49) contain all the strain terms to have a consistent linearization in the establishment of the tangent stiffness matrix.

To alleviate shear locking, the MITC scheme used in the linear formulation of the MITC3+ shell element is also employed for the incremental covariant transverse shear strains in the nonlinear formulation. Therefore, the covariant transverse shear strains in Equations (5.46)-(5.49) are substituted by

$${}^0\epsilon_{r\xi}^{AS} = \frac{2}{3}({}^0\epsilon_{r\xi}^{(B)} - \frac{1}{2}{}^0\epsilon_{s\xi}^{(B)}) + \frac{1}{3}({}^0\epsilon_{r\xi}^{(C)} + {}^0\epsilon_{s\xi}^{(C)}) + \frac{1}{3}{}^0\hat{c}(3s-1), \quad (5.50)$$

$${}^0\epsilon_{s\xi}^{AS} = \frac{2}{3}({}^0\epsilon_{s\xi}^{(A)} - \frac{1}{2}{}^0\epsilon_{r\xi}^{(A)}) + \frac{1}{3}({}^0\epsilon_{r\xi}^{(C)} + {}^0\epsilon_{s\xi}^{(C)}) + \frac{1}{3}{}^0\hat{c}(1-3r), \quad (5.51)$$

$${}^0\epsilon_{j\xi}^{AS} = {}^0e_{j\xi}^{AS} + {}^0\eta_{j\xi}^{AS}, \quad {}^0e_{j\xi}^{AS} = \mathbf{B}_{j\xi}^{AS} \mathbf{U}, \quad {}^0\eta_{j\xi}^{AS} = \frac{1}{2} \mathbf{U}^T \mathbf{N}_{j\xi}^{AS} \mathbf{U} \quad \text{with } j = r, s \quad (5.52)$$

in which ${}^0\hat{c} = {}^0\epsilon_{r\xi}^{(F)} - {}^0\epsilon_{r\xi}^{(D)} - {}^0\epsilon_{s\xi}^{(F)} + {}^0\epsilon_{s\xi}^{(E)}$, $\mathbf{B}_{j\xi}^{AS}$ and $\mathbf{N}_{j\xi}^{AS}$ are the strain-displacement matrices for the assumed covariant transverse shear strains. Of course, the tying positions defined in **Figure 5.2** and **Table 5.1** are used.

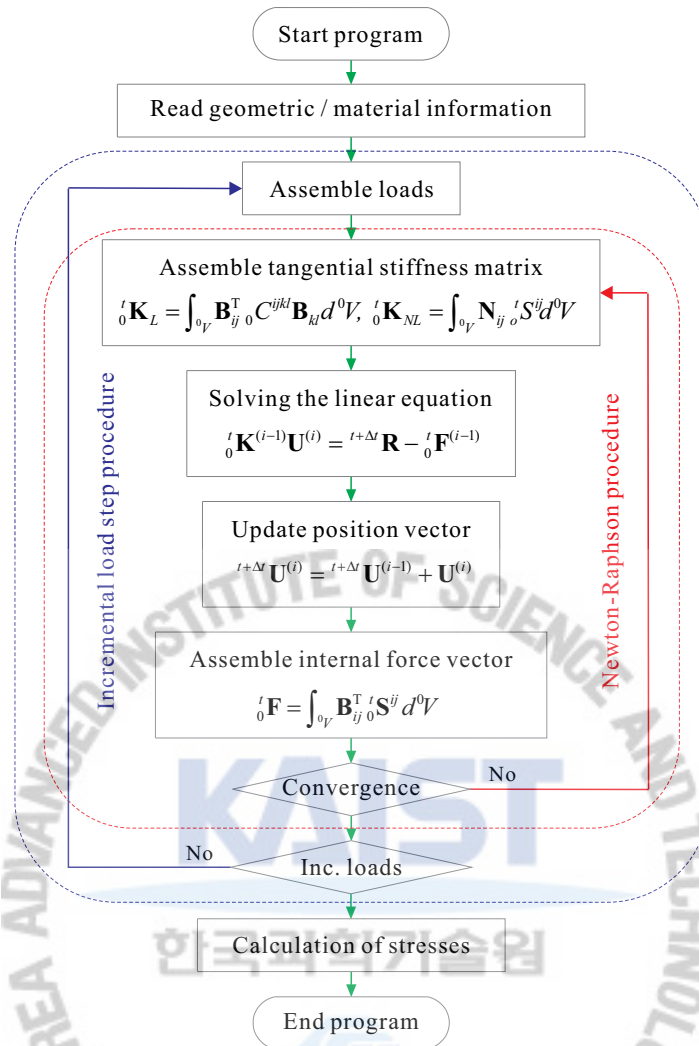


Figure 5.3. Flow chart of the iterative procedures for solving the linearized equilibrium equation in the total Lagrangian formulation.

Finally, the global equilibrium equations are solved in iterative incremental manner, using the full Newton-Raphson method as shown in **Figure 5.3**. For the evaluation of the element stiffness matrix and internal nodal force vector, we use 7-point Gauss integration in the r - s plane (as for the MITC6 shell element) due to the cubic bubble function. Hence, since also 6 tying points and the fourth node are used, compared to the MITC3 shell element (using 3 tying points and 3-point Gauss integration), the MITC3+ shell element requires for the evaluation of these element quantities clearly more computational time.

5.3 Numerical Examples

To assess the performance of the MITC3+ shell element in geometric nonlinear analysis, the solutions

of several benchmark problems are given in this section. The problems involve the large displacement and large rotation response of shells with various shell geometries. The results calculated using the following MITC shell elements are given

- MITC3: 3-node triangular shell element
- MITC3+: 3-node triangular shell element enriched by a cubic bubble function
- MITC4: 4-node quadrilateral shell element

In each example, the reference solutions are given by either an analytical result or a calculated solution using a fine uniform mesh of the MITC9 shell element (these meshes used twice the number of elements in each direction as employed in the MITC4 element solutions) [22]. The MITC9 element is known to satisfy the ellipticity and consistency conditions and to show good convergence behavior [22, 26, 27]. For comparison, we also plot the results of the linear analysis calculated using the MITC9 shell element. The iterations to solve the nonlinear equations have been performed in each load step to a convergence tolerance of 0.1 percent on the relative incremental energy.

Note that in some benchmark problems, point loads are used, which cause a stress singularity at the point of loading. However, the use of point loads is acceptable in the studies here given because the meshes are not very fine (the point loads act as an equivalent pressure applied over a small area) [1].

5.3.1 Cantilever Plate Subjected to End Shear Force

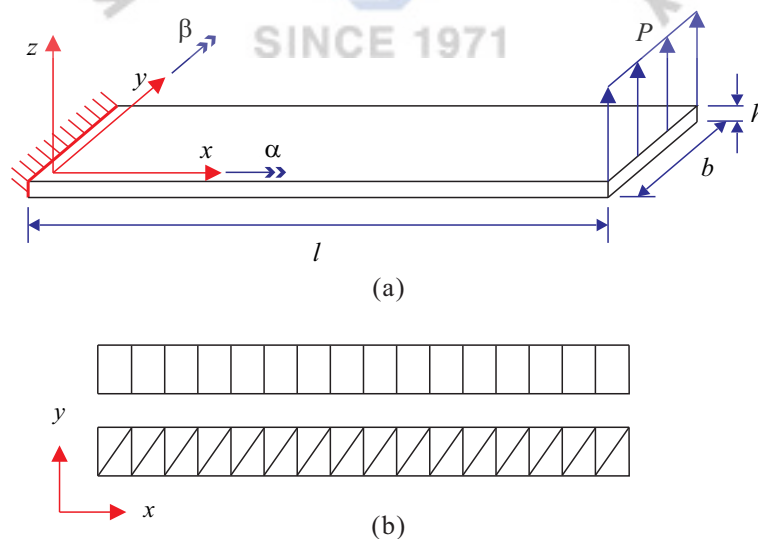


Figure 5.4. Cantilever plate subjected to end shear force. (a) Problem description. (b) Meshes used for the MITC4 (top), MITC3 and MITC3+ (bottom) shell elements.

The cantilever plate shown in **Figure 5.4(a)** is subjected to a shear force at the free end. This problem has been considered many times before, see e.g. [145-147]. The material properties, geometry and applied force are chosen as $E = 1.2 \times 10^6$, $\nu = 0$, $l = 10$, $b = 1$, $h = 0.1$ and $P_{\max} = 4$. **Figure 5.4(b)** shows the 16×1 mesh used for the solution with the MITC4 shell element and the corresponding mesh used for the MITC3 and MITC3+ shell elements. The reference solutions are calculated using a 32×2 element mesh of the MITC9 shell element.

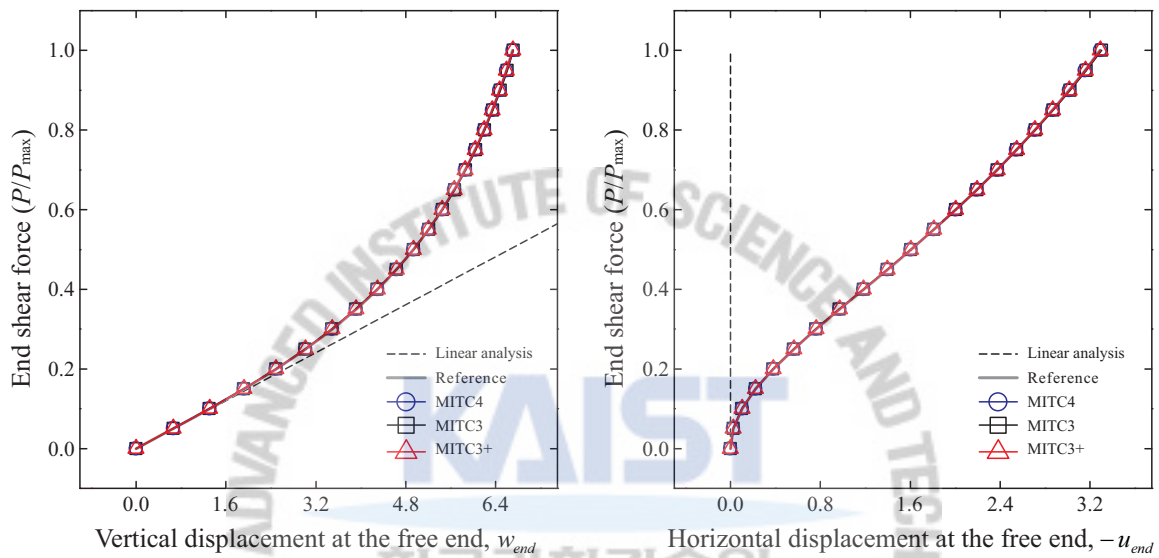


Figure 5.5. Load-displacement curves for the cantilever plate subjected to end shear force. For the triangular element meshes, essentially the same response is measured at the two corners.

Table 5.2. Relative errors in the vertical and horizontal displacements at the free end for the cantilever plate subjected to end shear force. Relative error (%) = $|w^{ref} - w^h| / |w^{ref}| \times 100$ or $|v^{ref} - v^h| / |v^{ref}| \times 100$ where w^{ref} and v^{ref} denote the reference solution, and w^h and v^h are finite element solutions.

Normalized load P / P_{\max}	Relative errors in the vertical displacement			Relative errors in the horizontal displacement		
	MITC4	MITC3	MITC3+	MITC4	MITC3	MITC3+
0.1	0.0916	0.3588	0.0611	0.2317	0.9173	0.1738
0.2	0.0641	0.2605	0.0361	0.1834	0.7361	0.1336
0.3	0.0372	0.1432	0.0115	0.1269	0.5116	0.0837
0.4	0.0093	0.0349	0.0163	0.0674	0.2951	0.0337
0.5	0.0142	0.0527	0.0365	0.0249	0.1183	0.0062
0.6	0.0294	0.1194	0.0496	0.0100	0.0299	0.0349
0.7	0.0444	0.1724	0.0632	0.0379	0.1475	0.0632
0.8	0.0517	0.2115	0.0694	0.0591	0.2437	0.0812

0.9	0.0603	0.2427	0.0788	0.0796	0.3186	0.0996
1.0	0.0657	0.2642	0.0821	0.0942	0.3799	0.1125
Average	0.0468	0.1860	0.0504	0.0915	0.3698	0.0822

w^{ref} and v^{ref} : Reference solutions calculated using the 16×1 element mesh of the MITC9 shell elements

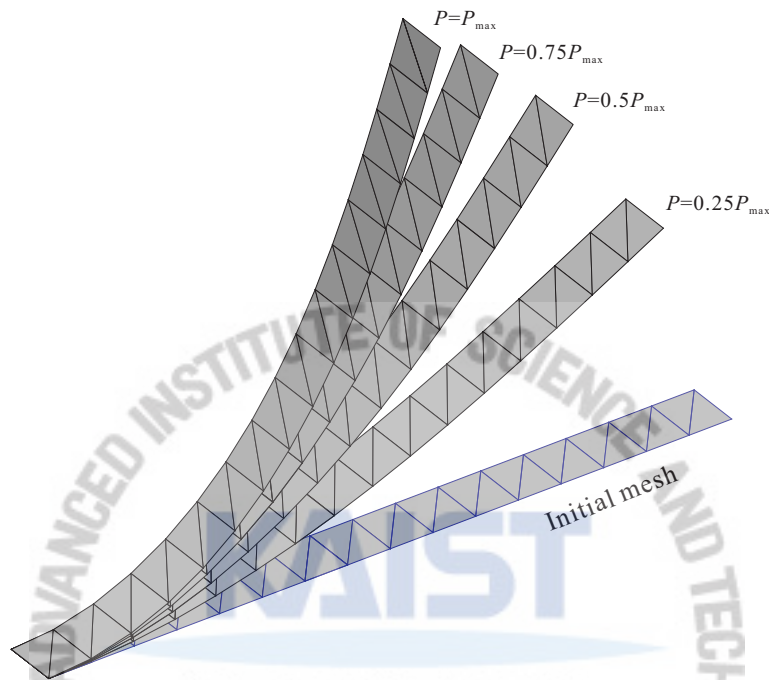


Figure 5.6. Deformed configurations of the cantilever plate under end shear force.

Figure 5.5 shows the calculated load-displacement curves and the same results are tabulated in **Table 5.2**. **Figure 5.6** depicts the deformed configurations of the cantilever plate obtained using the MITC3+ shell element at various load levels ($P = 0.25P_{max}$, $0.5P_{max}$, $0.75P_{max}$, and P_{max}). All shell elements considered show excellent performance in the solution of this problem.

5.3.2 Cantilever Plate Subjected to End Moment

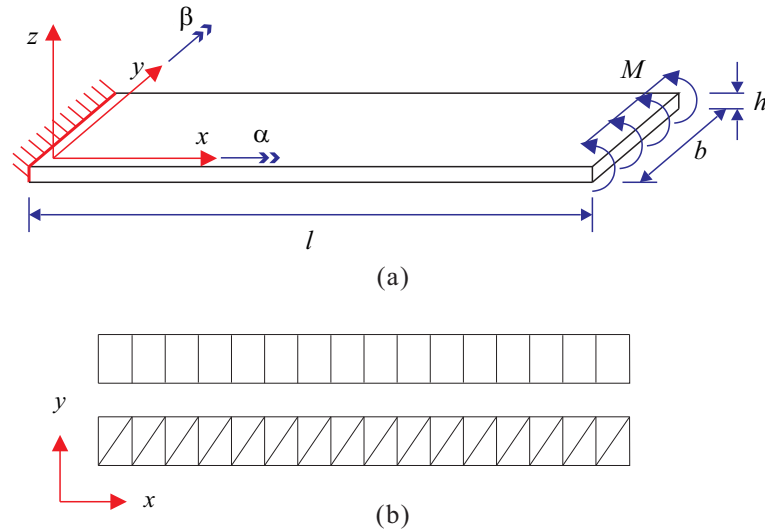


Figure 5.7. Cantilever plate subjected to end moment. (a) Problem description. (b) Meshes used for the MITC4 (top), MITC3 and MITC3+ (bottom) shell elements.

Figure 5.7 shows the cantilever plate subjected to a moment at the free end. This is a good problem to test the large rotation capability of shell elements [139, 140, 148, 149]. The cantilever plate has length $l = 12$, width $b = 1$, thickness $h = 0.1$, Young's modulus $E = 1.2 \times 10^6$ and Poisson's ratio $\nu = 0$. We use the end moment $M_{\max} = 2\pi M_0$ with $M_0 = EI/L$, and hence the cantilever rolls up into a complete circle. The structure is modeled using a 16×1 element mesh of the MITC4 shell element and the corresponding MITC3 and MITC3+ shell element meshes, see **Figure 5.4(b)**. The reference solutions are calculated using a 32×2 element mesh of the MITC9 shell element.

The cantilever forms a circular arc of radius R given by the classical formula $R = EI/M$. Thus, the analytical tip displacements are derived as

$$\frac{u}{l} = \frac{M_0}{M} \sin\left(\frac{M}{M_0}\right) - 1, \quad \frac{w}{l} = \frac{M_0}{M} \left(1 - \cos\frac{M}{M_0}\right). \quad (5.53)$$

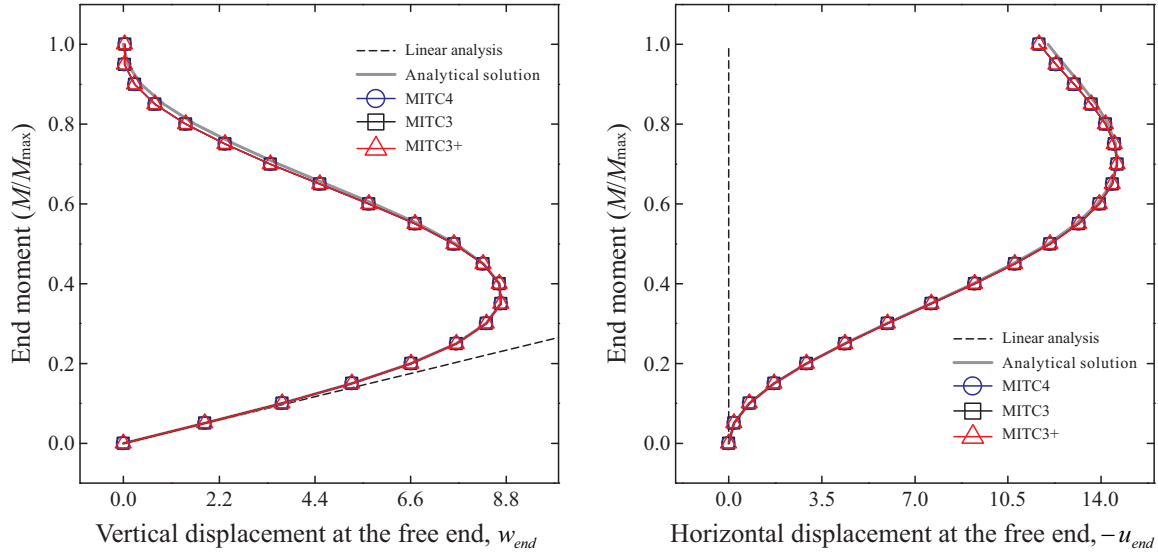


Figure 5.8. Load-displacement curves for the cantilever plate subjected to end moment. For the triangular element meshes, essentially the same response is measured at the two corners.

Table 5.3. Relative errors in the vertical and horizontal displacements at the free end for the cantilever plate subjected to end moment. Relative error (%) = $|w^{ref} - w^h| / |w^{ref}| \times 100$ or $|u^{ref} - u^h| / |u^{ref}| \times 100$ where w^{ref} and u^{ref} denote the reference solution, and w^h and u^h are finite element solutions.

Normalized load M / M_{max}	Relative errors in the vertical displacement			Relative errors in the horizontal displacement		
	MITC4	MITC3	MITC3+	MITC4	MITC3	MITC3+
0.1	0.0302	0.0302	0.0302	0.0362	0.0362	0.0362
0.2	0.1015	0.1015	0.1015	0.1199	0.1199	0.1199
0.3	0.1428	0.1428	0.1428	0.3398	0.3398	0.3398
0.4	0.0174	0.0174	0.0174	0.5569	0.5569	0.5569
0.5	0.5301	0.5301	0.5301	0.6750	0.6750	0.6750
0.6	1.9780	1.9780	1.9780	0.5695	0.5695	0.5695
0.7	5.3451	5.3451	5.3451	0.1233	0.1233	0.1233
0.8	13.349	13.349	13.349	0.7288	0.7288	0.7288
0.9	37.330	37.330	37.364	1.8797	1.8797	1.8797
1.0	-	-	-	2.7917	2.7917	2.7583
Average	6.5360	6.5360	6.5398	0.7821	0.7821	0.7787

w^{ref} and u^{ref} : Analytical solutions given by Equation (5.53).

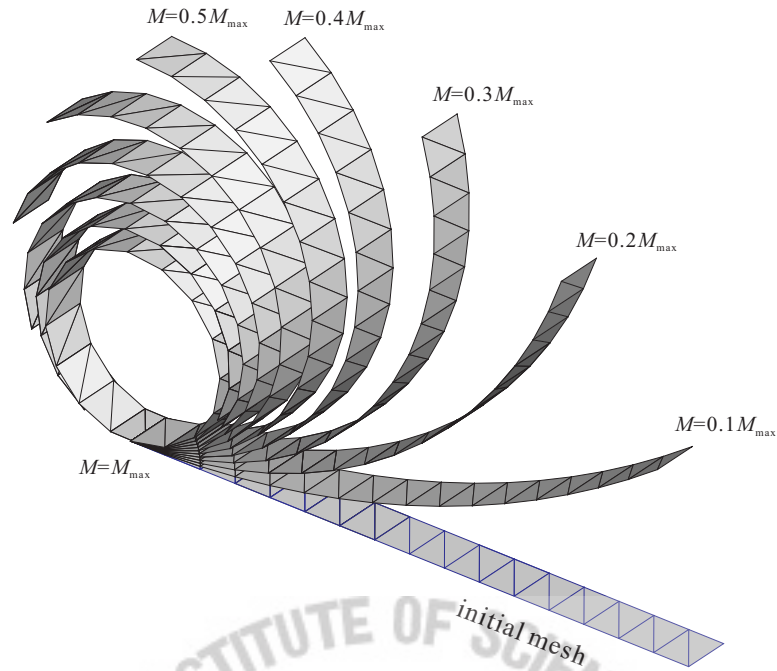


Figure 5.9. Deformed configurations of the cantilever plate under end moment.

Figure 5.8 depicts the calculated load-displacement curves and **Table 5.3** presents the displacements at the free end for this problem. **Figure 5.9** shows successive deformed configurations calculated using the MITC3+ shell element at various load stages ($M = 0.1M_{\max}, 0.2M_{\max}, 0.3M_{\max}, \dots, M_{\max}$). All computed results show good agreement with the analytical solutions.

5.3.3 Slit Annular Plate under End Shear Force

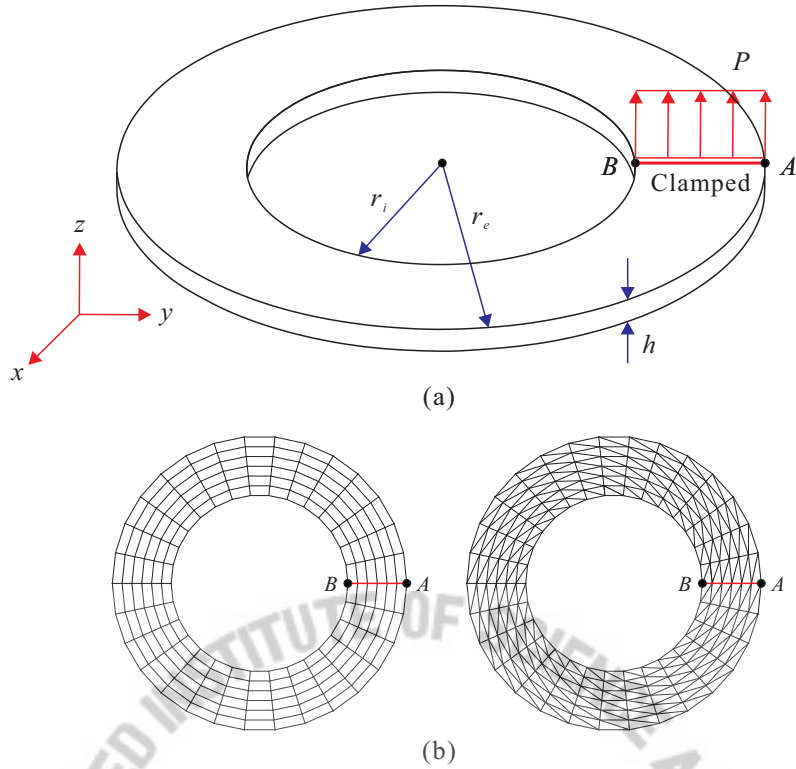


Figure 5.10. Slit annular plate under end shear force. (a) Problem description. (b) Meshes used.

A slit annular plate shown in **Figure 5.10(a)** is examined. This example was suggested by Başar and Ding [150] and has been widely considered [139-141, 151-154]. The geometry and elastic material properties are given by $r_i = 6$, $r_e = 10$, $h = 0.03$, $E = 21 \times 10^6$ and $\nu = 0$. The transverse shear force $P_{\max} = 3.2$ is incrementally applied at one end of the slit while the other end of the slit is fully clamped. The plate undergoes large displacements and large rotations. This structure is modeled using a 6×30 element mesh of the MITC4 shell element and the corresponding MITC3 and MITC3+ shell element meshes, see **Figure 5.10(b)**. The reference solutions are obtained using a 12×60 element mesh of the MITC9 shell element.

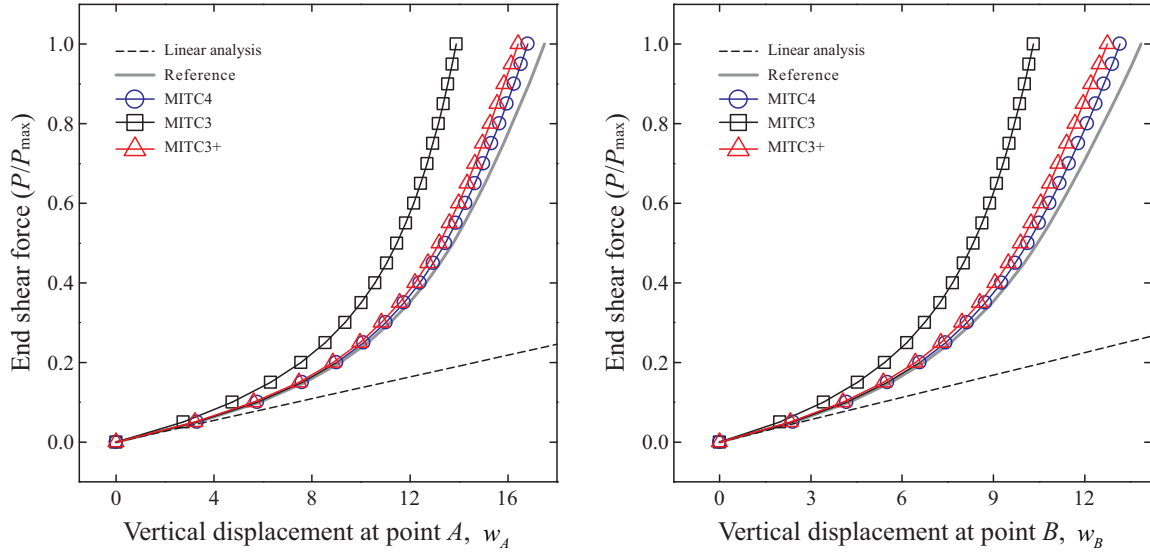


Figure 5.11. Load-displacement curves for the slit annular plate under end shear force.

Table 5.4. Relative errors in the vertical displacements at point *A* and *B* for slit annular plate under transverse end shear force. Relative error (%) = $\frac{|w^{ref} - w^h|}{|w^{ref}|} \times 100$ where w^{ref} and w^h denote the reference and finite element solutions, respectively.

Normalized load P / P_{max}	Relative errors in the vertical displacement at point <i>A</i>			Relative errors in the vertical displacement at point <i>B</i>		
	MITC4	MITC3	MITC3+	MITC4	MITC3	MITC3+
0.1	1.5972	19.067	4.0407	2.0637	19.844	4.9036
0.2	1.4592	17.434	3.1043	1.9778	19.030	4.0838
0.3	1.6257	16.503	3.1621	2.2202	18.942	4.2687
0.4	1.9299	16.373	3.5276	2.6072	19.452	4.7875
0.5	2.2547	16.619	3.9930	3.0144	20.162	5.3828
0.6	2.5799	17.090	4.5250	3.4173	20.979	6.0425
0.7	2.8945	17.769	5.1221	3.8008	21.965	6.7895
0.8	3.2398	18.653	5.5707	4.2093	23.126	7.3167
0.9	3.6011	19.613	6.0335	4.6480	24.342	7.8624
1.0	3.8708	20.560	6.1635	4.9516	25.509	7.9616
Average	2.5053	17.968	4.5242	3.2910	21.335	5.9399

w^{ref} : Reference solutions calculated using the 6×30 element mesh of the MITC9 shell elements

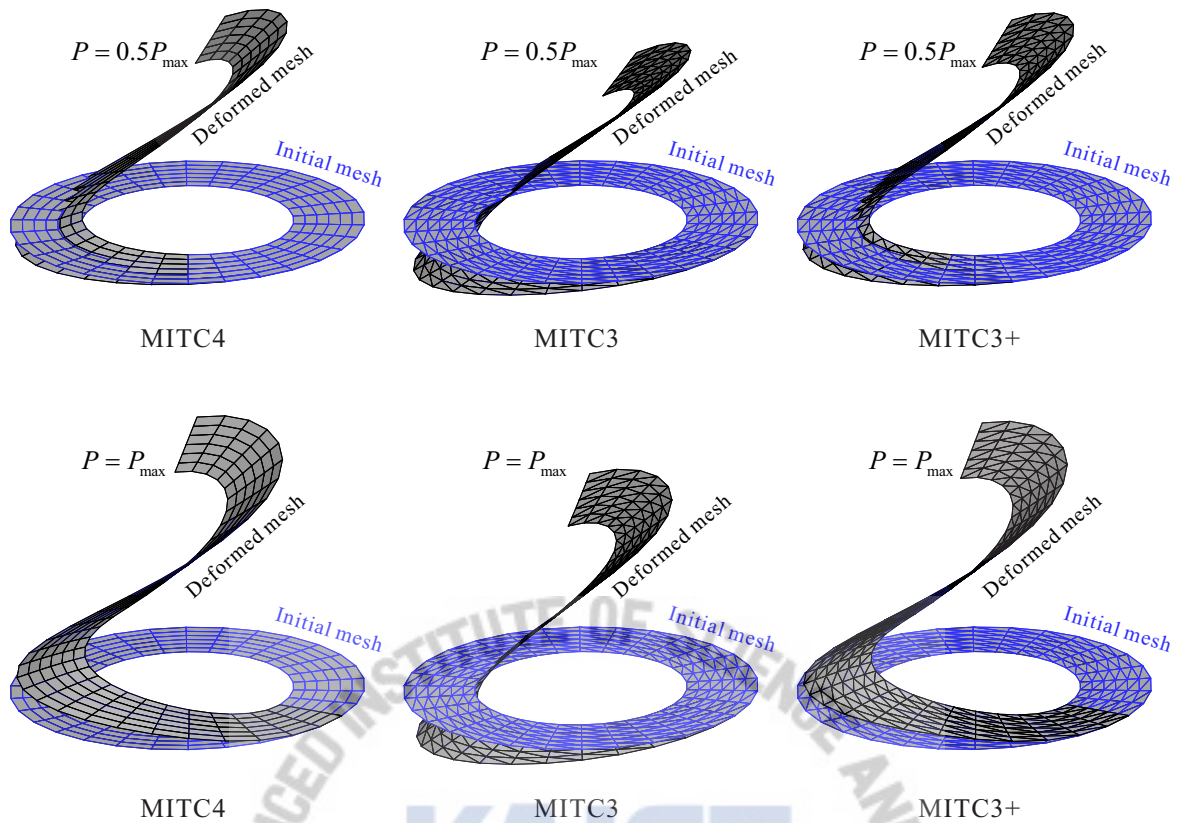


Figure 5.12. Deformed configurations of the slit annular plate under end shear force.

The load-displacement curves at two different points, *A* and *B*, are depicted in **Figure 5.11**. Also, the same results are listed in **Table 5.4**. The deformed configurations calculated using the MITC4, MITC3 and MITC3+ shell elements are shown in **Figure 5.12**. As seen, the MITC3 shell element displays too stiff a behavior. However, the results using the MITC3+ shell element are in agreement with those using the MITC4 shell element and reasonably close to the reference solutions.

5.3.4 Hemisphere Shell Subjected to Alternating Radial Forces

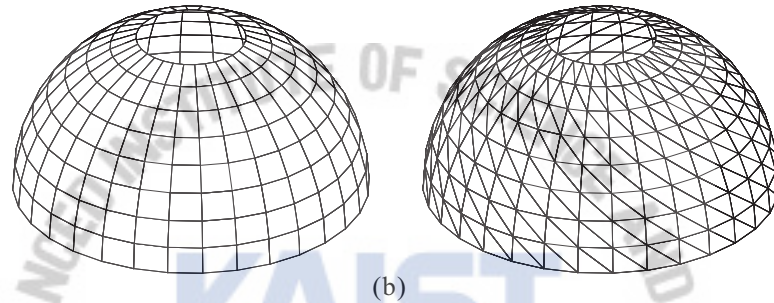
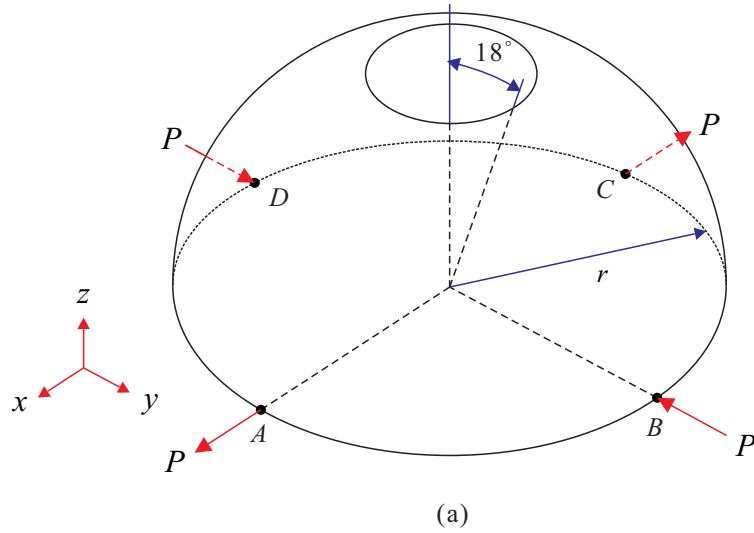


Figure 5.13. Hemisphere shell subjected to alternating radial forces. (a) Problem solved. (b) Meshes used (8×32).

Next benchmark problem is a hemispherical shell with an 18° circular cutout, as shown in **Figure 5.13(a)**. The shell is pinched along one direction at points B and D and pulled along the perpendicular direction at points A and C [120, 145, 147, 151, 152]. The material and geometric properties are given by $E = 6.825 \times 10^7$, $\nu = 0.3$, $r = 10$, and the thickness is 0.04. The point load is incrementally applied to a maximum value $P_{\max} = 400$. The shell is modeled using 8×32 and 12×48 element meshes of the MITC4 shell element and the corresponding MITC3 and MITC3+ shell element meshes, see **Figure 5.13(b)**. A 24×96 element mesh of the MITC9 shell element is used to obtain the reference solutions.

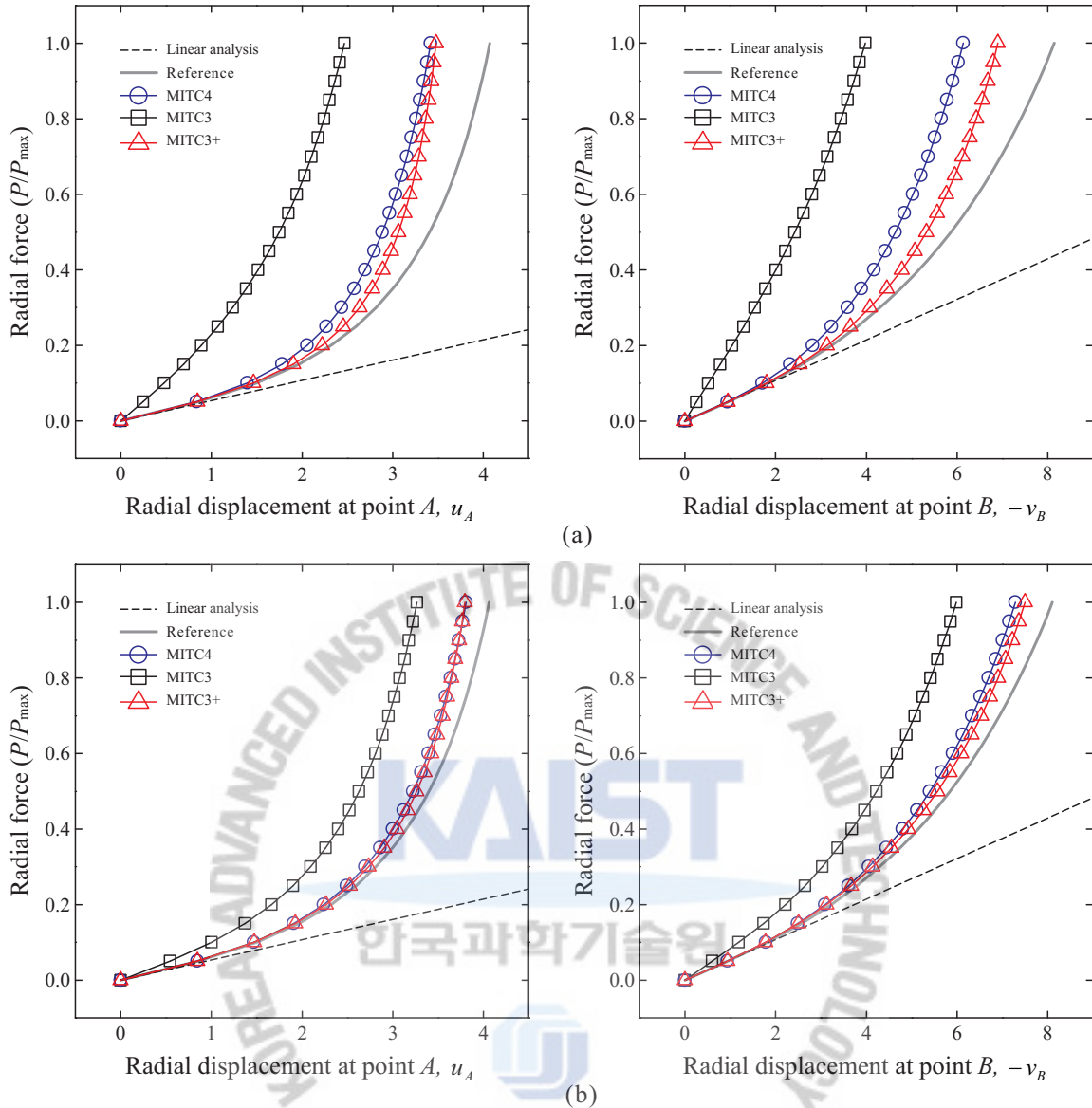


Figure 5.14. Load-displacement curves for the hemisphere shell subjected to alternating radial forces when (a) 8×32 and (b) 12×48 element meshes are used.

Table 5.5. Relative errors in the radial displacements at point A and B for the hemisphere shell subjected to alternating radial forces. Relative error (%) = $|u^{ref} - u^h| / |u^{ref}| \times 100$ or $|v^{ref} - v^h| / |v^{ref}| \times 100$ where u^{ref} and v^{ref} denote the reference solution, and u^h and v^h are finite element solutions.

Normalized load P / P_{max}	Relative errors in the displacement at point A			Relative errors in the displacement at point B		
	MITC4	MITC3	MITC3+	MITC4	MITC3	MITC3+
0.1	0.9285	15.978	1.3626	1.1691	16.000	2.2284
0.2	1.4665	14.256	1.6563	1.9768	14.974	2.8722
0.3	1.6875	13.305	1.7372	2.3749	14.738	2.9756

0.4	1.8621	12.695	1.8652	2.7121	14.719	3.0115
0.5	1.9998	12.254	2.0145	2.9814	14.751	3.0208
0.6	2.1217	11.914	2.2080	3.2229	14.792	3.0846
0.7	2.2460	11.644	2.4330	3.4805	14.852	3.2167
0.8	2.3517	11.412	2.6722	3.6963	14.881	3.3913
0.9	2.4509	11.210	2.9114	3.9057	14.903	3.5965
1.0	2.5401	11.037	3.1480	4.1014	14.918	3.8287
Average	1.9655	12.571	2.2008	2.9621	14.953	3.1226

u^{ref} and v^{ref} : Reference solutions calculated using the 12×48 element mesh of the MITC9 shell elements

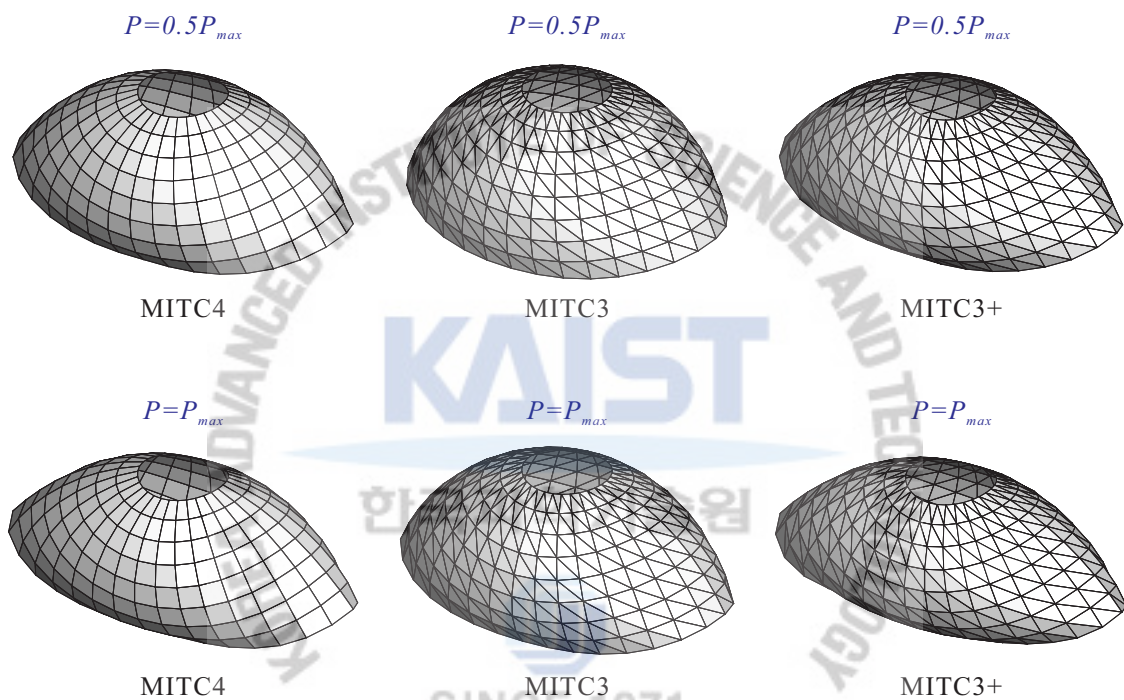


Figure 5.15. Deformed configurations of the hemisphere shell subjected to alternating radial forces.

Figure 5.14 shows the load-radial displacement curves at the loaded points A and B . **Table 5.5** tabulates the same results of **Figure 5.14**. The deformed configurations obtained using a 8×32 element mesh of the MITC4 shell element and the corresponding MITC3 and MITC3+ shell element meshes are shown in **Figure 5.15**. For the meshes used, the MITC4 and MITC3+ shell elements produce much better solution accuracy than the MITC3 shell element in this problem.

5.3.5 Clamped Semi-Cylindrical Shell under Point Load

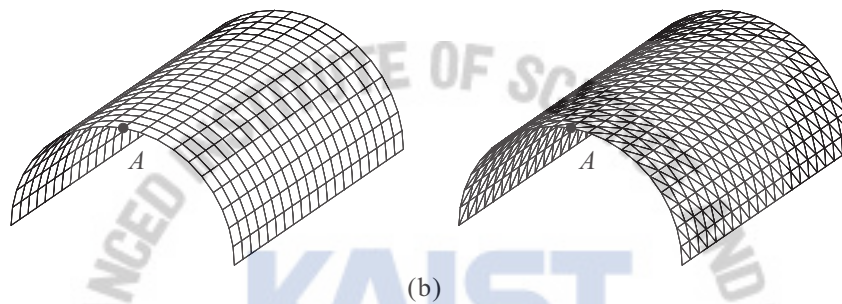
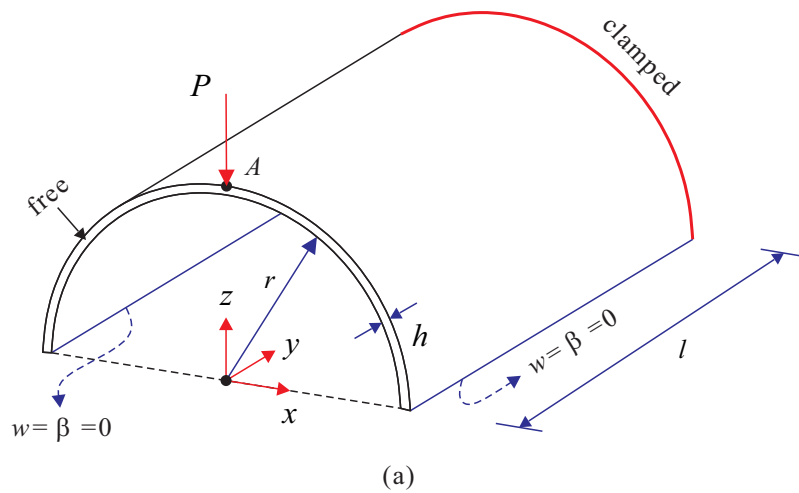


Figure 5.16. Clamped semi-cylindrical shell under point load. (a) Problem description (b) Meshes used (20×20)

A well-known benchmark problem for geometric nonlinear analysis of shells is the semi-cylindrical shell under a point load shown in **Figure 5.16(a)** [139-142]. The length and radius of the half cylinder are $l=0.3048$ and $r=1.016$, respectively, and the thickness is $h=0.03$; the material constants are $E=2.0685 \times 10^7$ and $\nu=0.3$. The load applied to the shell increases up to $P_{\max}=2000$. The structure is modeled using 20×20 and 32×32 element meshes of the MITC4 shell element and the corresponding MITC3 and MITC3+ shell element meshes, see **Figure 5.16(b)**. The reference solutions are obtained using a 64×64 element mesh of the MITC9 shell element.

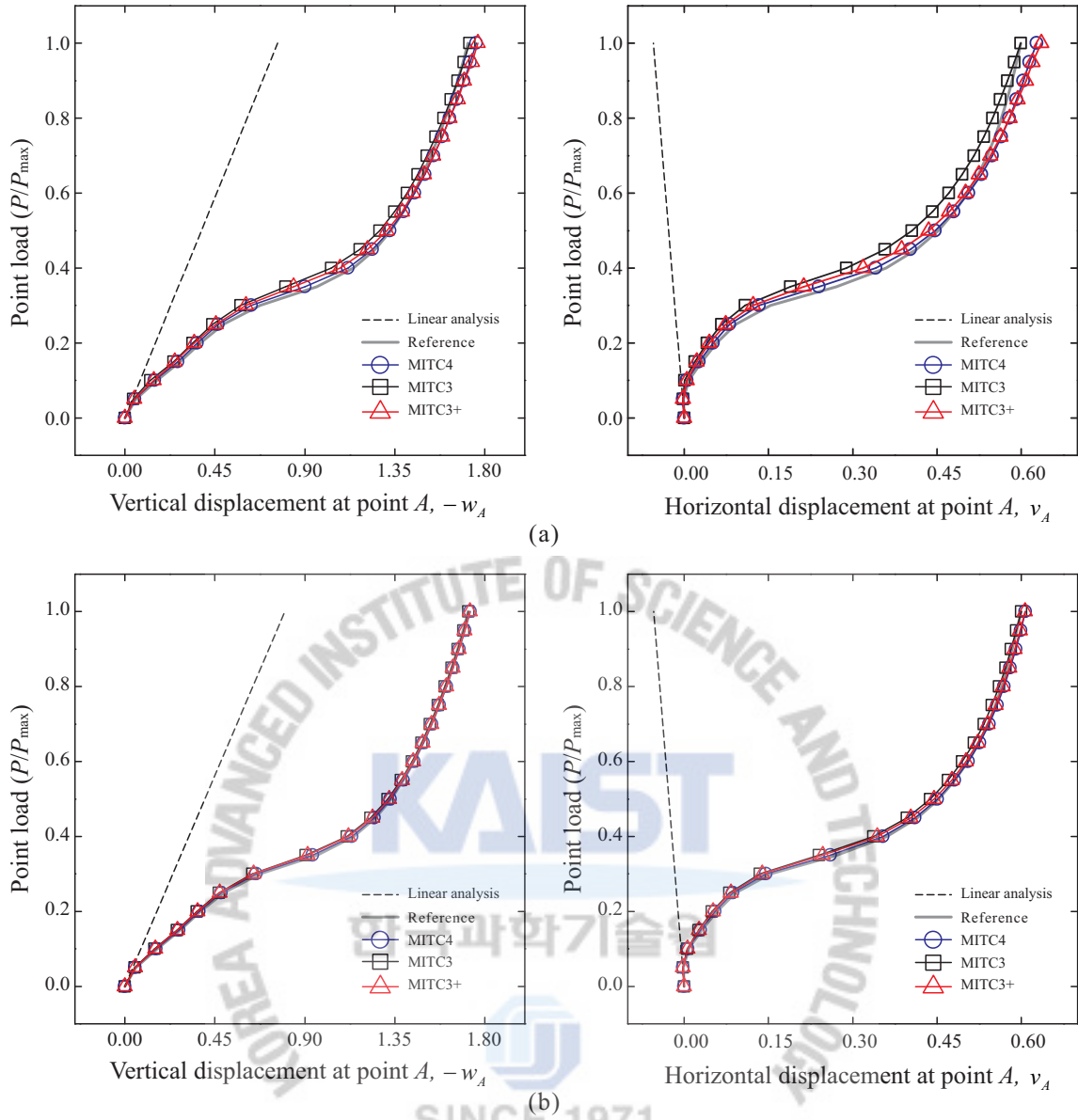


Figure 5.17. Load-displacement curves for the clamped semi-cylindrical shell under point load when (a) 20×20 and (b) 32×32 element meshes are used.

Table 5.6. Relative errors in the vertical and horizontal displacements at point A for the clamped semi-cylindrical shell under a point load. Relative error (%) = $|w^{ref} - w^h| / |w^{ref}| \times 100$ or $|v^{ref} - v^h| / |v^{ref}| \times 100$ where w^{ref} and v^{ref} denote the reference solution, and w^h and v^h are finite element solutions.

Normalized load P / P_{max}	Relative errors in the vertical displacement			Relative errors in the horizontal displacement		
	MITC4	MITC3	MITC3+	MITC4	MITC3	MITC3+
0.1	3.5799	7.4891	5.5065	18.929	36.429	24.762
0.2	1.7906	4.4274	3.8040	5.3651	14.244	11.879
0.3	2.7969	5.8230	4.7734	5.6135	12.446	9.8334

0.4	0.8735	3.0748	2.2711	1.8427	6.5769	4.6288
0.5	0.1804	1.2776	0.6989	0.4528	3.2554	1.7271
0.6	0.0692	0.6781	0.1937	0.1247	2.0033	0.6533
0.7	0.2285	0.3656	0.0718	0.5130	1.2778	0.0278
0.8	0.3556	0.1622	0.2495	0.8267	0.7577	0.4302
0.9	0.4927	0.0060	0.3845	1.0846	0.3358	0.8139
1.0	0.6232	0.1048	0.5067	1.3280	0.0417	1.1595
Average	1.0990	2.3409	1.8460	3.6080	7.7367	5.5914

w^{ref} and v^{ref} : Reference solutions calculated using the 32×32 element mesh of the MITC9 shell elements

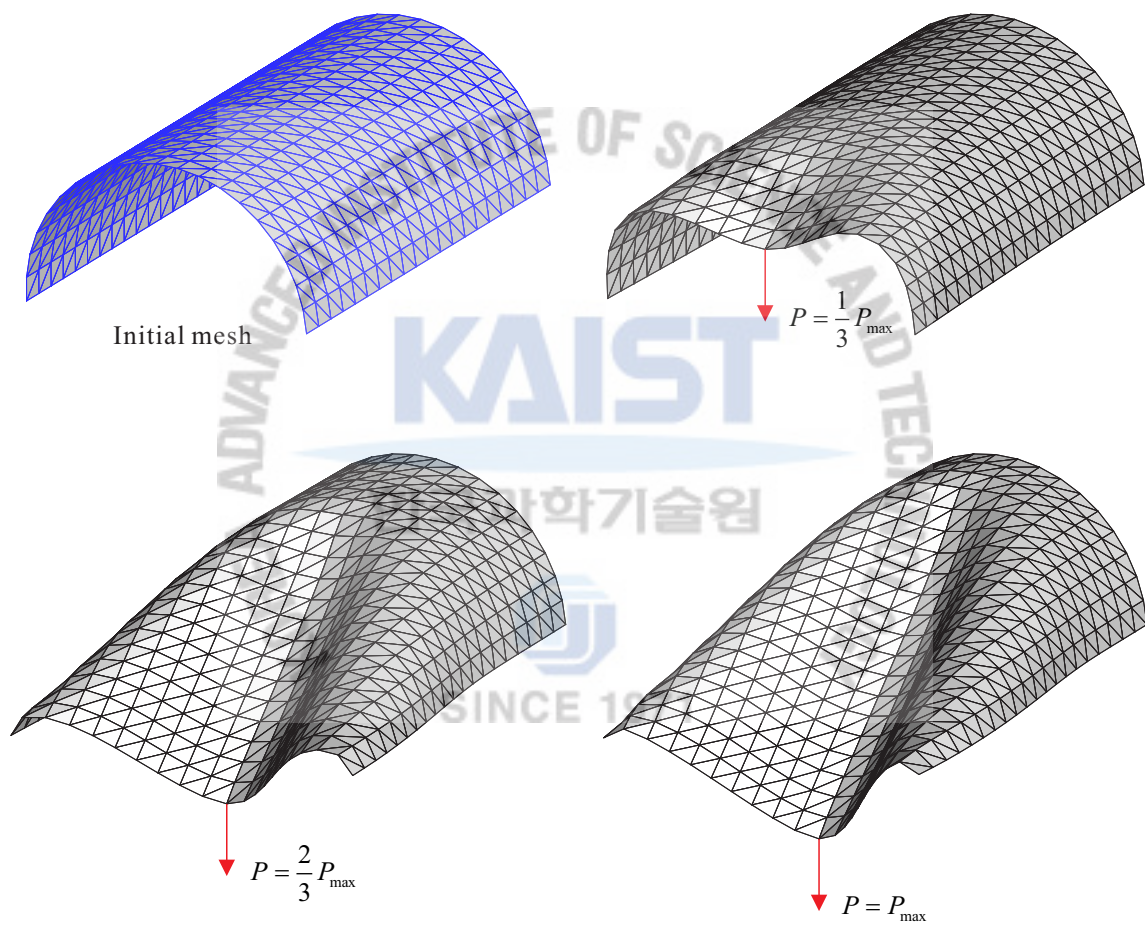


Figure 5.18. Deformed configurations of the clamped semi-cylindrical shell under point load.

Figure 5.17 and **Table 5.6** give the obtained load-displacement curves and tabulated data, respectively. **Figure 5.18** shows the deformed shapes calculated using the 20×20 element mesh of the MITC3+ shell finite elements at various load levels, $P = P_{max} / 3$, $2P_{max} / 3$, and P_{max} . The three shell elements show good performance in the solution of this shell problem with the meshes used.

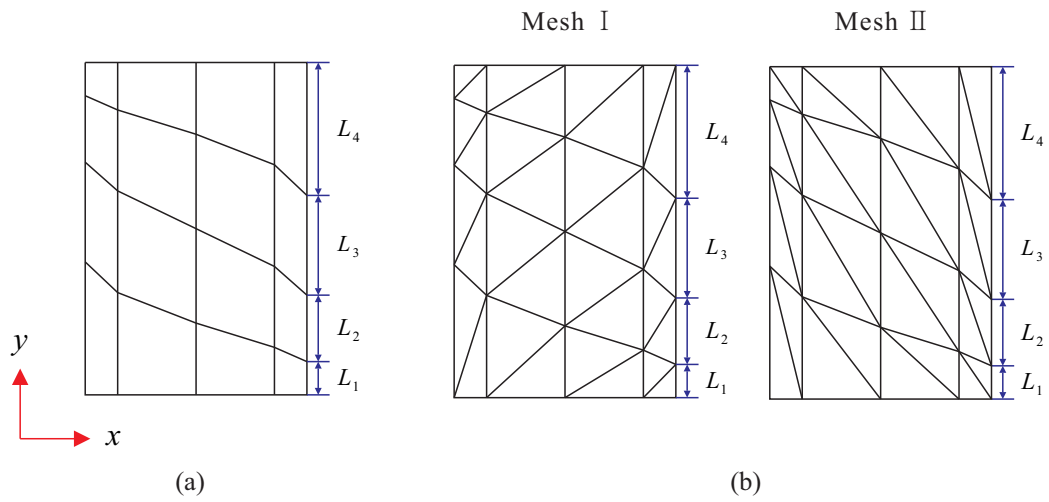
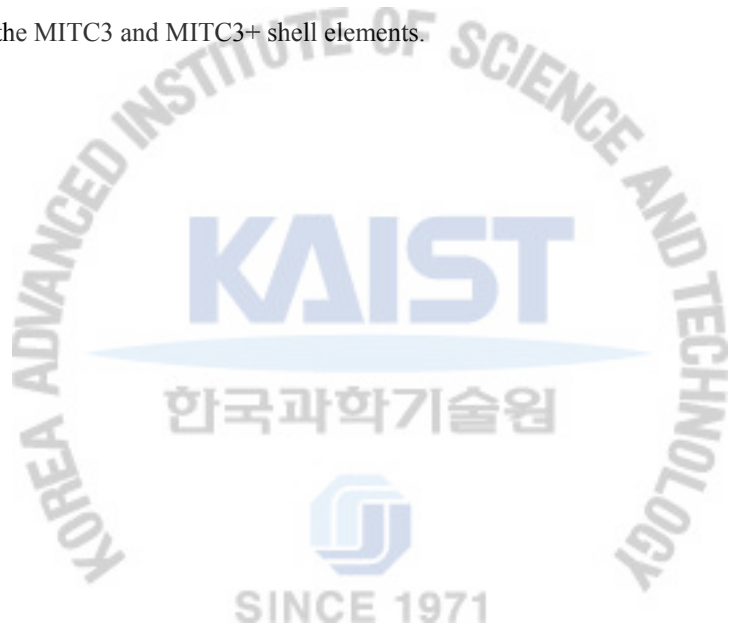


Figure 5.19. Distorted mesh patterns of the clamped semi-cylindrical shell ($N = 4$) (a) for the MITC4 shell element and (b) for the MITC3 and MITC3+ shell elements.



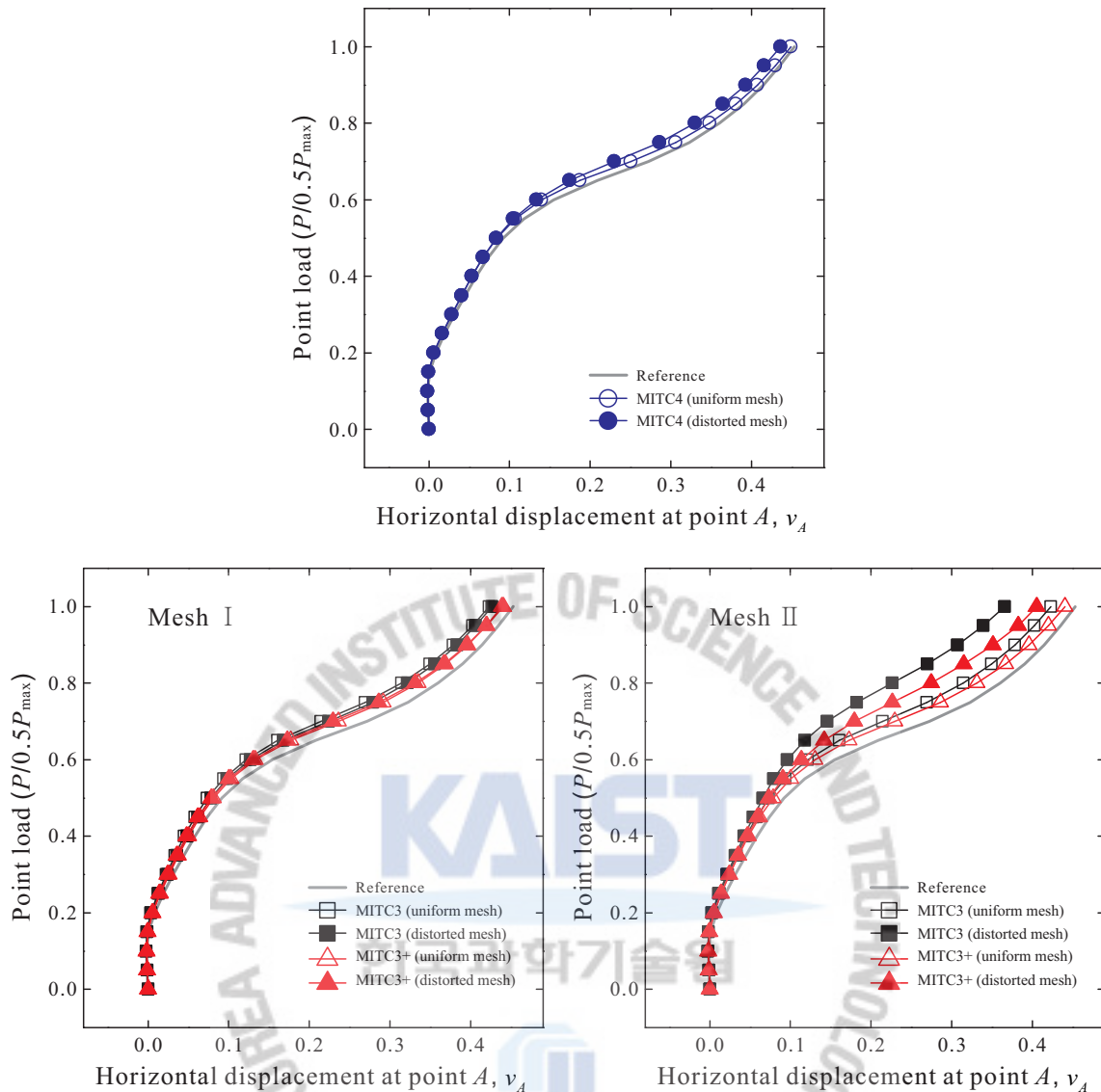


Figure 5.20. Load-displacement curves for the clamped semi-cylindrical shell with the distorted mesh patterns shown in Figure 5.19.

The analysis with the distorted mesh patterns shown in **Figure 5.19** is performed. For an $N \times N$ element mesh, each edge is discretized with the following ratio : $L_1 : L_2 : L_3 : \dots : L_N = 1 : 2 : 3 : \dots : N$. The solutions are obtained with a 24×24 element mesh of the MITC4, MITC3 and MITC3+ shell elements. **Figure 5.20** and **Table 5.6** show the calculated load-displacement curves and tabulated values when the distorted mesh patterns in **Figure 5.19** are used. The MITC3+ shell element shows a good performance regardless of which mesh pattern in **Figure 5.19(b)** is used.

5.3.6 Fully Clamped Plate under Uniform Pressure

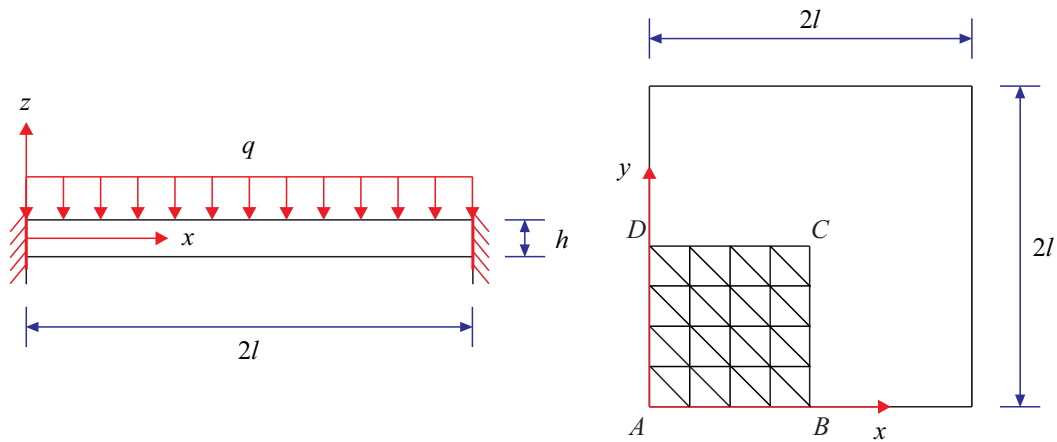


Figure 5.21. Fully clamped plate under uniform pressure and mesh used (4×4).

Figure 5.21 shows the fully clamped plate under uniform pressure [115, 120, 146, 148, 154, 155]. A square plate of dimensions $2l \times 2l$ and uniform thickness h is considered and all edges are fully clamped with the hard boundary condition [1]. Due to symmetry, only one-quarter of the plate is modeled, with the following boundary conditions: $u_x = \theta_y = 0$ along BC , $u_y = \theta_x = 0$ along DC and $u_x = u_y = \theta_x = \theta_y = 0$ along AB and AD . The material properties used are $E = 1.7472 \times 10^3$ and $\nu = 0.3$. The pressure applied to the plate increases up to $q_{\max} = h^3 \times 10^5$. The length of the plate is $l = 1$ and four different plate thicknesses ($h/L = 1/10, 1/100, 1/1,000$ and $1/10,000$) are considered. This problem is modeled using a 10×10 element mesh of the MITC4 shell element and the corresponding MITC3 and MITC3+ shell element meshes. The reference solutions are calculated using a 20×20 element mesh of the MITC9 shell element.

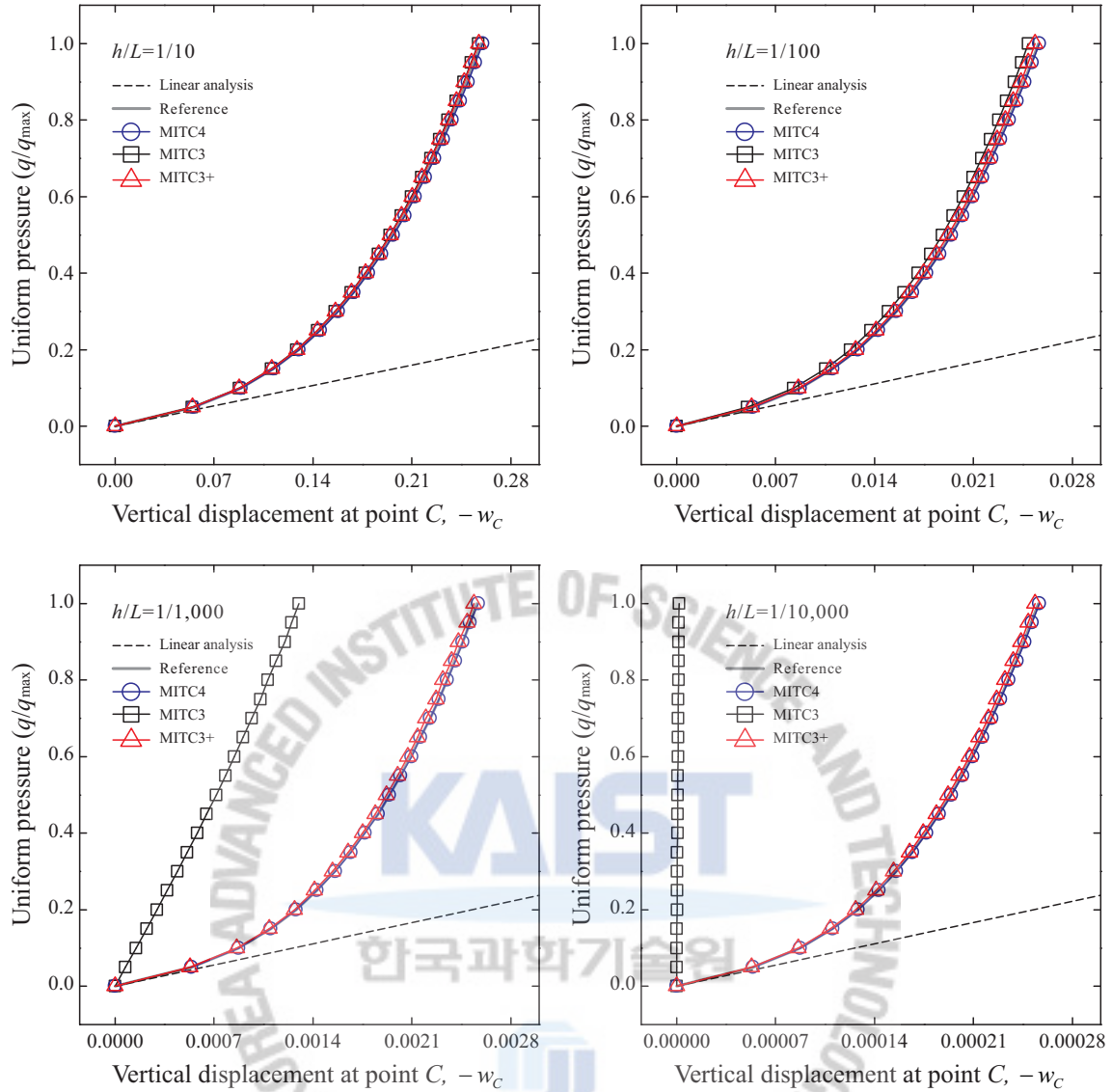


Figure 5.22. Load-displacement curves for the fully clamped plate under uniform pressure.

Table 5.7. Relative errors in the vertical displacement at point C for the fully clamped plate under uniform pressure (for the cases $h/L = 1/10$ and $h/L = 1/100$). Relative error (%) = $|w^{ref} - w^h| / |w^{ref}| \times 100$ where w^{ref} and w^h is denote the reference and finite element solutions, respectively.

Normalized load q/q_{max}	Relative errors in the vertical displacement at point C					
	$h/L = 1/10$ case			$h/L = 1/100$ case		
	MITC4	MITC3	MITC3+	MITC4	MITC3	MITC3+
0.1	0.1798	1.3936	1.1351	0.1145	5.4983	1.3746
0.2	0.2772	1.1548	0.9547	0.1561	4.1374	1.1710
0.3	0.3114	1.0424	0.8581	0.1931	3.6036	1.0940
0.4	0.3359	0.9797	0.8006	0.2266	3.3428	1.0198
0.5	0.3413	0.9372	0.7641	0.2062	3.1443	0.9794

0.6	0.3544	0.9026	0.7277	0.2391	3.0607	0.9565
0.7	0.3597	0.8792	0.7060	0.2247	2.9663	0.9438
0.8	0.3663	0.8548	0.6863	0.2130	2.9399	0.9374
0.9	0.3739	0.8362	0.6674	0.2034	2.8885	0.9357
1.0	0.3743	0.8257	0.6598	0.2344	2.8516	0.8984
Average	0.3274	0.9806	0.7960	0.2011	3.4433	1.0311

w^{ref} : Reference solutions calculated using the 10×10 element mesh of the MITC9 shell elements

Table 5.8. Relative errors in the vertical displacement at point C for the fully clamped plate under uniform pressure (for the cases $h/L = 1/1,000$ and $h/L = 1/10,000$). Relative error (%) = $\left| \frac{w^{ref} - w^h}{w^{ref}} \right| \times 100$ where w^{ref} and w^h denote the reference and finite element solutions, respectively.

Normalized load q/q_{max}	Relative errors in the vertical displacement at point C					
	$h/L = 1/1,000$ case			$h/L = 1/10,000$ case		
	MITC4	MITC3	MITC3+	MITC4	MITC3	MITC3+
0.1	0.1261	82.900	1.3179	0.1261	99.803	1.3316
0.2	0.0000	76.819	0.7813	0.2031	99.731	1.1560
0.3	0.6452	71.550	0.6452	0.2189	99.667	1.0816
0.4	0.5682	67.000	0.5682	0.2210	99.609	1.0371
0.5	0.0000	63.127	1.0309	0.2268	99.556	1.0002
0.6	0.4785	59.612	0.9569	0.2200	99.506	0.9803
0.7	0.0000	56.639	1.3453	0.2157	99.458	0.9617
0.8	0.0000	54.043	1.2766	0.2174	99.412	0.9461
0.9	0.0000	51.220	1.2195	0.2116	99.369	0.9319
1.0	0.3906	49.219	0.7813	0.2110	99.327	0.9180
Average	0.2208	63.213	0.9923	0.2071	99.544	1.0345

w^{ref} : Reference solutions calculated using the 10×10 element mesh of the MITC9 shell elements

Figure 5.22, Table 5.7 and Table 5.8 show the calculated vertical displacement at point C versus the uniform pressure. The solutions using the MITC3 shell element deteriorate as the shell thickness decreases due to shear locking. However, the MITC3+ and MITC4 shell finite elements show excellent results compared to the reference solutions.

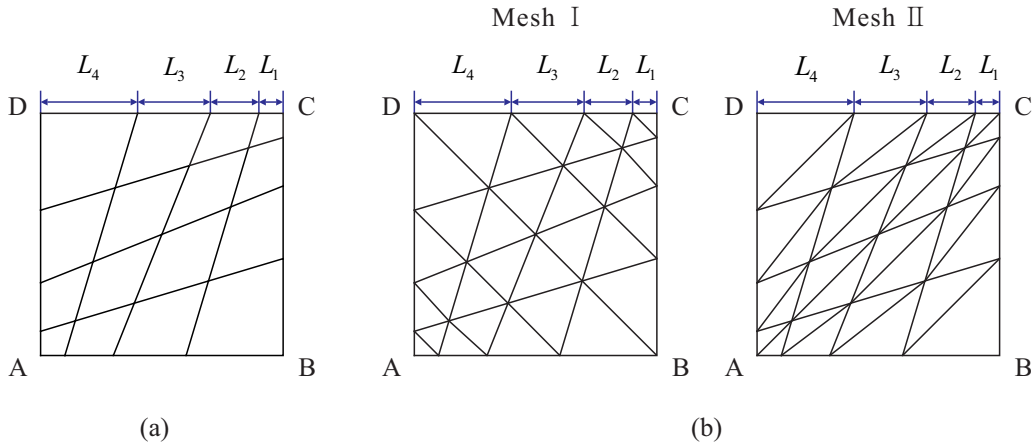


Figure 5.23. Distorted meshes of the fully clamped plate (a) for the MITC4 shell element and (b) for the MITC3 and MITC3+ shell elements.

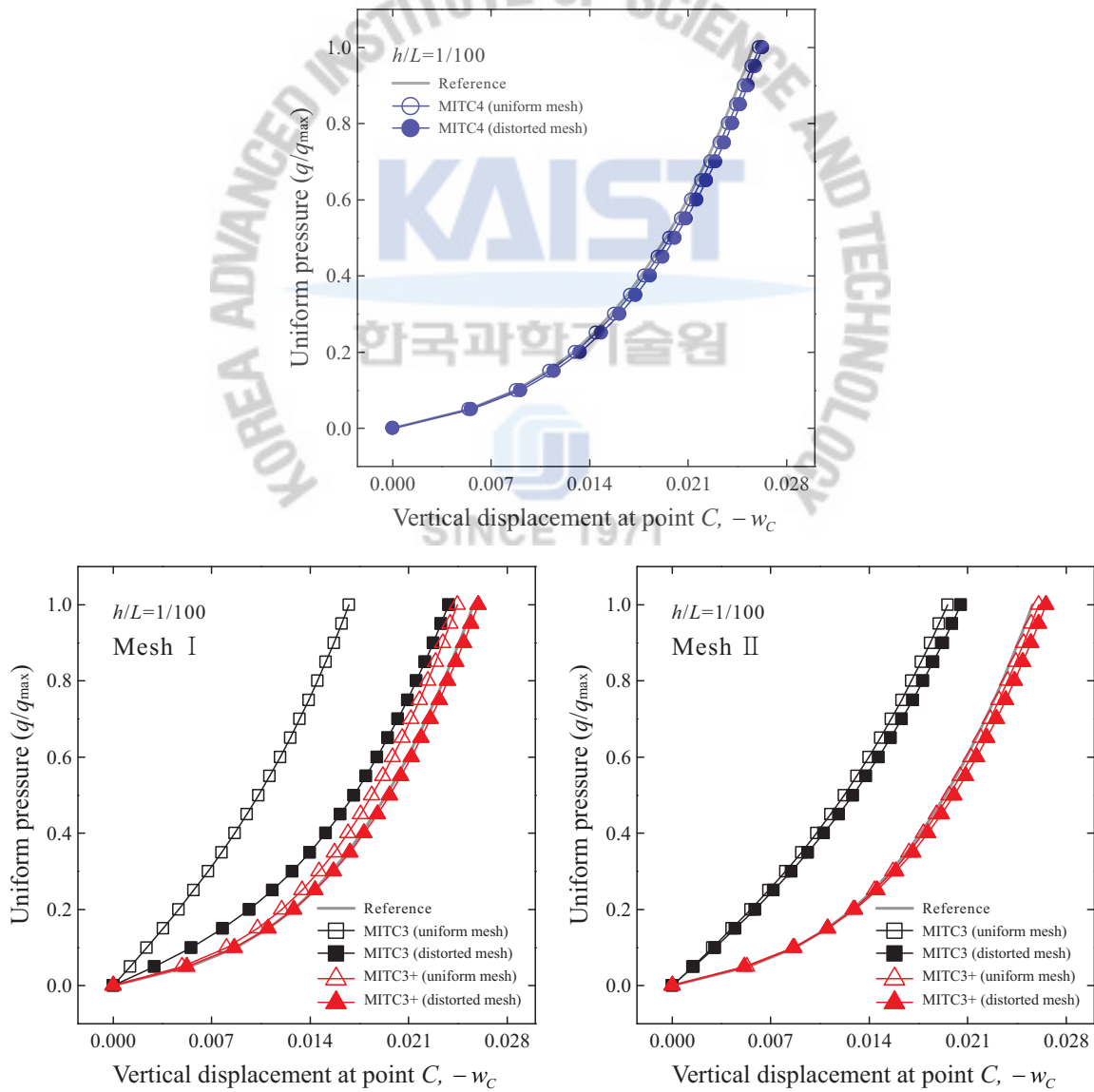


Figure 5.24. Load-displacement curves for the fully clamped plate with the distorted meshes shown in Figure 5.23.

The same problem with the distorted 4×4 element mesh shown in **Figure 5.23** is also considered when $h/L = 1/100$. In the distorted element meshes, each edge is divided by the ratio : $L_1 : L_2 : L_3 : L_4 = 1 : 2 : 3 : 4$. **Figure 5.24** shows the calculated load-displacement curves. The MITC3+ and MITC4 shell elements show an excellent performance even when the distorted meshes are used. It is also observed that, compared to the MITC3 shell element, the MITC3+ shell element gives less sensitive solutions to mesh patterns.



Chapter 6. 3-Node Triangular Shell Element with Improved Membrane Behaviors

6.1 The Enriched MITC3+ Shell Finite Element for Linear Analysis

In this section, a new triangular shell finite element with improved membrane behaviors is presented. The proposed shell element (hereafter named enriched MITC3+) is based on the MITC3+ shell element [29] which uses a cubic bubble function for the rotations and assumed shear strain to alleviate the transverse shear locking phenomenon. In order to improve membrane behaviors, the partition of unity approximation is applied into only membrane part of the MITC3+ shell element. For geometric nonlinear analysis, the total Lagrangian formulation is employed allowing for large displacements and large rotations. The enriched MITC3+ shell element passes the three basic tests (the isotropy, patch and zero energy mode tests) and shows excellent convergence behavior in several problems. The nonlinear performance of the enriched MITC3+ shell element was numerically studied by solving several benchmark tests.

6.1.1 Displacement Interpolation of the MITC3+ Shell Element

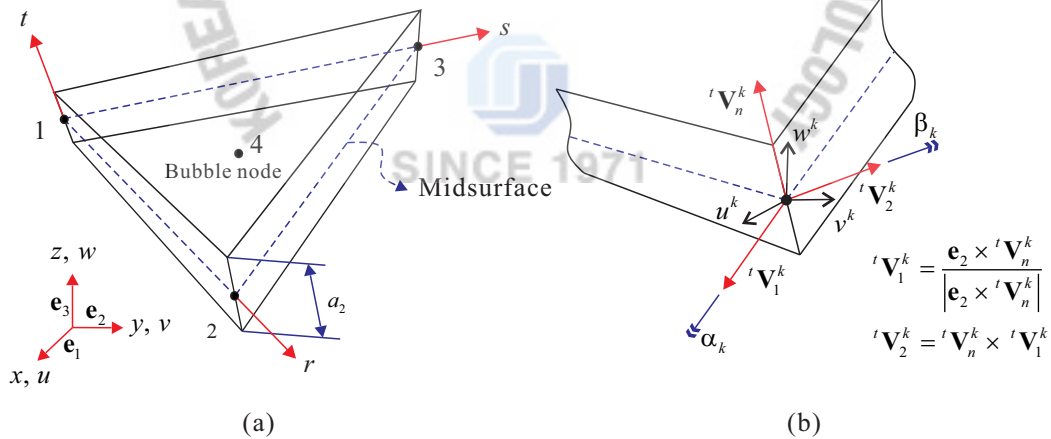


Figure 6.1. The MITC3+ shell finite element with the bubble node: (a) Geometry of the MITC3+ shell finite element. (b) Definition of rotational degrees of freedom α_k and β_k .

The geometry interpolation of the MITC3+ shell element for linear analysis, shown in Figure 6.1, is given by [29, 156]

$$\bar{\mathbf{x}}(r, s, t) = \sum_{i=1}^3 h_i(r, s) \bar{\mathbf{x}}_i + \frac{t}{2} \sum_{i=1}^4 a_i f_i(r, s) \mathbf{V}_n^i$$

$$\text{with } h_1 = 1 - r - s, \quad h_2 = r, \quad h_3 = s, \quad a_4 \mathbf{V}_n^4 = \frac{1}{3} (a_1 \mathbf{V}_n^1 + a_2 \mathbf{V}_n^2 + a_3 \mathbf{V}_n^3), \quad (6.1)$$

in which $h_i(r, s)$ is the two-dimensional interpolation function of the standard isoparametric procedure corresponding to node i , $\bar{\mathbf{x}}_i$ is the position vector of node i in the global Cartesian coordinate system, a_i and \mathbf{V}_n^i denote the shell thickness and the director vector at node i , respectively, and $f_i(r, s)$ are the two-dimensional interpolation functions that include the cubic bubble function f_4 corresponding to the internal node 4

$$f_1 = h_1 - \frac{1}{3} f_4, \quad f_2 = h_2 - \frac{1}{3} f_4, \quad f_3 = h_3 - \frac{1}{3} f_4, \quad f_4 = 27rs(1 - r - s). \quad (6.2)$$

Unlike the standard 3-node shell elements [23], the MITC3+ shell element has an internal node and the corresponding a cubic bubble function for rotations in the geometry interpolation.

From Equation (6.1), the displacement interpolation of the MITC3+ shell element is obtained by [29, 156]

$$\bar{\mathbf{u}}(r, s, t) = \sum_{i=1}^3 h_i(r, s) \bar{\mathbf{u}}_i + \frac{t}{2} \sum_{i=1}^4 a_i f_i(r, s) (-\mathbf{V}_2^i \alpha_i + \mathbf{V}_1^i \beta_i), \quad (6.3)$$

in which $\bar{\mathbf{u}}_i = [\bar{u}_i \quad \bar{v}_i \quad \bar{w}_i]^T$ is the nodal displacement vector in the global Cartesian coordinate system, \mathbf{V}_1^i and \mathbf{V}_2^i are the unit vectors orthogonal to \mathbf{V}_n^i and to each other, and α_i and β_i are the rotations of the director vector \mathbf{V}_n^i about \mathbf{V}_1^i and \mathbf{V}_2^i , respectively, at node i .

The additional internal node, with rotation degrees of freedom only, is positioned on the flat surface defined by the three corner nodes of the element. Only the bending and transverse shear strain fields are enriched by the bubble function, and the geometry of the element remains flat, as for the MITC3 element, in a large deformation analysis. Of course, static condensation can be carried out on the element level for the rotation α_4 and β_4 , and hence in practice the MITC3+ shell element is really a 3-node element with 5 degrees of freedom per node.

6.1.2 The Partition of Unity Approximation to Improve Membrane Behaviors

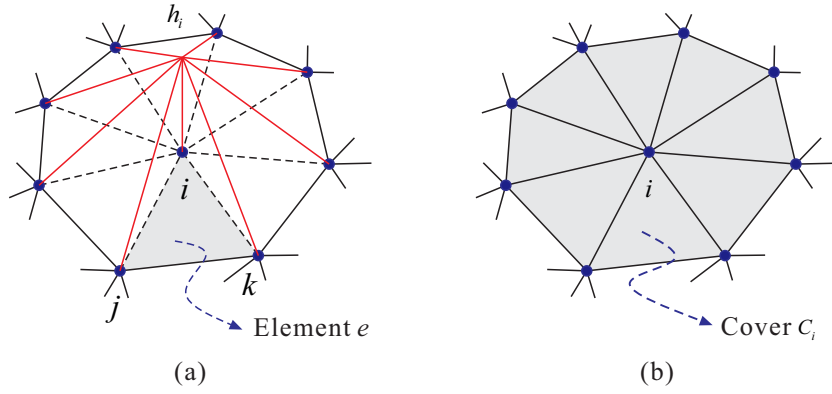


Figure 6.2. Description of sub-domain; (a) usual interpolation function, h_i and an element, e , (b) cover region, C_i constructed by all the elements connected to node i .

A partition of unity is a set of functions that, for every point in the domain under consideration, sum to unity and subordinate to each cover. The cover of a node is defined as the region around a node consisting of all the elements that share that node shown in **Figure 6.2**. The finite shape function, h_i , then form a partition of unity subordinate to the cover C_i . A partition of unity based displacement approximation applied only to only the tangential displacements associated with membrane strains of the MITC3+ shell element is given by

$$\mathbf{u} = \sum_{i=1}^3 h_i u_i^l(\mathbf{x}) + \sum_{i=1}^4 a_i f_i(-\mathbf{V}_2^i \alpha_i + \mathbf{V}_1^i \beta_i), \quad (6.4)$$

where $u_i^l(\mathbf{x})$ is not a nodal displacement vector as in the standard finite element method but a vector of nodal displacement functions (also called local approximation) defined on the cover, C_i . In the above Equation (6.4), the finite element shape functions are used as the partition of unity functions and the local approximation is constructed by polynomials. A more detailed description of the partition of unity method can be found in References [28, 33-41, 84, 92-98, 157, 158]. The local approximation on the cover C_i is constructed as

$$u_i^l(\mathbf{x}) = \begin{bmatrix} \mathbf{p}^T(\mathbf{x}) \mathbf{a}^u \\ \mathbf{p}^T(\mathbf{x}) \mathbf{a}^v \\ \bar{w}_i \end{bmatrix} = \begin{bmatrix} \sum_{k=0}^{m-1} p_{k+1} a_{ki}^u & \sum_{k=0}^{m-1} p_{k+1} a_{ki}^v & \bar{w}_i \end{bmatrix}^T, \quad (6.5)$$

in which $\mathbf{p}^T(\mathbf{x}) = [1 \ x \ y \ xy \ \dots]$ is a polynomial basis vector, m is the number of monomials in the basis, and a_{ki}^u and a_{ki}^v are the additional degrees of freedom for the cover region, \bar{w}_i is the nodal displacement corresponding to node i . In the development of the shell element, the only linear polynomial in Equation (6.5) is adopted and the local approximation can be rewritten by

$$u_i^l(\mathbf{x}) = \begin{bmatrix} a_{0i}^u + x a_{1i}^u + y a_{2i}^u \\ a_{0i}^v + x a_{1i}^v + y a_{2i}^v \\ \bar{w}_i \end{bmatrix}, \quad (6.6)$$

where a_{0i}^u to a_{2i}^u , and a_{0i}^v to a_{2i}^v are the corresponding to unknown coefficients to be determined. Enforc-

ing $u_i^l(\mathbf{x})$ to be equal to the nodal value at node i gives

$$u_i^l(x_i, y_i) = \begin{bmatrix} a_{0i}^u + x_i a_{1i}^u + y_i a_{2i}^u \\ a_{0i}^v + x_i a_{1i}^v + y_i a_{2i}^v \\ \bar{w}_i \end{bmatrix} = \begin{bmatrix} \bar{u}_i \\ \bar{v}_i \\ \bar{w}_i \end{bmatrix} \quad (6.7)$$

and therefore

$$a_{0i}^u = \bar{u}_i - x_i a_{1i}^u - y_i a_{2i}^u \quad \text{and} \quad a_{0i}^v = \bar{v}_i - x_i a_{1i}^v - y_i a_{2i}^v. \quad (6.8)$$

Substituting Equation (6.8) into Equation (6.7), the local approximation expressed as

$$u_i^l(\mathbf{x}) = \begin{bmatrix} \bar{u}_i + \xi_i \hat{u}_i^\xi + \eta_i \hat{u}_i^\eta \\ \bar{v}_i + \xi_i \hat{v}_i^\xi + \eta_i \hat{v}_i^\eta \\ \bar{w}_i \end{bmatrix} \quad (6.9)$$

$$\text{with } x - x_i = \xi_i, \quad y - y_i = \eta_i, \quad \hat{u}_i^\xi = a_{1i}^u, \quad \hat{u}_i^\eta = a_{2i}^u, \quad \hat{v}_i^\xi = a_{1i}^v \quad \text{and} \quad \hat{v}_i^\eta = a_{2i}^v. \quad (6.10)$$

Finally, substituting Equations (6.9) and (6.10) into Equation (6.4), the partition of unity based displacement approximation for the 3-node shell finite element with a cubic bubble function is given by

$$\mathbf{u}(r, s, t) = \bar{\mathbf{u}}(r, s, t) + \hat{\mathbf{u}}(r, s) \quad \text{with} \quad \hat{\mathbf{u}}(r, s) = \sum_{i=1}^3 \mathbf{H}_i(r, s) \hat{\mathbf{u}}_i, \quad (6.11)$$

in which $\hat{\mathbf{u}}_i = [\hat{u}_i^\xi \quad \hat{u}_i^\eta \quad \hat{v}_i^\xi \quad \hat{v}_i^\eta \quad 0]^T$ are unknown coefficient vector for the displacements and the \mathbf{H}_i are the linear cover interpolation matrices for the displacements

$$\mathbf{H}_i = h_i \begin{bmatrix} \xi_i & \eta_i & 0 & 0 & 0 \\ 0 & 0 & \xi_i & \eta_i & 0 \\ 0 & 0 & 0 & 0 & 0 \end{bmatrix}. \quad (6.12)$$

The partition of unity based displacement approximation in Equation (6.11) consists of two parts: the standard displacement interpolation of the MITC3+ shell element, $\bar{\mathbf{u}}$ and the additional quadratic term, $\hat{\mathbf{u}}$. Note that resulting global partition of unity approximation may be linearly dependent when both the partition of unity functions (used as the finite element shape function in this research) and the local approximation are chosen as polynomials. To avoid linear dependencies for the triangular element, we enforce not only $u_i = 0$ but also $\hat{\mathbf{u}}_i = \mathbf{0}$ when imposing the essential boundary conditions at the node i [28, 93, 98].

6.1.3 Assumed Covariant Transverse Shear Strain Fields

For linear analysis, the linear part of the Green-Lagrange strain tensor is used and its covariant strain components are

$$e_{ij} = \frac{1}{2}(\mathbf{g}_i \cdot \mathbf{u}_{,j} + \mathbf{g}_j \cdot \mathbf{u}_{,i}), \quad (6.13)$$

in which

$$\mathbf{g}_i = \frac{\partial \mathbf{x}}{\partial r_i} = \frac{\partial(\bar{\mathbf{x}} + \hat{\mathbf{x}})}{\partial r_i} = \frac{\partial \bar{\mathbf{x}}}{\partial r_i} = \bar{\mathbf{g}}_i, \quad \mathbf{u}_{,i} = \frac{\partial \mathbf{u}}{\partial r_i} = \frac{\partial(\bar{\mathbf{u}} + \hat{\mathbf{u}})}{\partial r_i} = \bar{\mathbf{u}}_{,i} + \hat{\mathbf{u}}_{,i} \quad (6.14)$$

with

$$r_1 = r, \quad r_2 = s, \quad r_3 = t. \quad (6.15)$$

Therefore, the partition of unity based covariant strain components are also divided into two parts

$$e_{ij} = \bar{e}_{ij} + \hat{e}_{ij} \quad (6.16)$$

$$\text{with } \bar{e}_{ij} = \frac{1}{2}(\bar{\mathbf{g}}_i \cdot \bar{\mathbf{u}}_{,j} + \bar{\mathbf{g}}_j \cdot \bar{\mathbf{u}}_{,i}) \quad \text{and} \quad \hat{e}_{ij} = \frac{1}{2}(\bar{\mathbf{g}}_i \cdot \hat{\mathbf{u}}_{,j} + \bar{\mathbf{g}}_j \cdot \hat{\mathbf{u}}_{,i}), \quad (6.17)$$

in which \bar{e}_{ij} and \hat{e}_{ij} correspond to the standard linear displacement interpolation and the additional quadratic term, respectively.

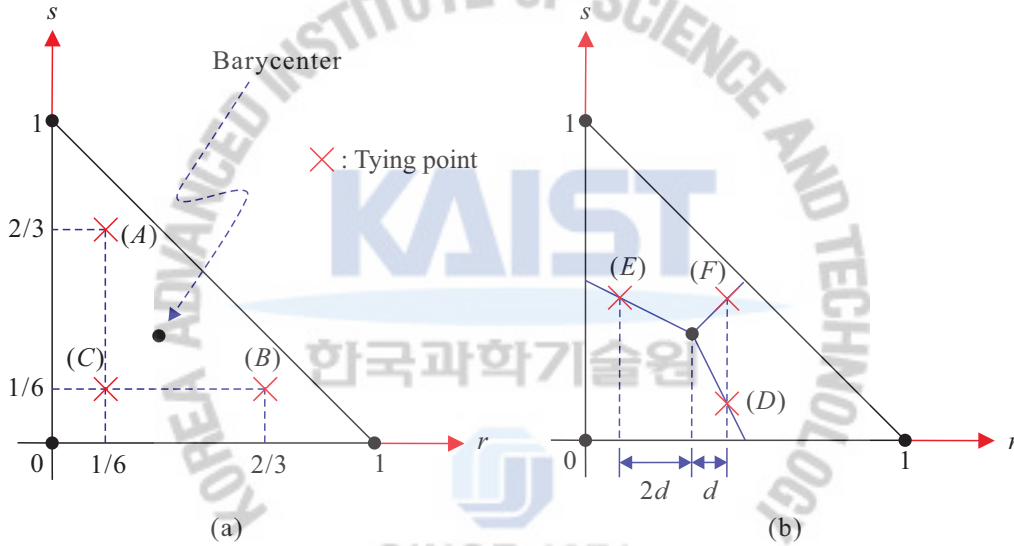


Figure 6.3. Tying points (A), (B), (C), (D), (E) and (F) for the assumed transverse shear strains of the MITC3+ shell finite element.

To reduce the locking phenomenon, the MITC (Mixed Interpolation of Tensorial Components) method is used. Since the 3-node triangular shell element is always flat, present shell element is free from the membrane locking and thus the covariant in-plane strain components are directly calculated using Equations (6.16) and (6.17). However, the covariant transverse shear strain fields are established using the MITC scheme to alleviate transverse shear locking. The assumed transverse shear strain field used for the MITC3+ shell element [29, 156] is directly used because additional unknown coefficients $\hat{\mathbf{u}}$ are not involved in determining the transverse shear strain fields. Therefore, the assumed transverse shear strain fields of the enriched MITC3+ shell element are given by

$$e_{rt}^{AS} = \frac{2}{3}(\bar{e}_{rt}^{(B)} - \frac{1}{2}\bar{e}_{st}^{(B)}) + \frac{1}{3}(\bar{e}_{rt}^{(C)} + \bar{e}_{st}^{(C)}) + \frac{1}{3}\hat{c}(3s-1), \quad (6.18)$$

$$e_{st}^{AS} = \frac{2}{3}(\bar{e}_{st}^{(A)} - \frac{1}{2}\bar{e}_{rt}^{(A)}) + \frac{1}{3}(\bar{e}_{rt}^{(C)} + \bar{e}_{st}^{(C)}) + \frac{1}{3}\hat{c}(1-3r), \quad (6.19)$$

where $\hat{c} = \bar{e}_{rt}^{(F)} - \bar{e}_{rt}^{(D)} - \bar{e}_{st}^{(F)} + \bar{e}_{st}^{(E)}$ and the tying positions (A), (B), (C), (D), (E), and (F) are presented in **Figure 6.3** and **Table 6**. As suggested [29, 156], $d = 1/10,000$ is used. If $d = 0.0$ is used, there is one spurious zero eigenvalue for a single element, which however disappears as soon as two elements are used in the mesh. This shell element is referred to as the enriched MITC3+ shell element hereafter. The enriched MITC3+ shell element is based on the ‘basic mathematical shell model’ [100, 103, 105] and the MITC scheme. The enriched MITC3+ shell element passes the basic numerical tests, namely, the isotropy, zero energy mode, and patch tests.

Table 6.1. Tying positions for the assumed transverse shear strain of the enriched MITC3+ shell element. The distance d defined in Figure 6.3(b), and $d = 1/10,000$ is used [29, 156].

	Tying position	r	s
Figure 6.3(a)	(A)	1/6	2/3
	(B)	2/3	1/6
	(C)	1/6	1/6
Figure 6.3(b)	(D)	$1/3 + d$	$1/3 - 2d$
	(E)	$1/3 - 2d$	$1/3 + d$
	(F)	$1/3 + d$	$1/3 + d$

6.2 The Enriched MITC3+ Shell Element for Geometric Nonlinear Analysis

In this section, the geometric nonlinear formulation of the enriched MITC3+ shell element is presented. The total Lagrangian formulation is employed allowing for large displacements and large rotations. In the formulation, a superscript (and subscript) τ is used to denote “time” for general analysis, with in static solutions “time” simply denoting the load step and configuration [1, 42].

The large displacement kinematics and the interpolation of the Green-Lagrange strain components are discussed. With the given expressions, the general incremental equations used in the total Lagrangian formulation are presented.

6.2.1 Large Displacement Kinematics

The geometry of the enriched MITC3+ shell finite element in the configuration at time τ is interpolated with

$${}^\tau \mathbf{x}(r, s, t) = {}^\tau \bar{\mathbf{x}}(r, s, t) + {}^\tau \hat{\mathbf{x}}(r, s) \quad (6.20)$$

with

$${}^\tau \bar{\mathbf{x}}(r, s, t) = \sum_{i=1}^3 h_i(r, s) {}^\tau \bar{\mathbf{x}}_i + \frac{t}{2} \sum_{i=1}^4 a_i f_i(r, s) {}^\tau \mathbf{V}_n^i \quad (6.21)$$

$$\text{and } {}^\tau \hat{\mathbf{x}}(r, s) = \sum_{i=1}^3 \mathbf{H}_i(r, s) {}^\tau \hat{\mathbf{x}}_i \quad (6.22)$$

in which ${}^\tau \mathbf{x}_i = [{}^\tau x_i \quad {}^\tau y_i \quad {}^\tau z_i]^\top$ is the position vector of node i in the configuration at time τ , ${}^\tau \mathbf{V}_n^i = [{}^\tau V_{nx}^i \quad {}^\tau V_{ny}^i \quad {}^\tau V_{nz}^i]^\top$ denotes the director vector at node i in the configuration at time τ , and ${}^\tau \hat{\mathbf{x}}_i = [{}^\tau \hat{x}_i^\xi \quad {}^\tau \hat{x}_i^\eta \quad {}^\tau \hat{y}_i^\xi \quad {}^\tau \hat{y}_i^\eta \quad 0]^\top$ are coefficient vectors for the positions in the configuration at time τ .

The incremental partition of unity displacements from the configuration at time τ to the configuration at time $\tau + \Delta\tau$ are

$$\mathbf{u}(r, s, t) = {}^{\tau+\Delta\tau} \mathbf{x}(r, s, t) - {}^\tau \mathbf{x}(r, s, t), \quad (6.23)$$

and, using Equation (6.20), the Equation (6.23) can be written as

$$\mathbf{u}(r, s, t) = \bar{\mathbf{u}}(r, s, t) + \hat{\mathbf{u}}(r, s) \quad (6.24)$$

$$\mathbf{u}(r, s, t) = \sum_{i=1}^3 h_i(r, s) \mathbf{u}_i + \frac{t}{2} \sum_{i=1}^4 a_i f_i(r, s) ({}^{\tau+\Delta\tau} \mathbf{V}_n^i - {}^\tau \mathbf{V}_n^i), \quad (6.25)$$

where \mathbf{u}_i is the vector of incremental nodal displacements based on the partition of unity. Using Equation (6.20), Equation (6.23) can be rewritten as

$$\mathbf{u}(r, s, t) = \bar{\mathbf{u}}(r, s, t) + \hat{\mathbf{u}}(r, s) \quad (6.26)$$

with

$$\bar{\mathbf{u}}(r, s, t) = \sum_{i=1}^3 h_i(r, s) \bar{\mathbf{u}}_i + \frac{t}{2} \sum_{i=1}^4 a_i f_i(r, s) ({}^{\tau+\Delta\tau} \mathbf{V}_n^i - {}^\tau \mathbf{V}_n^i), \quad (6.27)$$

$$\hat{\mathbf{u}}(r, s) = \sum_{i=1}^3 \mathbf{H}_i \hat{\mathbf{u}}_i, \quad (6.28)$$

where $\bar{\mathbf{u}}_i = [\bar{u}_i \quad \bar{v}_i \quad \bar{w}_i]^\top$ and $\hat{\mathbf{u}}_i = [\hat{u}_i^\xi \quad \hat{u}_i^\eta \quad \hat{v}_i^\xi \quad \hat{v}_i^\eta \quad 0]^\top$ are the vector of incremental nodal displacements and the vector of incremental unknown coefficients at node i from time τ to time $\tau + \Delta\tau$, respectively. Note that $\bar{\mathbf{u}}(r, s, t)$ and $\hat{\mathbf{u}}(r, s)$ are the displacement and unknown coefficient vector in the linear formulation, see Equation (6.11), but here it is the vector of incremental displacements and unknown coefficients, respectively.

The director vector at time $\tau + \Delta\tau$ at node i is obtained from the director vector at time τ

$${}^{\tau+\Delta\tau} \mathbf{V}_n^i = {}^{\tau+\Delta\tau} \mathbf{Q}^i {}^\tau \mathbf{V}_n^i, \quad (6.29)$$

in which ${}^{\tau+\Delta\tau} \mathbf{Q}^i$ is the rotation matrix which rotates the director vector at node i from the configuration at time τ to the configuration at time $\tau + \Delta\tau$. Additionally, the two unit vectors ${}^\tau \mathbf{V}_1^i$ and ${}^\tau \mathbf{V}_2^i$ are obtained by (see **Figure 6.1(b)**),

$${}^\tau \mathbf{V}_1^i = \frac{\mathbf{e}_2 \times {}^\tau \mathbf{V}_n^i}{|\mathbf{e}_2 \times {}^\tau \mathbf{V}_n^i|}, \quad {}^\tau \mathbf{V}_2^i = {}^\tau \mathbf{V}_n^i \times {}^\tau \mathbf{V}_1^i. \quad (6.30)$$

For the vector-like parameterization of finite rotations [1, 144, 159, 160], see Appendix A, the well-known formula is employed as follow

$${}^{\tau+\Delta\tau} \mathbf{Q}^i = \mathbf{I}_3 + \frac{\sin({}^{\tau+\Delta\tau} \theta^i)}{{}^{\tau+\Delta\tau} \theta^i} {}^{\tau+\Delta\tau} \boldsymbol{\Theta}^i + \frac{1}{2} \left[\frac{\sin({}^{\tau+\Delta\tau} \theta^i / 2)}{{}^{\tau+\Delta\tau} \theta^i / 2} \right]^2 ({}^{\tau+\Delta\tau} \boldsymbol{\Theta}^i)^2 \quad (6.31)$$

with

$${}^{\tau+\Delta\tau} \boldsymbol{\Theta}^i = \begin{bmatrix} 0 & -{}^{\tau+\Delta\tau} \theta_3^i & {}^{\tau+\Delta\tau} \theta_2^i \\ {}^{\tau+\Delta\tau} \theta_3^i & 0 & -{}^{\tau+\Delta\tau} \theta_1^i \\ -{}^{\tau+\Delta\tau} \theta_2^i & {}^{\tau+\Delta\tau} \theta_1^i & 0 \end{bmatrix}, \quad (6.32)$$

$${}^{\tau+\Delta\tau} \theta^i = \alpha_i {}^\tau \mathbf{V}_1^i + \beta_i {}^\tau \mathbf{V}_2^i, \quad (6.33)$$

in which \mathbf{I}_3 is the 3×3 identity matrix, ${}^{\tau+\Delta\tau} \boldsymbol{\Theta}^i$ is the skew-symmetric matrix operator (also called spin tensor), ${}^{\tau+\Delta\tau} \boldsymbol{\Theta}^i = [{}^{\tau+\Delta\tau} \theta_1^i \quad {}^{\tau+\Delta\tau} \theta_2^i \quad {}^{\tau+\Delta\tau} \theta_3^i]^T$, and ${}^{\tau+\Delta\tau} \theta^i = \sqrt{({}^{\tau+\Delta\tau} \theta_1^i)^2 + ({}^{\tau+\Delta\tau} \theta_2^i)^2 + ({}^{\tau+\Delta\tau} \theta_3^i)^2}$.

Using a Taylor series expansion, the finite rotation tensor ${}^{\tau+\Delta\tau} \mathbf{Q}^i$ can be represented by

$${}^{\tau+\Delta\tau} \mathbf{Q}^i = \mathbf{I}_3 + {}^{\tau+\Delta\tau} \boldsymbol{\Theta}^i + \frac{1}{2!} ({}^{\tau+\Delta\tau} \boldsymbol{\Theta}^i)^2 + \frac{1}{3!} ({}^{\tau+\Delta\tau} \boldsymbol{\Theta}^i)^3 + \dots \quad (6.34)$$

Using only the terms up to quadratic order in Equation (6.34), the following equation is obtained

$${}^{\tau+\Delta\tau} \mathbf{V}_n^i - {}^\tau \mathbf{V}_n^i = {}^{\tau+\Delta\tau} \boldsymbol{\Theta}^i \times {}^\tau \mathbf{V}_n^i + \frac{1}{2} {}^{\tau+\Delta\tau} \boldsymbol{\Theta}^i \times ({}^{\tau+\Delta\tau} \boldsymbol{\Theta}^i \times {}^\tau \mathbf{V}_n^i), \quad (6.35)$$

and using Equation (6.33) in Equation (6.35), we obtain for a ‘consistent linearization’ of the element displacements [1]

$${}^{\tau+\Delta\tau} \mathbf{V}_n^i - {}^\tau \mathbf{V}_n^i = -\alpha_i {}^\tau \mathbf{V}_2^i + \beta_i {}^\tau \mathbf{V}_1^i - \frac{1}{2} (\alpha_i^2 + \beta_i^2) {}^\tau \mathbf{V}_n^i. \quad (6.36)$$

Substituting Equation (6.36) into Equation (6.27), the vector of incremental displacements including second-order rotation effects is

$$\bar{\mathbf{u}}(r, s, t) = \sum_{i=1}^3 h_i(r, s) \bar{\mathbf{u}}_i + \frac{t}{2} \sum_{i=1}^4 a_i f_i(r, s) \left[-\alpha_i {}^\tau \mathbf{V}_2^i + \beta_i {}^\tau \mathbf{V}_1^i - \frac{1}{2} (\alpha_i^2 + \beta_i^2) {}^\tau \mathbf{V}_n^i \right], \quad (6.37)$$

in which α_i and β_i are the incremental rotations of the director vector ${}^\tau \mathbf{V}_n^i$ about ${}^\tau \mathbf{V}_1^i$ and ${}^\tau \mathbf{V}_2^i$, respectively, at node i .

Note that the incremental displacements of Equation (6.37) consists of two parts, the linear part $\bar{\mathbf{u}}$, and the quadratic part $\bar{\mathbf{u}}_q$, hence

$$\bar{\mathbf{u}}(r, s, t) = \bar{\mathbf{u}}_l(r, s, t) + \bar{\mathbf{u}}_q(r, s, t) \quad (6.38)$$

with

$$\bar{\mathbf{u}}_l(r, s, t) = \sum_{i=1}^3 h_i(r, s) \bar{\mathbf{u}}_i + \frac{t}{2} \sum_{i=1}^4 a_i f_i(r, s) (-\alpha_i {}^\tau \mathbf{V}_2^i + \beta_i {}^\tau \mathbf{V}_1^i), \quad (6.39)$$

$$\bar{\mathbf{u}}_q(r, s, t) = -\frac{t}{4} \sum_{i=1}^4 a_i f_i(r, s) [(\alpha_i^2 + \beta_i^2) {}^\tau \mathbf{V}_n^i]. \quad (6.40)$$

6.2.2 Green-Lagrange Strain and Its Interpolation

The covariant components of the Green-Lagrange strain tensor in the configuration at time τ , referred to the configuration at time 0 (also called reference configuration), are defined by [1]

$${}^\tau \varepsilon_{ij} = \frac{1}{2} ({}^\tau \mathbf{g}_i \cdot {}^\tau \mathbf{g}_j - {}^0 \mathbf{g}_i \cdot {}^0 \mathbf{g}_j) \quad (6.41)$$

with

$${}^0 \mathbf{g}_i = \frac{\partial({}^0 \bar{\mathbf{x}} + {}^0 \hat{\mathbf{x}})}{\partial r_i} = \frac{\partial {}^0 \bar{\mathbf{x}}}{\partial r_i}, \quad {}^\tau \mathbf{g}_i = \frac{\partial({}^\tau \bar{\mathbf{x}} + {}^\tau \hat{\mathbf{x}})}{\partial r_i} = {}^0 \mathbf{g}_i + {}^\tau \bar{\mathbf{u}}_{,i} + {}^\tau \hat{\mathbf{u}}_{,i}, \quad (6.42)$$

in which

$${}^\tau \bar{\mathbf{u}}_{,i} = \frac{\partial {}^\tau \bar{\mathbf{u}}}{\partial r_i}, \quad {}^\tau \hat{\mathbf{u}}_{,i} = \frac{\partial {}^\tau \hat{\mathbf{u}}}{\partial r_i}, \quad {}^\tau \bar{\mathbf{u}} = {}^\tau \bar{\mathbf{x}} - {}^0 \bar{\mathbf{x}}, \quad {}^\tau \hat{\mathbf{u}} = {}^\tau \hat{\mathbf{x}}, \quad r_1 = r, \quad r_2 = s, \quad r_3 = t. \quad (6.43)$$

Hence the incremental covariant strains based on the partition of unity approximation are

$${}^0 \varepsilon_{ij} = {}^{\tau+\Delta\tau} \varepsilon_{ij} - {}^\tau \varepsilon_{ij} = \frac{1}{2} (\mathbf{u}_{,i} \cdot {}^\tau \mathbf{g}_j + {}^\tau \mathbf{g}_i \cdot \mathbf{u}_{,j} + \mathbf{u}_{,i} \cdot \mathbf{u}_{,j}) \quad \text{with} \quad \mathbf{u}_{,i} = \frac{\partial(\bar{\mathbf{u}} + \hat{\mathbf{u}})}{\partial r_i}. \quad (6.44)$$

Using Equations (6.41)-(6.43) in Equation (6.44), these covariant strains are approximated as

$${}^0 \varepsilon_{ij} = {}^0 e_{ij} + {}^0 \eta_{ij}, \quad (6.45)$$

where ${}^0 e_{ij}$ and ${}^0 \eta_{ij}$ are the linear and nonlinear parts, respectively,

$${}^0 e_{ij} = \frac{1}{2} \left(\frac{\partial(\bar{\mathbf{u}}_l + \hat{\mathbf{u}})}{\partial r_i} \cdot ({}^t \bar{\mathbf{g}}_j + {}^t \hat{\mathbf{g}}_j) + ({}^t \bar{\mathbf{g}}_i + {}^t \hat{\mathbf{g}}_i) \cdot \frac{\partial(\bar{\mathbf{u}}_l + \hat{\mathbf{u}})}{\partial r_j} \right) = \mathbf{B}_{ij} \mathbf{U}, \quad (6.46)$$

$${}^0 \eta_{ij} = \frac{1}{2} \left(\frac{\partial(\bar{\mathbf{u}}_l + \hat{\mathbf{u}})}{\partial r_i} \cdot \frac{\partial(\bar{\mathbf{u}}_l + \hat{\mathbf{u}})}{\partial r_j} \right) + \frac{1}{2} \left(\frac{\partial \bar{\mathbf{u}}_q}{\partial r_i} \cdot ({}^t \bar{\mathbf{g}}_j + {}^t \hat{\mathbf{g}}_j) + ({}^t \bar{\mathbf{g}}_i + {}^t \hat{\mathbf{g}}_i) \cdot \frac{\partial \bar{\mathbf{u}}_q}{\partial r_j} \right) = \frac{1}{2} \mathbf{U}^T \mathbf{N}_{ij} \mathbf{U}, \quad (6.47)$$

in which \mathbf{B}_{ij} and \mathbf{N}_{ij} are the strain-displacement matrices and \mathbf{U} is the vector of incremental nodal displacements $\bar{\mathbf{u}}_i$, α_i and β_i , and incremental unknown coefficient vector $\hat{\mathbf{u}}_i$ for all element nodes. In addition, the strain variations are

$$\delta {}^0 e_{ij} = \mathbf{B}_{ij} \delta \mathbf{U}, \quad \delta {}^0 \eta_{ij} = \delta \mathbf{U}^T \mathbf{N}_{ij} \mathbf{U}. \quad (6.48)$$

Note that Equations (6.45)-(6.48) contain all the strain terms to have a consistent linearization in the establishment of the tangent stiffness matrix.

To alleviate shear locking, the MITC scheme used in the linear formulation of the enriched MITC3+ shell element is also employed for the incremental covariant transverse shear strains in the nonlinear formulation. The additional coefficient vector $\hat{\mathbf{u}}$ are not used in determining the transverse shear strain fields, as mentioned in section 6.1.3, the incremental covariant Green-Lagrange strain for assumed transverse shear strain field can be rewritten as

$${}_0\tilde{\boldsymbol{\varepsilon}}_{ij} = {}_0\tilde{\boldsymbol{\varepsilon}}_{ij} + {}_0\tilde{\boldsymbol{\eta}}_{ij} \quad (6.49)$$

with

$${}_0\tilde{\boldsymbol{\varepsilon}}_{ij} = \frac{1}{2} \left(\frac{\partial \bar{\mathbf{u}}_l}{\partial r_i} \cdot ({}^t\bar{\mathbf{g}}_j + {}^t\hat{\mathbf{g}}_j) + ({}^t\bar{\mathbf{g}}_i + {}^t\hat{\mathbf{g}}_i) \cdot \frac{\partial \bar{\mathbf{u}}_l}{\partial r_j} \right), \quad (6.50)$$

$${}_0\tilde{\boldsymbol{\eta}}_{ij} = \frac{1}{2} \left(\frac{\partial \bar{\mathbf{u}}_l}{\partial r_i} \cdot \frac{\partial \bar{\mathbf{u}}_l}{\partial r_j} \right) + \frac{1}{2} \left(\frac{\partial \bar{\mathbf{u}}_q}{\partial r_i} \cdot ({}^t\bar{\mathbf{g}}_j + {}^t\hat{\mathbf{g}}_j) + ({}^t\bar{\mathbf{g}}_i + {}^t\hat{\mathbf{g}}_i) \cdot \frac{\partial \bar{\mathbf{u}}_q}{\partial r_j} \right). \quad (6.51)$$

Therefore, the covariant transverse shear strains in Equations (6.49)-(6.51) are substituted by

$${}_0\boldsymbol{\varepsilon}_{r\xi}^{AS} = \frac{2}{3} ({}_0\tilde{\boldsymbol{\varepsilon}}_{r\xi}^{(B)} - \frac{1}{2} {}_0\tilde{\boldsymbol{\varepsilon}}_{s\xi}^{(B)}) + \frac{1}{3} ({}_0\tilde{\boldsymbol{\varepsilon}}_{r\xi}^{(C)} + {}_0\tilde{\boldsymbol{\varepsilon}}_{s\xi}^{(C)}) + \frac{1}{3} {}_0\hat{c}(3s-1), \quad (6.52)$$

$${}_0\boldsymbol{\varepsilon}_{st}^{AS} = \frac{2}{3} ({}_0\tilde{\boldsymbol{\varepsilon}}_{st}^{(A)} - \frac{1}{2} {}_0\tilde{\boldsymbol{\varepsilon}}_{rt}^{(A)}) + \frac{1}{3} ({}_0\tilde{\boldsymbol{\varepsilon}}_{rt}^{(C)} + {}_0\tilde{\boldsymbol{\varepsilon}}_{st}^{(C)}) + \frac{1}{3} {}_0\hat{c}(1-3r), \quad (6.53)$$

$${}_0\boldsymbol{\varepsilon}_{jt}^{AS} = {}_0\mathbf{e}_{jt}^{AS} + {}_0\boldsymbol{\eta}_{jt}^{AS}, \quad {}_0\mathbf{e}_{jt}^{AS} = \mathbf{B}_{jt}^{AS} \mathbf{U}, \quad {}_0\boldsymbol{\eta}_{jt}^{AS} = \frac{1}{2} \mathbf{U}^T \mathbf{N}_{jt}^{AS} \mathbf{U} \quad \text{with } j = r, s \quad (6.54)$$

in which ${}_0\hat{c} = {}_0\tilde{\boldsymbol{\varepsilon}}_{rt}^{(F)} - {}_0\tilde{\boldsymbol{\varepsilon}}_{rt}^{(D)} - {}_0\tilde{\boldsymbol{\varepsilon}}_{st}^{(F)} + {}_0\tilde{\boldsymbol{\varepsilon}}_{st}^{(E)}$, \mathbf{B}_{jt}^{AS} and \mathbf{N}_{jt}^{AS} are the strain-displacement matrices for the assumed covariant transverse shear strains. Of course, the tying positions defined in **Figure 6.3** and **Table 6**. are used.

6.2.3 Total Lagrangian Formulation and Incremental Equilibrium Equation

The nonlinear response is calculated using an incremental formulation, in which the configuration is sought for time (load step) $\tau + \Delta\tau$, when the configuration for time τ is known. Applying the principle of virtual work to the configuration at time $\tau + \Delta\tau$, the following equilibrium equation is obtained [1, 18]

$$\int_{{}^0V} {}^{\tau+\Delta\tau} S^{ij} \delta {}^{\tau+\Delta\tau} \varepsilon_{ij} d^0V = {}^{\tau+\Delta\tau} \mathfrak{R}, \quad (6.55)$$

where 0V is the initial volume, ${}^{\tau+\Delta\tau} S^{ij}$ and ${}^{\tau+\Delta\tau} \varepsilon_{ij}$ are the contravariant components of the second Piola-Kirchhoff stress tensor and the covariant components of the Green-Lagrange strain tensor, respectively, at time $\tau + \Delta\tau$, referred to the configuration at time 0, and ${}^{\tau+\Delta\tau} \mathfrak{R}$ is the external virtual work due to the applied surface and body forces.

The stress and strain tensors are incrementally decomposed as follows

$${}^{\tau+\Delta\tau} S^{ij} = {}^{\tau} S^{ij} + {}_0 S^{ij}, \quad (6.56)$$

$${}^{\tau+\Delta\tau}{}_{0}\boldsymbol{\varepsilon}_{ij} = {}^{\tau+\Delta\tau}{}_{0}\boldsymbol{\varepsilon}_{ij} + {}_{0}\boldsymbol{\varepsilon}_{ij} = {}^{\tau+\Delta\tau}{}_{0}\boldsymbol{\varepsilon}_{ij} + {}_{0}\boldsymbol{e}_{ij} + {}_{0}\boldsymbol{\eta}_{ij}. \quad (6.57)$$

Substituting from Equations (6.56) and (6.57) into Equation (6.55) and using ${}_{0}S^{ij} = {}_{0}C^{ijkl}{}_{0}\boldsymbol{\varepsilon}_{kl}$ and $\delta_{0}\boldsymbol{\varepsilon}_{kl} = \delta_{0}\boldsymbol{e}_{ij}$, the linearized equilibrium equation is obtained by

$$\int_{0V} {}_{0}C^{ijkl}{}_{0}\boldsymbol{e}_{kl}\delta_{0}\boldsymbol{e}_{ij}d^0V + \int_{0V} {}^{\tau}S^{ij}\delta_{0}\boldsymbol{\eta}_{ij}d^0V = {}^{\tau+\Delta\tau}\mathfrak{R} - \int_{0V} {}^{\tau}S^{ij}\delta_{0}\boldsymbol{e}_{ij}d^0V, \quad (6.58)$$

in which ${}_{0}C^{ijkl}$ is the fourth-order contravariant constitutive tensor corresponding to the strain-stress law for shells.

Using Equations (6.46)-(6.47) in Equation (6.58), the following incremental equilibrium equation is obtained by

$${}^{\tau}\mathbf{K}\mathbf{U} = ({}^{\tau}\mathbf{K}_L + {}^{\tau}\mathbf{K}_{NL})\mathbf{U} = {}^{\tau+\Delta\tau}\mathbf{R} - {}^{\tau}\mathbf{F}, \quad (6.59)$$

where

$${}^{\tau}\mathbf{K}_L = \int_{0V} \mathbf{B}_{ij}^T {}_{0}C^{ijkl} \mathbf{B}_{kl} d^0V, \quad {}^{\tau}\mathbf{K}_{NL} = \int_{0V} \mathbf{N}_{ij} {}^{\tau}S^{ij} d^0V, \quad {}^{\tau}\mathbf{F} = \int_{0V} \mathbf{B}_{ij}^T {}^{\tau}S^{ij} d^0V, \quad (6.60)$$

in which ${}^{\tau}\mathbf{K}_L$ and ${}^{\tau}\mathbf{K}_{NL}$ are the linear and nonlinear tangent stiffness matrices, respectively, and ${}^{\tau}\mathbf{F}$ is the vector of nodal point forces equivalent to the element stresses at time τ . For the evaluation of the element stiffness matrix and internal nodal force vector, 7-point Gauss integration in the r - s plane (as for the 6-node shell element) is adopted due to the cubic bubble function and additional quadratic unknown coefficient.

With the full Newton-Raphson iteration scheme, the equations for the i -th iteration in a finite elements model are

$${}^{\tau}\mathbf{K}^{(i-1)}\mathbf{U}^{(i)} = {}^{\tau+\Delta\tau}\mathbf{R} - {}^{\tau}\mathbf{F}^{(i-1)} \quad \text{with} \quad {}^{\tau+\Delta\tau}\mathbf{U}^{(i)} = {}^{\tau+\Delta\tau}\mathbf{U}^{(i-1)} + \mathbf{U}^{(i)}. \quad (6.61)$$

The configuration at time $\tau + \Delta\tau$ is determined iterating on Equation (6.61) until equilibrium is fulfilled with a preset energy tolerance ε_E [1],

$$\mathbf{U}^{(i)T} ({}^{\tau+\Delta\tau}\mathbf{R} - {}^{\tau+\Delta\tau}\mathbf{F}^{(i-1)}) \leq \varepsilon_E (\mathbf{U}^{(1)T} ({}^{\tau+\Delta\tau}\mathbf{R} - {}^{\tau}\mathbf{F})). \quad (6.62)$$

6.2.4 Condensing Out in the Present Element

The bubble function does not affect the mid-surface displacement of the shell element, and the corresponding degrees of freedom can be statically condensed out on the element level. In order to establish the equations used in static condensation, the stiffness matrix and corresponding displacement and force vectors of the element under consideration are partitioned into the following form

$$\begin{bmatrix} {}^{\tau}\mathbf{K}_{aa}^{(i-1)} & {}^{\tau}\mathbf{K}_{ac}^{(i-1)} \\ {}^{\tau}\mathbf{K}_{ca}^{(i-1)} & {}^{\tau}\mathbf{K}_{cc}^{(i-1)} \end{bmatrix} \begin{bmatrix} \Delta\mathbf{U}_a^{(i)} \\ \Delta\mathbf{U}_c^{(i)} \end{bmatrix} = \begin{bmatrix} {}^{\tau+\Delta\tau}\mathbf{R}_a \\ {}^{\tau+\Delta\tau}\mathbf{R}_c \end{bmatrix} - \begin{bmatrix} {}^{\tau}\mathbf{F}_a^{(i-1)} \\ {}^{\tau}\mathbf{F}_c^{(i-1)} \end{bmatrix}, \quad (6.63)$$

where $\Delta\mathbf{U}_a^{(i)}$ and $\Delta\mathbf{U}_c^{(i)}$ are the vector of displacements combined with the unknown coefficient vector to be retained and the vector of bubble displacements to be condensed out, respectively. The matrix ${}^{\tau}\mathbf{K}_{aa}^{(i-1)}$,

${}^\tau_0\mathbf{K}_{ac}^{(i-1)}$, ${}^\tau_0\mathbf{K}_{ca}^{(i-1)}$ and ${}^\tau_0\mathbf{K}_{cc}^{(i-1)}$ and vector ${}^{\tau+\Delta\tau}\mathbf{R}_a$ and ${}^{\tau+\Delta\tau}\mathbf{R}_c$ correspond to the displacement vectors $\Delta\mathbf{U}_a^{(i)}$ and $\Delta\mathbf{U}_c^{(i)}$.

Using the second matrix equation in Equation (6.63), we obtain

$$\Delta\mathbf{U}_c^{(i)} = {}^\tau_0\mathbf{K}_{cc}^{(i-1)-1} ({}^{\tau+\Delta\tau}\mathbf{R}_c - {}^\tau_0\mathbf{F}_c^{(i-1)} - {}^\tau_0\mathbf{K}_{ca}^{(i-1)}\Delta\mathbf{U}_a^{(i)}). \quad (6.64)$$

The relation in Equation (6.64) is used to substitute $\Delta\mathbf{U}_c^{(i)}$ into the first matrix equation in Equation (6.63) to obtain the condensed equations

$${}^\tau_0\mathbf{K}_{con}^{(i-1)} \Delta\mathbf{U}_a^{(i)} = {}^{\tau+\Delta\tau}\mathbf{R}_{con} - {}^\tau_0\mathbf{F}_{con}^{(i-1)}, \quad (6.65)$$

where

$${}^\tau_0\mathbf{K}_{con}^{(i-1)} = {}^\tau_0\mathbf{K}_{aa}^{(i-1)} - {}^\tau_0\mathbf{K}_{ac}^{(i-1)} {}^\tau_0\mathbf{K}_{cc}^{(i-1)-1} {}^\tau_0\mathbf{K}_{ca}^{(i-1)}, \quad (6.66)$$

$${}^{\tau+\Delta\tau}\mathbf{R}_{con} = {}^{\tau+\Delta\tau}\mathbf{R}_a - {}^\tau_0\mathbf{K}_{ac}^{(i-1)} {}^\tau_0\mathbf{K}_{cc}^{(i-1)-1} {}^{\tau+\Delta\tau}\mathbf{R}_c, \quad (6.67)$$

$${}^\tau_0\mathbf{F}_{con}^{(i-1)} = {}^\tau_0\mathbf{F}_a^{(i-1)} + {}^\tau_0\mathbf{K}_{ac}^{(i-1)} {}^\tau_0\mathbf{K}_{cc}^{(i-1)-1} {}^\tau_0\mathbf{F}_c^{(i-1)}. \quad (6.68)$$

6.3 Computational Efficiency

In this section, some important aspects of the computational efficiency are studied when using the enriched MITC3+ shell element. The standard 3- and 6-node shell elements (the MITC3 and MITC6 shell elements) and the enriched MITC3+ shell element are considered.

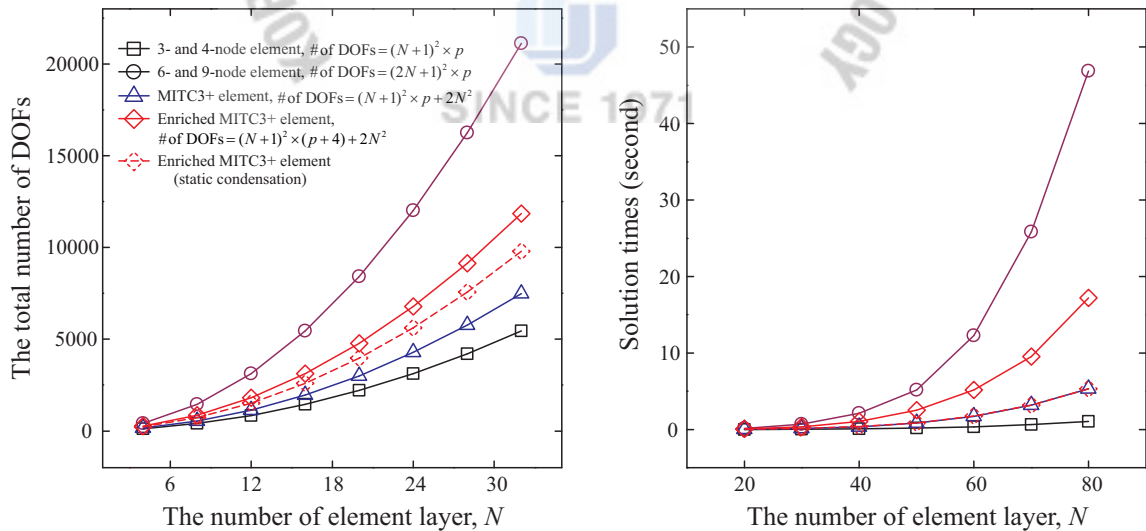


Figure 6.4. (a) The total number of degrees of freedom (DOFs) and (b) solution times for solving the linear equations when increasing the number of element layers, N , along an edge p denotes the number of DOFs per node in the standard shell element, hence $p = 5$ for Scordelis-Lo roof shown in Figure 6.12.

Of course, the enriched MITC3+ shell element generate symmetric stiffness or coefficient matrices. The numerical operations for the factorizations of the banded stiffness matrices are then approximately $(1/2)nm_k^2$ where n is the number of equations and m_k is the half-handwidth. Let the number of elements along the sides be N , and let us ignore in all cases the zero entries within the band, then we have for Scordelis-Lo roof problem, see **Figure 6.12**,

- for the solution of the enriched MITC3+, $n = (N+1)^2 \times (p+4)$, $m_k = (N+1) \times (p+4)$;
- for the solution using the 3- or 4-node element, $n = (N+1)^2 \times p$, $m_k = (N+1) \times p$;
- for the solution using the 6- or 9-node element, $n = (2N+1)^2 \times p$, $m_k = (2N+1) \times p$.

All degrees of freedom for the enriched MITC3+ shell element are associated with vertex nodes which are shared by several elements and the assembled system of equations is in general smaller than when using the 6-node shell elements where edge nodes are only shared by 2 elements. Therefore, the enriched MITC3+ shell element gives less equations and a smaller bandwidth than the 6-node shell elements. This fact shows the effectiveness of the enriched MITC3+ shell element from a computational point of view. **Figure 6.4** shows how the number of nodal degrees increases as a function of the number of elements used in the meshing of **Figure 6.12**.

Table 6.2. Solution times (in second) for solving the linear problem shown in Figure 6.12. (DOFs: degrees of freedom)

N	Linear element (Standard 3- and 4-node)		Quadratic elements (Standard 6- and 9-node)		Enriched MITC3+ (condensed out)	
	Free DOFs	Time	Free DOFs	Time	Free DOFs	Time
20	2,080	0.000	8,160	0.140	5,320 (3,720)	0.062 (0.031)
40	8,160	0.078	32,320	2.122	21,040 (14,640)	1.045 (0.374)
60	18,240	0.359	72,480	12.29	47,160 (32,760)	5.101 (1.731)
80	32,320	1.045	128,640	46.85	83,680 (58,080)	17.20 (5.335)

It is valuable to compare solution times required for the three shell finite elements considered. In all the cases, of course, symmetric stiffness matrices are generated. To obtain more insight into the computational efforts needed in the respective solutions, it is focused on the solution of the linear equations using direct Gauss elimination, in which the factorization of the stiffness matrices represents the major expense. To check computational times, we use a quad-core machine (Intel(R) Core i7-3770 CPU @ 3.40 GHz, 8GB RAM, Windows 7 64bit) for all solution cases. **Figure 6.4** and **Table 6.2** show the solution times for linear analysis of the Scordelis-Lo roof problem. As expected, the factorization time for the enriched MITC3+ shell element is much smaller than for the quadratic shell element.

6.4 Numerical Examples

To assess the performance of the enriched MITC3+ shell element in linear and nonlinear analyses, the solutions of several benchmark problems are given in this section, see **Table 6.3**. The nonlinear problems involve the large displacement and large rotation response of shells with various shell geometries. The results calculated using the following MITC shell elements are given in **Table 6.4**.

Table 6.3. List of ten benchmark problems solved.

Benchmark problems	Problem type		Descriptions	Results
Cantilever beam for mesh distortion test	P	L	Figure 6.5	Table 6.5, Figure 6.5
Cook's skew beam	P	L	Figure 6.6	Table 6.6
MacNeal's cantilever beam	P	L	Figure 6.7	Table 6.7-Table 6.8
Curved cantilever beam	P,S	L,N	Figure 6.8	Table 6.9, Table 6.17-Table 6.18, Figure 6.8, Figure 6.19-Figure 6.20
Hemispherical shell	S	L,N	Figure 6.9	Table 6.10-Table 6.11, Table 6.19-Table 6.24, Figure 6.11, Figure 6.21-Figure 6.23
Scordelis-Lo (Barrel Vault) roof	S	L,N	Figure 6.12	Table 6.12-Table 6.13, Table 6.25-Table 6.28, Figure 6.13, Figure 6.24-Figure 6.25
Raasch's hook problem	S	L	Figure 6.14	Table 6.14, Figure 6.14
Cantilever beam subjected to a tip moment	P	N	Figure 6.15	Table 6.15, Figure 6.15-Figure 6.16
Column under an eccentric compressive load	P	N	Figure 6.17	Table 6.16, Figure 6.17-Figure 6.18
Slit annular plate	S	N	Figure 6.26	Table 6.29-Table 6.30, Figure 6.27-Figure 6.28

P: Plane stress problem, S: Shell problem, L: Linear analysis, N: Nonlinear analysis

In each example, the reference solutions are given by either an analytical result or a calculated solution using a fine uniform mesh of the MITC9 shell element (these meshes used twice the number of elements in each direction as employed in the MITC4 element solutions). The MITC9 element is known to satisfy the ellipticity and consistency conditions and to show good convergence behavior [26, 27].

By imposing $w = \alpha = \beta = 0$ for all nodes, plane stress condition is used for some benchmark problems in linear and nonlinear analyses to verify the effect on membrane behaviors.

Note that in some benchmark problems, point loads are used, which cause a stress singularity at the point of loading. However, the use of point loads is acceptable in the studies here given because the meshes are not very fine (the point loads act as an equivalent pressure applied over a small area) [1].

Table 6.4. Summary of element models for comparison.

Symbols	Brief description	Ref.
MITC3	3-node triangular shell element with the MITC method	[23]
MITC4	4-node quadrilateral shell element with the MITC method	[19]
MITC4*	MITC4 shell element with incompatible modes	[63, 64].
MITC3+	Triangular shell element with an enrichment by cubic bubble function	[29, 156]
Enriched MITC3+	MITC3+ shell element with improved membrane behaviors	
MITC6	6-node triangular shell element with the MITC method	[23]
MITC9	9-node quadrilateral shell element with the MITC method	[21]
Q6	4-node isoparametric element with internal parameters	[63]
QM6	4-node isoparametric element with internal parameters	[64]
P-S	Assumed stress elements (hybrid element by the Hellinger-Reissner)	[161]
QE2	4-node quadrilateral enhanced strain element	[162]
ALL-3I/ EX/ LS	Allman 88 triangular element with corner drilling freedoms	[121]
FF84	1984 free formulation element of Bergan and Felippa	[163]
LST-Ret	Retrofitted linear strain triangular element	[121]
OPT	Triangular element with the optimal assumed natural deviatoric strain	[121]
HL	A plane element based in the assumed stress hybrid principle	[164]
XSHELL41/ 42	4-node quasi-conforming flat shell element with drilling DOFs	[124]
PEAS7	Enhanced assumed strain elements	[113]
PN340	8-node brick element representing constant stress fields	[165]
RGD20	Refined hybrid isoparametric element	[166]
QUAD4	4-node shell element with modifications which relax excessive constraints	[16]
Simo et al.	Geometrically exact stress resultant shell model	[149, 167]
ANS6S	6-node C^0 curved shell element with the assumed natural strain	[168]
S3R	General purpose 3-node shell element in ABAQUS	[116]
C0	C^0 triangular plate element with one-point quadrature	[169]
DSG	3- and 4-node shell finite element with discrete shear gap method	[170]
RTS18	Flat triangular element based on the refined non-conforming method	[171]
QHP	4-node quadrilateral shell element with physical hourglass control	[128]
URI-4	9-node uniformly reduced integrated element	[131]
SRI-4	Bilinear degenerated shell element with selective reduced integration	[12]
DKQ-4	4-node discrete Kirchhoff quadrilateral element	[130]
Allman	Discrete Kirchhoff-Mindlin triangle with Allman's rotational DOFs	[117, 118]
Cook, Flat-stiffened	Stabilized 18 DOF triangular flat shell element	[119]
Providas and Kattis	Triangular shell element with an arbitrary small true drilling stiffness	[120]
Collapsed Plane42	Triangular element obtained from Plane42 quadrilateral element of ANSYS	[126]
Plane82	8-node quadrilateral element of ANSYS	[126]

6.4.1 Linear Benchmark Problems

Several benchmark problems are examined to demonstrate the efficiency of the present element. To test enhanced membrane behavior, we select membrane-dominant problem sets.

6.4.1.1 Cantilever Beam for Mesh Distortion Test

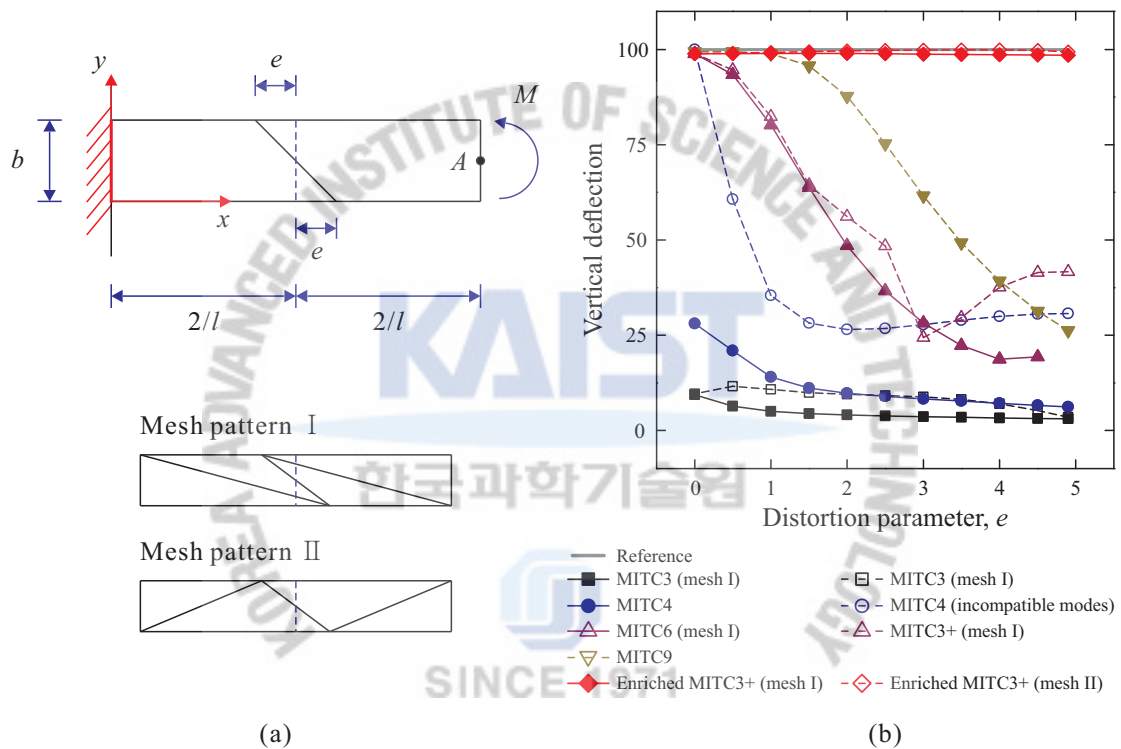


Figure 6.5. Cantilever beam for distortion test. (a) Problem description and mesh pattern used for the MITC3, MITC3+ and enriched MITC3+ shell elements. (b) Vertical deflection versus distortion parameter e .

The cantilever beam to test distortion sensitivity shown in **Figure 6.5** is discretized by two elements. The shape of the two elements varies with the distorted parameter e . The cantilever beam has the geometry of length $l = 10$, width $b = 2$ and thickness $h = 1$, its Young modulus $E = 1500$ and the Poisson ratio $\nu = 0.25$. The moment $M = 2000$ is applied at the free end. When distorted parameter e is equal to zero, both element are rectangular. But with the increase of distorted parameter e , the mesh will be distorted more and more seriously. The results of the tip deflection at point A are shown in **Figure 6.5** and **Table 6.5**. Beside the present elements, the solutions obtained by other elements are also given for comparison. Enriched MITC3+ shell element can keep providing the exact solution when e varies from 0 to 5. The present element gives the best

performance and is more robust than other elements compared with. The enriched MITC3+ shell element can overcome the trapezoidal locking completely.

Table 6.5. Vertical deflections and relative errors at point A for the cantilever beam for distortion test shown in Figure 6.5(a). Relative error (%) = $(v_A^{ref} - v_A) / v_A^{ref} \times 100$ where v_A^{ref} and v_A denote the reference and finite element solutions, respectively.

Element type	Vertical displacement, v_A and its relative error					
	$e = 0.0$	$e = 1.0$	$e = 2.0$	$e = 3.0$	$e = 4.0$	$e = 4.9$
MITC3 ^I	9.4 (90.6)	5.0 (95.0)	4.1 (95.9)	3.6 (96.4)	3.3 (96.7)	3.1 (96.9)
MITC3 ^{II}	9.6 (90.4)	10.8 (89.2)	9.5 (90.5)	8.8 (91.2)	7.0 (93.0)	3.5 (96.5)
MITC4	28.0 (72.0)	14.1 (85.9)	9.8 (90.2)	8.3 (91.7)	7.1 (92.9)	6.2 (93.8)
MITC4*	100.0 (0.0)	35.5 (64.5)	26.5 (73.5)	27.8 (72.2)	29.9 (70.1)	30.7 (69.3)
MITC6 ^I [23]	98.9 (1.1)	80.2 (19.8)	48.5 (51.5)	28.2 (71.8)	18.7 (81.3)	43.1 (56.9)
MITC6 ^{II} [23]	98.9 (1.1)	82.4 (17.6)	56.2 (43.8)	24.4 (75.6)	37.6 (62.4)	41.7 (58.3)
MITC9 [21]	99.4 (0.6)	98.9 (1.1)	87.7 (12.3)	61.6 (38.4)	39.2 (60.8)	26.3 (73.7)
QM6 [64]	100.0 (0.0)	62.7 (37.3)	54.4 (45.6)	53.6 (46.4)	51.2 (48.8)	46.8 (53.2)
P-S [161]	100.0 (0.0)	62.9 (37.1)	55.0 (45.0)	54.7 (45.3)	53.1 (46.9)	49.8 (50.2)
QE2 [162]	100.0 (0.0)	63.4 (36.6)	56.5 (43.5)	57.5 (42.5)	57.9 (42.1)	56.9 (43.1)
Enriched MITC3+ ^I	98.9 (1.1)	99.0 (1.0)	98.9 (1.1)	98.8 (1.2)	98.6 (1.4)	98.5 (1.5)
Enriched MITC3+ ^{II}	98.9 (1.1)	99.2 (0.8)	99.6 (0.4)	99.8 (0.2)	99.9 (0.1)	99.4 (0.6)

Reference (analytic) solution $v_A^{ref} = 100$
I and II : mesh patterns shown in Figure 6.5(b)

6.4.1.2 Cook's Skew Beam

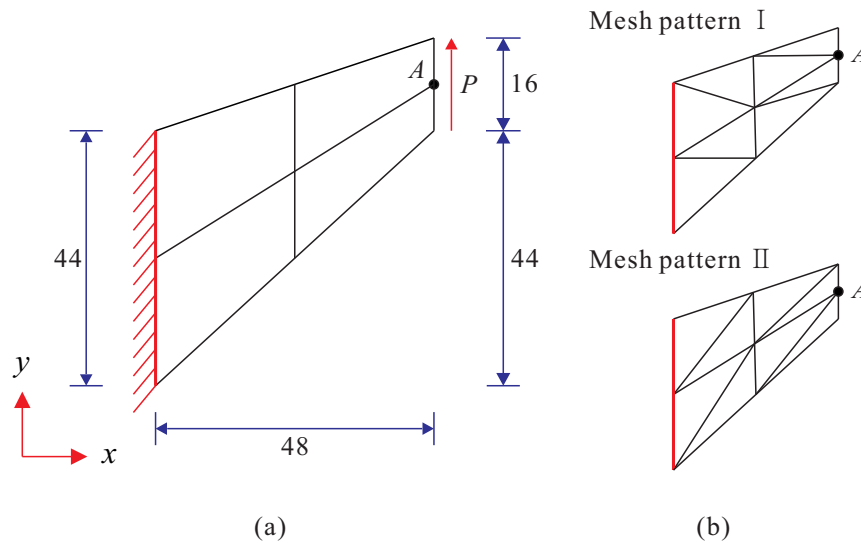


Figure 6.6. Cook's skew beam. (a) Problem description. (b) Mesh patterns (2×2) used for the MITC3, MITC3+ and enriched MITC3+ shell elements.

This problem shown in **Figure 6.6** was proposed by Cook et al. [4], which involves a skew beam with distributed shear load $P = 1/16$ at the right end. Young's modulus is $E = 1.0$ and the Poisson's ratio is $\nu = 1/3$. The problem is modelled using 2×2 , 4×4 and 8×8 meshes of different shell elements. The deflection at point A is computed and listed in **Table 6.6** along with the results of other types of elements. Compared with the other elements, the present elements give the best results of all known triangular elements, such as OPT, LST-Ret and All-3I.

Table 6.6. Vertical displacements and relative errors at point A for the Cook's skew beam shown in Figure 6.6(a). Relative error (%) = $(v_A^{ref} - v_A) / v_A^{ref} \times 100$ where v_A^{ref} and v_A denote the reference and finite element solutions, respectively.

Element type	Displacement (Relative error)		
	2×2 element mesh	4×4 element mesh	8×8 element mesh
MITC3 ^I	11.97 (49.92)	18.26 (23.60)	22.00 (7.95)
MITC3 ^{II}	6.71 (71.92)	11.22 (53.05)	17.31 (27.57)
MITC4	3.48 (85.44)	18.25 (23.64)	22.05 (7.74)
MITC4*	5.08 (78.74)	22.97 (3.89)	23.65 (1.05)
ALL-3I [121]	21.61 (9.58)	23.00 (3.77)	23.66 (1.00)
ALL-EX [121]	19.01 (20.46)	21.83 (8.66)	23.43 (1.97)
ALL-LS [121]	19.43 (18.70)	22.32 (6.61)	23.44 (1.92)
FF84 [163]	20.36 (14.81)	22.42 (6.19)	23.41 (2.05)
LST-Ret [121]	19.82 (17.07)	22.62 (5.36)	23.58 (1.34)
OPT [121]	20.56 (13.97)	22.45 (6.07)	23.43 (1.97)
HL [164]	18.17 (23.97)	22.03 (7.82)	23.39 (2.13)

Q6 [63]	22.94 (4.02)	23.48 (1.76)	23.80 (0.42)
QM6 [64]	21.05 (11.92)	23.02 (3.68)	23.65 (1.05)
Enriched MITC3+ ^I	22.78 (4.69)	23.59 (1.29)	23.81 (0.38)
Enriched MITC3+ ^{II}	20.06 (16.07)	22.97 (3.89)	23.70 (0.84)

Reference solution $v_A^{ref} = 23.9$ [4]

I and II : mesh patterns shown in Figure 6.6(b)

6.4.1.3 MacNeal's Cantilever Beam

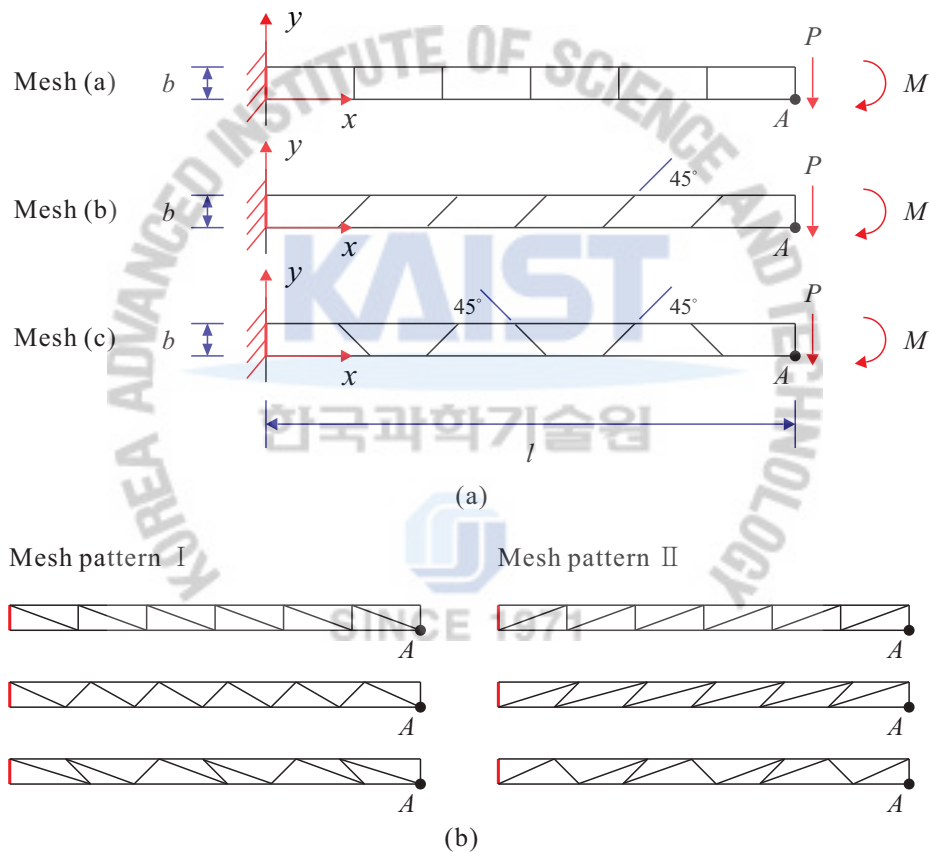


Figure 6.7. MacNeal's cantilever beam subjected to two different loading: Unit tip shear force, P and tip bending moment, M . (a) Problem description. (b) Mesh patterns (1×6) used for the MITC3, MITC3+ and enriched MITC3+ shell elements.

MacNeal's cantilever beam [143] shown in **Figure 6.7(a)** is a frequently used test problem due to its simplicity and fact that the principle element deformation modes can be evoked by loads applied to the free end. Three different mesh shapes shown in **Figure 6.7(b)**, rectangular (mesh (a)), parallelogram (mesh (b))

and trapezoidal (mesh (c)), are adopted. Two types of loading, viz., unit tip shear force, $P = 1$, and tip moment, $M = 0.2$, are considered. The cantilever beam has geometry of length $l = 6$, width $b = 0.2$ and thickness $h = 0.1$. The material properties of the cantilever beam are given by $E = 10^7$, $\nu = 0.3$. The results of the tip displacement at point A are shown in **Table 6.7** and **Table 6.8**. Besides the presented elements, the results obtained by other element models are also given for comparison. The enriched MITC3+ element possess high accuracy for all three mesh divisions and is insensitive to three types of distortion. Thus, The present element can successfully avoid trapezoidal locking, which can always keep the second-order completeness in Cartesian coordinates under distortion meshes.

Table 6.7. Vertical displacements and relative errors at point A for the MacNeal’s thin cantilever beam subjected to unit shear force shown in Figure 6.7(a). Relative error (%) = $(v_A^{ref} - v_A) / v_A^{ref} \times 100$ where v_A^{ref} and v_A denote the reference and finite element solutions, respectively.

Element type	Load P		
	Mesh (a)	Mesh (b)	Mesh (c)
	Displacement (Error)	Displacement (Error)	Displacement (Error)
MITC3 ^I	-0.0034 (96.85)	-0.0024 (97.78)	-0.0016 (98.52)
MITC3 ^{II}	-0.0034 (96.85)	-0.0012 (98.89)	-0.0021 (98.06)
MITC4	-0.0101 (90.66)	-0.0037 (96.58)	-0.0029 (97.32)
MITC4*	-0.1073 (0.74)	-0.0683 (36.82)	-0.0056 (94.82)
Q6 [63]	-0.1073 (0.70)	-0.0732 (32.30)	-0.0115 (89.40)
QM6 [64]	-0.1073 (0.70)	-0.0673 (37.70)	-0.0048 (95.60)
P-S [161]	-0.1073 (0.70)	-0.0863 (20.20)	-0.0239 (77.90)
XSHELL41 [124]	-0.0977 (9.60)	-0.0098 (90.90)	-0.0124 (88.50)
XSHELL42 [124]	-0.0977 (9.60)	-0.0963 (10.90)	-0.0895 (17.20)
PEAS7 [113]	-0.1062 (1.80)	-0.0859 (20.50)	-0.0235 (78.30)
PN340 [165]	-0.1062 (1.80)	-0.0670 (38.00)	-0.0070 (93.50)
RGD20 [166]	-0.1060 (1.90)	-0.0676 (37.60)	-0.0051 (95.30)
Enriched MITC3+ ^I	-0.1063 (1.67)	-0.1049 (2.96)	-0.1039 (3.89)
Enriched MITC3+ ^{II}	-0.1063 (1.67)	-0.1029 (4.81)	-0.1042 (3.61)

Reference solution $v_A^{ref} = -0.1081$ [143]

I and II : mesh patterns shown in Figure 6.7(b)

Table 6.8. Vertical displacements and relative errors at point A for the MacNeal’s thin cantilever beam subjected to end moment shown in Figure 6.7(a). Relative error (%) = $(v_A^{ref} - v_A) / v_A^{ref} \times 100$ where v_A^{ref} and v_A denote the reference and finite element solutions, respectively.

Element type	Load M		
	Mesh (a)	Mesh (b)	Mesh (c)
	Displacement (Error)	Displacement (Error)	Displacement (Error)

MITC3 ^I	-0.0002 (96.30)	-0.0001 (98.15)	-0.0001 (98.15)
MITC3 ^{II}	-0.0002 (96.30)	-0.0001 (98.15)	-0.0001 (98.15)
MITC4	-0.0005 (90.74)	-0.0002 (96.30)	-0.0001 (98.15)
MITC4*	-0.0054 (0.00)	-0.0039 (27.78)	-0.0003 (94.44)
Q6 [63]	-0.0054 (0.00)	-0.0041 (24.10)	-0.0005 (90.70)
QM6 [64]	-0.0054 (0.00)	-0.0039 (27.80)	-0.0002 (96.30)
P-S [161]	-0.0054 (0.00)	-0.0046 (14.80)	-0.0009 (83.30)
Enriched MITC3 ^{+I}	-0.0054 (0.00)	-0.0054 (0.00)	-0.0054 (0.00)
Enriched MITC3 ^{+II}	-0.0054 (0.00)	-0.0054 (0.00)	-0.0054 (0.00)

Reference solution $v_A^{ref} = -0.0054$ [143]

I and II : mesh patterns shown in Figure 6.7(b)

6.4.1.4 Curved Cantilever Beam

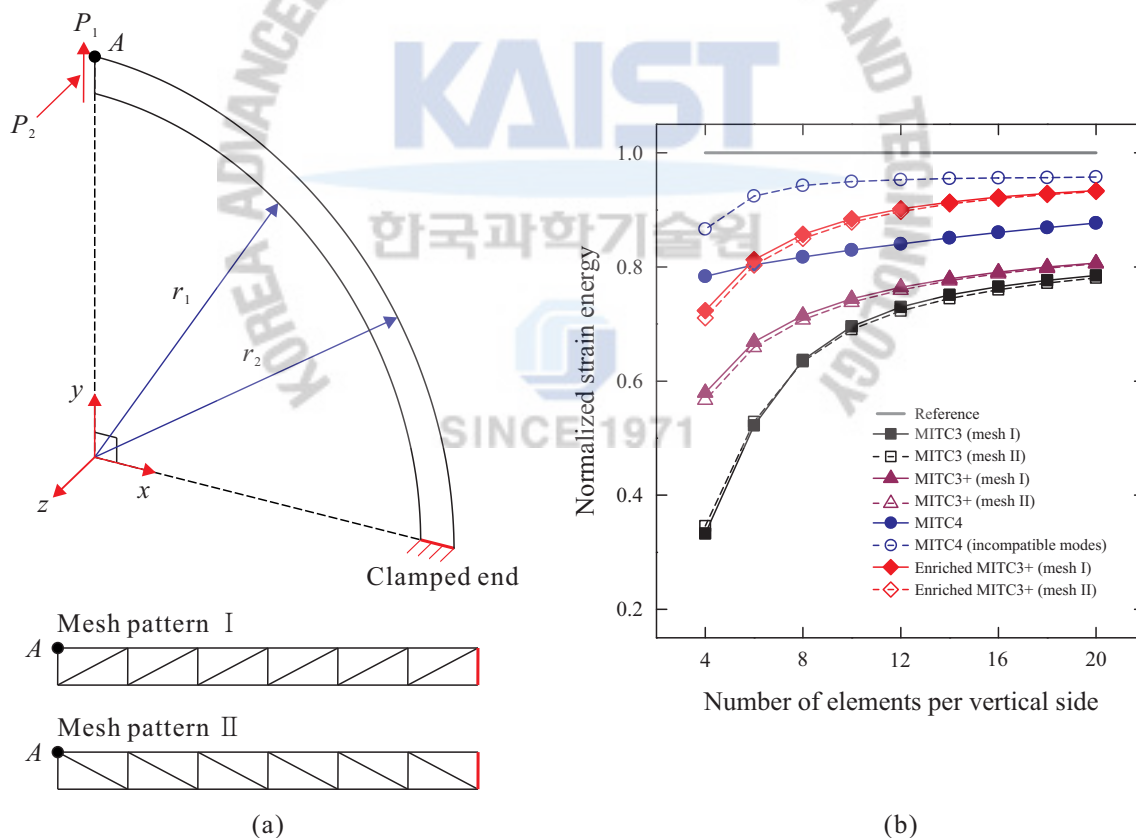


Figure 6.8. Curved cantilever beam. (a) Problem description and mesh patterns (1×6) used for the MITC3, MITC3+ and enriched MITC3+ shell elements. (b) Normalized strain energy in the linear analysis of the curved cantilever beam.

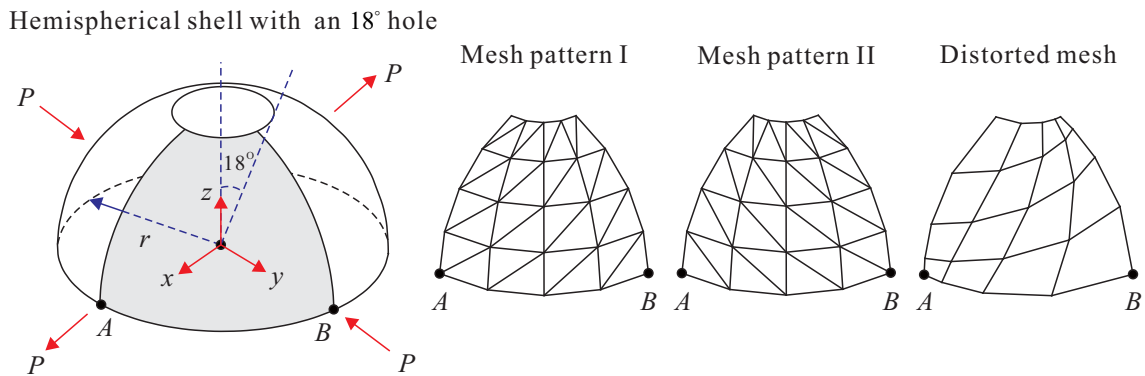
The curved cantilever beam shown in Figure 6.8(a) is clamped at one end and loaded by two unit forces at the other. The forces are applied along the in-plane axis and the out-of-plane axis. The problem geometry and material properties are $r_1 = 4.12$, $r_2 = 4.32$, $E = 1.0 \times 10^7$, $\nu = 0.25$ and the thickness of the curved cantilever beam is $h = 0.1$. The elements used for analyzing the curved cantilever beam would unavoidably be distorted. In addition to this, a coarse mesh of 1×6 would make a high aspect ratio for each element. The displacements at point A are computed and normalized by the reference solution of MacNeal and Harder [143]. The reference solution of the curved beam problem is 0.08734 for in-plane loading and 0.5022 for out-of-plane loading. From the vertical and horizontal reference displacements, we obtain the reference solution of the strain energy, $0.29477 = 0.5 \times (0.08734 + 0.5022)$. The results are shown in Figure 6.8(b) and Table 6.9 compared with other elements. The present element produces much better solution accuracy than other elements in this problem.

Table 6.9. Displacements and normalized displacements at point A for the curved cantilever beam shown in Figure 6.8(a). The solutions are obtained with a 1×6 element mesh. Normalized displacement (ND) = v_A / v_A^{ref} and w_A / w_A^{ref} , where v_A^{ref} and w_A^{ref} is the reference solution and v_A and w_A denote the finite element solutions.

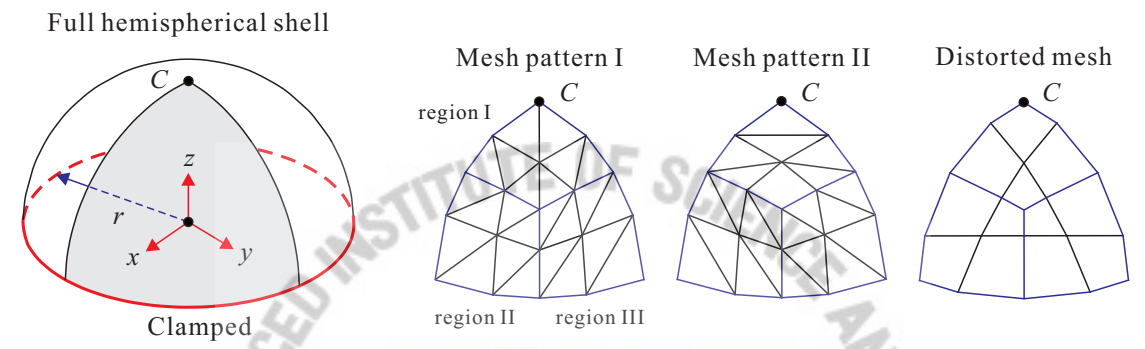
Element type	Load P_1 and P_2	
	Displacement (ND), v_A	Displacement (ND), $-w_A$
MITC3 ^I	0.0022 (0.0249)	0.3121 (0.6214)
MITC3 ^{II}	0.0022 (0.0253)	0.3153 (0.6278)
MITC4	0.0064 (0.0734)	0.4741 (0.9441)
MITC4*	0.0775 (0.8875)	0.4741 (0.9441)
XSHELL41 [124]	0.0801 (0.9170)	0.4339 (0.8640)
XSHELL42 [124]	0.0834 (0.9550)	0.4339 (0.8640)
QUAD4 [16]	0.0728 (0.8330)	0.4776 (0.9510)
Enriched MITC3+ ^I	0.0728 (0.9966)	0.3990 (0.7944)
Enriched MITC3+ ^{II}	0.0737 (0.9974)	0.3931 (0.7828)

Reference solution : $v_A^{ref} = 0.08734$ and $-w_A^{ref} = 0.5022$ [143]
I and II : mesh patterns shown in Figure 6.8(a)

6.4.1.5 Hemispherical Shell



(a)



(b)

Figure 6.9. Descriptions of the hemispherical shell problems: (a) Hemispherical shell with 18° hole and (b) full hemispherical shell. Mesh patterns used for the MITC3, MITC3+ and enriched MITC3+ shell elements. Distorted meshes shown in Figure 6.10 are used.

Two geometries have been used for this problem; one is a hemispherical shell with an 18° hole shown in **Figure 6.9**(a) and another is a full hemispherical shell shown in **Figure 6.9**(b). Both shells have the same radius, thickness, material properties but different loading conditions. The radius of hemispherical shells is $r = 10$ and its thickness $h = 0.04$. The material has a Young's modulus of $E = 6.825 \times 10^7$ and a Poisson's ratio of $\nu = 0.3$. The problems are modeled using only one quarter of the hemisphere due to symmetry.

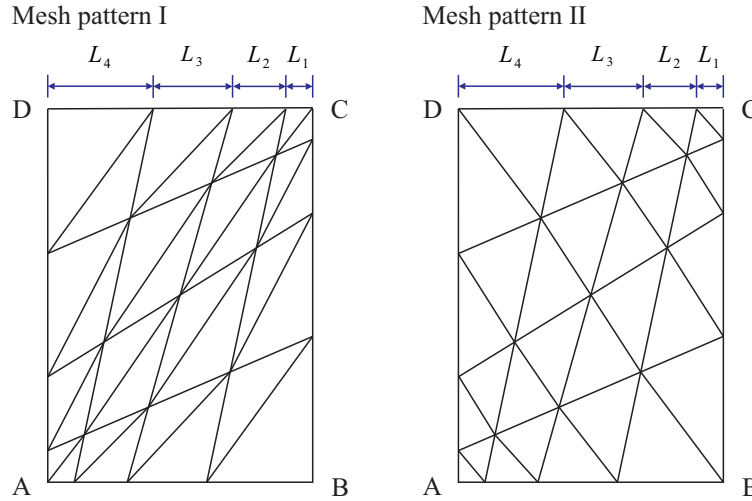


Figure 6.10. Distorted meshes used for the numerical problems solved when $N = 4$.

For a hemispherical shell with an 18° hole, two pairs of opposite radial concentrated loads $P = 2$ are applied. This problem is a very useful example to check the ability of the element to handle rigid body rotation about the shell surface and the inextensible bending modes. We study the performance not only using uniform meshes but also distorted meshes, as shown in **Figure 6.10**. When the $N \times N$ distorted mesh is used, each edge is divided by the ratio $L_1 : L_2 : L_3 : \dots, L_N = 1 : 2 : 3 : \dots, N$, leading to quite distorted meshes. Shell elements without the membrane locking treatment cannot correctly solve this problem when the distorted meshes are used. The analytical radial displacement coincident at point load is 0.094 [143], the solutions given in **Figure 6.11(a)** and **Table 6.10** are normalized with this value. The solution for the MITC4 shell element is significantly deteriorated due to the effect of mesh distortion. However, The numerical results confirm the assertion that linear triangles are free from membrane locking without additional measures taken for the membrane part. Of course MITC3 does not behave well due to transverse shear locking. It can be observed that the present results agree well with analytic solutions.

Table 6.10. Radial displacements and normalized displacements at point A for the hemispherical shell with 18° hole shown in Figure 6.9(a). Normalized displacement (ND) = u_A / u_A^{ref} where u_A^{ref} and u_A denote the reference and finite element solutions, respectively.

Element type	Mesh		
	4 × 4 Displacement (ND)	8 × 8 Displacement (ND)	16 × 16 Displacement (ND)
MITC3 ^I	0.004 (0.043)	0.028 (0.298)	0.077 (0.819)
MITC3 ^{II}	0.004 (0.043)	0.029 (0.309)	0.080 (0.851)
MITC4	0.097 (1.032)	0.094 (1.000)	0.093 (0.989)
MITC4*	0.097 (1.032)	0.094 (1.000)	0.093 (0.989)
Simo et al. [149, 167]	0.094 (1.004)	0.094 (0.998)	0.094 (0.999)

XSHELL41 [124]	0.098 (1.038)	0.095 (1.012)	0.094 (1.001)
XSHELL42 [124]	0.025 (0.269)	0.062 (0.659)	0.091 (0.970)
ANS6S [168]	0.088 (0.949)	0.091 (0.982)	0.093 (1.001)
S3R [172]	0.033 (0.357)	0.085 (0.913)	0.091 (0.981)
C0 [169]	0.081 (0.870)	0.089 (0.960)	-
DSG [170]	0.090 (0.965)	0.091 (0.981)	0.092 (0.989)
RTS18 [171]	0.091 (0.968)	0.096 (1.021)	0.094 (1.000)
Enriched MITC3 ^I	0.097 (1.032)	0.094 (1.000)	0.093 (0.989)
Enriched MITC3 ^{II}	0.094 (1.000)	0.093 (0.989)	0.093 (0.989)

Reference solution $u_A^{ref} = 0.0094$ [143]

I and II : mesh patterns shown in Figure 6.9(a)

For a full hemispherical shell, shell is clamped at the bottom and subjected to a uniform pressure load. This problem possess no available analytic solution, therefore the reference solution is calculated using a mesh of 30×30 MITC9 shell finite elements which is known to satisfy the ellipticity and the consistency conditions and to show adequate convergence behaviors, see Refs. [21, 26, 101]. The results of normalized strain energy compare well with the results from other shell elements as shown in **Table 6.11** and **Figure 6.11(b)**. From the obtained results it is clear that the convergence of enriched MITC3+ shell element for this problem is fast compared to other elements.

Table 6.11. Strain energy (SE) and relative errors in strain energy for the full hemispherical shell shown in Figure 6.9(b). Relative error (RE) (%) = $(SE^{ref} - SE) / SE^{ref} \times 100$ where SE^{ref} and SE denote the reference and finite element strain energy, respectively.

Element type	Uniform mesh			Distorted mesh		
	2×2	4×4	6×6	2×2	4×4	6×6
	SE×10 ⁴ (RE)					
MITC3 ^I	13.19 (0.61)	18.27 (0.85)	19.77 (0.92)	12.38 (0.57)	16.74 (0.77)	18.43 (0.85)
MITC3 ^{II}	11.83 (0.55)	17.60 (0.82)	19.41 (0.90)	12.35 (0.57)	17.92 (0.83)	19.50 (0.90)
MITC3 ^{+I}	14.72 (0.68)	18.84 (0.87)	20.10 (0.93)	13.69 (0.63)	17.76 (0.82)	19.16 (0.89)
MITC3 ^{+II}	12.84 (0.59)	18.09 (0.84)	19.72 (0.91)	14.34 (0.66)	18.86 (0.87)	20.05 (0.93)
MITC4	14.55 (0.67)	19.43 (0.90)	20.54 (0.95)	14.61 (0.68)	18.87 (0.87)	20.07 (0.93)
MITC4*	15.47 (0.72)	19.89 (0.92)	20.78 (0.96)	15.60 (0.72)	19.67 (0.91)	20.61 (0.95)
Enriched MITC3 ^{+I}	17.16 (0.79)	20.36 (0.94)	21.10 (0.98)	15.59 (0.72)	19.33 (0.89)	20.48 (0.95)
Enriched MITC3 ^{+II}	14.87 (0.69)	19.58 (0.91)	20.71 (0.96)	16.46 (0.76)	20.39 (0.94)	21.31 (0.99)

Reference solution $SE^{ref} = 21.60 \times 10^4$

I and II : mesh patterns shown in Figure 6.9(a)

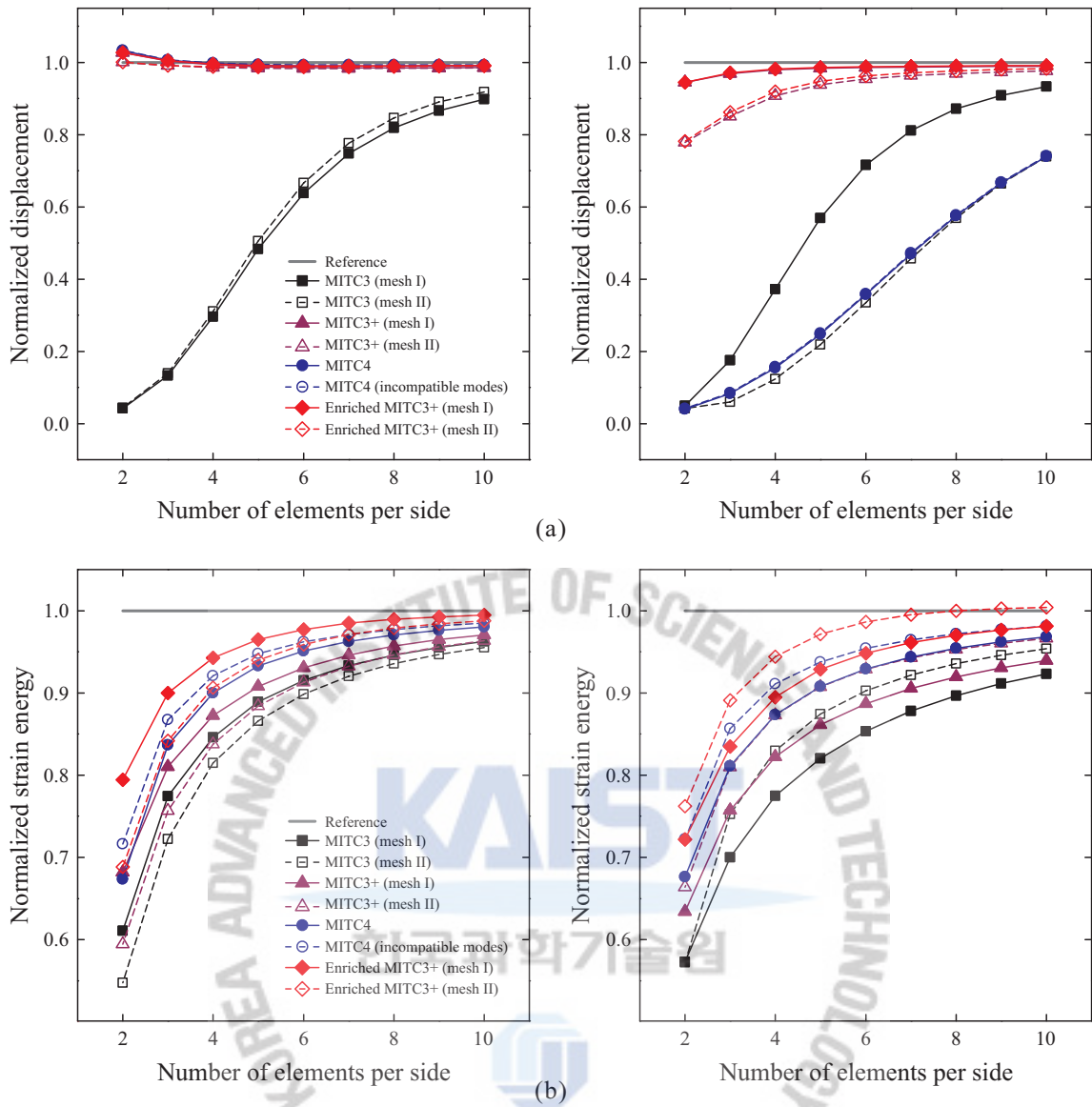


Figure 6.11. Convergence curves for the hemispherical shell problems. (a) Normalized displacement of the hemispherical shell with an 18° hole using the uniform meshes (left) and the distorted meshes (right). (b) Normalized strain energy of the full hemispherical shell with the uniform meshes (left) and the distorted meshes (right).

6.4.1.6 Scordelis-Lo (Barrel Vault) Roof

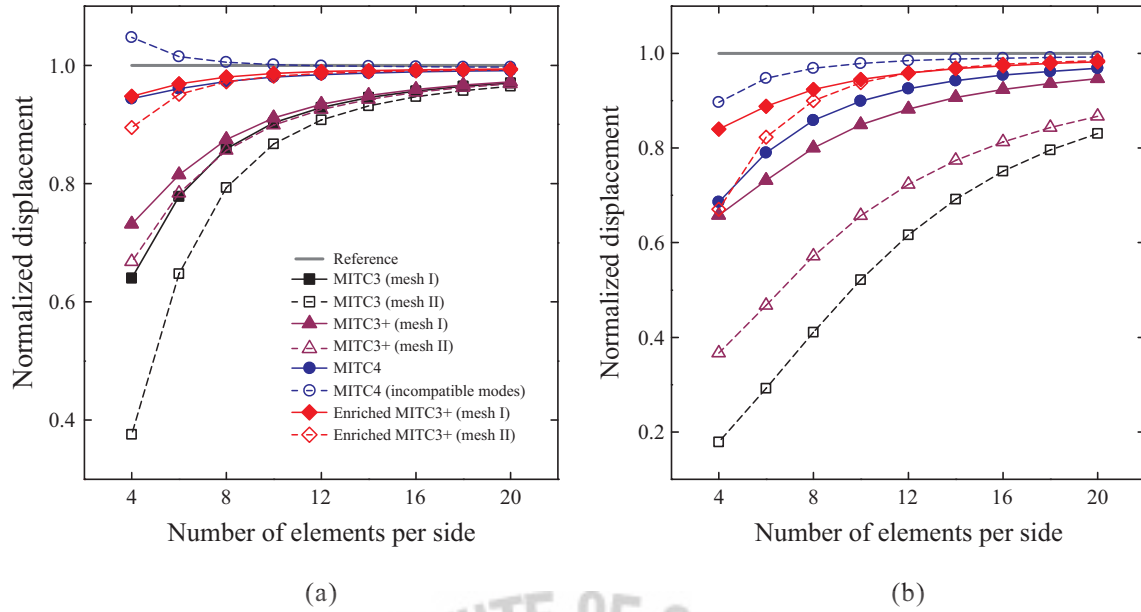


Figure 6.13. Normalized displacement of the Scordelis-Lo roof with (a) the uniform meshes (b) the distorted meshes shown in Figure 6.10.

Table 6.12. Displacements and normalized displacements at point A for the Scordelis-Lo roof using the uniform meshes. Normalized displacement (ND) = w_A / w_A^{ref} where w_A^{ref} and w_A denote the reference and finite element solutions, respectively.

Element type	Uniform mesh		
	4 × 4	8 × 8	16 × 16
	Displacement (ND)	Displacement (ND)	Displacement (ND)
MITC3 ^I	0.1936 (0.6402)	0.2597 (0.8588)	0.2892 (0.9563)
MITC3 ^{II}	0.1137 (0.3760)	0.2398 (0.7930)	0.2863 (0.9468)
MITC3+ ^I	0.2211 (0.7312)	0.2644 (0.8743)	0.2901 (0.9593)
MITC3+ ^{II}	0.2019 (0.6677)	0.2588 (0.8558)	0.2885 (0.9540)
MITC4	0.2852 (0.9431)	0.2942 (0.9729)	0.2990 (0.9888)
MITC4*	0.3167 (1.0473)	0.3040 (1.0053)	0.3017 (0.9977)
QPH [128]	0.2843 (0.9400)	0.2964 (0.9800)	0.3054 (1.0100)
Simo et al. [167]	0.3275 (1.0830)	0.3069 (1.0150)	0.3024 (1.0000)
QUAD4 [16]	0.3175 (1.0500)	0.3048 (1.0080)	-
URI-4	0.3686 (1.2190)	0.3187 (1.0540)	0.3075 (1.0170)
SRI-4	0.2915 (0.9640)	0.2976 (0.9840)	0.3021 (0.9990)
DKQ-4	0.3169 (1.0480)	0.3039 (1.0050)	0.3015 (0.9970)
Enriched MITC3+ ^I	0.2866 (0.9478)	0.2964 (0.9802)	0.3001 (0.9924)
Enriched MITC3+ ^{II}	0.2705 (0.8945)	0.2940 (0.9722)	0.2996 (0.9907)

Reference solution $w_A^{ref} = 0.3024$ [143]

I and II : mesh patterns shown in Figure 6.12(b)

Table 6.13. Displacements and normalized displacements at point A for the Scordelis-Lo roof using the distorted meshes. Normalized displacement (ND) = w_A / w_A^{ref} where w_A^{ref} and w_A denote the reference and finite element solutions, respectively.

Element type	Distorted mesh shown in Figure 6.10		
	4×4	8×8	16×16
	Displacement (ND)	Displacement (ND)	Displacement (ND)
MITC3 ^I	0.1753 (0.5797)	0.2355 (0.7788)	0.2777 (0.9183)
MITC3 ^{II}	0.0540 (0.1786)	0.1242 (0.4107)	0.2270 (0.7507)
MITC3+ ^I	0.1990 (0.6581)	0.2421 (0.8006)	0.2794 (0.9239)
MITC3+ ^{II}	0.1108 (0.3664)	0.1729 (0.5718)	0.2458 (0.8128)
MITC4	0.2075 (0.6862)	0.2596 (0.8585)	0.2885 (0.9540)
MITC4*	0.2713 (0.8972)	0.2930 (0.9689)	0.2994 (0.9901)
Enriched MITC3+ ^I	0.2541 (0.8403)	0.2793 (0.9236)	0.2946 (0.9742)
Enriched MITC3+ ^{II}	0.2027 (0.6703)	0.2722 (0.9001)	0.2955 (0.9772)
Reference solution w_A^{ref} [143] = 0.3024			
I and II : mesh patterns shown in Figure 6.12(b)			

6.4.1.7 Raasch's Hook Problem

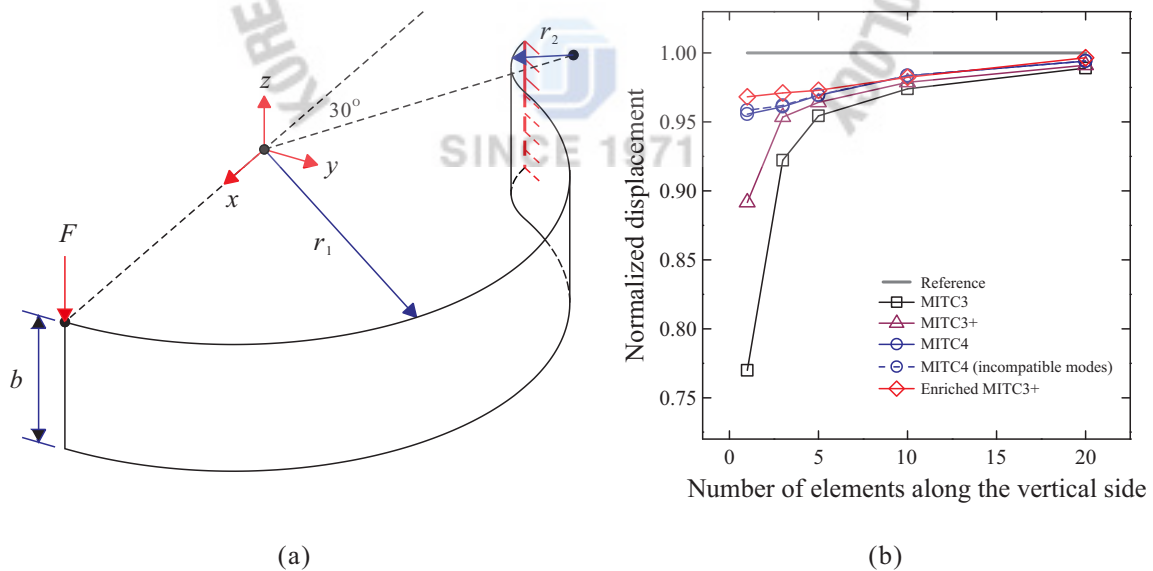


Figure 6.14. Raasch's Hook. (a) Problem description. (b) Normalized displacement in the linear analysis of the Raasch's Hook problem.

The Raasch's Hook problem [173] is useful in the evaluation of a given element's ability to properly reproduce coupling among bending, extension and twisting deformation patterns. A curved strip is clamped rigidly at one end and subjected to a unit load distributed along the width of the free end, see **Figure 6.14(a)**. The width and radius of the Raasch's hook are $b = 20$, $r_1 = 46$ and $r_2 = 14$, respectively, and the thickness is $h = 0.03$; the material constants are $E = 3.3 \times 10^3$ and $\nu = 0.35$. The linear loading $\mathbf{F} = F\mathbf{e}_z$, where $F = 1$ is applied on the side of the hook. The reference solution of 5.027 for the displacement in the load direction of the free edge is used [173]. The structure is modeled using 1×9 , 3×18 , 5×36 , 10×72 and 20×144 element meshes of the shell elements. **Figure 6.14(b)** and **Table 6.14** present the tip deflection at free end that was normalized by the reference solution. The performance of the enriched MITC3+ shell element is compared to those obtained with the different types of other MITC shell elements. The results show that the proposed shell element possesses fast convergence to the reference solution.

Table 6.14. Displacements and normalized displacements at point A for the Raasch's Hook problem shown in Figure 6.14(a). Normalized displacement (ND) = w_A / w_A^{ref} where w_A^{ref} and w_A denote the reference and finite element solutions, respectively.

Element type	Mesh				
	1×9	3×18	5×36	10×72	20×144
	Disp. (ND)				
MITC3	-3.853 (0.766)	-4.617 (0.918)	-4.778 (0.951)	-4.877 (0.970)	-4.951 (0.985)
MITC3+	-4.463 (0.888)	-4.774 (0.950)	-4.827 (0.960)	-4.899 (0.975)	-4.962 (0.987)
MITC4	-4.784 (0.952)	-4.811 (0.957)	-4.852 (0.965)	-4.923 (0.979)	-4.976 (0.990)
MITC4*	-4.797 (0.954)	-4.816 (0.958)	-4.854 (0.966)	-4.923 (0.979)	-4.976 (0.990)
Enriched MITC3+	-4.847 (0.964)	-4.861 (0.967)	-4.871 (0.969)	-4.918 (0.978)	-4.988 (0.992)
Allman	-4.233 (0.842)	-4.644 (0.924)	-4.805 (0.956)	-5.330 (1.060)	-7.343 (1.461)
Cook, Flat-stiffened	-4.249 (0.845)	-4.656 (0.926)	-4.902 (0.975)	-5.951 (1.184)	-9.582 (1.906)
Providas and Kattis	-4.265 (0.848)	-4.687 (0.932)	-5.106 (1.016)	-7.132 (1.419)	-15.13 (3.010)
OPT	-4.261 (0.848)	-4.644 (0.924)	-4.756 (0.946)	-4.876 (0.970)	-4.972 (0.989)
Reference solution $w_A^{ref} = -5.027$ [173]					

6.4.2 Nonlinear Benchmark Problems

In this section, the performance of the enriched MITC3+ shell element is evaluated in the nonlinear range. The iterations to solve the nonlinear equations have been performed in each load step to a convergence tolerance of 0.1 percent on the relative incremental energy.

6.4.2.1 Cantilever Beam Subjected to a Tip Moment

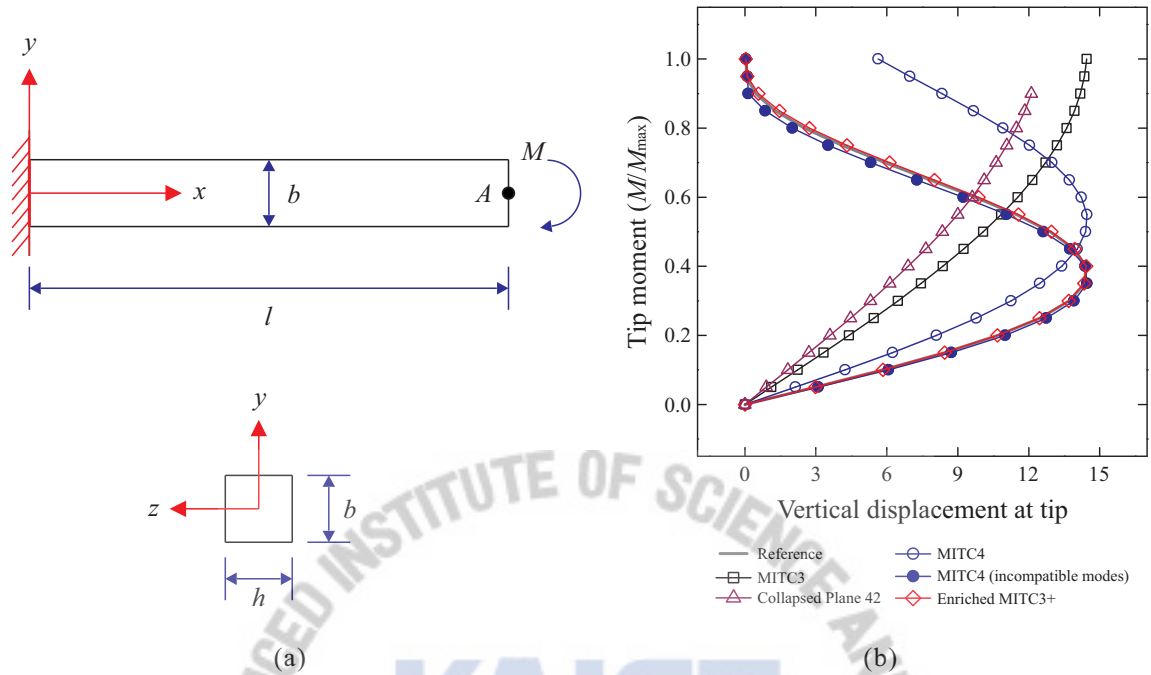


Figure 6.15. Cantilever beam subjected to a tip moment. (a) Problem description. (b) Load-displacement curve for the cantilever beam subjected to a tip moment.

A cantilever beam subjected to a tip moment $M = 10\pi$ as shown in **Figure 6.15(a)** is considered for large deformation test. The length, depth and thickness of the beam are $l = 20$, $b = 1$ and $h = 1$, respectively. The Young's modulus and Poisson's ratio are taken as $E = 1200$ and $\nu = 0.2$, respectively. By classical beam theory, this tip moment is just sufficient to roll up the cantilever beam into a circular ring with its ends butting each other. This cantilever beam is modeled using a 2×20 element mesh and results are not depend on mesh patterns for triangular elements. The reference solutions are obtained using a 4×40 element mesh of the MITC9 shell element. The vertical displacement at point A for this problem are plotted in **Figure 6.15(b)** and listed in **Table 6.15**. As we can see, the present element gives better performance than collapsed Plane 42 triangular element [174], MITC3 and MITC4 element, and compares favorably with MITC9 element [22]. The final deformed shapes are shown in **Figure 6.16**. The present element is able to simulate very large deformation accurately.

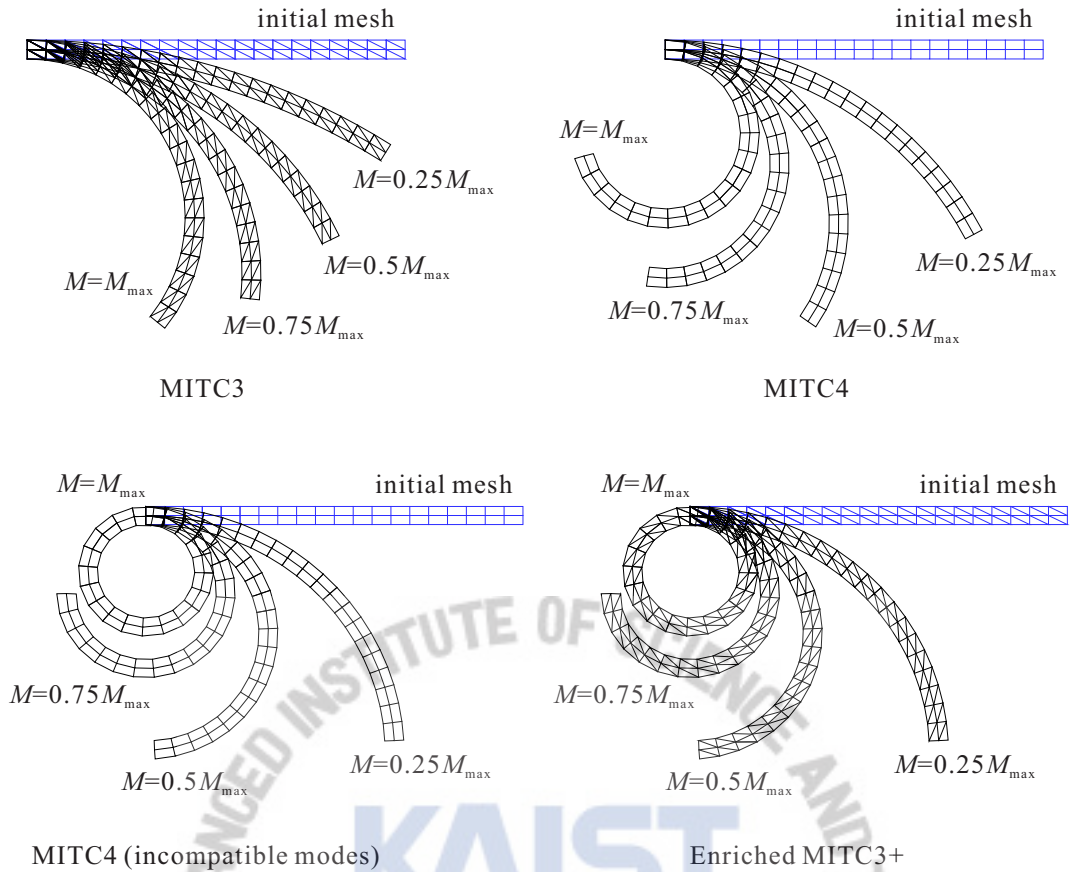


Figure 6.16. Deformed configurations of the cantilever beam subjected a tip moment.

Table 6.15. Normalized load-vertical deflections at point *A* for the cantilever beam subjected a tip moment.

Normalized load	MITC3	MITC4	MITC4*	Enriched MITC3+	Collapsed Plane42 triangle	Plane82	Reference
0.1	2.23	4.24	6.07	5.84	1.81	5.84	5.84
0.2	4.41	8.10	11.01	10.68	3.60	10.66	10.70
0.3	6.47	11.25	13.91	13.69	5.31	13.68	13.71
0.4	8.37	13.40	14.39	14.42	6.90	14.50	14.42
0.5	10.07	14.40	12.61	12.96	8.35	13.22	12.90
0.6	11.53	14.22	9.24	9.88	9.61	10.38	9.74
0.7	12.72	12.98	5.32	6.12	10.62	6.82	5.92
0.8	13.60	10.91	2.01	2.73	11.48	3.46	2.53
0.9	14.18	8.33	0.14	0.57	12.11	1.06	0.46
1.0	14.45	5.64	0.05	0.04	-	0.03	0.07

The reference solutions are obtained using a 4×40 element mesh of the MITC9 shell elements

6.4.2.2 Column under an Eccentric Compressive Load

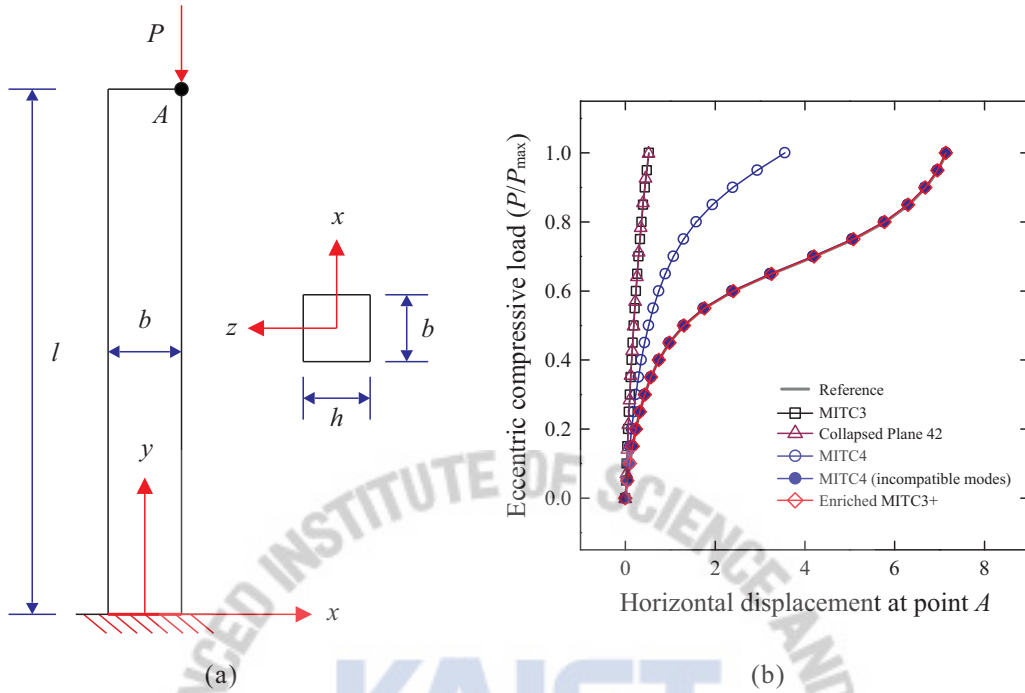


Figure 6.17. Column under an eccentric compressive load. (a) Problem description. (b) Load-displacement curves for the column.

A column is subjected to an eccentric compressive load shown in **Figure 6.17(a)**. The length l , width b and thickness h are 10, 1 and 1, respectively. The Young's modulus and Poisson's ratio are given by $E = 10^6$ and $\nu = 0$, respectively. The geometry is meshed with 2×10 elements as shown in **Figure 6.18**. The reference solutions are obtained using a 4×20 element mesh of the MITC9 shell element. The horizontal deflection at point A for the column and the corresponding load-deflection responses are plotted in **Figure 6.17(b)** and listed in **Table 6.16**. The final deformed shapes are shown in **Figure 6.18**. As seen from these results, the deflections given by the present element are almost the same as that of the reference using the MITC9 shell element, MITC4 with incompatible modes, whereas the collapsed Plane 42 [174], MITC3 and MITC4 element yields very bad results.

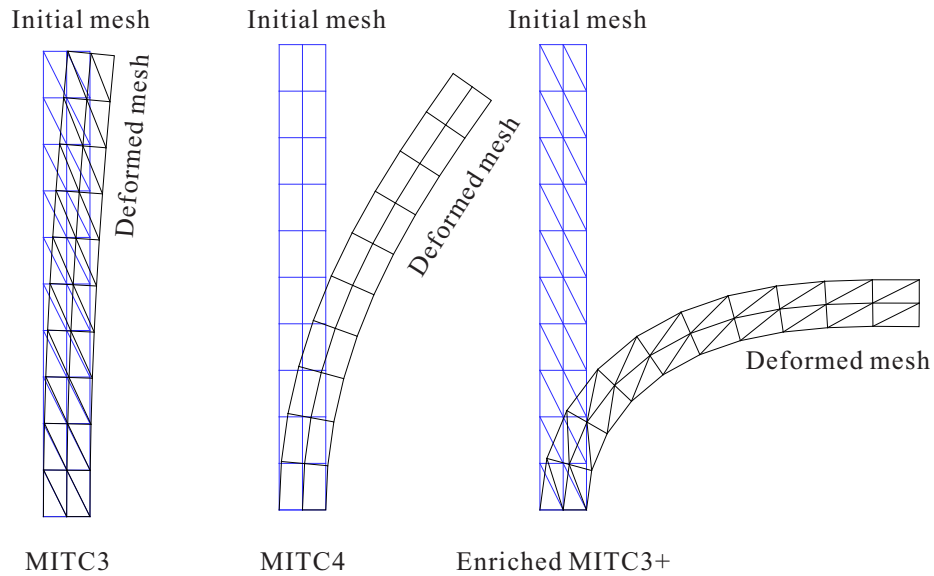


Figure 6.18. Deformed configurations for the column under an eccentric compressive load.

Table 6.16. Normalized load-horizontal deflections at point *A* for the column under an eccentric compressive load.

Normalized load	MITC3	MITC4	MITC4*	Enriched MITC3+	Collapsed Plane42 triangle	Plane82	Reference
0.071	0.0207	0.0429	0.0667	0.0668	0.0414	0.0090	0.0669
0.143	0.0430	0.0923	0.1499	0.1503	0.0846	0.0210	0.1505
0.214	0.0669	0.1499	0.2562	0.2570	0.0130	0.0360	0.2574
0.286	0.0926	0.2178	0.3965	0.3980	0.0178	0.0560	0.3987
0.357	0.1204	0.2987	0.5891	0.5917	0.0228	0.0870	0.5928
0.429	0.1506	0.3969	0.8672	0.8718	0.0282	0.1360	0.8736
0.500	0.1833	0.5181	1.2946	1.3032	0.0339	0.2300	1.3062
0.571	0.2189	0.6709	1.9911	2.0072	0.0401	0.4380	2.0127
0.643	0.2579	0.8687	3.0960	3.1210	0.0468	0.9060	3.1312
0.714	0.3007	1.1320	4.4440	4.4682	0.0541	1.7620	4.4843
0.786	0.3479	1.4931	5.5777	5.5928	0.0622	2.8370	5.6125
0.857	0.4002	1.9979	6.3531	6.3596	0.0711	3.9350	6.3798
0.929	0.4583	2.6912	6.8441	6.8452	0.0812	4.9430	6.8638
1.000	0.5234	3.5544	7.1415	7.1392	0.0926	5.8620	7.1553

The reference solutions are obtained using a 4×20 element mesh of the MITC9 shell elements

6.4.2.3 Curved Cantilever Beam

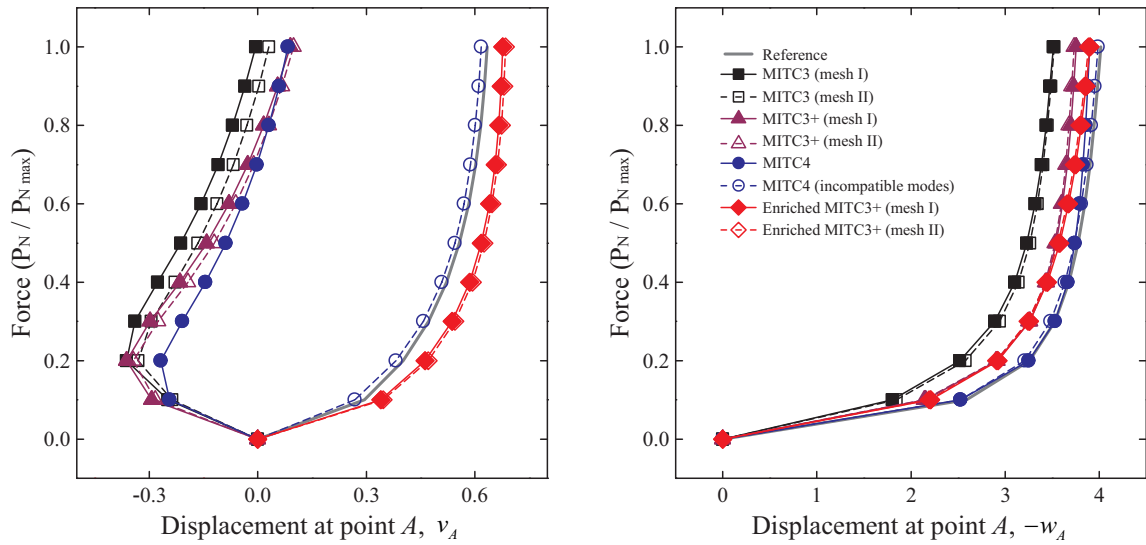


Figure 6.19. Load-displacement curves for the curved cantilever beam.

The curved cantilever beam shown in Figure 6.8(a) is clamped at one end and subjected to two forces at the other. This problem is tested in the linear range, see section 6.1.4. The material properties and geometry are chosen as the same in the linear analysis. The forces applied to the cantilever beam are increased up to $P_N = 100 \times (P_1 + P_2)$. The problem is modeled using a 1×6 element mesh of the MITC4, MITC3, MITC3+ and enriched MITC3+ shell element. The reference solutions are calculated using 2×12 element mesh of the MITC9 shell element. Figure 6.19(b), Table 6.17 and Table 6.18 show the calculated displacement at point A versus the forces, and Figure 6.20 shows the deformed shapes calculated using the 1×6 element mesh of the MITC4, MITC3, and enriched MITC3+ shell finite element. The vertical displacements using the MITC4, MITC3 and MITC3+ shell element display much too stiff compared with the reference. However, the MITC4 with incompatible modes and enriched MITC3+ shell finite element show excellent results compared to the reference solutions.

Table 6.17. Normalized load-vertical displacements at point A for the curved beam.

Nor. load	MITC3 (mesh I)	MITC3 (mesh II)	MITC3+ (mesh I)	MITC3+ (mesh II)	MITC4	MITC4*	Enriched MITC3+ (mesh I)	Enriched MITC3+ (mesh II)	Ref. MITC9
0.1	-0.247	-0.237	-0.293	-0.283	-0.244	0.268	0.339	0.347	0.295
0.2	-0.362	-0.330	-0.363	-0.343	-0.268	0.382	0.462	0.471	0.401
0.3	-0.339	-0.294	-0.298	-0.275	-0.209	0.457	0.536	0.545	0.472
0.4	-0.276	-0.228	-0.215	-0.193	-0.144	0.509	0.585	0.593	0.522
0.5	-0.213	-0.166	-0.141	-0.121	-0.088	0.544	0.618	0.625	0.557
0.6	-0.157	-0.113	-0.079	-0.061	-0.042	0.570	0.640	0.647	0.583
0.7	-0.110	-0.068	-0.028	-0.012	-0.003	0.588	0.655	0.663	0.602

0.8	-0.070	-0.030	0.016	0.030	0.031	0.601	0.666	0.673	0.616
0.9	-0.035	0.003	0.055	0.066	0.059	0.610	0.673	0.680	0.626
1.0	-0.005	0.031	0.090	0.099	0.084	0.617	0.677	0.685	0.634

Nor. Load : $P_N / P_{N \max}$

Ref. : Reference solutions obtained using a 2×12 element mesh of the MITC9 shell elements

Table 6.18. Normalized load-horizontal displacements at point A for the curved beam.

Nor. load	MITC3 (mesh I)	MITC3 (mesh II)	MITC3+ (mesh I)	MITC3+ (mesh II)	MITC4	MITC4*	Enriched MITC3+ (mesh I)	Enriched MITC3+ (mesh II)	Ref. MITC9
0.1	-1.804	-1.847	-2.155	-2.143	-2.526	-2.529	-2.212	-2.195	-2.591
0.2	-2.519	-2.578	-2.915	-2.906	-3.252	-3.207	-2.926	-2.910	-3.261
0.3	-2.892	-2.943	-3.263	-3.252	-3.533	-3.485	-3.258	-3.242	-3.532
0.4	-3.102	-3.142	-3.441	-3.428	-3.667	-3.637	-3.452	-3.435	-3.681
0.5	-3.232	-3.262	-3.545	-3.530	-3.743	-3.738	-3.581	-3.564	-3.777
0.6	-3.320	-3.344	-3.613	-3.596	-3.793	-3.811	-3.676	-3.659	-3.848
0.7	-3.385	-3.404	-3.661	-3.644	-3.828	-3.869	-3.750	-3.732	-3.903
0.8	-3.436	-3.451	-3.699	-3.680	-3.856	-3.916	-3.809	-3.792	-3.947
0.9	-3.478	-3.490	-3.729	-3.710	-3.878	-3.955	-3.859	-3.842	-3.985
1.0	-3.514	-3.524	-3.755	-3.735	-3.897	-3.989	-3.902	-3.885	-4.017

Nor. Load : $P_N / P_{N \max}$

Ref. : Reference solutions obtained using a 2×12 element mesh of the MITC9 shell elements

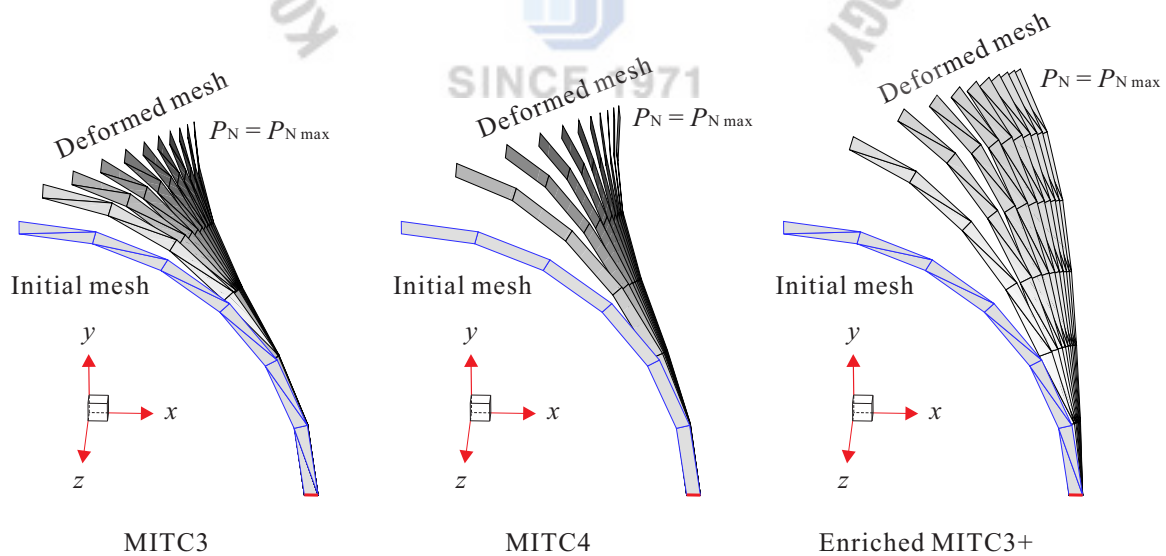


Figure 6.20. Deformed configurations for the curved cantilever beam.

6.4.2.4 Hemispherical Shell

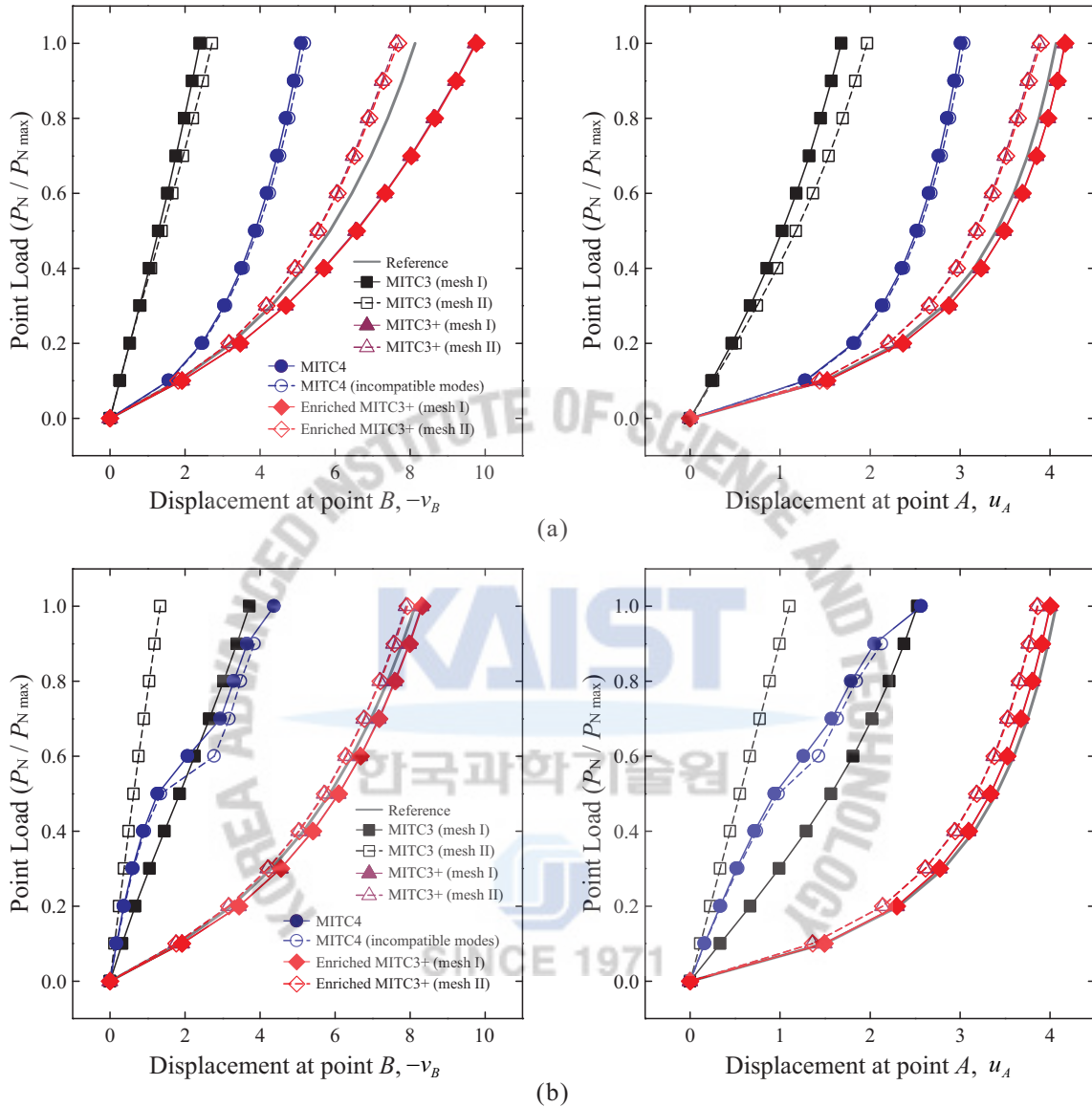


Figure 6.21. Load-displacement curves for the hemispherical shell with an 18° hole when (a) the uniform meshes and (b) the distorted meshes are used.

Again we consider two hemispherical shell problems, hemispherical shell with an 18° hole and full hemispherical shell, as shown **Figure 6.9(a)**. The material and geometric properties are given as the same in the linear analysis, see Section 6.1.5. Taking advantage of symmetry, a quadrant of the shell is used.

Table 6.19. Normalized load-radial displacements at the point B for the hemispherical shell with an 18° hole with the uniform meshes. The results are obtained using the 6×6 element mesh of the shell elements.

Nor. Load	MITC3 (mesh I)	MITC3 (mesh II)	MITC3+ (mesh I)	MITC3+ (mesh II)	MITC4	MITC4*	Enriched MITC3+ (mesh I)	Enriched MITC3+ (mesh II)	Ref.
0.1	-0.262	-0.257	-1.915	-1.813	-1.563	-1.577	-1.919	-1.817	-1.825
0.2	-0.525	-0.528	-3.463	-3.168	-2.442	-2.474	-3.474	-3.178	-3.233
0.3	-0.784	-0.809	-4.679	-4.162	-3.041	-3.085	-4.693	-4.177	-4.303
0.4	-1.039	-1.095	-5.686	-4.925	-3.498	-3.552	-5.705	-4.944	-5.154
0.5	-1.286	-1.382	-6.554	-5.534	-3.869	-3.932	-6.576	-5.559	-5.856
0.6	-1.526	-1.666	-7.321	-6.041	-4.182	-4.252	-7.344	-6.071	-6.449
0.7	-1.757	-1.944	-8.009	-6.478	-4.453	-4.528	-8.034	-6.514	-6.958
0.8	-1.979	-2.213	-8.636	-6.872	-4.691	-4.771	-8.661	-6.915	-7.400
0.9	-2.193	-2.472	-9.211	-7.246	-4.903	-4.988	-9.235	-7.296	-7.788
1.0	-2.398	-2.719	-9.745	-7.628	-5.094	-5.184	-9.767	-7.688	-8.132

Nor. Load : $P_N / P_{N \max}$

Ref. : Reference solutions obtained using a 16×16 element mesh of the MITC9 shell elements

Table 6.20. Normalized load-radial displacements at the point A for the hemispherical shell with an 18° hole with the uniform meshes. The results are obtained using the 6×6 element mesh of the shell elements.

Nor. load	MITC3 (mesh I)	MITC3 (mesh II)	MITC3+ (mesh I)	MITC3+ (mesh II)	MITC4	MITC4*	Enriched MITC3+ (mesh I)	Enriched MITC3+ (mesh II)	Ref.
0.1	0.241	0.258	1.522	1.438	1.279	1.289	1.524	1.441	1.498
0.2	0.463	0.508	2.361	2.203	1.816	1.833	2.365	2.208	2.321
0.3	0.668	0.746	2.875	2.655	2.131	2.153	2.878	2.662	2.818
0.4	0.855	0.970	3.228	2.956	2.351	2.375	3.232	2.966	3.156
0.5	1.026	1.177	3.489	3.177	2.519	2.545	3.493	3.188	3.405
0.6	1.181	1.368	3.691	3.351	2.652	2.680	3.694	3.364	3.597
0.7	1.323	1.541	3.850	3.497	2.763	2.793	3.853	3.512	3.750
0.8	1.453	1.697	3.978	3.628	2.858	2.888	3.981	3.644	3.876
0.9	1.572	1.839	4.082	3.752	2.939	2.971	4.084	3.770	3.981
1.0	1.682	1.967	4.166	3.879	3.011	3.043	4.169	3.898	4.070

Nor. Load : $P_N / P_{N \max}$

Ref. : Reference solutions obtained using a 16×16 element mesh of the MITC9 shell elements

For the hemispherical shell with an 18° hole, this problem is a very useful example to check the ability of the element to handle rigid body rotation about the normal to the shell surface and the inextensible bending modes. The point load is incrementally applied to a maximum value $P_{\max} = 400/2$. The shell is

modeled using a 6×6 element mesh of the shell element with the uniform and distorted meshes. A 16×16 element mesh of the MITC9 shell element is used to obtain the reference solutions.

Table 6.21. Normalized load-radial displacements at the point B for the hemispherical shell with an 18° hole with the distorted meshes shown in Figure 6.10. The results are obtained using the 6×6 element mesh of the shell elements.

Nor. load	MITC3 (mesh I)	MITC3 (mesh II)	MITC3+ (mesh I)	MITC3+ (mesh II)	MITC4	MITC4*	Enriched MITC3+ (mesh I)	Enriched MITC3+ (mesh II)	Ref.
0.1	-0.316	-0.120	-1.912	-1.749	-0.170	-0.176	-1.913	-1.760	-1.825
0.2	-0.669	-0.243	-3.435	-3.153	-0.365	-0.378	-3.440	-3.167	-3.233
0.3	-1.050	-0.367	-4.545	-4.202	-0.595	-0.618	-4.554	-4.219	-4.303
0.4	-1.449	-0.495	-5.400	-5.029	-0.880	-0.920	-5.411	-5.049	-5.154
0.5	-1.854	-0.626	-6.090	-5.706	-1.265	-1.347	-6.102	-5.727	-5.856
0.6	-2.256	-0.760	-6.667	-6.275	-2.074	-2.779	-6.680	-6.297	-6.449
0.7	-2.647	-0.899	-7.161	-6.762	-2.946	-3.176	-7.175	-6.787	-6.958
0.8	-3.023	-1.042	-7.591	-7.186	-3.303	-3.483	-7.608	-7.214	-7.400
0.9	-3.379	-1.189	-7.972	-7.560	-3.658	-3.848	-7.990	-7.591	-7.788
1.0	-3.716	-1.341	-8.312	-7.894	-4.373	-	-8.333	-7.927	-8.132

Nor. Load : $P_N / P_{N \max}$

Ref. : Reference solutions obtained using a 16×16 element mesh of the MITC9 shell elements

Table 6.22. Normalized load-radial displacements at the point A for the hemispherical shell with an 18° hole with the distorted meshes shown in Figure 6.10. The results are obtained using the 6×6 element mesh of the shell elements.

Nor. load	MITC3 (mesh I)	MITC3 (mesh II)	MITC3+ (mesh I)	MITC3+ (mesh II)	MITC4	MITC4*	Enriched MITC3+ (mesh I)	Enriched MITC3+ (mesh II)	Ref.
0.1	0.334	0.112	1.494	1.359	0.161	0.166	1.495	1.365	1.498
0.2	0.668	0.224	2.297	2.136	0.333	0.343	2.299	2.142	2.321
0.3	0.991	0.334	2.772	2.611	0.516	0.533	2.775	2.617	2.818
0.4	1.293	0.444	3.096	2.938	0.716	0.742	3.100	2.945	3.156
0.5	1.566	0.554	3.335	3.182	0.940	0.983	3.340	3.189	3.405
0.6	1.810	0.664	3.523	3.373	1.261	1.430	3.528	3.380	3.597
0.7	2.025	0.774	3.674	3.526	1.575	1.636	3.680	3.534	3.750
0.8	2.214	0.884	3.801	3.654	1.792	1.849	3.806	3.662	3.876
0.9	2.380	0.995	3.907	3.762	2.050	2.131	3.913	3.771	3.981
1.0	2.525	1.106	3.999	3.855	2.569	-	4.005	3.864	4.070

Nor. Load : $P_N / P_{N \max}$

Ref. : Reference solutions obtained using a 16×16 element mesh of the MITC9 shell elements

Figure 6.21 shows the load-radial displacement curves at the loaded point *A* and *B*. **Table 6.19 - Table 6.22** list the same deflections and **Figure 6.22** shows the deformed configurations obtained using a 6×6 element mesh of the enriched MITC3+ shell element. The enriched MITC3+ shell element shows a good performance regardless of which mesh pattern in **Figure 6.10** is used.

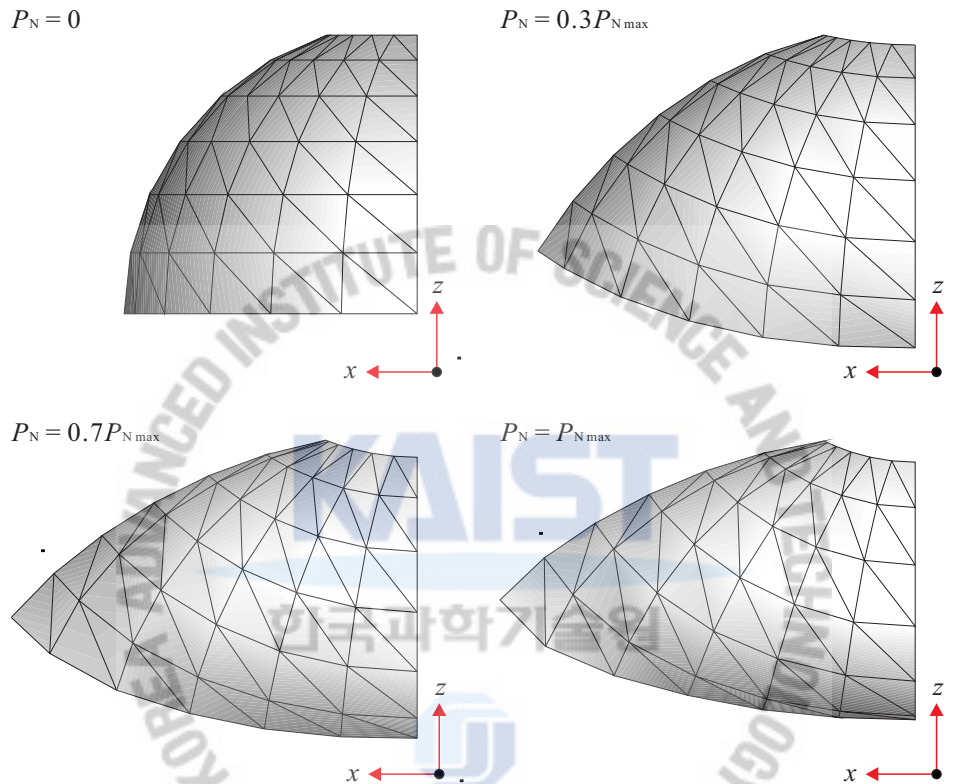


Figure 6.22. Deformed configurations for the hemispherical shell with an 18° hole.

For the full hemispherical shell, the load applied to *z*-direction at point *C* is increased up to $P_{NZ \max} = 150000 / 4$. The shell is modeled using $3 \times 4 \times 4$ and $3 \times 6 \times 6$ element meshes of the shell element and the reference solution is obtained by $3 \times 8 \times 8$ element mesh of the MITC9 shell element. **Figure 6.23** shows the load-radial displacement curves at the loaded points *C*. Numerical results are also tabulated in **Table 6.23** and **Table 6.24**. The MITC4 with incompatible modes and enriched MITC3+ shell elements produce much better solution accuracy than the MITC3 and MITC4 shell element in this problem.

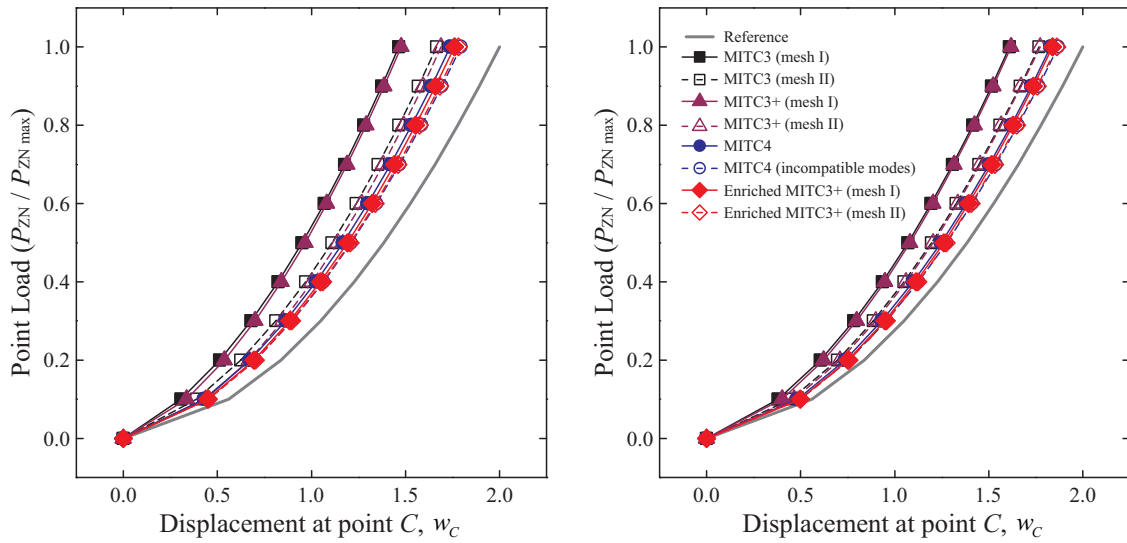


Figure 6.23. Load-displacement curves for the full hemispherical shell with a $3 \times 4 \times 4$ element mesh (left) and a $3 \times 6 \times 6$ element mesh (right).

Table 6.23. Normalized load-vertical displacements at the point C for the full hemispherical shell with $3 \times 4 \times 4$ element meshes.

Nor. load	MITC3 (mesh I)	MITC3 (mesh II)	MITC3+ (mesh I)	MITC3+ (mesh II)	MITC4	MITC4*	Enriched MITC3+ (mesh I)	Enriched MITC3+ (mesh II)	Ref.
0.1	0.307	0.389	0.336	0.439	0.430	0.451	0.448	0.453	0.560
0.2	0.513	0.625	0.538	0.669	0.673	0.702	0.694	0.702	0.837
0.3	0.679	0.811	0.700	0.850	0.863	0.897	0.885	0.896	1.049
0.4	0.822	0.969	0.840	1.004	1.025	1.064	1.047	1.061	1.227
0.5	0.951	1.110	0.967	1.142	1.169	1.212	1.191	1.207	1.384
0.6	1.068	1.237	1.083	1.267	1.299	1.346	1.322	1.339	1.526
0.7	1.177	1.355	1.190	1.383	1.420	1.469	1.442	1.461	1.657
0.8	1.279	1.465	1.291	1.491	1.532	1.584	1.555	1.575	1.778
0.9	1.375	1.569	1.386	1.593	1.638	1.693	1.660	1.682	1.892
1.0	1.466	1.667	1.477	1.690	1.738	1.796	1.760	1.783	2.000

Nor. Load : $P_{NZ} / P_{NZ \max}$

Ref. : Reference solutions obtained using a $3 \times 8 \times 8$ element mesh of the MITC9 shell elements

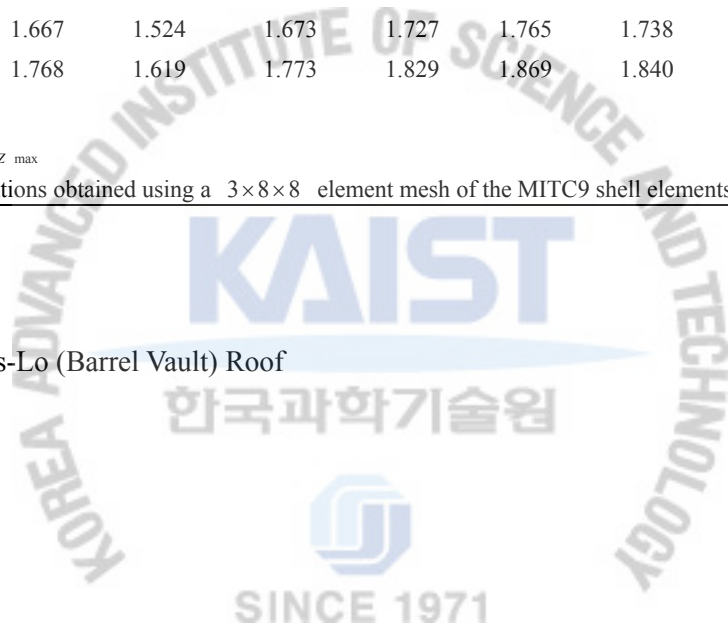
Table 6.24. Normalized load-vertical displacements at the point *C* for the full hemispherical shell with $3 \times 6 \times 6$ element meshes.

Nor. load	MITC3 (mesh I)	MITC3 (mesh II)	MITC3+ (mesh I)	MITC3+ (mesh II)	MITC4	MITC4*	Enriched MITC3+ (mesh I)	Enriched MITC3+ (mesh II)	Ref.
0.1	0.380	0.449	0.403	0.465	0.484	0.498	0.498	0.500	0.560
0.2	0.605	0.695	0.623	0.709	0.736	0.756	0.752	0.757	0.837
0.3	0.783	0.887	0.797	0.899	0.932	0.956	0.948	0.956	1.049
0.4	0.935	1.051	0.947	1.060	1.099	1.126	1.114	1.125	1.227
0.5	1.071	1.195	1.082	1.204	1.246	1.276	1.260	1.274	1.384
0.6	1.194	1.327	1.204	1.335	1.380	1.413	1.394	1.408	1.526
0.7	1.308	1.448	1.318	1.455	1.504	1.538	1.516	1.533	1.657
0.8	1.415	1.561	1.424	1.567	1.619	1.655	1.630	1.649	1.778
0.9	1.516	1.667	1.524	1.673	1.727	1.765	1.738	1.758	1.892
1.0	1.611	1.768	1.619	1.773	1.829	1.869	1.840	1.862	2.000

Nor. Load : $P_{NZ} / P_{NZ \max}$

Ref. : Reference solutions obtained using a $3 \times 8 \times 8$ element mesh of the MITC9 shell elements

6.4.2.5 Scordelis-Lo (Barrel Vault) Roof



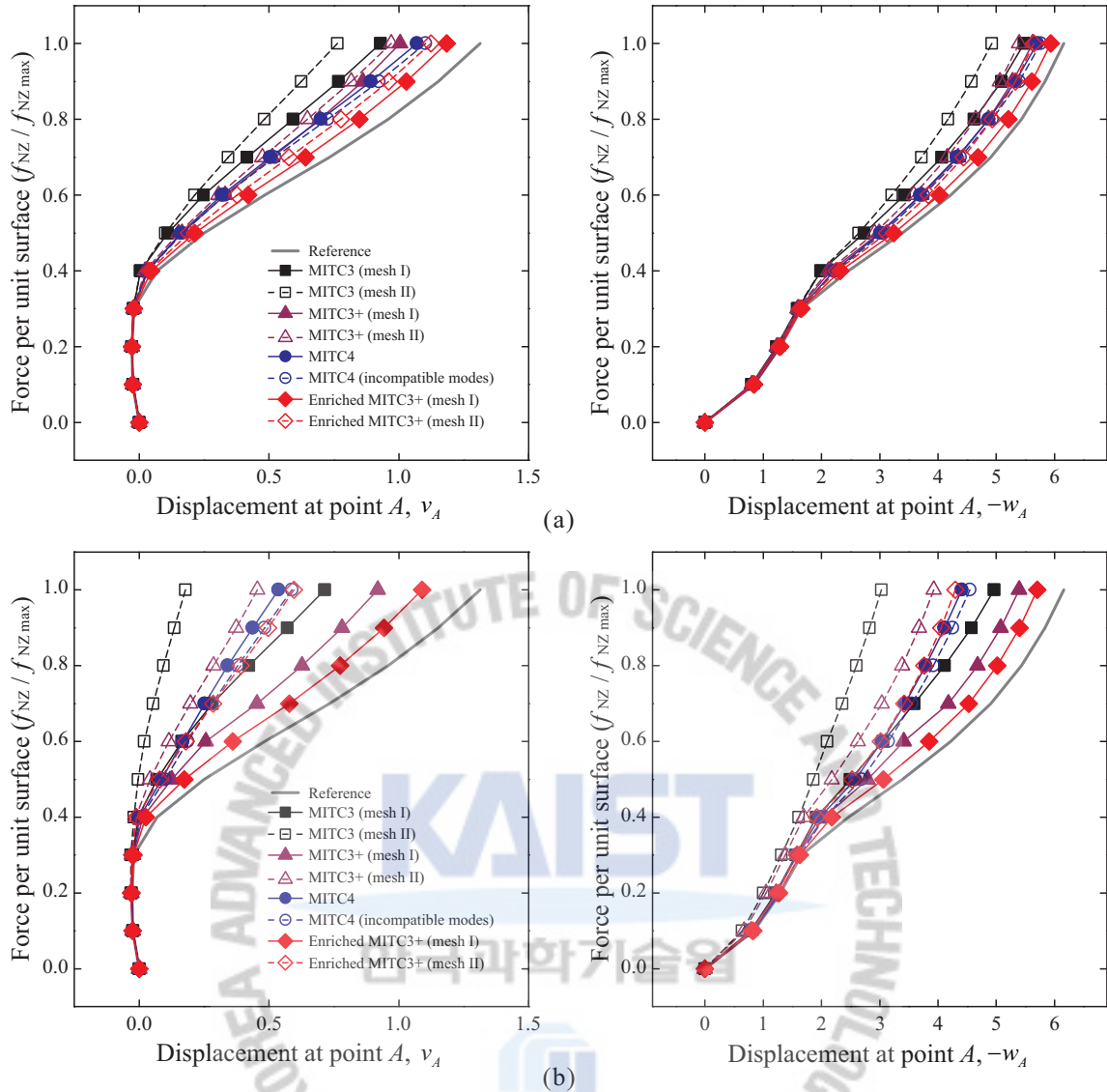


Figure 6.24. Load-displacement curves for the Scordelis-Lo roof with (a) the uniform meshes and (b) the distorted meshes.

Scordelis-Lo Roof problem is also considered in nonlinear range. The same geometry and material properties that is used in the linear analysis are adopted. The load applied to the shell increases up to $f_{Nz} = 50 \times 90$ per unit area. The shell is modeled using 14×14 element meshes of the shell elements and 24×24 element meshes of the MITC9 shell element is used to obtain the reference solutions. **Figure 6.24** shows the calculated load-displacement curves when the uniform and distorted mesh patterns in **Figure 6.10**. Numerical results are also presented in **Table 6.25-Table 6.28**. Figure 6.24. The deformed configurations calculated in the enriched MITC3+ shell element are depicted in **Figure 6.25**. The enriched MITC3+ shell element exhibits the best performance, even though the distorted meshes are used.

Table 6.25. Normalized load-horizontal displacements at the point *A* for the Scordelis-Lo roof with the uniform meshes. The results are obtained using the 14×14 element mesh of the shell elements.

Nor. load	MITC3 (mesh I)	MITC3 (mesh II)	MITC3+ (mesh I)	MITC3+ (mesh II)	MITC4	MITC4*	Enriched MITC3+ (mesh I)	Enriched MITC3+ (mesh II)	Ref.
0.1	-0.024	-0.024	-0.024	-0.024	-0.024	-0.025	-0.024	-0.024	-0.025
0.2	-0.028	-0.029	-0.027	-0.028	-0.028	-0.028	-0.027	-0.028	-0.028
0.3	-0.022	-0.023	-0.020	-0.022	-0.021	-0.021	-0.020	-0.021	-0.021
0.4	0.004	0.005	0.029	0.023	0.031	0.034	0.047	0.038	0.068
0.5	0.110	0.101	0.164	0.152	0.161	0.167	0.214	0.192	0.250
0.6	0.248	0.213	0.330	0.305	0.319	0.330	0.420	0.376	0.483
0.7	0.415	0.343	0.513	0.475	0.504	0.523	0.641	0.577	0.732
0.8	0.594	0.482	0.696	0.648	0.700	0.726	0.848	0.776	0.959
0.9	0.768	0.624	0.861	0.817	0.893	0.924	1.029	0.960	1.152
1.0	0.929	0.763	1.006	0.971	1.070	1.103	1.185	1.123	1.314

Nor. Load : $f_{NZ} / f_{NZ \max}$

Ref. : Reference solutions obtained using a 24×24 element mesh of the MITC9 shell elements

Table 6.26. Normalized load-vertical displacements at the point *A* for the Scordelis-Lo roof with the uniform meshes. The results are obtained using the 14×14 element mesh of the shell elements.

Nor. load	MITC3 (mesh I)	MITC3 (mesh II)	MITC3+ (mesh I)	MITC3+ (mesh II)	MITC4	MITC4*	Enriched MITC3+ (mesh I)	Enriched MITC3+ (mesh II)	Ref.
0.1	-0.810	-0.798	-0.813	-0.802	-0.836	-0.844	-0.844	-0.835	-0.845
0.2	-1.245	-1.228	-1.251	-1.234	-1.277	-1.287	-1.291	-1.276	-1.291
0.3	-1.599	-1.581	-1.612	-1.590	-1.633	-1.643	-1.653	-1.634	-1.655
0.4	-1.992	-1.987	-2.161	-2.119	-2.218	-2.245	-2.323	-2.259	-2.460
0.5	-2.736	-2.643	-2.990	-2.911	-3.011	-3.047	-3.241	-3.120	-3.387
0.6	-3.426	-3.205	-3.713	-3.582	-3.700	-3.747	-4.029	-3.834	-4.215
0.7	-4.064	-3.716	-4.342	-4.157	-4.327	-4.384	-4.689	-4.436	-4.902
0.8	-4.624	-4.173	-4.866	-4.649	-4.871	-4.935	-5.207	-4.929	-5.433
0.9	-5.093	-4.575	-5.282	-5.062	-5.330	-5.393	-5.612	-5.326	-5.840
1.0	-5.482	-4.923	-5.624	-5.396	-5.706	-5.765	-5.939	-5.643	-6.163

Nor. Load : $f_{NZ} / f_{NZ \max}$

Ref. : Reference solutions obtained using a 24×24 element mesh of the MITC9 shell elements

Table 6.27. Normalized load-horizontal displacements at the point A for the Scordelis-Lo roof with the distorted meshes. The results are obtained using the 14×14 element mesh of the shell elements.

Nor. load	MITC3 (mesh I)	MITC3 (mesh II)	MITC3+ (mesh I)	MITC3+ (mesh II)	MITC4	MITC4*	Enriched MITC3+ (mesh I)	Enriched MITC3+ (mesh II)	Ref.
0.1	-0.025	-0.023	-0.025	-0.023	-0.024	-0.025	-0.025	-0.026	-0.025
0.2	-0.030	-0.032	-0.029	-0.030	-0.029	-0.029	-0.029	-0.032	-0.028
0.3	-0.024	-0.032	-0.023	-0.028	-0.024	-0.023	-0.022	-0.028	-0.021
0.4	-0.004	-0.020	0.014	-0.012	0.001	0.007	0.026	-0.009	0.068
0.5	0.069	-0.004	0.125	0.042	0.086	0.099	0.174	0.078	0.250
0.6	0.165	0.020	0.257	0.114	0.168	0.187	0.361	0.179	0.483
0.7	0.282	0.054	0.453	0.198	0.252	0.280	0.579	0.285	0.732
0.8	0.423	0.094	0.627	0.287	0.342	0.379	0.773	0.392	0.959
0.9	0.571	0.136	0.782	0.373	0.438	0.483	0.943	0.497	1.152
1.0	0.715	0.178	0.919	0.456	0.537	0.589	1.090	0.596	1.314

Nor. Load : $f_{NZ} / f_{NZ \max}$

Ref. : Reference solutions obtained using a 24×24 element mesh of the MITC9 shell elements

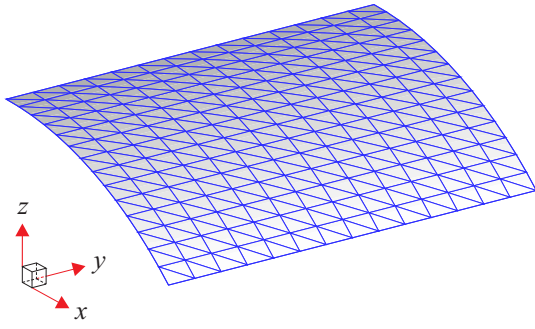
Table 6.28. Normalized load-vertical displacements at the point A for the Scordelis-Lo roof with the distorted meshes. The results are obtained using the 14×14 element mesh of the shell elements.

Nor. load	MITC3 (mesh I)	MITC3 (mesh II)	MITC3+ (mesh I)	MITC3+ (mesh II)	MITC4	MITC4*	Enriched MITC3+ (mesh I)	Enriched MITC3+ (mesh II)	Ref.
0.1	-0.785	-0.636	-0.789	-0.671	-0.803	-0.838	-0.828	-0.814	-0.845
0.2	-1.213	-1.002	-1.222	-1.048	-1.230	-1.276	-1.270	-1.237	-1.291
0.3	-1.563	-1.313	-1.582	-1.379	-1.577	-1.627	-1.629	-1.577	-1.655
0.4	-1.916	-1.607	-2.048	-1.698	-1.970	-2.049	-2.175	-1.918	-2.460
0.5	-2.494	-1.859	-2.789	-2.181	-2.582	-2.684	-3.060	-2.529	-3.387
0.6	-3.054	-2.099	-3.416	-2.627	-3.038	-3.150	-3.851	-3.017	-4.215
0.7	-3.592	-2.356	-4.180	-3.034	-3.429	-3.554	-4.526	-3.421	-4.902
0.8	-4.115	-2.601	-4.682	-3.384	-3.786	-3.920	-5.021	-3.762	-5.433
0.9	-4.575	-2.824	-5.074	-3.676	-4.114	-4.252	-5.401	-4.051	-5.840
1.0	-4.965	-3.028	-5.391	-3.925	-4.412	-4.551	-5.706	-4.297	-6.163

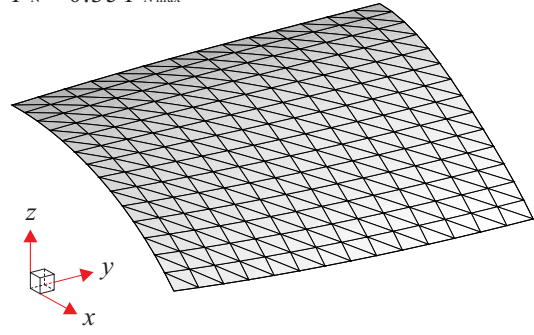
Nor. Load : $f_{NZ} / f_{NZ \max}$

Ref. : Reference solutions obtained using a 24×24 element mesh of the MITC9 shell elements

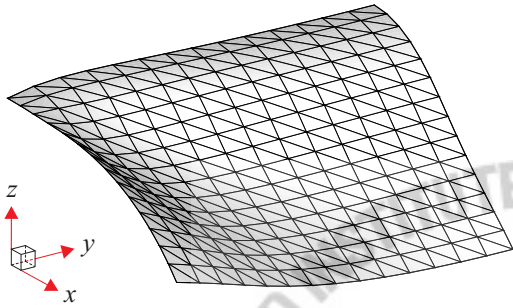
initial mesh



$F_N = 0.35 F_{N \max}$



$F_N = 0.7 F_{N \max}$



$F_N = F_{N \max}$

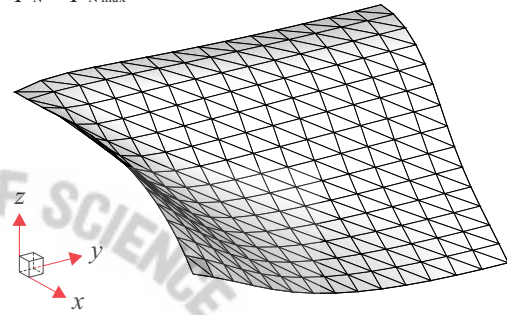
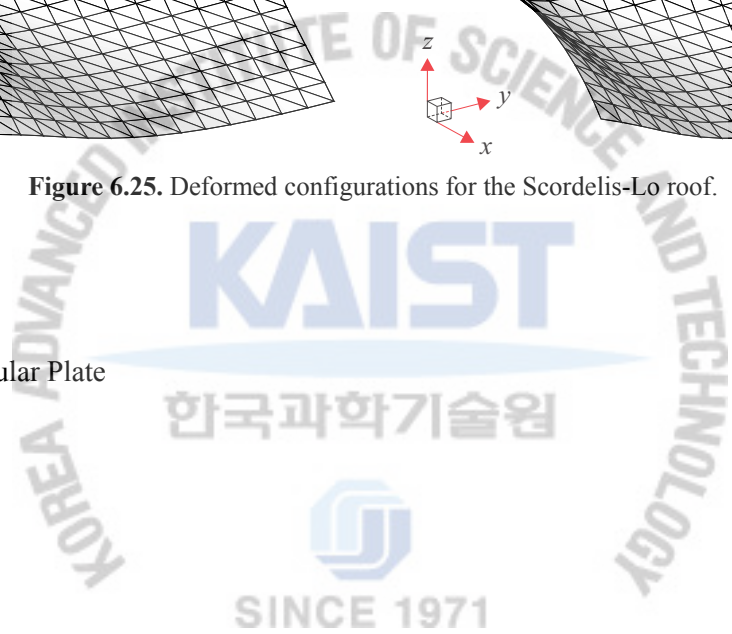


Figure 6.25. Deformed configurations for the Scordelis-Lo roof.

6.4.2.6 Slit Annular Plate



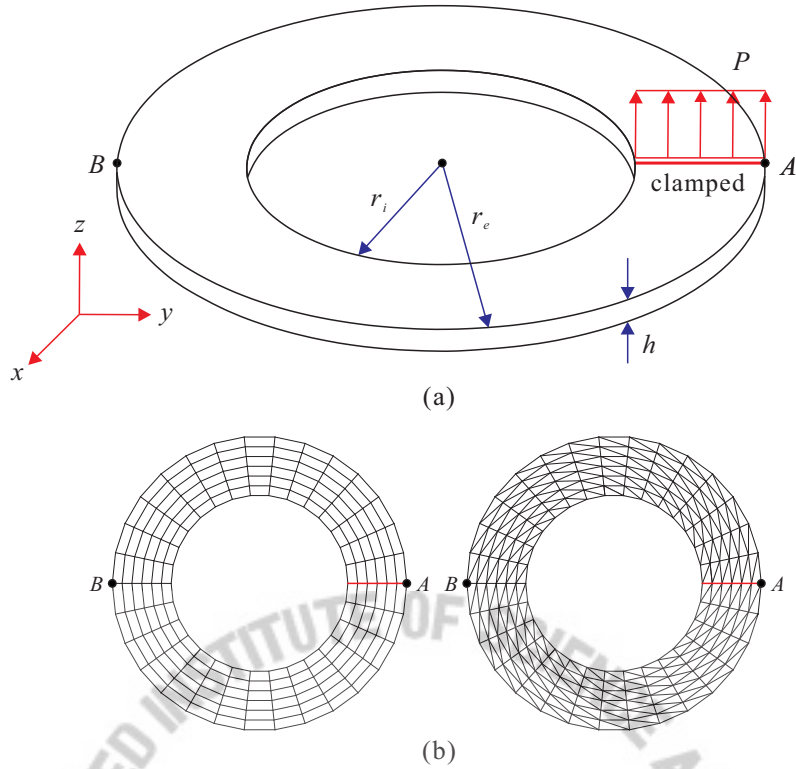


Figure 6.26. Slit annular plate subjected to lifting line force. (a) Problem description. (b) Mesh patterns used for the MITC3, MITC3+ and enriched MITC3+ shell elements.

A slit annular plate, as shown in **Figure 6.26(a)** is considered. This example was suggested by Bařar and Ding [150] and has been widely considered [139, 140, 151, 156]. The geometry and elastic material properties are given by $r_i = 6$, $r_e = 10$, $h = 0.03$, $E = 21 \times 10^6$ and $\nu = 0$. The transverse shear force $P_{\max} = 3.2$ is incrementally applied at one end of the slit while the other end of the slit is fully clamped. The plate undergoes large displacements and large rotations. This structure is modeled using a 6×30 element mesh of the shell element. For triangular shell element two different types of mesh patterns are used, see in **Figure 6.26(b)**. The reference solutions are obtained using a 12×60 element mesh of the MITC9 shell element. The load-displacement curves at two different points, A and B , are depicted in **Figure 6.27**. The displacements calculated are also tabulated in **Table 6.29** and **Table 6.30**. The deformed configurations calculated using the MITC3, MITC4, MITC3+ and enriched MITC3+ shell elements are shown in **Figure 6.28**. As seen, the MITC3 shell element displays too stiff a behavior. However, the results using the enriched MITC3+ shell element are in agreement with those using the MITC4 shell element with incompatible modes and reasonably close to the reference solutions.

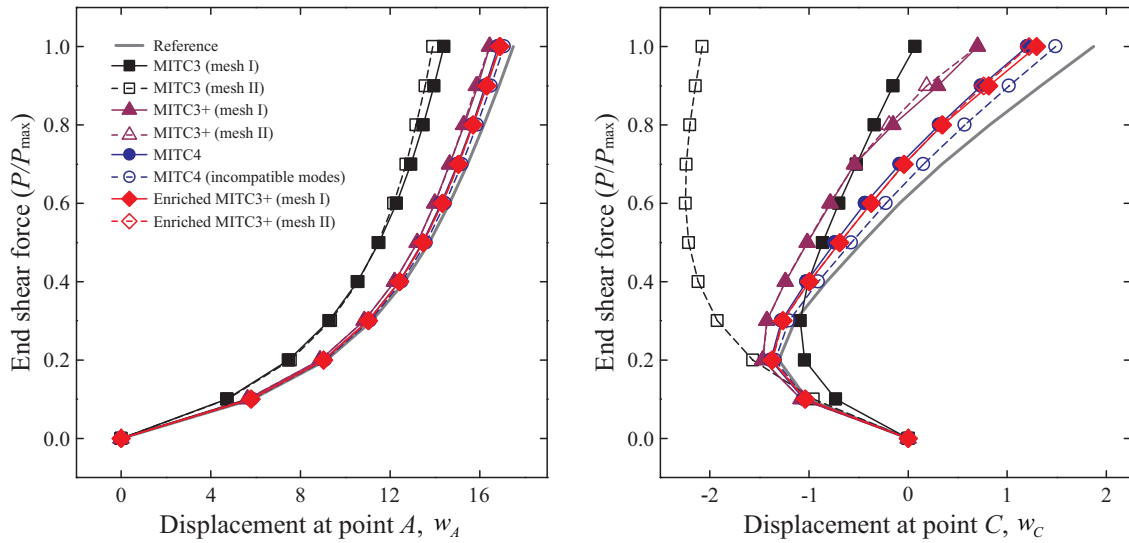


Figure 6.27. Load-displacement curves for the slit annular plate subjected to lifting line force.

Table 6.29. Normalized load-vertical displacements at the point A for the slit annular plate subjected to lift line force when the 6×30 element mesh is used.

Nor. load	MITC3 (mesh I)	MITC3 (mesh II)	MITC3+ (mesh I)	MITC3+ (mesh II)	MITC4	MITC4*	Enriched MITC3+ (mesh I)	Enriched MITC3+ (mesh II)	Ref.
0.1	4.706	4.743	5.630	5.630	5.764	5.839	5.797	5.797	5.862
0.2	7.467	7.548	8.858	8.858	9.009	9.089	9.023	9.024	9.143
0.3	9.268	9.347	10.841	10.842	11.013	11.107	11.023	11.025	11.196
0.4	10.540	10.573	12.196	12.197	12.399	12.518	12.419	12.421	12.640
0.5	11.504	11.464	13.201	13.200	13.439	13.587	13.476	13.477	13.742
0.6	12.275	12.148	13.992	13.990	14.273	14.452	14.322	14.325	14.643
0.7	12.915	12.698	14.649	14.653	14.995	15.198	15.038	15.044	15.435
0.8	13.462	13.157	15.296	15.274	15.650	15.873	15.694	15.692	16.165
0.9	13.945	13.550	15.907	15.841	16.249	16.493	16.322	16.296	16.846
1.0	14.387	13.895	16.441	16.414	16.813	17.073	16.909	16.865	17.484

Nor. Load : $f_{NZ} / f_{NZ \max}$

Ref. : Reference solutions obtained using a 12×60 element mesh of the MITC9 shell elements

Table 6.30. Normalized load-vertical displacements at the point C for the slit annular plate subjected to lift line force when the 6×30 element mesh is used.

Nor. load	MITC3 (mesh I)	MITC3 (mesh II)	MITC3+ (mesh I)	MITC3+ (mesh II)	MITC4	MITC4*	Enriched MITC3+ (mesh I)	Enriched MITC3+ (mesh II)	Ref.
0.1	-0.731	-0.956	-1.080	-1.078	-1.052	-1.037	-1.039	-1.036	-1.019
0.2	-1.042	-1.569	-1.468	-1.465	-1.386	-1.341	-1.374	-1.370	-1.304
0.3	-1.090	-1.924	-1.424	-1.423	-1.278	-1.200	-1.265	-1.261	-1.139
0.4	-1.006	-2.119	-1.239	-1.241	-1.026	-0.906	-0.997	-0.996	-0.822
0.5	-0.863	-2.215	-1.015	-1.020	-0.737	-0.573	-0.688	-0.688	-0.466
0.6	-0.697	-2.247	-0.784	-0.790	-0.431	-0.225	-0.372	-0.370	-0.087
0.7	-0.522	-2.238	-0.543	-0.539	-0.082	0.155	-0.043	-0.037	0.339
0.8	-0.341	-2.200	-0.151	-0.190	0.316	0.574	0.347	0.339	0.821
0.9	-0.151	-2.145	0.301	0.188	0.738	1.019	0.813	0.763	1.338
1.0	0.069	-2.077	0.700	0.703	1.204	1.491	1.299	1.219	1.871

Nor. Load : $f_{NZ} / f_{NZ \max}$

Ref. : Reference solutions obtained using a 12×60 element mesh of the MITC9 shell elements

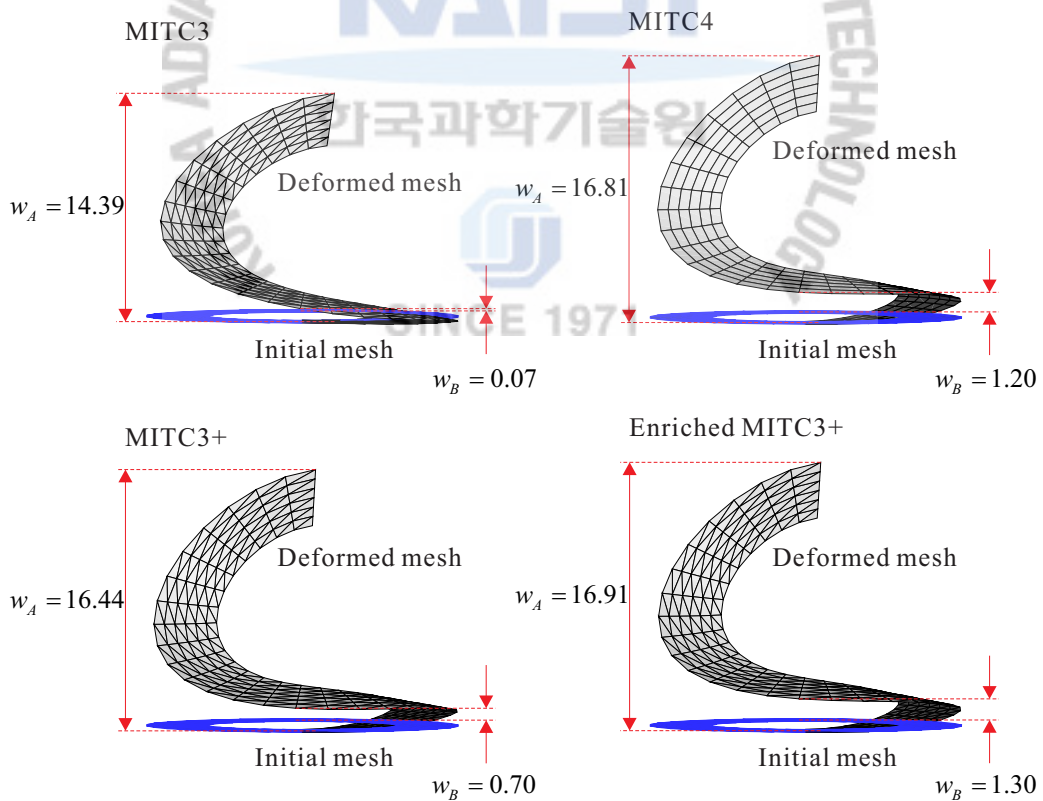


Figure 6.28. Deformed configuration for the slit annular plate subjected to lifting line force.

Chapter 7. Conclusions and Future Works

7.1 Conclusions

This thesis focused on a general procedure to improve solutions of the classical shell finite element using the partition of unity concept. The proposed shell elements are a direct extension of the traditional finite element formulation for the analyses of linear and nonlinear elastic shell structures. The partition of unity based shell elements provide smoother solutions and good convergence, and can be used with relatively coarse meshes. It has been demonstrated that the proposed elements are very effective and reliable both in linear and nonlinear analyses.

First, a partition of unity based 3-node triangular shell finite element was presented. The shell element was based on the MITC method to alleviate transverse shear locking, and referred to as the enriched MITC3 shell element. The enriched MITC3 shell finite element is obtained by applying linear displacement interpolation covers to the standard 3-node shell element, and using the MITC procedure. Good convergence behavior in the analysis of various shell problems has been seen, even when distorted meshes were used. The fact that, in the solutions considered, the enriched 3-node element sometimes performed significantly better than the MITC4 and MITC6 shell elements when distorted meshes were used is particularly noteworthy. The effectiveness of using the enrichment scheme only locally was also illustrated by using the cover interpolation functions only in critical areas of an analysis domain. It is concluded that cover interpolations and the MITC method are promising schemes for enriching shell element behaviors.

Second, a partition of unity based 4-node quadrilateral shell finite element was also proposed and called the enriched MITC4 shell element. To reduce the transverse shear locking, the enriched MITC4 shell element adopts the MITC4 method for the linear displacements and applies the MITC9 procedure for additional high order coefficients. Unlike the enriched MITC3 shell element, a special treatment constraining the additional unknown coefficients around the boundary nodes of the domain is applied to avoid the linear dependence problem. Good convergence behavior in the analysis of various benchmark shell problems has been seen, even when distorted meshes were used.

Third, the formulation of the MITC3+ shell element was reviewed and extended to geometric nonlinear analysis. The total Lagrangian formulation was employed allowing for large displacements and large rotations. The nonlinear formulation is based on the same discretization assumptions that are employed in the linear formulation of the element. The nonlinear performance of the MITC3+ shell element was numerically investigated by solving several benchmark problems. In the tests considered, the predictive capability of the MITC3+ shell element was seen to be much better than of the MITC3 shell element. Indeed, the MITC3+

element gave results that were practically as accurate as the MITC4 shell element. Also, considering the excellent behavior of the MITC3+ shell element in linear analysis, it is concluded that the element is a very attractive element for general shell analyses.

Finally, a triangular shell finite element with improved membrane behaviors is proposed. The partition of unity approximation was only applied into the membrane part of the MITC3+ shell element to enhance membrane behaviors. The key theoretical and numerical aspects of this element were discussed and the formulation of the shell was extended to geometric nonlinear analysis. A number of benchmark problems were studied to evaluate its performances in linear and geometric nonlinear ranges. The results confirm that the present method can provide accurate solutions for membrane dominant problems. It is concluded that the partition of unity approximation is an effective remedy for improving membrane behaviors in the triangular shell element.

7.2 Future Works

Based on the observed good behavior of the partition of unity based shell finite elements, it is expected that the partition of unity approximation will likely also be effective in other structural elements such as flat shell and beam elements. It would be valuable to mathematically analyze the method, to further test the scheme, and to develop the formulation for large strain solutions of shell structures [175] and for solving problems containing very high stress gradients, like shell problems containing cracks [40, 157, 158]. In all of these developments, the ultimate aim should probably be to establish automatic procedures for improving stress solutions [176-181].

As an extension of this work, we recommend the following future works.

In Chapter 3, 4 and 6, performance was obtained through a complete set of benchmark problems and its fundamental information. Based on the detailed solution, the free vibration analysis of shell problems needs to be proposed and their solution needs to be provided. Also, using a posteriori error estimators [177-181], element size and polynomial order can be effectively controlled around the area where stress concentration is expected.

In Chapter 5, nonlinear extension of the MITC3+ shell element would be important developments in the specific topics. However, there are of course many more areas of research developments considering the general elasto-plastic analysis of shells. These include the large strain analysis of shells, the analysis of composite shells, the modeling of contact conditions, and the analysis of shells in multi-physics conditions.

Appendix A. The Finite Rotations

In this Appendix, the mathematical formulation of the finite rotations is reviewed. This explanations about the finite rotation are extracted from Reference [159]. The finite rotation is useful for the finite shell element in geometrical nonlinear analysis. One difficulty for studying the finite rotation is that different normalization has been used by different research groups.

A.1 Spatial Rotations

The two-dimensional plane rotations can be dealt with in finite element analysis. A rotation in the plane (x_1, x_2) is defined by just a scalar with the rotation angle θ about the perpendicular axis. Plane rotations commute $\theta_1 + \theta_2 = \theta_2 + \theta_1$ because the rotation angle θ is numbers. However the study of spatial finite three dimensional rotation is more difficult because they do not obey the laws of vector calculus. Within the framework of matrix algebra, finite rotations can be represented in two ways; \mathbf{R} is 3×3 orthogonal matrices called rotation tensor or rotators and $\mathbf{\Omega}$ is real skew-symmetric matrices called spin tensor or spinors.

The spin tensor is important in theory and modeling since the matrix entries are closely related to the ingredients of Euler's theorem. The rotation tensor is convenient for numerical analysis and related to the polar factorization of a transformation matrix. The two representations are connected as shown in **Figure A.1(a)**, which also includes the axial and skew vector introduced below. Of the $\mathbf{\Omega} \rightarrow \mathbf{R}$ links, the Rodrigues-Cayley formulation is historically the first, see reference [182].

The spin tensor $\mathbf{\Omega}$ which is a 3×3 skew-symmetric matrix and it is defined by three scalar parameters. These three numbers can be arranged as components of an axial vector ω . Although the axial vector ω looks like a 3-vector, it violates certain properties of classical vectors such as the composition rule. Therefore the term pseudovector is sometimes used for ω . This Appendix is aimed to convey that finite three-dimensional rotations can appear in alternative mathematical representations, as **Figure A.1(a)**.

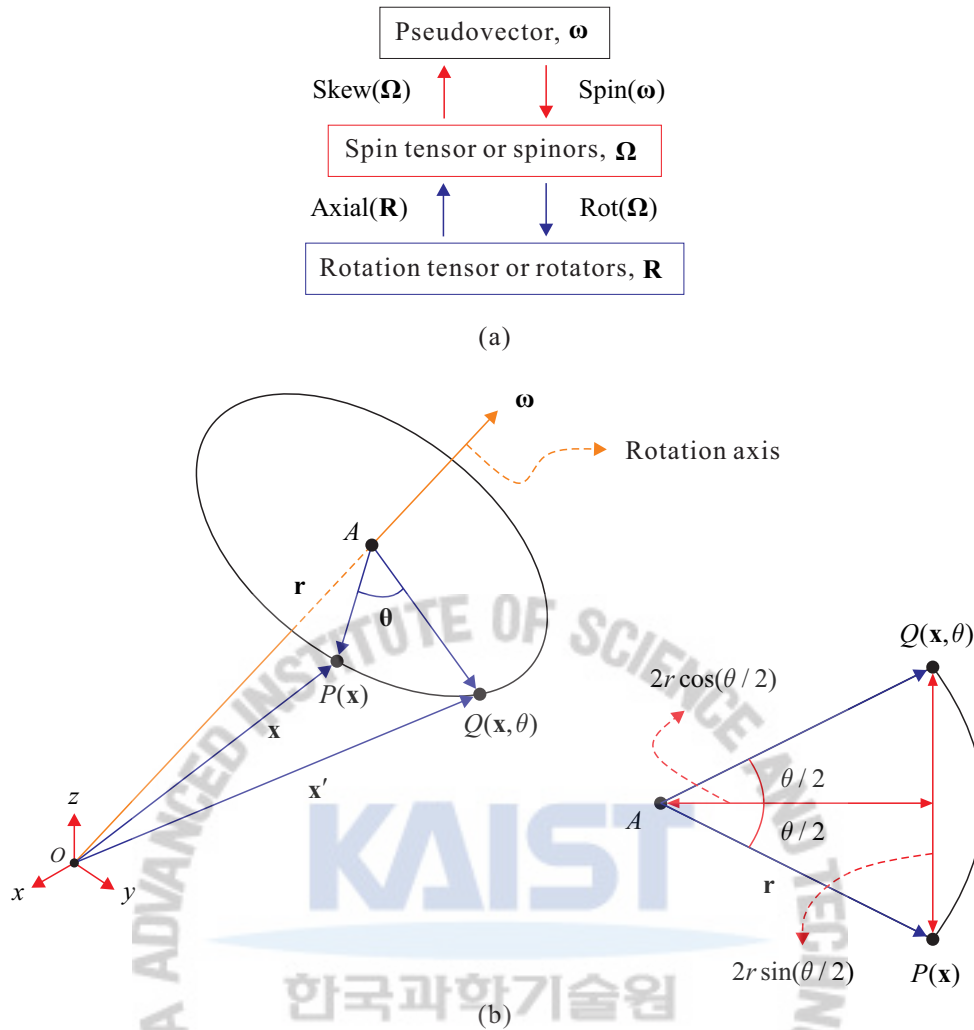


Figure A.1. (a) Representations of finite spatial rotations. (b) The rotation angle is positive obeying the right-hand screw rule about the rotation axis.

A.2 Spin Tensor Ω

A three dimensional rotation by an angle θ about an axis of rotation ω is represented by **Figure A.1(b)**. The origin of coordinates O is placed on ω . The rotation axis consists of three directors ω_1 , ω_2 and ω_3 . At least one of three directors should be nonzero. These components may be scaled by a nonzero factor γ through which the vector can be normalized in various ways. The rotation takes an arbitrary point $P(\mathbf{x})$, located by its position vector \mathbf{x} , into $Q(\mathbf{x}, \theta)$, located by its position vector \mathbf{x}' . The center of rotation C is defined by projecting P on the rotation axis. The plane of rotation CPQ is normal to that axis at C . The radius of rotation is vector \mathbf{r} of magnitude r from C to P . As shown in **Figure A.1(b)** the distance between P and Q is $2r \sin(\theta/2)$. The positive sense of θ obeys the RHS screw rule: positive counter-clockwise if observed from the tip of the rotation axis. The angle shown in **Figure A.1(b)** is positive.

A.3 Spin Tensor and Axial Vector

With the three directors ω_1 , ω_2 , and ω_3 of the axis $\boldsymbol{\omega}$, the 3×3 skew-symmetric spin tensor $\boldsymbol{\Omega}$ can be represented by

$$\boldsymbol{\Omega} = \text{Spin}(\boldsymbol{\omega}) = \begin{bmatrix} 0 & -\omega_3 & \omega_2 \\ \omega_3 & 0 & -\omega_1 \\ -\omega_2 & \omega_1 & 0 \end{bmatrix} = -\boldsymbol{\Omega}^T. \quad (8.1)$$

The cross product of $\boldsymbol{\omega}$ and \mathbf{v} is equivalent as

$$\boldsymbol{\omega} \times \mathbf{v} = \boldsymbol{\Omega} \mathbf{v} = \text{Spin}(\boldsymbol{\omega}) \mathbf{v} = -\text{Spin}(\mathbf{v}) \boldsymbol{\omega} = -\mathbf{v} \times \boldsymbol{\omega}. \quad (8.2)$$

In particular $\boldsymbol{\Omega} \boldsymbol{\omega} = 0$, and $\mathbf{v}^T \boldsymbol{\Omega} \mathbf{v} = 0$, as may be directly verified. The operation converse to Equation (8.1) extracts the 3-vector $\boldsymbol{\omega}$, called axial vector or pseudovector, from a given spin tensor

$$\boldsymbol{\omega} = \text{Axial}(\boldsymbol{\Omega}) = [\omega_1 \quad \omega_2 \quad \omega_3]^T. \quad (8.3)$$

The length of the vector $\boldsymbol{\omega}$ is calculated by

$$\omega = |\boldsymbol{\omega}| = +\sqrt{\omega_1^2 + \omega_2^2 + \omega_3^2}. \quad (8.4)$$

A.4 From Spin Tensor to Rotation Tensor

Figure A.1 illustrates that a rotation tensor is a linear operator that maps an arbitrary point $P(\mathbf{x})$ to $Q(\mathbf{x}')$ given the rotation axis \mathbf{w} and the angle θ . The rotator representations in the form of 3×3 rotation matrices \mathbf{R} are obtained by

$$\mathbf{x}' = \mathbf{R} \mathbf{x}, \quad \mathbf{x} = \mathbf{R}^T \mathbf{x}'. \quad (8.5)$$

The rotation matrix is proper orthogonal which satisfies $\mathbf{R}^T \mathbf{R} = \mathbf{I}$ and $\det(\mathbf{R}) = 1$. It must reduce to \mathbf{I} if the rotation vanishes.

A.5 Rotator Parameterizations

The rotation tensor \mathbf{R} has the trace property. Hence the rotation tensor is represented by

$$\text{trace}(\mathbf{R}) = 1 + 2 \cos \theta. \quad (8.6)$$

To construct the rotation tensor \mathbf{R} from rotation data, the rotation tensor is assumed to be analytic in $\boldsymbol{\Omega}$. Hence it must have the Taylor expansion as follows:

$$\mathbf{R} = \mathbf{I} + c_1 \boldsymbol{\Omega} + c_2 \boldsymbol{\Omega}^2 + c_3 \boldsymbol{\Omega}^3 + \dots, \quad (8.7)$$

where the c_i must vanish when the angle θ is equal to zero. By the Cayley-Hamilton theorem, $\boldsymbol{\Omega}$ satis-

fies its own characteristic equation,

$$\mathbf{\Omega}^3 = -\omega^2 \mathbf{\Omega}, \quad \mathbf{\Omega}^4 = -\omega^2 \mathbf{\Omega}^2, \quad \text{and} \quad \mathbf{\Omega}^n = -\omega^2 \mathbf{\Omega}^{n-2}, \quad n \geq 3. \quad (8.8)$$

Hence if $n = 3, 5, \dots$ the odd powers $\mathbf{\Omega}^n$ are skew-symmetric with distinct pure imaginary eigenvalues, whereas if $n = 2, 4, \dots$, then even power $\mathbf{\Omega}^n$ are symmetric with repeated real eigenvalues. Due to the Cayley-Hamilton theorem, all power of order 3 or higher can be eliminated. Therefore rotation tensor \mathbf{R} must be a linear function of \mathbf{I} , $\mathbf{\Omega}$ and $\mathbf{\Omega}^2$. Hence the rotation tensor is rewritten by

$$\mathbf{R} = \mathbf{I} + \alpha(\gamma \mathbf{\Omega}) + \beta(\gamma \mathbf{\Omega})^2, \quad (8.9)$$

where γ is the normalization factor of the spin tensor and α and β are scalar functions of θ and of invariants of $\mathbf{\Omega}$ or ω . Since the only invariant of the latter is ω , it is anticipated that $\alpha = \alpha(\theta, \omega)$ and $\beta = \beta(\theta, \omega)$, both vanishing when the angle θ becomes zero. Approach to determine those coefficients for $\gamma = 1$ is discussed in the next sections. **Table A.1** lists several representations of a rotator in terms of the scaled $\mathbf{\Omega}$.

Table A.1. Rotation tensor with several spin tensor normalizations.

Parameterization	γ	α	β	Spin tensor	Rotation tensor \mathbf{R}
None (unscaled)	γ	$\frac{\sin \theta}{\omega}$	$\frac{2 \sin^2(\theta/2)}{\omega^2}$	$\mathbf{\Omega}$	$\mathbf{I} + \frac{\sin \theta}{\omega} \mathbf{\Omega} + \frac{2 \sin^2(\theta/2)}{\omega^2} \mathbf{\Omega}^2$
Unit axial-vector	$\frac{1}{\omega}$	$\sin \theta$	$2 \sin^2(\theta/2)$	$\mathbf{N} = \gamma \mathbf{\Omega}$	$\mathbf{I} + \sin \theta \mathbf{N} + 2 \sin^2(\theta/2) \mathbf{N}^2$
Rodrigues-Cayley	$\frac{\tan(\theta/2)}{\omega}$	$2 \cos^2(\theta/2)$	$2 \cos^2(\theta/2)$	$\mathbf{\Sigma} = \gamma \mathbf{\Omega}$	$\mathbf{I} + 2 \cos^2(\theta/2) (\mathbf{\Sigma} + \mathbf{\Sigma}^2)$
Fraeijs de Veubeke	$\frac{\sin(\theta/2)}{\omega}$	$2 \cos(\theta/2)$	2	$\mathbf{\Omega}_p = \gamma \mathbf{\Omega}$	$\mathbf{I} + 2 \cos^2(\theta/2) \mathbf{\Omega}_p + 2 \mathbf{\Omega}_p^2$
Exponential map	$\frac{\theta}{\omega}$	$\frac{\sin \theta}{\theta}$	$\frac{2 \sin^2(\theta/2)}{\theta^2}$	$\mathbf{\Theta} = \gamma \mathbf{\Omega}$	$\mathbf{I} + \frac{\sin \theta}{\theta} \mathbf{\Theta} + \frac{2 \sin^2(\theta/2)}{\theta^2} \mathbf{\Theta}^2$

A.6 Rotation Tensor from Algebra

It is possible to find α and β for $\gamma = 1$ directly from algebraic conditions. Taking the trace of the rotation tensor in Equation (8.9) for $\gamma = 1$ and applying the trace property in Equation (8.6) require

$$3 - 2\beta\omega^2 = 1 + 2 \cos \theta, \quad \text{with} \quad \beta = \frac{1 - \cos \theta}{\omega^2} = \frac{2 \sin^2(\theta/2)}{\omega^2}. \quad (8.10)$$

Using the orthogonal property of the rotation tensor,

$$\mathbf{I} = \mathbf{R}^T \mathbf{R} = (\mathbf{I} - \alpha \boldsymbol{\Omega} + \beta \boldsymbol{\Omega}^2)(\mathbf{I} + \alpha \boldsymbol{\Omega} + \beta \boldsymbol{\Omega}^2), \quad (8.11)$$

$$\mathbf{I} = \mathbf{I} + (2\beta - \alpha^2) \boldsymbol{\Omega}^2 + \beta \boldsymbol{\Omega}^4 = \mathbf{I} + (2\beta - \alpha^2 - \beta^2 \omega^2) \boldsymbol{\Omega}^2. \quad (8.12)$$

we can obtain the following condition,

$$2\beta - \alpha^2 - \beta^2 \omega^2 = 0 \quad \text{with} \quad \alpha = \frac{\sin \theta}{\omega}. \quad (8.13)$$

Finally, the rotation tensor can be represented by, see **Table A.1**,

$$\mathbf{R} = \mathbf{I} + \frac{\sin \theta}{\omega} \boldsymbol{\Omega} + \frac{1 - \cos \theta}{\omega^2} \boldsymbol{\Omega}^2 = \mathbf{I} + \frac{\sin \theta}{\omega} \boldsymbol{\Omega} + \frac{2 \sin^2(\theta/2)}{\omega^2} \boldsymbol{\Omega}^2. \quad (8.14)$$

From a numerical standpoint the sine-squared form should be preferred to avoid the cancellation in computing $1 - \cos \theta$ for small θ . Replacing the components of $\boldsymbol{\Omega}$ and $\boldsymbol{\Omega}^2$ gives the explicit rotator form

$$\mathbf{R} = \frac{1}{\omega^2} = \begin{bmatrix} \omega_1^2 + (\omega_2^2 + \omega_3^2) \cos \theta & 2\omega_1 \omega_2 \sin^2(\theta/2) - \omega_3 \omega \sin \theta & 2\omega_1 \omega_3 \sin^2(\theta/2) + \omega_2 \omega \sin \theta \\ 2\omega_1 \omega_2 \sin^2(\theta/2) + \omega_3 \omega \sin \theta & \omega_2^2 + (\omega_3^2 + \omega_1^2) \cos \theta & 2\omega_2 \omega_3 \sin^2(\theta/2) - \omega_1 \omega \sin \theta \\ 2\omega_1 \omega_3 \sin^2(\theta/2) - \omega_2 \omega \sin \theta & 2\omega_2 \omega_3 \sin^2(\theta/2) + \omega_1 \omega \sin \theta & \omega_3^2 + (\omega_1^2 + \omega_2^2) \cos \theta \end{bmatrix}. \quad (8.15)$$

If $\gamma \neq 1$ but nonzero, the results are $\alpha = \sin \theta / (\gamma \omega)$ and $\beta = (1 - \cos \theta) / (\gamma^2 \omega^2)$. It follows that Equation (8.14) and (8.15) are independent of γ , as was to be expected.

Appendix B. Path Following Techniques

The load and displacement control methods fail to find the complete equilibrium path presenting limit points with ‘snap-throughs’ and ‘snap-backs’ behaviors. The arc-length control method is aimed to handle these critical points. Hence the finite element solution with this method can draw the entire load-displacement curves. The general algorithm of this approach is given in this section.

B.1 Limit Points Analysis

In relation to structural analysis, Riks [183] and Wempner [184] published the first attempt in this respect, using a linear constraint equation such that the iterative change was normal to the tangent. Later, several scholars modified the method by the means of altering the constraint equation, and therefore, the way of the corrector steps of the iterative procedure was developed. For example, Ramm [185] used a different linear constraint such that iterative change was normal to the secant change. The previous two methods were the first versions of the linearized arc-length method. At the same time, Crisfield [186] proposed the spherical arc-length method which uses a quadratic constraint or the Euclidean norm of the incremental displacement to a fixed quantity. To avoid the problems that arise in choice of a proper root, as Crisfield method required, a consistently linearized version of arc-length method using the same quadratic constraint was proposed by Schweizerhof and Wriggers [187].

The equilibrium equation in term of the residuum \mathbf{r} is given by

$$\mathbf{r}(\mathbf{d}, \lambda) = \mathbf{q}_i(\mathbf{d}) - \lambda \mathbf{q}_e = 0, \quad (9.1)$$

where \mathbf{d} is the displacement vector, λ is the scalar and load level parameter, \mathbf{q}_i is the internal force vector which is function of the nodal displacements, and \mathbf{q}_e is the external load vector. The additional constraint is added to complete the set of equations. This constraint equation is the arc length s which is defined by

$$s = \int ds \quad (9.2)$$

with

$$ds = \sqrt{d\mathbf{d}^T d\mathbf{d} + d\lambda^2 \psi^2 \mathbf{q}_e^T \mathbf{q}_e}. \quad (9.3)$$

The aim of the arc-length method is to find the intersection of a given arc length s with the equilibrium equation as follows:

$$\mathbf{r}(s) = \mathbf{q}_i(\mathbf{d}(s)) - \lambda(s) \mathbf{q}_e = 0. \quad (9.4)$$

To solve Equation (9.4), a predictor-corrector scheme is used. Initially, the differential form of (9.3) can be replaced with an incremental form, such that

$$a^i = (\Delta \mathbf{d}^i)^T \Delta \mathbf{d}^i + (\Delta \lambda^i)^2 \psi^2 \mathbf{q}_e^T \mathbf{q}_e - \Delta l^2 = 0, \quad (9.5)$$

where Δl is the incremental length which is the constant radius of the desired intersection with the equilibrium path, ψ is the scaling parameter to combine different dimensions for the load and displacement terms. The vector $\Delta \mathbf{d}$ and the scalar $\Delta \lambda$ are incrementals and are related back to the last converged equilibrium state. Meanwhile $\delta \mathbf{d}$ and $\delta \lambda$ are the iterative displacement vector and load level respectively. These are associated to the previous iteration step that, in most cases, is not an equilibrium state.

The distinguished feature of the arc-length method is that the load level λ is also a parameter to be determined. Therefore, the total unknowns are $n+1$; n from the displacement variables of vector \mathbf{d} and the one of the load parameter λ . To solve for these, equation (9.1) gives a total of n equilibrium equations, while equation (9.5) gives one constraint equation.

These $n+1$ equations can be solved by iteratively applying the Newton-Raphson method to (9.1) and (9.5). This idea was first proposed by Riks [183, 188] and Wempner [184], though with a different constraint equation.

A truncated Taylor series of (9.1) and (9.5) respectively yields

$$\mathbf{r}^{i+1} = \mathbf{r}^i + \frac{\partial \mathbf{r}}{\partial \mathbf{d}} \delta \mathbf{d}^i + \frac{\partial \mathbf{r}}{\partial \lambda} \delta \lambda^i = \mathbf{r}^i + \mathbf{K}_t \delta \mathbf{d}^i + \mathbf{q}_e \delta \lambda^i = 0 \quad (9.6)$$

and

$$a^{i+1} = a^i + \frac{\partial a}{\partial \mathbf{d}} \delta \mathbf{d}^i + \frac{\partial a}{\partial \lambda} \delta \lambda^i = a^i + 2(\Delta \mathbf{d}^i)^T \delta \mathbf{d}^i + 2\Delta \lambda^i \delta \lambda^i \psi^2 \mathbf{q}_e^T \mathbf{q}_e = 0, \quad (9.7)$$

where \mathbf{K}_t is the tangent stiffness matrix. The other terms have been already defined. Equations (9.6) and (9.7) can be combined in a different fashion

$$\begin{bmatrix} \delta \mathbf{d}^i \\ \delta \lambda^i \end{bmatrix} = - \begin{bmatrix} \mathbf{K}_t & -\mathbf{q}_e \\ 2(\Delta \mathbf{d}^i)^T & 2\Delta \lambda^i \psi^2 \mathbf{q}_e^T \mathbf{q}_e \end{bmatrix}^{-1} \begin{bmatrix} \mathbf{r}^i \\ a^i \end{bmatrix}. \quad (9.8)$$

At this point, there are different ways to obtain the solution of (9.8). Two different possibilities are given next.

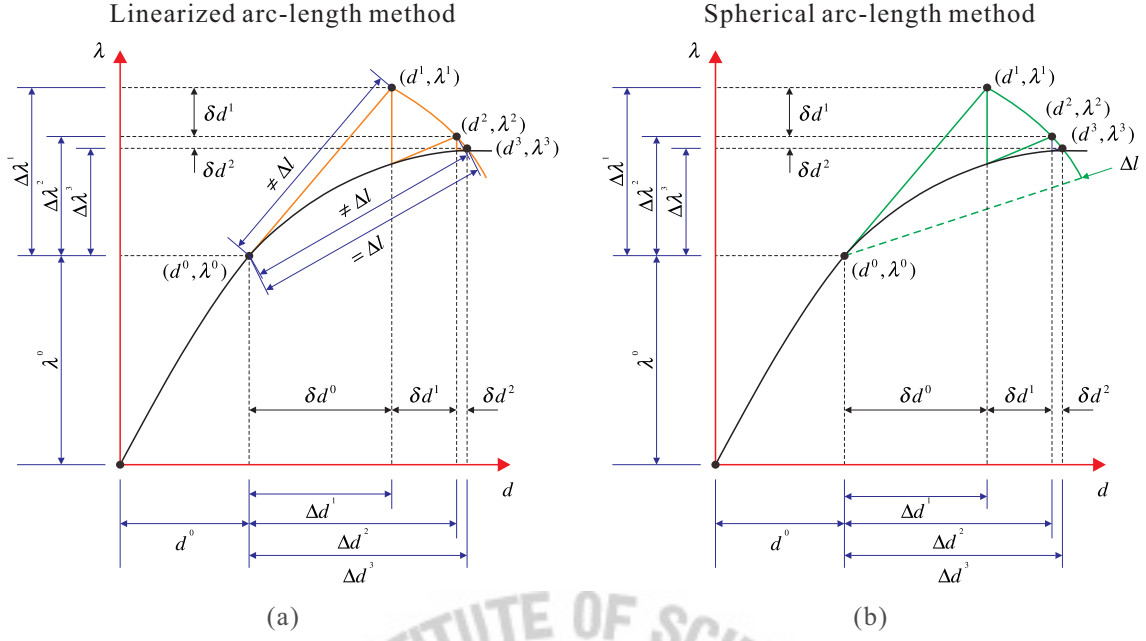


Figure B.1. (a) The linearized arc-length method. (b) The spherical arc-length method.

B.1 Linearized Arc-Length Method

The simplest way is to solve Equation (9.8) directly [187]. One may first find an expression for $\delta \mathbf{d}$ and then replace it into $\delta \lambda$. Consequently, from equation (9.6), $\delta \mathbf{d}$ can be given by

$$\delta \mathbf{d}^i = -\mathbf{K}_t^{-1} \mathbf{r}^i + \delta \lambda^i \mathbf{K}_t^{-1} \mathbf{q}_e. \quad (9.9)$$

Equation (9.9) is exactly for displacement control. Therefore by means of the two iterative displacement vectors $\delta \bar{\mathbf{d}}^i$ and $\delta \mathbf{d}_t^i$, equation (9.9) can be rewritten as

$$\delta \mathbf{d}^i = \delta \bar{\mathbf{d}}^i + \delta \lambda^i \delta \mathbf{d}_t^i \quad (9.10)$$

with

$$\delta \bar{\mathbf{d}}^i = -\mathbf{K}_t^{-1} \mathbf{r}^i \quad \text{and} \quad \delta \mathbf{d}_t^i = \mathbf{K}_t^{-1} \mathbf{q}_e. \quad (9.11)$$

Substituting Equation (9.10) into Equation (9.7) leads to

$$2(\Delta \mathbf{d}^i)^T (\delta \bar{\mathbf{d}}^i + \delta \lambda^i \delta \mathbf{d}_t^i) + 2\Delta \lambda^i \delta \lambda^i \psi^2 \mathbf{q}_e^T \mathbf{q}_e = -\frac{a^i}{2}. \quad (9.12)$$

Therefore, the iterative load level $\delta \lambda$ can be given by

$$\delta \lambda^i = \frac{-(a^i/2) - (\Delta \mathbf{d}^i)^T \delta \bar{\mathbf{d}}^i}{(\Delta \mathbf{d}^i)^T \delta \mathbf{d}_t^i + \Delta \lambda^i \psi^2 \mathbf{q}_e^T \mathbf{q}_e}. \quad (9.13)$$

The incremental displacements and load level should be updated as

$$\Delta \mathbf{d}^{i+1} = \Delta \mathbf{d}^i + \delta \mathbf{d}^i, \quad (9.14)$$

$$\Delta \lambda^{i+1} = \Delta \lambda^i + \delta \lambda^i. \quad (9.15)$$

B.2 Spherical Arc-Length Method

To solve equation (9.8) Crisfield [186] suggested another alternative method, that is the spherical arc-length method. Here, the constraint equation (9.5) for a , is satisfied through the entire set of iterations and not only when convergence is achieved, as in the linearized arc-length. Substituting Equation (9.10) into Equation (9.14) leads to

$$\Delta \mathbf{d}^{i+1} = \Delta \mathbf{d}^i + \delta \bar{\mathbf{d}}^i + \delta \lambda^i \delta \mathbf{d}_t^i, \quad (9.16)$$

where $\delta \lambda$ is the only unknown. The constraint Equation (9.5) can be rewritten as

$$(\Delta \mathbf{d}^i)^T \Delta \mathbf{d}^i + (\Delta \lambda^i)^2 \psi^2 \mathbf{q}_e^T \mathbf{q}_e = (\Delta \mathbf{d}^{i+1})^T \Delta \mathbf{d}^{i+1} + (\Delta \lambda^{i+1})^2 \psi^2 \mathbf{q}_e^T \mathbf{q}_e = \Delta l^2. \quad (9.17)$$

The radius of the desired intersection is always constant during the iterative process and therefore a^i is equal to zero, see Figure B.1(b). Substitution of Equation (9.16) into Equation (9.17) leads to the scalar quadratic equation:

$$c_1 (\delta \lambda^i)^2 + c_2 \delta \lambda^i + c_3 = 0, \quad (9.18)$$

where

$$c_1 = (\delta \mathbf{d}_t^i)^T \delta \mathbf{d}_t^i + \psi^2 \mathbf{q}_e^T \mathbf{q}_e, \quad (9.19)$$

$$c_2 = 2(\delta \mathbf{d}_t^i)^T (\delta \mathbf{d}^i + \delta \bar{\mathbf{d}}^i) + 2\Delta \lambda^i \psi^2 \mathbf{q}_e^T \mathbf{q}_e, \quad (9.20)$$

$$c_3 = (\delta \mathbf{d}^i + \delta \bar{\mathbf{d}}^i)(\delta \mathbf{d}^i + \delta \bar{\mathbf{d}}^i)^T - \Delta l^2 + (\Delta \lambda^i)^2 \psi^2 \mathbf{q}_e^T \mathbf{q}_e. \quad (9.21)$$

After solving (9.18) for $\delta \lambda^i$ Equation (9.16) can be fully computed. Finally, with the aid of Equation (9.15), the complete iteration is defined.

The main disadvantage of the spherical arc-length method, compared to the Linearized version, is the additional computational cost to solve the quadratic equation, and then the choice of the proper root that yields from Equation (9.18).

Reference

- [1] Bathe KJ. Finite element procedures: Klaus-Jurgen Bathe; 2006.
- [2] Zienkiewicz OC, Morice P. The finite element method in engineering science: McGraw-hill London; 1971.
- [3] Hughes TJ. The finite element method: linear static and dynamic finite element analysis: Courier Dover Publications; 2012.
- [4] Cook RD. Concepts and applications of finite element analysis: John Wiley & Sons; 2007.
- [5] Ahmad S, Irons BM, Zienkiewicz O. Analysis of thick and thin shell structures by curved finite elements. *International Journal for Numerical Methods in Engineering*. 1970;2:419-51.
- [6] Reissner E. The effect of transverse shear deformation on the bending of elastic plates. *Journal of applied Mechanics*. 1945;12:69-77.
- [7] Mindlin RD. Influence of rotary inertia and shear on flexural motions of isotropic, elastic plates. *J of Appl Mech*. 1951;18:31-8.
- [8] Zienkiewicz O, Taylor R, Too J. Reduced integration technique in general analysis of plates and shells. *International Journal for Numerical Methods in Engineering*. 1971;3:275-90.
- [9] Pawsey SF, Clough RW. Improved numerical integration of thick shell finite elements. *International Journal for Numerical Methods in Engineering*. 1971;3:575-86.
- [10] Hughes TJ, Cohen M, Haroun M. Reduced and selective integration techniques in the finite element analysis of plates. *Nuclear Engineering and Design*. 1978;46:203-22.
- [11] Pugh E, Hinton E, Zienkiewicz O. A study of quadrilateral plate bending elements with 'reduced' integration. *International Journal for Numerical Methods in Engineering*. 1978;12:1059-79.
- [12] Hughes TJ, Liu WK. Nonlinear finite element analysis of shells-part II. two-dimensional shells. *Computer Methods in Applied Mechanics and Engineering*. 1981;27:167-81.
- [13] Stolarski H, Belytschko T. Shear and membrane locking in curved C^0 elements. *Computer Methods in Applied Mechanics and Engineering*. 1983;41:279-96.
- [14] Lee S, H. Plan T. Improvement of plate and shell finite elements by mixed formulations. *AIAA journal*. 1978;16:29-34.
- [15] Noor AK, Peters JM. Mixed models and reduced/selective integration displacement models for nonlinear analysis of curved beams. *International Journal for Numerical Methods in Engineering*. 1981;17:615-31.

- [16] Macneal RH. A simple quadrilateral shell element. *Computers & Structures*. 1978;8:175-83.
- [17] Macneal RH. Derivation of element stiffness matrices by assumed strain distributions. *Nuclear Engineering and Design*. 1982;70:3-12.
- [18] Dvorkin EN, Bathe KJ. A continuum mechanics based four-node shell element for general non-linear analysis. *Engineering computations*. 1984;1:77-88.
- [19] Bathe KJ, Dvorkin EN. A formulation of general shell elements—the use of mixed interpolation of tensorial components. *International Journal for Numerical Methods in Engineering*. 1986;22:697-722.
- [20] Dvorkin EN, Vassolo SI. A quadrilateral 2-D finite element based on mixed interpolation of tensorial components. *Engineering computations*. 1989;6:217-24.
- [21] Bucalem ML, Bathe KJ. Higher-order MITC general shell elements. *International Journal for Numerical Methods in Engineering*. 1993;36:3729-54.
- [22] Bathe KJ, Lee PS, Hiller JF. Towards improving the MITC9 shell element. *Computers & Structures*. 2003;81:477-89.
- [23] Lee PS, Bathe KJ. Development of MITC isotropic triangular shell finite elements. *Computers & Structures*. 2004;82:945-62.
- [24] Beirão da Veiga L, Chapelle D, Paris Suarez I. Towards improving the MITC6 triangular shell element. *Computers & Structures*. 2007;85:1589-610.
- [25] Kim DN, Bathe KJ. A triangular six-node shell element. *Computers & Structures*. 2009;87:1451-60.
- [26] Lee PS, Bathe KJ. The quadratic MITC plate and MITC shell elements in plate bending. *Advances in Engineering Software*. 2010;41:712-28.
- [27] Bathe KJ, Lee PS. Measuring the convergence behavior of shell analysis schemes. *Computers & Structures*. 2011;89:285-301.
- [28] Jeon HM, Lee PS, Bathe KJ. The MITC3 shell finite element enriched by interpolation covers. *Computers & Structures*. 2014;134:128-42.
- [29] Lee Y, Lee PS, Bathe KJ. The MITC3+ shell element and its performance. *Computers & Structures*. 2014;138:12-23.
- [30] Bischoff M, Bletzinger K. Stabilized DSG plate and shell elements. *Trends in Computational Structural Mechanics, CIMNE, Barcelona*. 2001:253-63.
- [31] Koschnick F, Bischoff M, Camprubí N, Bletzinger KU. The discrete strain gap method and membrane locking. *Computer Methods in Applied Mechanics and Engineering*. 2005;194:2444-63.
- [32] Simo JC, Rifai M. A class of mixed assumed strain methods and the method of incompatible modes. *International Journal for Numerical Methods in Engineering*. 1990;29:1595-638.

- [33] Babuska I, Melenk JM. The partition of unity finite element method. DTIC Document; 1995.
- [34] Melenk JM, Babuška I. The partition of unity finite element method: basic theory and applications. *Computer Methods in Applied Mechanics and Engineering*. 1996;139:289-314.
- [35] Duarte CA, Oden JT. An h - p adaptive method using clouds. *Computer Methods in Applied Mechanics and Engineering*. 1996;139:237-62.
- [36] Oden JT, Duarte C, Zienkiewicz OC. A new cloud-based hp finite element method. *Computer Methods in Applied Mechanics and Engineering*. 1998;153:117-26.
- [37] Strouboulis T, Babuška I, Copps K. The design and analysis of the generalized finite element method. *Computer Methods in Applied Mechanics and Engineering*. 2000;181:43-69.
- [38] Strouboulis T, Copps K, Babuška I. The generalized finite element method. *Computer Methods in Applied Mechanics and Engineering*. 2001;190:4081-193.
- [39] Duarte CA, Babuška I, Oden JT. Generalized finite element methods for three-dimensional structural mechanics problems. *Computers & Structures*. 2000;77:215-32.
- [40] Duarte C, Hamzeh O, Liszka T, Tworzydło W. A generalized finite element method for the simulation of three-dimensional dynamic crack propagation. *Computer Methods in Applied Mechanics and Engineering*. 2001;190:2227-62.
- [41] Taylor RL, Zienkiewicz OC, Oñate E. A hierarchical finite element method based on the partition of unity. *Computer Methods in Applied Mechanics and Engineering*. 1998;152:73-84.
- [42] Jeon HM, Lee Y, Lee PS, Bathe KJ. The MITC3+ shell element in geometric nonlinear analysis. *Computers & Structures*. 2015;146:91-104.
- [43] Belytschko T, Tsay CS. A stabilization procedure for the quadrilateral plate element with one-point quadrature. *International Journal for Numerical Methods in Engineering*. 1983;19:405-19.
- [44] Belytschko T, Lin JI, Chen-Shyh T. Explicit algorithms for the nonlinear dynamics of shells. *Computer Methods in Applied Mechanics and Engineering*. 1984;42:225-51.
- [45] Park K, Stanley G. A curved C^0 shell element based on assumed natural-coordinate strains. *Journal of applied Mechanics*. 1986;53:278-90.
- [46] Huang H, Hinton E. A new nine node degenerated shell element with enhanced membrane and shear interpolation. *International Journal for Numerical Methods in Engineering*. 1986;22:73-92.
- [47] Braess D. Enhanced assumed strain elements and locking in membrane problems. *Computer Methods in Applied Mechanics and Engineering*. 1998;165:155-74.
- [48] Timoshenko SG, Goodier JN: *Theory of elasticity*. Hill Book Co, New York. 1970.
- [49] Nagtegaal JC, Parks DM, Rice J. On numerically accurate finite element solutions in the fully plastic range. *Computer Methods in Applied Mechanics and Engineering*. 1974;4:153-77.

- [50] Hughes TJ. Generalization of selective integration procedures to anisotropic and nonlinear media. *International Journal for Numerical Methods in Engineering*. 1980;15:1413-8.
- [51] Doll S, Schweizerhof K, Hauptmann R, Freischläger C. On volumetric locking of low-order solid and solid-shell elements for finite elastoviscoplastic deformations and selective reduced integration. *Engineering computations*. 2000;17:874-902.
- [52] Wells G, Sluys L, De Borst R. A p -adaptive scheme for overcoming volumetric locking during plastic flow. *Computer Methods in Applied Mechanics and Engineering*. 2002;191:3153-64.
- [53] Naylor D. Stresses in nearly incompressible materials by finite elements with application to the calculation of excess pore pressures. *International Journal for Numerical Methods in Engineering*. 1974;8:443-60.
- [54] Malkus DS, Hughes TJ. Mixed finite element methods—reduced and selective integration techniques: a unification of concepts. *Computer Methods in Applied Mechanics and Engineering*. 1978;15:63-81.
- [55] Jankovich E, et al., Leblanc F, Durand M, Bercovier M. A finite element method for the analysis of rubber parts, experimental and analytical assessment. *Computers & Structures*. 1981;14:385-91.
- [56] Oden J, Kikuchi N. Finite element methods for constrained problems in elasticity. *International Journal for Numerical Methods in Engineering*. 1982;18:701-25.
- [57] Taylor RL, Pister KS, Herrmann LR. On a variational theorem for incompressible and nearly-incompressible orthotropic elasticity. *International Journal of Solids and Structures*. 1968;4:875-83.
- [58] Argyris JH, Dunne P, Angelopoulos T, Bichat B. Large natural strains and some special difficulties due to non-linearity and incompressibility in finite elements. *Computer Methods in Applied Mechanics and Engineering*. 1974;4:219-78.
- [59] Simo J, Taylor R, Pister K. Variational and projection methods for the volume constraint in finite deformation elasto-plasticity. *Computer Methods in Applied Mechanics and Engineering*. 1985;51:177-208.
- [60] Canga ME, Becker EB. An iterative technique for the finite element analysis of near-incompressible materials. *Computer Methods in Applied Mechanics and Engineering*. 1999;170:79-101.
- [61] Schlebusch R, Matheas J, Zastrau B. On the avoidance of Poisson thickness locking in surface-related shell theories by an extension of the EAS method. *Machine Dynamics Problems*. 2002;26:101-14.
- [62] Irons BM, Razzaque A. Experience with the patch test for convergence of finite elements. *The Mathematical Foundations of the Finite Element Method with Applications to Partial Differential Equations*. 1972;557:587.
- [63] Wilson E, Taylor R, Doherty W, Ghaboussi J. Incompatible displacement models (isoparametric finite elements in solid and thick shell structural analysis). *Numerical and computer methods in structural mechanics (A 74-17756 06-32)* New York, Academic Press, Inc, 1973. 1973:43-57.

- [64] Taylor RL, Beresford PJ, Wilson EL. A non-conforming element for stress analysis. *International Journal for Numerical Methods in Engineering*. 1976;10:1211-9.
- [65] Fröier M, Nilsson L, Samuelsson A. The rectangular plane stress element by Turner, Pian and Wilson. *International Journal for Numerical Methods in Engineering*. 1974;8:433-7.
- [66] Oñate E. *Structural Analysis with the Finite Element Method. Linear Statics: Volume 2: Beams, Plates and Shells*: Springer; 2013.
- [67] Sussman T, Bathe KJ. Spurious modes in geometrically nonlinear small displacement finite elements with incompatible modes. *Computers & Structures*. 2014;140:14-22.
- [68] MacNeal R. *Finite elements: their design and performance*. 1994. M Dekker.406-10.
- [69] Ramm E. A plate/shell element for large deflections and rotations. *Formulations and computational algorithms in finite element analysis*. 1977:264-93.
- [70] Krakeland B. Nonlinear analysis of shells using degenerate isoparametric elements. *Finite Elements in Nonlinear Mechanics*. 1978;1:265-84.
- [71] Dvorkin EN, Oñate E, Oliver J. On a non-linear formulation for curved Timoshenko beam elements considering large displacement/rotation increments. *International Journal for Numerical Methods in Engineering*. 1988;26:1597-613.
- [72] Dvorkin EN, Toscano RG. *Finite element analysis of the collapse and post-collapse behavior of steel pipes applications to the oil industry*: Springer; 2013.
- [73] Lucy LB. A numerical approach to the testing of the fission hypothesis. *The astronomical journal*. 1977;82:1013-24.
- [74] Nayroles B, Touzot G, Villon P. Generalizing the finite element method: diffuse approximation and diffuse elements. *Computational mechanics*. 1992;10:307-18.
- [75] Belytschko T, Lu YY, Gu L. Element-free Galerkin methods. *International Journal for Numerical Methods in Engineering*. 1994;37:229-56.
- [76] Liu WK, Jun S, Zhang YF. Reproducing kernel particle methods. *International journal for numerical methods in fluids*. 1995;20:1081-106.
- [77] Liu GR, Gu Y. A point interpolation method for two-dimensional solids. *International Journal for Numerical Methods in Engineering*. 2001;50:937-51.
- [78] Atluri S, Zhu T. A new meshless local Petrov-Galerkin (MLPG) approach in computational mechanics. *Computational mechanics*. 1998;22:117-27.
- [79] Zhu T, Zhang JD, Atluri S. A local boundary integral equation (LBIE) method in computational mechanics, and a meshless discretization approach. *Computational mechanics*. 1998;21:223-35.
- [80] Liu G, Gu Y. Local point interpolation method for stress analysis of two-dimensional solids. 2001.

- [81] Lam K, Wang Q, Li H. A novel meshless approach—Local Kriging (LoKriging) method with two-dimensional structural analysis. *Computational mechanics*. 2004;33:235-44.
- [82] Yongchang C, Hehua Z. A meshless local natural neighbour interpolation method for stress analysis of solids. *Engineering analysis with boundary elements*. 2004;28:607-13.
- [83] Braun J, Sambridge M. A numerical method for solving partial differential equations on highly irregular evolving grids. *Nature*. 1995;376:655-60.
- [84] Rajendran S, Zhang B. A “FE-meshfree” QUAD4 element based on partition of unity. *Computer Methods in Applied Mechanics and Engineering*. 2007;197:128-47.
- [85] Belytschko T, Organ D, Krongauz Y. A coupled finite element-element-free Galerkin method. *Computational mechanics*. 1995;17:186-95.
- [86] Hegen D. Element-free Galerkin methods in combination with finite element approaches. *Computer Methods in Applied Mechanics and Engineering*. 1996;135:143-66.
- [87] Liu GR, Gu Y. Meshless local Petrov–Galerkin (MLPG) method in combination with finite element and boundary element approaches. *Computational mechanics*. 2000;26:536-46.
- [88] Huerta A, Fernandez Mendez S. Enrichment and coupling of the finite element and meshless methods. 2000.
- [89] Xiao Q, Dhanasekar M. Coupling of FE and EFG using collocation approach. *Advances in Engineering Software*. 2002;33:507-15.
- [90] Hao S, Park HS, Liu WK. Moving particle finite element method. *International Journal for Numerical Methods in Engineering*. 2002;53:1937-58.
- [91] Liu WK, Han W, Lu H, Li S, Cao J. Reproducing kernel element method. Part I: Theoretical formulation. *Computer Methods in Applied Mechanics and Engineering*. 2004;193:933-51.
- [92] Shi GH. Manifold method of material analysis. DTIC Document; 1992.
- [93] Tian R, Yagawa G, Terasaka H. Linear dependence problems of partition of unity-based generalized FEMs. *Computer Methods in Applied Mechanics and Engineering*. 2006;195:4768-82.
- [94] Tian R, Yagawa G. Generalized nodes and high-performance elements. *International Journal for Numerical Methods in Engineering*. 2005;64:2039-71.
- [95] Babuška I, Banerjee U. Stable generalized finite element method (SGFEM). *Computer Methods in Applied Mechanics and Engineering*. 2012;201:91-111.
- [96] Xu J, Rajendran S. A ‘FE-Meshfree’TRIA3 element based on partition of unity for linear and geometry nonlinear analyses. *Computational mechanics*. 2013;51:843-64.
- [97] Cai Y, Zhuang X, Augarde C. A new partition of unity finite element free from the linear dependence problem and possessing the delta property. *Computer Methods in Applied Mechanics and Engineering*. 2010;199:1036-43.

- [98] Kim J, Bathe KJ. The finite element method enriched by interpolation covers. *Computers & Structures*. 2013;116:35-49.
- [99] Lee PS, Noh HC, Bathe KJ. Insight into 3-node triangular shell finite elements: the effects of element isotropy and mesh patterns. *Computers & Structures*. 2007;85:404-18.
- [100] Chapelle D, Bathe KJ. *The finite element analysis of shells: fundamentals*: Springer; 2011.
- [101] Hiller JF, Bathe KJ. Measuring convergence of mixed finite element discretizations: an application to shell structures. *Computers & Structures*. 2003;81:639-54.
- [102] Bathe KJ, Iosilevich A, Chapelle D. An inf-sup test for shell finite elements. *Computers & Structures*. 2000;75:439-56.
- [103] Chapelle D, Bathe KJ. The mathematical shell model underlying general shell elements. *International Journal for Numerical Methods in Engineering*. 2000;48:289-313.
- [104] Bathe KJ. The inf-sup condition and its evaluation for mixed finite element methods. *Computers & Structures*. 2001;79:243-52.
- [105] Lee PS, Bathe KJ. Insight into finite element shell discretizations by use of the “basic shell mathematical model”. *Computers & Structures*. 2005;83:69-90.
- [106] Bathe KJ, Chapelle D, Lee PS. A shell problem ‘highly sensitive’ to thickness changes. *International Journal for Numerical Methods in Engineering*. 2003;57:1039-52.
- [107] Schweitzer MA. A Parallel Multilevel Partition of Unity Method for Elliptic Partial Differential Equations 2002.
- [108] Chessa J, Wang H, Belytschko T. On the construction of blending elements for local partition of unity enriched finite elements. *International Journal for Numerical Methods in Engineering*. 2003;57:1015-38.
- [109] Fries TP, Belytschko T. The extended/generalized finite element method: An overview of the method and its applications. *International Journal for Numerical Methods in Engineering*. 2010;84:253-304.
- [110] An X, Li L, Ma G, Zhang H. Prediction of rank deficiency in partition of unity-based methods with plane triangular or quadrilateral meshes. *Computer Methods in Applied Mechanics and Engineering*. 2011;200:665-74.
- [111] An XM, Zhao ZY, Zhang HH, Li LX. Investigation of linear dependence problem of three-dimensional partition of unity-based finite element methods. *Computer Methods in Applied Mechanics and Engineering*. 2012;233:137-51.
- [112] Xu J, Rajendran S. A partition-of-unity based ‘FE-Meshfree’ QUAD4 element with radial-polynomial basis functions for static analyses. *Computer Methods in Applied Mechanics and Engineering*. 2011;200:3309-23.
- [113] Andelfinger U, Ramm E. EAS-elements for two-dimensional, three-dimensional, plate and shell structures and their equivalence to HR-elements. *International Journal for Numerical Methods*

in Engineering. 1993;36:1311-37.

[114] Kim JH, Kim YH. Three-node macro triangular shell element based on the assumed natural strains. Computational mechanics. 2002;29:441-58.

[115] Kim JH, Kim YH. A three-node C^0 ANS element for geometrically non-linear structural analysis. Computer Methods in Applied Mechanics and Engineering. 2002;191:4035-59.

[116] Hibbitt, Karlsson, Sorensen. ABAQUS: Theory Manual: Hibbitt, Karlsson and Sorensen; 1997.

[117] Katili I. A new discrete Kirchhoff-Mindlin element based on Mindlin-Reissner plate theory and assumed shear strain fields—part I: An extended DKT element for thick-plate bending analysis. International Journal for Numerical Methods in Engineering. 1993;36:1859-83.

[118] Allman D. A compatible triangular element including vertex rotations for plane elasticity analysis. Computers & Structures. 1984;19:1-8.

[119] Cook RD. Further development of a three-node triangular shell element. International Journal for Numerical Methods in Engineering. 1993;36:1413-25.

[120] Providas E, Kattis M. A simple finite element model for the geometrically nonlinear analysis of thin shells. Computational mechanics. 1999;24:127-37.

[121] Felippa CA. A study of optimal membrane triangles with drilling freedoms. Computer Methods in Applied Mechanics and Engineering. 2003;192:2125-68.

[122] Nguyen-Van H, Mai-Duy N, Tran-Cong T. An improved quadrilateral flat element with drilling degrees of freedom for shell structural analysis. CMES: Computer Modeling in Engineering and Sciences. 2009;49:81-110.

[123] Liu J, Riggs H, Tessler A. A four-node, shear-deformable shell element developed via explicit Kirchhoff constraints. International Journal for Numerical Methods in Engineering. 2000;49:1065-86.

[124] Kim K, Lomboy G, Voyiadjis G. A 4-node assumed strain quasi-conforming shell element with 6 degrees of freedom. International Journal for Numerical Methods in Engineering. 2003;58:2177-200.

[125] Liu WK, Law E, Lam D, Belytschko T. Resultant-stress degenerated-shell element. Computer Methods in Applied Mechanics and Engineering. 1986;55:259-300.

[126] Kohnke P. ANSYS: theory of reference release 5.4. ANSYS. Inc, Canonsburg. 1997.

[127] Groenwold AA, Stander N. An efficient 4-node 24 dof thick shell finite element with 5-point quadrature. Engineering computations. 1995;12:723-47.

[128] Belytschko T, Leviathan I. Physical stabilization of the 4-node shell element with one point quadrature. Computer Methods in Applied Mechanics and Engineering. 1994;113:321-50.

[129] Ibrahimbegović A, Frey F. Stress resultant geometrically non-linear shell theory with drilling rotations. Part III: Linearized kinematics. International Journal for Numerical Methods in Engineer-

ing. 1994;37:3659-83.

[130] Taylor RL. Finite element analysis of linear shell problems. Whiteman, JR (ed), Proceedings of the Mathematics in Finite Elements and Applications 1987. p. 191-203.

[131] Belytschko T, Wong BL, Stolarski H. Assumed strain stabilization procedure for the 9-node Lagrange shell element. International Journal for Numerical Methods in Engineering. 1989;28:385-414.

[132] Samtech S. SAMCEF User manuals. Version; 1999.

[133] Choi CK, Lee TY. Efficient remedy for membrane locking of 4-node flat shell elements by non-conforming modes. Computer Methods in Applied Mechanics and Engineering. 2003;192:1961-71.

[134] Morley LSD. Skew plates and structures: Pergamon Press; [distributed in the Western Hemisphere by Macmillan, New York]; 1963.

[135] Timoshenko S, Woinowsky-Krieger S. Theory of plates and shells: McGraw-hill New York; 1959.

[136] Bathe KJ. Fundamental considerations for the finite element analysis of shell structures. Computers & Structures. 1998;66:19-36.

[137] Bathe KJ, Iosilevich A, Chapelle D. An evaluation of the MITC shell elements. Computers & Structures. 2000;75:1-30.

[138] Belytschko T, Stolarski H, Liu WK, Carpenter N, Ong JS. Stress projection for membrane and shear locking in shell finite elements. Computer Methods in Applied Mechanics and Engineering. 1985;51:221-58.

[139] Sze K, Liu X, Lo S. Popular benchmark problems for geometric nonlinear analysis of shells. Finite elements in Analysis and Design. 2004;40:1551-69.

[140] Arciniega R, Reddy J. Tensor-based finite element formulation for geometrically nonlinear analysis of shell structures. Computer Methods in Applied Mechanics and Engineering. 2007;196:1048-73.

[141] Brank B, Damjanić F, Perić D. On implementation of a nonlinear four node shell finite element for thin multilayered elastic shells. Computational mechanics. 1995;16:341-59.

[142] Klinkel S, Gruttmann F, Wagner W. A continuum based three-dimensional shell element for laminated structures. Computers & Structures. 1999;71:43-62.

[143] Macneal RH, Harder RL. A proposed standard set of problems to test finite element accuracy. Finite elements in Analysis and Design. 1985;1:3-20.

[144] Argyris J. An excursion into large rotations. Computer Methods in Applied Mechanics and Engineering. 1982;32:85-155.

[145] Jiang L, Chernuka M. A simple four-noded corotational shell element for arbitrarily large rota-

tions. *Computers & Structures*. 1994;53:1123-32.

[146] To C, Liu M. Hybrid strain based three node flat triangular shell elements—II. Numerical investigation of nonlinear problems. *Computers & Structures*. 1995;54:1057-76.

[147] Briassoulis D. Non-linear behaviour of the RFNS element—large displacements and rotations. *Computer Methods in Applied Mechanics and Engineering*. 2003;192:2909-24.

[148] Kuo-Mo H, Yeh-Ren C. Nonlinear analysis of shell structures by degenerated isoparametric shell element. *Computers & Structures*. 1989;31:427-38.

[149] Simo J, Fox D, Rifai M. On a stress resultant geometrically exact shell model. Part III: Computational aspects of the nonlinear theory. *Computer Methods in Applied Mechanics and Engineering*. 1990;79:21-70.

[150] Başar Y, Ding Y. Finite-rotation shell elements for the analysis of finite-rotation shell problems. *International Journal for Numerical Methods in Engineering*. 1992;34:165-9.

[151] Sansour C, Bocko J. On hybrid stress, hybrid strain and enhanced strain finite element formulations for a geometrically exact shell theory with drilling degrees of freedom. *International Journal for Numerical Methods in Engineering*. 1998;43:175-92.

[152] Sansour C, Kollmann F. Families of 4-node and 9-node finite elements for a finite deformation shell theory. An assesment of hybrid stress, hybrid strain and enhanced strain elements. *Computational mechanics*. 2000;24:435-47.

[153] Hong WI, Kim JH, Kim YH, Lee SW. An assumed strain triangular curved solid shell element formulation for analysis of plates and shells undergoing finite rotations. *International Journal for Numerical Methods in Engineering*. 2001;52:747-61.

[154] Kim C, Sze K, Kim Y. Curved quadratic triangular degenerated-and solid-shell elements for geometric non-linear analysis. *International Journal for Numerical Methods in Engineering*. 2003;57:2077-97.

[155] Bucalem ML, Shimura da Nóbrega SH. A mixed formulation for general triangular isoparametric shell elements based on the degenerated solid approach. *Computers & Structures*. 2000;78:35-44.

[156] Jeon HM, Lee Y, Lee PS, Bathe KJ. The MITC3+ shell element in geometric nonlinear analysis. *Computers & Structures*. 2014.

[157] Belytschko T, Black T. Elastic crack growth in finite elements with minimal remeshing. *International Journal for Numerical Methods in Engineering*. 1999;45:601-20.

[158] Dolbow J, Belytschko T. A finite element method for crack growth without remeshing. *Int J Numer Meth Engng*. 1999;46:131-50.

[159] Felippa C, Haugen B. A unified formulation of small-strain corotational finite elements: I. Theory. *Computer Methods in Applied Mechanics and Engineering*. 2005;194:2285-335.

[160] Wisniewski K. Finite rotation shells. *Basic Equations and Finite Elements for Reissner Kinematics*, CIMNE-Springer. 2010.

- [161] Pian T, Sumihara K. Rational approach for assumed stress finite elements. *International Journal for Numerical Methods in Engineering*. 1984;20:1685-95.
- [162] Piltner R, Taylor R. A systematic construction of B-bar functions for linear and non-linear mixed-enhanced finite elements for plane elasticity problems. *International Journal for Numerical Methods in Engineering*. 1999;44:615-39.
- [163] Bergan P, Felippa C. A triangular membrane element with rotational degrees of freedom. *Computer Methods in Applied Mechanics and Engineering*. 1985;50:25-69.
- [164] Cook RD. Improved two-dimensional finite element. *Journal of the Structural Division*. 1974;100:1851-63.
- [165] Bassayya K, Bhattacharya K, Shrinivasa U. Eight-node brick, PN340, represents constant stress fields exactly. *Computers & Structures*. 2000;74:441-60.
- [166] Chen W, Cheung Y. Three-dimensional 8-node and 20-node refined hybrid isoparametric elements. *International Journal for Numerical Methods in Engineering*. 1992;35:1871-89.
- [167] Simo J, Fox D, Rifai M. On a stress resultant geometrically exact shell model. Part II: The linear theory; computational aspects. *Computer Methods in Applied Mechanics and Engineering*. 1989;73:53-92.
- [168] Sze K, Zhu D. A quadratic assumed natural strain curved triangular shell element. *Computer Methods in Applied Mechanics and Engineering*. 1999;174:57-71.
- [169] Belytschko T, Stolarski H, Carpenter N. A C^0 triangular plate element with one-point quadrature. *International Journal for Numerical Methods in Engineering*. 1984;20:787-802.
- [170] Bletzinger KU, Bischoff M, Ramm E. A unified approach for shear-locking-free triangular and rectangular shell finite elements. *Computers & Structures*. 2000;75:321-34.
- [171] Wanji C, Cheung Y. Refined non-conforming triangular elements for analysis of shell structures. *International Journal for Numerical Methods in Engineering*. 1999;46:433-55.
- [172] Hibbett, Karlsson, Sorensen. *ABAQUS/standard: User's Manual: Hibbett, Karlsson & Sorensen; 1998.*
- [173] Knight N. Raasch challenge for shell elements. *AIAA journal*. 1997;35:375-81.
- [174] Dunavant D. High degree efficient symmetrical Gaussian quadrature rules for the triangle. *International Journal for Numerical Methods in Engineering*. 1985;21:1129-48.
- [175] Sussman T, Bathe KJ. 3D-shell elements for structures in large strains. *Computers & Structures*. 2013;122:2-12.
- [176] Kim J, Bathe KJ. Towards a procedure to automatically improve finite element solutions by interpolation covers. *Computers & Structures*. 2014;131:81-97.
- [177] Babuška I, Rheinboldt WC. A-posteriori error estimates for the finite element method. *Internation-*

tional Journal for Numerical Methods in Engineering. 1978;12:1597-615.

[178] Zienkiewicz OC, Zhu JZ. A simple error estimator and adaptive procedure for practical engineering analysis. International Journal for Numerical Methods in Engineering. 1987;24:337-57.

[179] Babuška I, Rheinboldt WC. Error estimates for adaptive finite element computations. SIAM Journal on Numerical Analysis. 1978;15:736-54.

[180] Ainsworth M, Oden JT. A posteriori error estimation in finite element analysis: John Wiley & Sons; 2011.

[181] Ainsworth M, Oden JT. A posteriori error estimation in finite element analysis. Computer Methods in Applied Mechanics and Engineering. 1997;142:1-88.

[182] Cheng H, Gupta K. An historical note on finite rotations. Journal of applied Mechanics. 1989;56:139-45.

[183] Riks E. An incremental approach to the solution of snapping and buckling problems. International Journal of Solids and Structures. 1979;15:529-51.

[184] Wempner GA. Discrete approximations related to nonlinear theories of solids. International Journal of Solids and Structures. 1971;7:1581-99.

[185] Ramm E. Strategies for tracing the nonlinear response near limit points: Springer; 1981.

[186] Crisfield MA. A fast incremental/iterative solution procedure that handles “snap-through”. Computers & Structures. 1981;13:55-62.

[187] Schweizerhof K, Wriggers P. Consistent linearization for path following methods in nonlinear FE analysis. Computer Methods in Applied Mechanics and Engineering. 1986;59:261-79.

[188] Riks E. The application of Newton’s method to the problem of elastic stability. Journal of applied Mechanics. 1972;39:1060-5.

요 약 문

PU 기반 셀 유한요소

유한요소법은 셀 구조물의 선형 및 비선형 해석에 가장 널리 사용되는 수치해석기법이며, 지난 수십년간 보다 더 정확하고 일관된 수치적 결과를 얻기 위한 많은 연구가 활발하게 진행되었다. 하지만 눈부신 연구결과에도 불구하고, 응력이 집중되거나 특이해가 존재하는 특정영역에서의 유한요소 해는 상당한 오차를 보여주며 이러한 문제점을 해결하기 위한 노력은 지속적으로 진행 중이다.

최근, 기존 절점에 새로운 자유도를 추가 함으로써 요소 및 절점의 개수를 증가시키지 않고 고차 형상함수를 구성할 수 있는 PU 기반 유한요소법이 제안되었다. PU 기반 유한요소법은 기존 형상정보를 변화시키지 않고 정교한 수치 해석을 얻을 수 있다는 장점으로 2D 또는 3D 솔리드 요소의 범위에서 큰 주목을 받아 왔다. 셀 유한요소의 경우에는 셀 두께가 작아짐에 따라 발생하는 잠김현상에 대한 처리 기법이 제안되지 않아 PU 기반 유한요소법이 적용되는데 문제가 존재 했다.

본 학위논문에서는 PU 기반 3 절점 삼각형 및 4 절점 사각형 셀 유한요소들을 제안하였다. 기존 변형률과 고차 형상함수의 변위에 의한 변형률을 분리 하였으며 분리된 변형률에 각각 다른 대체변형률장을 구성함으로써 제안된 셀 요소의 잠김현상을 처리 할 수 있었다. 잘 알려진 수렴문제들을 통하여 기존에 존재 하는 셀 요소들과 성능을 비교 평가하였다. 또한 응력 집중을 가진 축 문제, 기하학적 거동이 복잡한 실제 셀 문제를 풀어봄으로써 PU 기반 셀 유한요소의 뛰어난 성능을 입증하였다.

또한, PU 기반 변위보간을 사용하여 3 절점 삼각형 셀 요소의 면거동 성능향상에 대한 가능성을 제안하였다. 4 절점 사각형 셀 유한요소의 경우, 비적합 모드 및 대체 변형장등을 사용하여 면거동의 성능을 개선할 수 있지만, 3 절점 삼각형 셀 요소의 경우에는 면거동 성능향상에 대한 적합한 방법론이 제시되지 않았다. 본 논문에서는 PU 를 사용한 변위보간을 통해 기존 삼각형 면거동을 효율적으로 보강하였으며 선형 및 비선형 영역에서 다양한 문제를 풀어 보면서 제안된 요소 셀 유한요소를 비교 검증하였다. 선형 및 비선형영역에서, PU 기반 변위보간을 통한 셀의 면 거동은 4 절점 사각형 셀 요소에서 사용되는 비적합 모드와 비교하여 뛰어난 성능을 보여주었다.

핵심어: PU 기반 유한 요소법; 셀 유한요소; 잠김현상; 비선형 해석; 대변위 및 대회전